Numerical modelling of natural convection of binary mixtures: case of a helium buoyant jet in an air-filled enclosure

Tran H.-L.

▶ **To cite this version:**

Tran H.-L.. Numerical modelling of natural convection of binary mixtures: case of a helium buoyant jet in an air-filled enclosure. Fluids mechanics [physics.class-ph]. Université Pierre et Marie Curie - Paris VI, 2013. English. NNT : . tel-00920867

HAL Id: tel-00920867

https://theses.hal.science/tel-00920867

Submitted on 20 Dec 2013

HAL is a multi-disciplinary open access archive for the deposit and dissemination of scientific research documents, whether they are published or not. The documents may come from teaching and research institutions in France or abroad, or from public or private research centers.

L'archive ouverte pluridisciplinaire **HAL**, est destinée au dépôt et à la diffusion de documents scientifiques de niveau recherche, publiés ou non, émanant des établissements d'enseignement et de recherche français ou étrangers, des laboratoires publics ou privés.

THÈSE DE DOCTORAT DE
l'UNIVERSITÉ PIERRE ET MARIE CURIE

Spécialité

Mécanique des Fluides

École doctorale Sciences Mécaniques, Acoustique, Electronique et Robotique de Paris (SMAER)

Présentée par

Huong-Lan TRAN

Pour obtenir le grade de

DOCTEUR de l'UNIVERSITÉ PIERRE ET MARIE CURIE

Sujet de la thèse :

Numerical modelling of natural convection of binary mixtures: case of a helium buoyant jet in an air-filled enclosure

soutenue le 30 Septembre 2013

devant le jury composé de :

M. Pierre-Yves Lagrée	Examinateur
Mme Anne Davaille	Rapporteur
M. Stéphane Viazzo	Rapporteur
M. Gilles Bernard-Michel	Examinateur
M. Patrick Le Quéré	Examinateur
Mme Anne Sergent	Examinateur

Preface

This dissertation is the result of my work during my PhD between 11/2009 and 9/2013. During this period, I spent my time in two laboratories: LTMF (Laboratoire d'Etudes des Transferts et de Mecanique des Fluides) in CEA, Saclay and LIMSI (Laboratoire d'Informatique pour la Mécanique et les Sciences de l'Ingénieur) in Orsay. My supervisors consist of three people: Patrick Le Quéré in LIMSI, Anne Sergent in LIMSI and Gilles Bernard-Michel in CEA. Anne began to participate in my work from 2011 and continued until my final defense on 30 September 2013.

To accomplish this thesis, I have learned a lot of things that I hadn't had experience before. Fluid mechanics and CFD codes were completely new to me, since I had had all my education in mathematics. It was a lot of fun and fascination to deal with something you had no idea about and began to master them. However, this route is not easy. I would not have been able to accomplish what I have presented in this dissertation without the help and encouragement from many people.

I would like to thank in the first place my advisors, who have given me this interesting subject and all the financial support for pursuing this work during nearly four years. Thanks to their patience, their guidance and encouragement during this time are the essential factors for my accomplishment.

Life in laboratories would be very boring without my nice colleagues and friends. We have had meals together, we have taken formations together, we have discussed and shared our ups and downs. And I would like to thank you for all these memories.

I also want to express my sincere gratitude to all my Vietnamese friends who have shared this period of life with me in France. In a new country everything was new and many difficulties came that I had not expected before. But you have made my winters less cold and my springs more beautiful. I own you my deepest thanks.

My last thank is to my beloved family, who have been always by my side over this long way. This dissertation is devoted to you. And I am happy that I can make you proud of me.

An old road is about to close and many new roads are going to open in front of me. I have grown up a lot along this way. Now it is time to begin a new travel.

Simulation numérique de convection naturelle d'un mélange binaire : cas d'un panache d'hélium en cavité

Résumé

Ce travail porte sur l'étude des mécanismes de mélange et dispersion d'un jet d'hélium dans une cavité semi-confinée remplie d'air. Ce phénomène est ici pris comme un cas mdèle de l'injection d'un gaz léger dans un fluide plus lourd, produisant ainsi un panache. Ce thème est en lien avec la sécurité des systèmes basés sur l'hydrogène.

Un modèle numérique a été développé combinant les conditions limites adéquates avec les équations de conservation de la masse du mélange, d'une espèce, de la quantité de mouvement, ainsi que la loi d'état et la variation des propriétes physiques.

En premier lieu, le panache d'un mélange eau glycérol est considéré comme cas de validation par comparaison avec des résultats expérimentaux [Rogers & Morris 09]. Le développement d'un panache axisymétrique est modélisé pour de grands nombres de Grashof et petit nombres de Reynolds d'injection. Un bon accord est obtenu pour la vitesse d'ascension du panache ainsi que le type et la forme de la tête. Un loi d'échelle modifiée est proposée.

Dans le cas du mélange hélium-air, une cavité 2D est tout d'abord considérée. Les lois d'échelle auto-similaires pour des panaches plans stationnaires en milieu infini [Gebhart et al. 88] ont été reproduites numériquement pour les profils de vitesse verticale et de masse volumique sur l'axe, pour les temps avant l'impact du panache sur le plafond. Puis une cavité cylindrique a été considérée pour modéliser une expérience menée au CEA [Cariteau & Tkatschenko 12]. Les résultats numériques sont comparés aux données des expériences et d'un benchmark numérique. L'effet de l'hypothèse d'axisymétrie a été mis en évidence.

Mots-clés mélange binaire, simulation, jet, panache, mélange hélium-air, mélange eau-glycerol

Numerical modelling of natural convection of binary mixtures: case of a helium buoyant jet in an air-filled enclosure

Abstract

This study focuses on the understanding of the dispersing and mixing mechanisms of helium in air in a semi-confined cavity. This phenomena is an example of a low-density fluid injected in a high-density ambient fluid which results in a buoyant plume. This is an important safety issue for all hydrogen-based systems. A numerical model has been developed combining the appropriate boundary conditions with the conservation equations for the mixture mass, species mass, momentum and the state law of the mixture as well as the variation laws of the physical properties. First a laminar starting plume of a glycerol-water mixture is considered as a validation test-case by comparison with experimental data [Rogers & Morris 09]. The propagation of the axisymmetric buoyant-jet is modeled for large Grashof numbers and small injection Reynolds numbers. A good agreement has been found for the ascent velocity as well as the two types of head shape. A modified scaling law of the ascent velocity versus a modified Reynolds number is proposed to take into account for the kinetic viscosities of both fluids. For the helium-air mixture, a 2D planar air-filled cavity was first considered. The auto-similar scaling laws for steady plane plumes in unconfined environment [Gebhart et al. 88] have been reproduced for the vertical velocity and the density profiles along the vertical centerline, when considering moments before the plume impact on the top wall. Then a cylindrical container is considered to model the CEA experiment [Cariteau & Tkatschenko 12]. Numerical results are compared to experimental data and to a numerical benchmark. The effect of the axisymmetry assumption is evident.

Keywords binary mixture, simulation, buoyant jet, starting plume, helium-air, glycerol-water

Résumé

0.1 Introduction

Les piles à combustible-hydrogène sont de nos jours plus en plus présents dans l'industrie, non seulement en tant que vecteur énergétique mais aussi comme source d'énergie. Néanmoins l'usage de l'hydrogène n'est pas sans inconvéniants et elle présente de nombreux risques.

Le CEA a contribué à évaluer et à réduire les risques liés à l'usage de l'hydrogène. L'un des objectifs principal était d'étudier expérimentalement la dispersion de l'hélium (comme remplacement à l'hydrogène) injecté verticalement dans la cavité cubique: GAMELAN. La distribution verticale de l'hélium a été mesurée. Pour les panaches pures, une distribution linéaire de la concentration a été mesurée pour une buse de 5 mm de diamètre alors que le modèle de Worster and Huppert (1983) prédisait un profil parabolique. Ce modèle est essentiellement basé sur les propriétés d'un coefficient d'entrainment α. Un benchmark a été organisé (BERNARD-MICHEL *et al.* 2012) afin d'analyser les structures cohérentes du jet à l'aide de calcul CFD mais les résultats obtenus avec des modèles RANS ($k-\epsilon$) et LES-2D n'étaient pas satisfaisants.

Le travail ci-présent a pour but de produire une modélisation précise des écoulements de type panache et de retrouver les résultats expérimentaux obtenus sur GAMELAN. Ce document est organisé comme suivant: Dans le chapitre deux, on décrit les modèles physiques des écoulements étudiés. Puis on introduit les modèles numériques associés dans le chapitre trois. Au chapitre quatre, l'étude des panaches 2D-turbulents et laminaires axisymmétrique sont présents et des comparaisons avec une expérience de référence (Roger and Moris 2009) sont effectuées. Dans le chapitre cinq, on présente des simulations de panaches axisymmétriques ainsi que des comparaisons avec les résultats obtenus sur GAMELAN (Cariteau and Tkatschenko 2012).

0.2 Modélisation physique

Le problème du mélange de deux fluides miscibles dans un domaine semi-confiné est modélisé par un fluide binaire à température et pression constante. En particulier, deux mélanges sont traités: le mélange glycérol-eau et le mélange hélium-air. Dans le cas du mélange glycérol-eau, le glycérol est décrit comme l'espèce 1. Dans le cas hélium-air, l'hélium est dénoté comme espèce 1. La fraction massique le l'espèce 1, Y_1, est le ratio de la masse de l'espèce 1, m_1, et la masse du mélange m. Le fraction massique de l'espèce 2, Y_2, est reliée à Y_1 par la relation

$$Y_1 + Y_2 = 1 \tag{1}$$

Le mélange est représenté par une densité ρ et une vitesse moyenne $\mathbf{u}$. Les équations régissant le problème, sont l'équation de continuité, une équation de transport pour l'espèce 1, une équation de quantité mouvement et une équation reliant le densité et la fraction massique qui dépend du mélange. A partir de ces équations (sauf l'équation de quantité de mouvements), on déduit une contrainte de divergence pour le champs de vitesse. Dans ce qui suit on résume l'ensemble complet des équations du problème sous une forme adimensionnée pour les deux mélange cités ci-dessus.

- Mélange glycérol-eau

$$\nabla.\mathbf{u} = 0 \tag{2}$$

$$\frac{\partial \rho Y_1}{\partial t} + \nabla.(\rho Y_1 \mathbf{u}) = \frac{1}{ReSc}\nabla.(D\rho\nabla Y_1) \tag{3}$$

$$\frac{\partial \rho \mathbf{u}}{\partial t} + \nabla.(\rho \mathbf{u} \otimes \mathbf{u}) = -\nabla\pi + \frac{1}{Re}\nabla.\underline{\underline{\tau}} + \frac{1}{Fr}(\rho - \rho^0)\mathbf{z} \tag{4}$$

$$\rho = 1 + (\frac{\overline{\rho_1}}{\overline{\rho_2}} - 1)Y_1 \tag{5}$$

- Mélange hélium-air

$$\nabla.\mathbf{u} = \frac{(\epsilon_M^{21} - 1)}{ReSc}\nabla.(D\rho\nabla Y_1) \tag{6}$$

$$\frac{\partial \rho Y_1}{\partial t} + \nabla.(\rho Y_1 \mathbf{u}) = \frac{1}{ReSc}\nabla.(D\rho\nabla Y_1) \tag{7}$$

$$\frac{\partial \rho \mathbf{u}}{\partial t} + \nabla.(\rho \mathbf{u} \otimes \mathbf{u}) = -\nabla\pi + \frac{1}{Re}\nabla.\underline{\underline{\tau}} + \frac{1}{Fr}(\rho - \rho^0)\mathbf{z} \tag{8}$$

$$\rho = \frac{1}{1 + (\epsilon_M^{21} - 1)Y_1} \tag{9}$$

Dans l' équation précédente $\overline{\rho_1}$ et $\overline{\rho_2}$ représente la densité du glycérol pure et de la densité de l' eau, respectivement. π est la pression et $\underline{\underline{\tau}}$ représente le tenseur des contraintes visqueuses d' un fluide Newtonien tel que :

$$\underline{\underline{\tau}} = \mu\left((\nabla\mathbf{u} + \nabla^T\mathbf{u}) - \frac{2}{3}\nabla.\mathbf{u}.\underline{\underline{I}}\right) \tag{10}$$

avec $\underline{\underline{I}}$ la matrice identité.

Les paramétres adimensionnés qui apparaissent dans les équation (3), (4), (6), (7), (8) and (9) sont

Nombre de Reynolds Re

$$Re = \frac{U_r L_r}{\nu_r}$$

Nombre de Froude Fr

$$Fr = \frac{U_r^2}{gL_r}$$

Rapport de masse molaire ϵ_M^{21}

$$\epsilon_M^{21} = \frac{M_2}{M_1}$$

Nombre de Schmidt Sc

$$Sc = \frac{\nu_r}{D_r}$$

tel que L_r, U_r, ν_r, D_r sont les paramètres de référence pour: la longueur, vitesse, viscosité cinématique et diffusivité massique, respectivement. g est la gravité. M_1 et M_2 sont les masses molaires des espèces 1 et 2, respectivement.

La variation des propriétés physiques comme le coefficient de diffusion massique D et la viscosité dynamique ν d'un mélange sont considérés. Les estimations de ces quantités en fonction des fractions massiques est donnés pour le mélange glycérol-eau et le mélange hélium-air.

0.3 Méthode Numérique

Le système (6), (7), (8) contient six variables: ρ, Y_1, $\mathbf{u}$, μ, D et π. On ajoute à ce système trois équations qui décrivent la variation de ρ, μ et D avec Y_1. Les six équations sont complétés par les conditions aux limites et les conditions initiales.

Le système est discrétisé en temps et en espace afin d'obtenir les équations discrétisés qui seront intégrés par rapport au temps en utilisant une méthode d'avancement en temps.

À chaque pas de temps, les équations sont résolus selon une certaine séquence tel que:

- L' équation de transport des espèces (7) est résolu.
- Les nouvelles propriétés physiques ρ, D, μ sont calculés.
- La pression et la vitesse sont calculés par la méthode de correction de pression en utilisant les équations (8) et (6).

0.3.1 Discrétisation spatiale

Les équations sont discrétisées spatialement par la méthode des volumes finis sur un maillage décallé. Les termes de diffusion sont approchés par deuxième ordre différence central. Les termes convectives sont calculés par deuxième ordre différence central ou troisième ordre schéma QUICK.

0.3.2 Discrétisation temporel

La discrétisation temporel est réalisé par un schéma semi-implicite en utilisant un schéma d' Euler implicite de deuxième ordre (BDF2) pour les termes diffusives. Les termes convectives sont traités explicitement par un schéma de Adams-Bashforth de deuxième ordre.

Le couplage pression-vitesse est calculé par une méthode de projection avec un pas de temps fractionnaire.

0.3.3 Couplage vitesse-pression: méthode de projection

Le couplage pression-vitesse est calculé par une méthode de projection avec un pas de temps fractionnaire. À chaque pas de temps trois étapes ont lieu:

- Premièrement: La pression est traité explicitement et un champ de vitesse provisoire est calculé.
- Deuxièmement: la correction de pression est calculé.
- Finalement: les nouveaux champs de vitesses et de pression sont calculés.

La méthode de projection est modifié afin de considérer l' écoulement à travers les frontières du domaines.

0.4 Détermination des conditions aux limites entrantes

Dans le cadre de notre étude, il est nécessaire de spécifier les conditions aux limites entrantes en vitesse $w_i(r,t)$ et du profil de concentration $Y_{1,i}(r,t)$. Le flux de masse total F_t est composé du flux convectif F_c ainsi que du flux diffusif F_d. Par les suite, deux cas différents seront traités 0.4.1 et 0.4.2.

0.4.1 Flux diffusif négligeable (cas du mélange eau-glycérol)

1. Y_1, profil plat : $Y_{1,i}(r,t) = \overline{Y_1}$
2. w, profil plat : $w_i^f = \overline{w}$

0.4.2 Flux diffusif important (cas du mélange air-hélium)

1. w en profil plat

$$w_i^f(t) = \overline{w} + \frac{1}{l(\Omega_i} \frac{(\epsilon_M^{21} - 1)}{ReSc} \int_{\partial\Omega_i} D\rho \frac{\partial Y_1}{\partial z} dT \tag{11}$$

2. Y_1 en profil plat

$$Y_1{}_i^{n+1}(r) = \frac{z_2}{z_1 - z_2} Y_1^{n+1}(z_1) - \frac{z_1}{z_1 - z_2} Y_1^n(r, z_2) \tag{12}$$

avec $$Y_1^{n+1}(z_1) = \begin{cases} \dfrac{(n+1)\delta t}{t_c}\overline{Y_1} & \text{if} \quad (n+1)\delta t \leq t_c \\ \overline{Y_1} & \text{if} \quad (n+1)\delta t > t_c \end{cases}$$

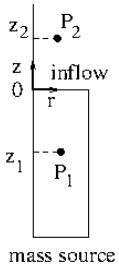

Le retard t_c est important si $\overline{w_i}$ est petit et vice versa. La position z_2 correspond à la position verticale la plus proche du fluide entrant (pour un maillage donné). z_1 est choisi près de l'injection si $\overline{w_i}$ est importante, et loin du point d'injection sinon. Il est nécessaire de s'assurer que $w_i(r,t)$ soit toujours positif.

0.5 Panaches démarrants laminaires à haut nombre de Schmidt: comparaison avec les données expérimentales

0.5.1 Paramètrage numérique et méthode d'analyse

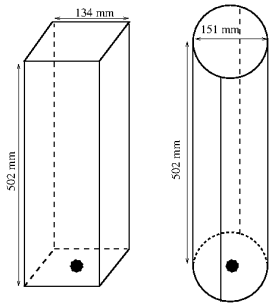

Figure 1: Gémotrie de l'expérience eau-glycérol [Rogers et Morris, 2009] (figure de gauche) et du domaine de calcul (figure de droite)

Paramètrage numérique L'expérience numérique est réalisée dans un container parallélépipède rectangle (figure 1) de section $13.4 \times 13.4\ cm^2$ et de hauteur $50.2\ cm$ dans les conditions normaux de pression-température ($22°C$ et $1atm$). Une solution d'eau-glycérol légèrement moins dense que la solution ambiante est injectée dans le container par une entrée circulaire de diamètre $d_i = 30mm$ située à la base du container. 13 cas test sont choisi à partir de cette expérience. Leur propriétés

physiques et ainsi que les paramètres adimensionnés associés sont présentés dans les tables 1 et 2. L'écoulement est supposé axisymmétrique. Les équations du mouvement sont résolu sous l'hypothèse axisymmétrique. Le container de la simulation numérique est un cylindre de même volume et hauteur que le container du système expérimental (voir figure1).

Case	ρ_i	Y_{1i}	ρ_a	Y_{1a}	$\frac{\rho_a-\rho_i}{\rho_a}$	ν_i	ν_a	$\frac{\nu_i}{\nu_a}$	Gr	Sc_a
D1	1174.5	0.6656	1177.54	0.6771	0.00258	14.19	15.47	0.917	1.3×10^7	64128
D2	1175.2	0.6683	1179.7	0.6852	0.00381	14.47	16.48	0.878	1.7×10^7	70976
D4	1204.5	0.7786	1215.95	0.8218	0.00942	37.87	60.32	0.628	2.8×10^6	592574
D5	1213.5	0.8125	1216.055	0.8222	0.00210	54.32	60.59	0.896	8.2×10^5	597078

Table 1: Propriétés physiques des cas tests glycerol-eau du panache forcé: ρ_a et ρ_i sont en $[kg\ m^{-3}]$, ν_a et ν_i sont en 10^{-6} $[m^2\ s^{-1}]$.

Caractéristiques du panache Les quantités utilisée pour caractériser le panache sont sa hauteur h, le diamètre de la conduite d_c, le diamètre de son tête d_h, la hauteur à laquelle se situe le tête l_h, le rapport d'aspect de le tête $RF_h = \frac{d_h}{l_h}$. Ces paramètres sont illustrés sur la Fig. 2

0.5.2 Comparaison avec l'expérience de [Rogers and Morris, 2009]

Vitesse ascendante la vitesse ascendante w_h reste stationnaire en temps pour chacun des 13 panaches simulés, ce qui est en accord avec les résultats de [Rogers

Case	$Q\ (m^3/s)$	Re_i	Ri_i
D1,1	3.3×10^{-8}	0.987	1.746
D1,2	6.7×10^{-8}	2.004	0.424
D1,3	1.67×10^{-7}	4.995	0.068
D1,4	2.67×10^{-7}	7.986	0.027
D1,5	4.0×10^{-7}	11.964	0.012
D5,1	1.33×10^{-7}	1.039	0.088
D5,2	2.0×10^{-7}	1.563	0.039

Case	$Q\ (m^3/s)$	Re_i	Ri_i
D4,1	3.3×10^{-8}	0.370	6.420
D4,2	6.7×10^{-8}	0.751	1.558
D4,3	1.33×10^{-7}	1.491	0.395
D4,4	2.67×10^{-7}	2.992	0.098
D4,5	4.0×10^{-7}	4.483	0.044
D2	2.67×10^{-7}	7.831	0.039

Table 2: Débit volumique et paramètres adimensionnés des cas tests glycérol-eau du panache forcé.

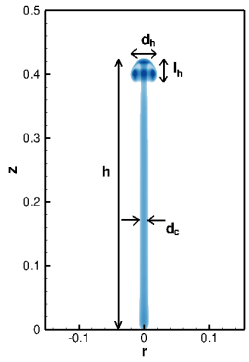

Figure 2: Les caractéristiques principales d'un panache.

and Morris, 2009]. Sur la figure 3-a les données expérimentales sont représentées par des symboles et celles provenant de résultats numériques sont représentées en traits pleins. L'écart de temps physique par paire de courbes croît quand la vitesse d'injection décroît. La superposition d'une paire de courbe correspond à une translation temporelle suivant l'écart en question (voir fig. 3-b). Ceci indique que les vitesses ascendantes calculées sont très proches (de l'ordre de 3%) de celles trouvées expérimentalement.

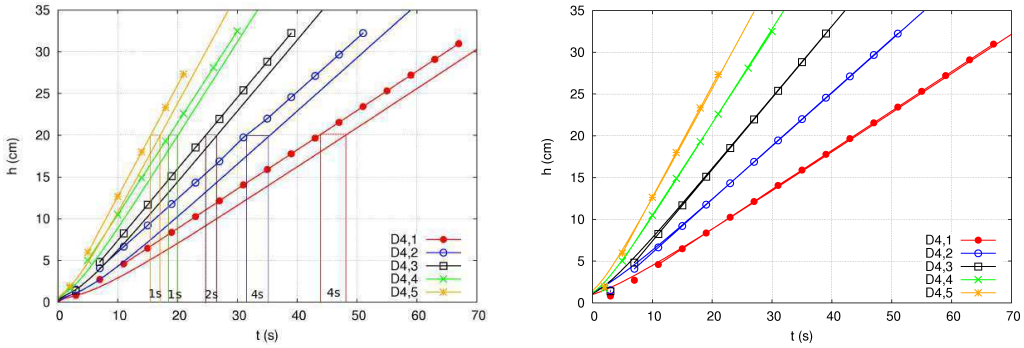

(a) (b)

Figure 3: a) Évolution en temps de la hauteur du panache dans le cas D4. b) a) Après translation temporelle des résultats numériques.

Pour décrire les données expérimentales, [Rogers and Morris, 2009] propose la relation empirique suivante

$$Ri_h = (4.3 \pm 0.2) Re_i^{-0.96 \pm 0.05} \tag{13}$$

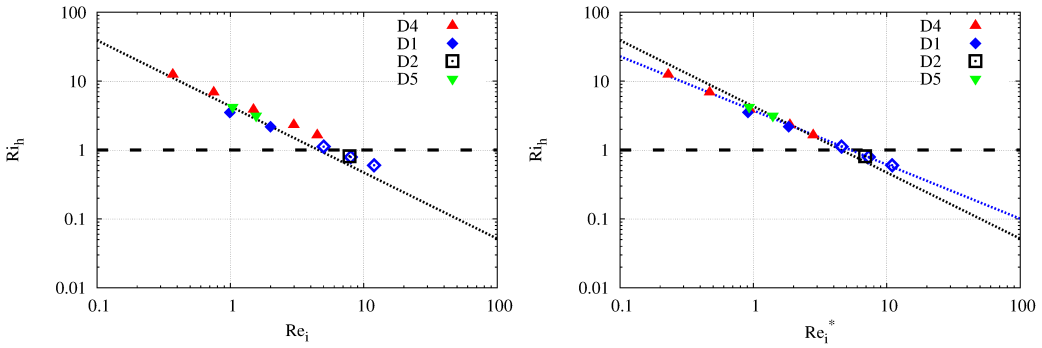

(a) (b)

Figure 4: La dépendence de Ri_h à Re_i ou à Re_i^* pour les résultats numériques. Les traits noirs et pointillés sont $Ri_h = 4.3Re_i^{-0.96}$ (a) et $Ri_h = 4.3Re_i^{*-0.96}$ (b). Le trait bleu et pointillé est $Ri_h = 3.74Re_i^{*-0.78}$.

où $Ri_h = \frac{g(\rho_a - \rho_i)d_i}{\rho_a w_h^2}$ and $Re_i = \frac{d_i \overline{w_i}}{\nu_i}$.

Les résultats numériques représentés par des symboles sur la Fig. 4a, indiquent que la variation de Ri_h avec Re_i n'est pas strictement alignée sur une droite. Même dans le cas D4, les résultats numériques ne sont pas conformes à la relation $Ri_h = 3.2Re_i^{-0.91}$. Si maintenant Re_i est remplacé par $Re_i^* = \frac{d_i \overline{w_i}}{\nu_a}$ les résultats deviennent alignés avec une droite. La courbe bleue en pointillée correspondante à la relation suivante

$$Ri_h = 3.74Re_i^{*-0.78} \tag{14}$$

fournit une meilleure concordance de Rih en fonction des Ri_e (voir fig.4b).

Afin de décrire la vitesse ascendante du panache dans un domaine ouvert, on remplace l'exposant -0.78 par -1 dans (14). Cela donne :

$$w_h = 0.583 \left(\frac{g(\rho_a - \rho_i)Q}{\rho_a \nu_a} \right)^{1/2} \tag{15}$$

Les simulations du cas D4,5 permettent d'examiner la relation (15) dans une cavité de diamètre croissant. Sur la figure 5, la vitesse ascendante w_h est représentée en fonction du diamètre de la cavité. Nous observons que w_h converges vers la valeur calculée avec la formule (15). Pour une cavité plus grande (diamètre=402mm), l'écart asymptotique n'est que moins de 1%. Cela indique que la formule (15) est plus adaptée à décrire la vitesse ascendante des panaches en domaine ouvert.

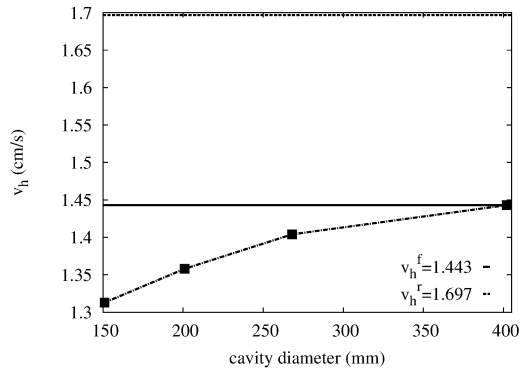

Figure 5: Vitesse ascendante du cas D4, 5 en fonction du diamètre de la cavité. v_h^f est la valeur calculée à partir de (15). v_h^r est la valeur calculée à partir d'équation 4 dans [Rogers and Morris, 2009].

Morphologie de la tête du panache Les têtes confinées du cas D5,2 sont comparées (fig 6.). Les résultats numériques capturent bien non seulement le profile globale de la tête mais aussi l'anneau tourbillonnaire qui se développe à l'intérieur de la tête. La largeur de la tête est de 10% plus petite et la longueur de la tête est de 5% plus large que les données expérimentales.

Les têtes dispersées ne restent pas compactes et ne contiennent pas un vortex stable et sont comparées dans la figure. 7 pour cas D2. Les résultats calculés obtiennent bien la forme générale de la tête, sauf pour l'instabilité développée au bord de la tête. Cela peut être dû à l'hypothèse axisymétrique parce que les têtes dispersées sont accompagnées par une petite asymétrie.

Le résumé des types de tête de simulations numériques sont présentés dans le tableau 3. Sauf pour le cas D1,3, dans lequel nous avons dispersé les têtes pour $Ri_h > 1$, types de tête concordent bien avec le critère proposé par [Rogers and Morris, 2009].

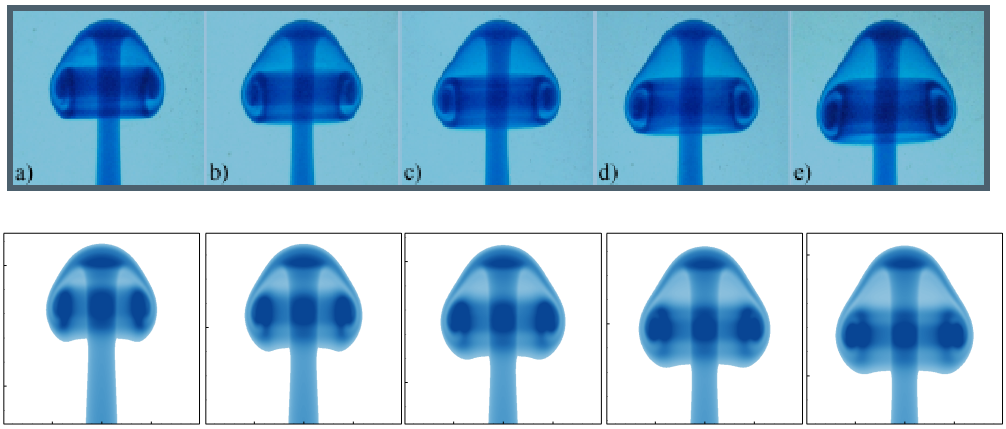

Figure 6: Les têtes confinées pour le cas D5, 2. De la première à la dernière image de la séquence, h augmente de 20.5 cm à 35.2 cm. En haut: résultats expérimentaux: chaque image est de 5 s d'intervalle. De la première à la dernière image, la taille de la tête augmente de 1.9 cmx 2.3 cm ($l_h \times d_h$) à 2.4cmx 3.1cm. En bas: la simulation numérique: chaque image est de 8,3 s d'intervalle. De la première à la dernière image, la taille de la tÃªte augmente de 2.0cm x 2.3cm à 2.6cm x 2.8cm.

Cas	Type de tête	Ri_h
D1,1	confinée	3.512
D1,2	confinée	2.181
D1,3	dispersée	1.116
D1,4	dispersée	0.786
D1,5	dispersée	0.597
D5,1	confinée	4.235
D5,2	confinée	3.149

Cas	Type de tête	Ri_h
D4,1	confinée	12.44
D4,2	confinée	6.854
D4,3	confinée	3.846
D4,4	confinée	2.312
D4,5	confinée	1.635
D2	dispersée	0.809

Table 3: Types de têtes obtenues avec des simulations numériques pour 13 plumes glycérol-eau.

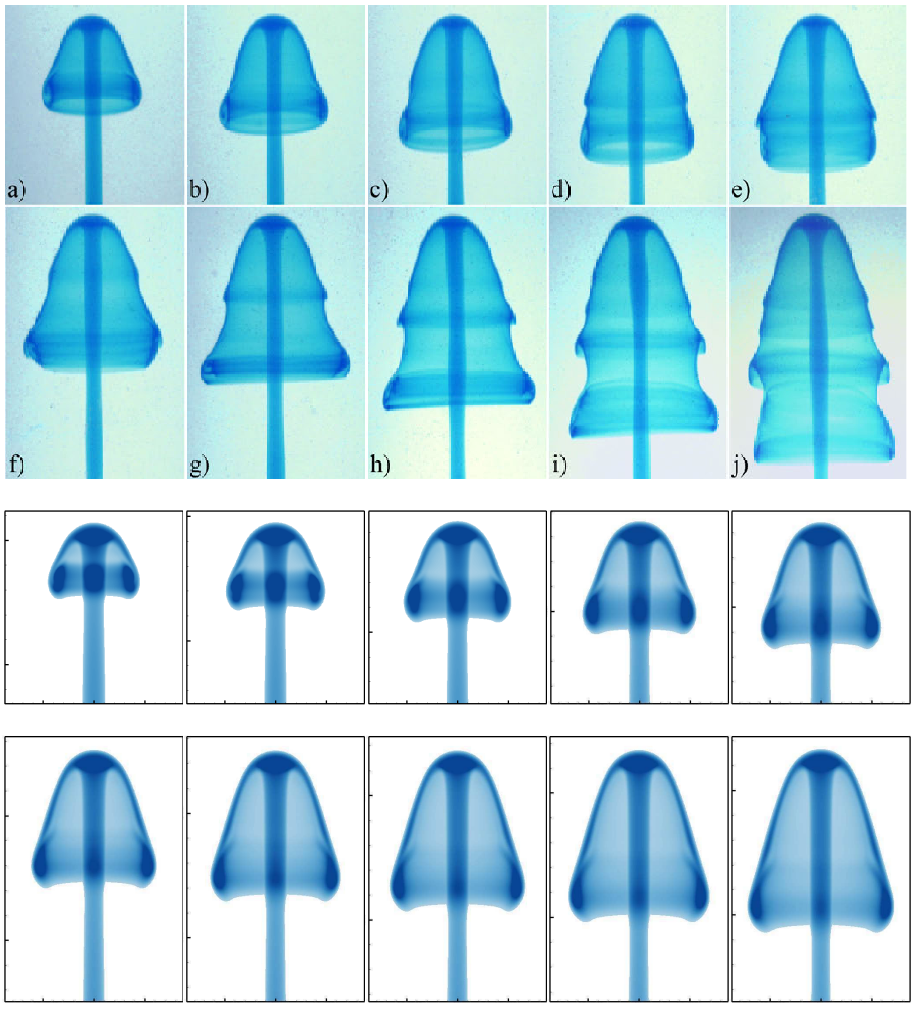

Figure 7: Des têtes dispersées dans le cas D2. De la première à la dernière image de la séquence, h augmente de 10.4 cm à 31.0 cm. En haut: résultats expérimentaux: chaque image est de 2 s d'intervalle. La taille de la première image est $l_h = 1.6$ cm et $d_h = 2.1$ cm. En bas: chaque image est de 2 s d'intervalle. La taille de la première image est $l_h = 1.6$ cm et $d_h = 1.9$ cm

0.6 Jets flottants du mélange hélium-air ou de l'hélium dans une cavité semi-confinée remplie d'air

0.6.1 Simulations plan du panache

Configuration et installation numérique L'enceinte est une cavité carrée de 1m de largeur (W) et une hauteur de 1 m (H) remplie d'air (Fig. 8). L'entrée est de 20 mm de large (d_i) et est située dans le centre du fond. Une ouverture d'une largeur de 20mm (d_o) située au pied d'une paroi latérale pour la dépressurisation.

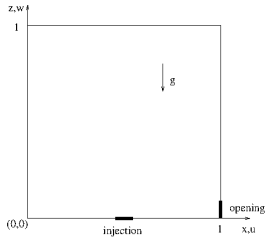

Figure 8: Une cavité carrée 2D avec une petite ouverture pour la dépressurisation.

Les trois paramètres adimensionnés de la situations d'injection sont donnés dans le tableau 4. L'injection vitesse $\overline{w_i}$ est fixée à $1.51 \times 10^{-3}\ m/s$ dans trois cas. Les deux premiers cas correspondent à l'injection d'un mélange air-hélium et le dernier cas à l'injection d'hélium pur.

$Y_{1\,i}$	Re_i	Ri_i	Sc_i	Gr
0.01	1.778	4.1	0.245	2.53×10^9
0.1	0.942	42.2	0.463	1.65×10^{10}
1.0	0.258	406	1.689	3.71×10^{10}

Table 4: Paramètres des trois situations d'injection des plumes hélium-air.

Comparaison avec les lois d'échelle et théorie de la similitude des plumes plan laminaire Tout d'abord, nous étudions la loi de décroissance des $w_c(z)$ et $(\rho_a - \rho_c)(z)$ pour le cas $Y_{1i} = 0.01$. Les profils de la vitesse verticale de w et $\rho_a - \rho$ le long de la ligne centrale sont présentés dans la figure. 9a à quatre moments différents avant le panache entre en collision avec la paroi supérieure jusqu'à ce que

$t = 12.0$.

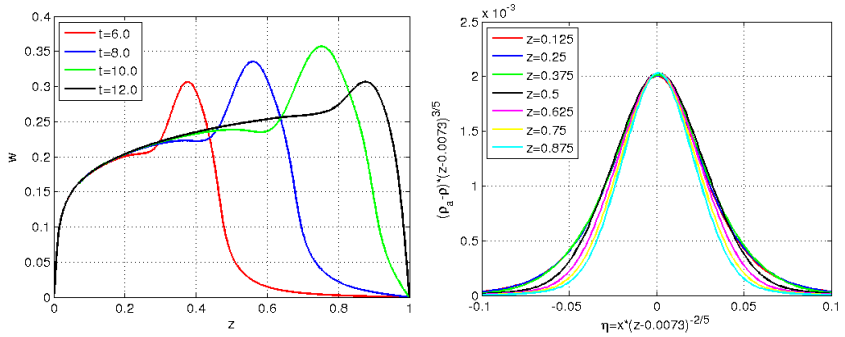

(a) (b)

Figure 9: Cas $Y_{1i} = 0.01$ avec 1024x1024 grille: a) profil de vitesse verticale le long de l'axe à $t = 6.0$, $t = 8.0$, $t = 10.0$ et $t = 12.0$ b) les profils horizontaux de densité différente à des hauteurs différentes à $t = 10.0$ avec un changement de variables:. $(\rho_a - \rho).(z - 0.0073)^{3/5}$ est tracée en fonction des $\eta = x.(z - 0.0073)^{-2/5}$.

Les parties inférieures des quatre courbes de la fig. 9a effondrement sur la même courbe, qui montre un comportement stable du conduit. Un raccord de la partie de conduit à partir de $z = 0$ à $z = 0.5$ donne

$$w_c = 0.2835\overline{z}_w^{1/5} \tag{16}$$

où $\overline{z}_w = z - 0.0077$.

De même pour la différence de densité, on a un montage

$$\rho_a - \rho_c(z) = 0.0020\overline{z}_\rho^{-3/5} \tag{17}$$

où $\overline{z}_\rho = z - 0.0073$.

Nous modifions l'echelle $w(x, z)$ et x et l'intrigue $w(x, z)(z - 0.0077)^{1/5}$ en fonction des $\eta_w = x(z - 0.0077)^{-2/5}$. Toutes les courbes ci-dessous $z = 0.5$ effondrement sur une courbe dans la région $-0.05 \leq \eta_w \leq 0.05$, comme dans la Fig. 9b. Il implique que les courbes $w(x, z)$ sont auto-similaire. L'auto-similitude des courbes pour $\rho_a - \rho(x, z)$ peut être représentée de façon similaire.

0.6.2 Simulations du panache axisymmetric

Description des cas de test La configuration pour la simulation numérique est basée sur le dispositif expérimental de GAMELAN ([Cariteau and Tkatschenko, 2012]), dont nous voulons reproduire les résultats. Les résultats expérimentaux montrent que l'hélium dont les profils de fractions volumiques ne dépendent que de la position verticale. Par conséquent, nous choisissons d'imiter le dispositif expérimental par une cavité cylindrique.

La cavité cylindrique complète est représentée sur la Fig. 10b, c. Cette cavité a un diamètre $d = 1050\ mm$, ce qui donne la même surface de section transversale A, constituant la cavité des GAME-LAN (Fig. 10a). Seule la partie de la sortie du tube d'injection est modélisée.

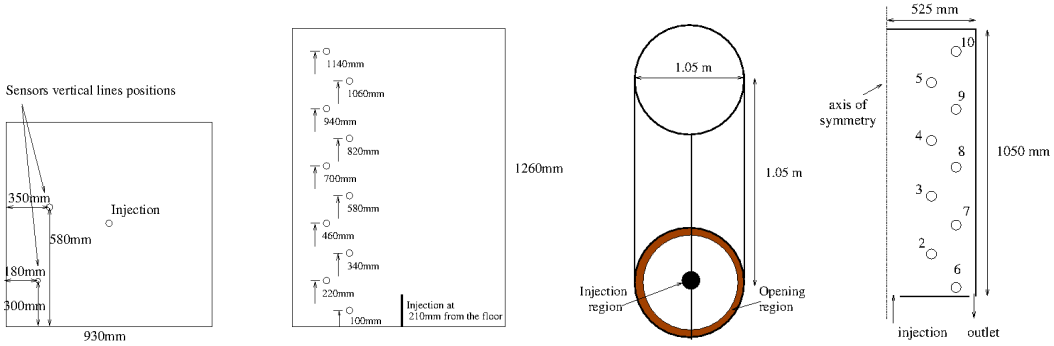

Figure 10: a) Installation de l'expérience de GAMELAN: vue de dessus et vue de côté ([Cariteau and Tkatschenko, 2012]) b) cavité cylindrique complet de la simulation numérique, c) Un plan axisymmétrique avec des positions de capteurs.

Les propriétés physiques de l'hélium et de l'air sont répertoriées dans le tableau 5.

Quatre cavités du même rapport d'aspect que la cavité complète (une cavité) à l'échelle de 1/10, 1/5, 2/5, 3/5 sont également simulées à aborder progressivement la cavité pleine. Le diamètre d'injection $d_i = 0,02m$ et un débit $Q = 4Nl/min$ sont conservés de la même façon que la cavité pleine. L'injection nombre de Richardson Ri_i de 11.6 indique qu'à la source le flux est dominé par la flottabilité. Dans tous

les cas, Sc_a est égal à 0.218.

Description de l'écoulement Les champs de tourbillon de la cavité 1 sont présentés dans la figure 11. Le diamètre de l'injection est une petite portion de la la paroi de fond, de sorte que les mouvements du panache concentré dans une petite portion du domaine. Dans la région restante du domaine de la circulation est presque stable. L'oscillation de la plume sur l' axe a été bloquée par l'hypothèse de révolution.

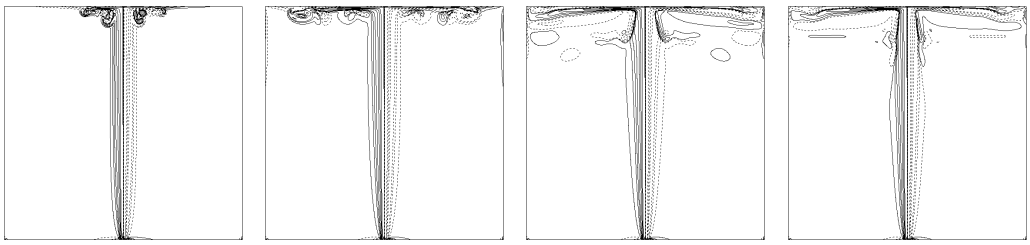

Figure 11: Isocontour de tourbillon respectivement à t = 12.75, 25.25, 125.25 et 275.25 pour la cavité 1 (de gauche à droite, de haut en bas).

Les champs de fraction de masse sont présentés dans la Fig. 12 de la cavité 1. Le profil de fraction d'hélium est presque une dimension à l'extérieur du panache.

La comparaison avec les résultats élément fini de la cavité 3/5. Les résultats des éléments finis de Gilles Bernard-Michel sont obtenus avec le code Cast3m du CEA avec la même hypothèse de révolution. La principale différence est qu'un schéma décentré est utilisé pour le terme de convection dans l'équation de quantité de mouvement et un profil de vitesse parabolique est utilisé à la limite d'entrée.

La fraction volumique de l'hélium à dix points est comparée sur la figure. 13

ρ_i	Y_{1i}	ρ_a	Y_{1a}	$\frac{\Delta\rho}{\rho_a}$	ν_i	ν_a	D
$[kg/m^3]$	[-]	$[kg/m^3]$	[-]	[-]	$[m^2/s]$	$[m^2/s]$	$[m^2/s]$
0.164	1	1.184	0	0.862	11.7×10^{-5}	1.51×10^{-5}	6.93×10^{-5}

Table 5: Propriétés physiques des simulations des panaches rondes d'hélium-air.

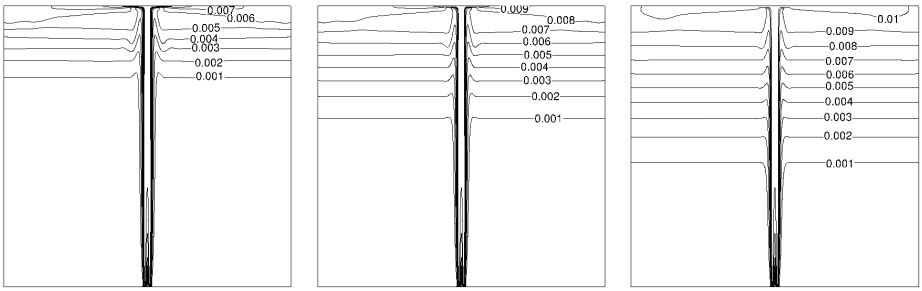

Figure 12: champs de fraction de l'hélium de masse: cavité 1 à t = 275,25, 500,25 et 800,25 (de gauche à droite).

limitée entre les résultats de l'elément (FE et les résultats des volumes finis (FV). Sur les résultats de l'axe FV sont toujours plus petits que les résultats de FE avec le plus grand écart d'environ 7 %. De l'axe, au début des résultats FV sont systématiquement plus élevés que les résultats FE. Mais dans les grands moments, il peut être prévu que les résultats FE dépasseront ceux de FV.

Nous pouvons expliquer les observations de la figure. 13b comme suit. Au début la turbulence n'a pas encore mis au point dans le flux, les résultats FV sont plus élevés parce qu'ils peuvent capturer la turbulence et le mélange est obtenu alors que les résultats de FE avec une grille grossière ne saisit pas bien la turbulence et reste laminaire. Par conséquent, les résultats de FV sont inférieurs à ceux de FE lorsque le temps augmente.

Comparaison avec l'expérience de GAMELAN et autres résultats numériques

Nous comparons nos résultats de DNS avec les données expérimentales et d'autres résultats numériques pour la cavité pleine. Il y a trois simulations sans modélisation de la turbulence (CEA DNS, JCR DNS, NCSRD DNS), une simulation des grandes échelles (CEA LES 2D), trois modèles $k-\epsilon$ (NCSRD RNG, NCSRD $k-\epsilon$, AL $k-\epsilon$) et un $k-\omega$ modèle (JCR SST). La discrétisation spatiale emploie soit par éléments finis ou volumes finis.

Les profils verticaux de la fraction volumique d'hélium à 115 s sont comparés sur la figure. 14. Les résultats obtenus avec l'hypothèse axisymétrique 2D montrent un comportement linéaire et sont en accord étroit avec l'autre. Cependant, la fraction

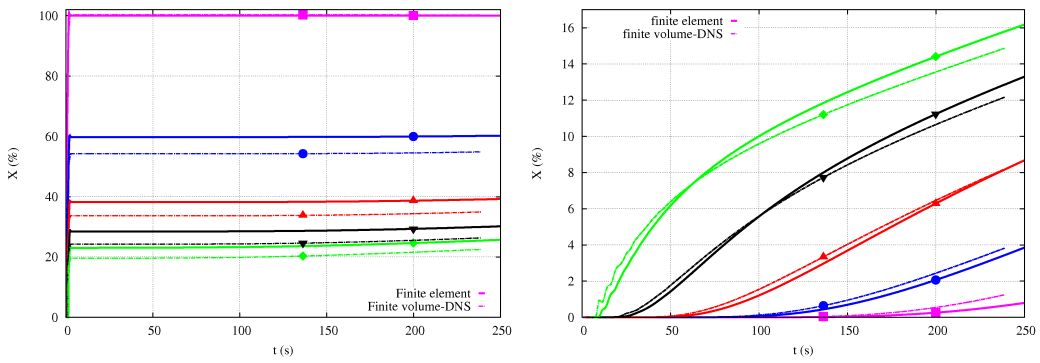

(a) (b)

Figure 13: Comparaison des DNS (courbes en pointillés) et éléments finis (courbes solides gras) résultats pour cavité 3/5: L'évolution temporelle du volume d'hélium fraction Y1 à (a) 5 points sur l'axe et (b) 5 points de retard sur l'axe.

volumique de l'hélium est très surestimée à des capteurs situés en haut et sous-estimé à près de capteurs bas comparés aux données expérimentales.

Les résultats obtenus avec une simulation 3D sont divisés en deux groupes. Le premier groupe constitué de deux $k-\epsilon$ modèles et le modèle RNG donnent des résultats très similaires et ils sont très diffusifs. Ils montrent tous que le fluide au niveau de la moitié supérieure du domaine est bien mélangé et devenu presque homogène. En conséquence, la fraction du volume maximum est fortement sous-estimée par rapport aux données expérimentales. Le second groupe constitué de deux simulations 3D DNS et un modèle SST semble donner des résultats plus proches de l'expérience. Cependant, la fraction de volume à capteurs près du sommet est encore plus élevé que les données expérimentales.

Les profils verticaux de la fraction volumique d'hélium à 275 s sont comparés sur la figure 15. Semblables à ceux de 115s, les résultats obtenus avec l'hypothèse axisymétrique 2D sont très linéaires et rapprochés. Cependant, le résultat LES est plus diffus que ue les résultats de la DNS.

Les résultats de 3D obtenus avec deux $k-\epsilon$ modèles et RNG modèle sont encore très diffusifs . Les résultats 3D DNS et SST sont les plus proches de l'expérience. Cependant, certains écarts considérables sont observés à mi-hauteur de la cavité.

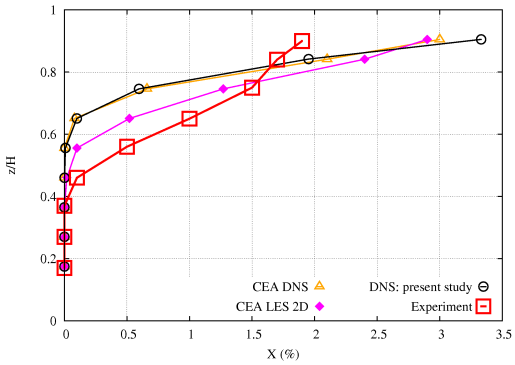

(a) With 2D axisymmetric hypothesis

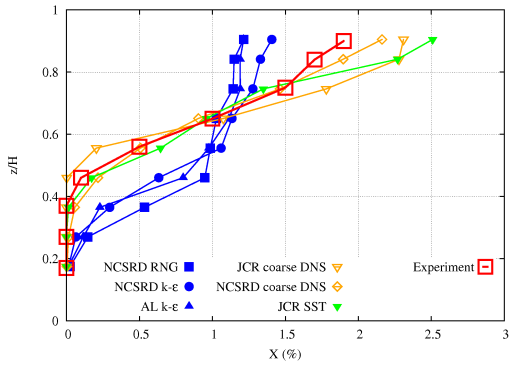

(b) Without 2D axisymmetric hypothesis

Figure 14: Cavité 1: profils verticaux de la fraction volumique d'hélium à 115 s a) avec l'hypothèse de révolution et b) sans hypothèse axisymétrique (3D)

En addition, une couche mince homogène observée dans les données expérimentales n'est pas produite par aucune de ces trois résultats.

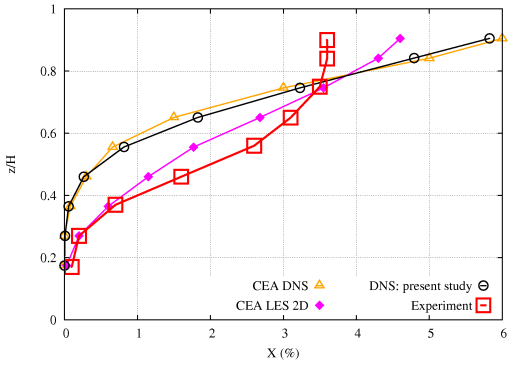

(a) With 2D axisymmetric hypothesis

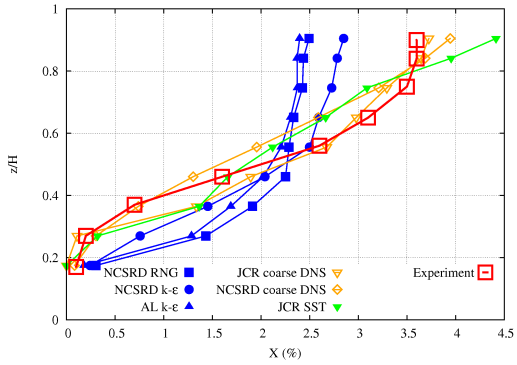

(b) Without 2D axisymmetric hypothesis

Figure 15: Cavité 1: profils verticaux de la fraction volumique d'hélium à 275 s a) avec l'hypothèse de révolution et b) sans hypothèse axisymétrique (3D).

De la comparaison ci-dessus à 115 s et 275 s, il a été montré qu'il y a une convention de proximité entre les résultats avec l'hypothèse de révolution. En utilisant DNS sans hypothèse de révolution, les résultats numériques sont grandement améliorés et sont assez proches des données expérimentales. Nous pouvons conclure que l'hypothèse de la révolution 2D est à l'origine du profil linéaire et qu'il existe

une grande différence entre les résultats numériques et les résultats expérimentaux.

0.7 Conclusions

Un nouveau traitement conservateur des conditions aux limites d'injection a été développé afin d'éviter l'apparition d'oscillations numériques et pour assurer la conservation de la masse injectée dans le système. Ce modèle a été validé sur des références des cas de test.

Dans notre processus de validation en profondeur du code, nous avons également mis en évidence un intéressant cas de référence 2D axisymmétric, sur la base des expériences Rogers et Morris (2009). Leur expérience bien instrumentée s'est avérée être un bon test transitoire en écoulements compressibles, avec des variations de densité. En outre, le nombre de Schmidt était très élevé, donc une interface rigide devait être modélisée pendant le transitoire. Nos simulations numériques pour la vitesse ascendante montrent un accord dans la plage de 3 %. Nous avons également amélioré le modèle proposé par Rogers et Morris (2019) pour la vitesse de remontée, et suggéré un nouveau modèle de panache ascendant dans un environnement libre.

Dans la deuxième partie, nous avons étudié 2D panaches d'avion avec différents régimes d'injection (flux, la concentration au point d'injection). Nous confirmons les lois théoriques d'évolution de la vitesse par rapport à la verticale et ainsi que d'autres paramètres.

Nous avons simulé un panache hélium-air rond sur la base des expériences du CEA de GAMELAN et comparé les résultats avec des expériences des autres partenaires du CEA calculs CFD. Les principaux résultats montrent que la turbulence n'est pas bien saisie pour la discrétisation 2D-axisymétrique. Il semble que la symétrie bloque le développement de l'instabilité turbulente. C'est pourquoi, nous obtenons des résultats de moins de diffusion que ceux évalués dans les expériences.

Les résultats 2D ne sont pourtant pas pires que ceux publiés avec des modèles RANS (BERNARD-MICHEL 2013) par rapport aux expériences. Il est en effet préférable de surestimer les concentrations dans les calculs de sécurité plutôt que de les sous-estimer. Par conséquent, la principale conclusion de cette section est

que pour le moment, seulement la démarche DNS (ou peut-être LES) est exacte afin de simuler des panaches presque purs dans une cavité. Il est conseillé d'exécuter le calcul de DNS symétrie axiale plutôt que 3D (ou 2D) Des calculs de RANS dans la perspective de calculs de sécurité. L'objectif ultime est de pouvoir réaliser un calcul 3D.

Contents

Résumé

0.1 Introduction . . . .
0.2 Modélisation physique . . . .
0.3 Méthode Numérique . . . .
0.3.1 Discrétisation spatiale . . . .
0.3.2 Discrétisation temporel . . . .
0.3.3 Couplage vitesse-pression: méthode de projection . . . .
0.4 Détermination des conditions aux limites entrantes . . . .
0.4.1 Flux diffusif négligeable (cas du mélange eau-glycérol) . . . .
0.4.2 Flux diffusif important (cas du mélange air-hélium) . . . .
0.5 Panaches démarrants laminaires à haut nombre de Schmidt: comparaison avec les données expérimentales . . . .
0.5.1 Paramètrage numérique et méthode d'analyse . . . .
0.5.2 Comparaison avec l'expérience de [Rogers and Morris, 2009] .
0.6 Jets flottants du mélange hélium-air ou de l'hélium dans une cavité semi-confinée remplie d'air . . . .
0.6.1 Simulations plan du panache . . . .
0.6.2 Simulations du panache axisymmetric . . . .
0.7 Conclusions . . . .

Introduction **1**

1 State of the art **5**

1.1 Buoyant convection from isolated sources 5
1.2 Vertical steady plumes in a uniform unconfined environment 6
1.2.1 Laminar plane plumes 7
1.2.2 Laminar round plumes 11
1.2.3 Transition from laminar to turbulent plumes 13

1.2.4 Turbulent plumes . . . 14
1.3 Laminar starting plumes . . . 17
1.4 Plumes in confined environment . . . 20
1.4.1 Theoretical models . . . 21
1.4.2 Validation of the models . . . 22
1.5 Numerical study of plumes . . . 24
1.6 Motivation . . . 26

2 Physical modeling **29**
2.1 Governing equations for a binary mixture fluid flow at constant pressure and temperature ([Taylor and Krishna, 1993]) . . . 30
2.1.1 Mass transport equation . . . 31
2.1.2 Momentum equation . . . 32
2.1.3 Equation relating the density and the mass fraction . . . 32
2.1.4 Low Mach approximation . . . 33
2.2 Estimation of the physical properties . . . 34
2.2.1 The case of a gas mixture . . . 34
2.2.2 The case of a glycerol-water mixture . . . 36
2.3 The complete set of governing equations in dimensionless form . . . 39
2.4 Dimensionless parameters . . . 41

3 Numerical methods **43**
3.1 Spatial discretization . . . 45
3.2 Temporal discretization . . . 48
3.3 Velocity-pressure coupling: fractional-step projection method . . . 50
3.4 Determination of the inflow boundary condition . . . 53
3.5 Solution of the algebraic equations . . . 56
3.5.1 Alternating Direction Implicit (ADI) method . . . 56
3.5.2 Multigrid method . . . 57
3.6 Implementation of the numerical method, code performance . . . 60
3.7 Conclusion . . . 61

4 Laminar starting forced plumes at high Schmidt numbers: validation with experimental data **63**

4.1 Introduction . . . 63

4.2 Description of the experiment of [Rogers and Morris, 2009] . . . 65

4.3 Numerical set up . . . 66

4.3.1 Numerical set up . . . 66

4.4 General plume characteristics . . . 68

4.4.1 Plume outer shape . . . 68

4.4.2 Plume ascent velocity . . . 71

4.4.3 Plume internal structure . . . 71

4.5 Parametric study for the numerical simulation . . . 75

4.5.1 Influence of variable viscosity . . . 76

4.5.2 Influence of the inlet velocity profile . . . 76

4.5.3 Influence of the convection schemes . . . 76

4.5.4 Influence of the spatial resolution . . . 77

4.6 Comparison with the experiment of [Rogers and Morris, 2009] . . . 84

4.6.1 General plume shape . . . 84

4.6.2 Ascent velocity . . . 85

4.6.3 Morphology of the plume heads . . . 90

4.7 Conclusions . . . 99

5 Buoyant jets of helium-air mixture or helium in a partially confined air-filled cavity **101**

5.1 Introduction . . . 101

5.2 Plane plume simulations . . . 102

5.2.1 Physical configuration and numerical set-up . . . 102

5.2.2 Flow description . . . 104

5.2.3 Transition to unsteadiness . . . 105

5.2.4 Comparison with scaling laws and similarity theory of laminar plane plumes . . . 106

5.3 Axisymmetric plume simulation . . . 113

5.3.1 Description of the test cases 113
5.3.2 Description of the flow 117
5.3.3 Comparison with the finite element results for cavity 3/5 . . 119
5.3.4 Comparison with GAMELAN experiment and other numerical results 121
5.3.5 Comparison with the model of [Worster and Huppert, 1983] . 124
5.4 Conclusions 126

Conclusion **127**

List of Figures **129**

List of Tables **135**

A Grid convergence study of helium-air round plume simulations **139**

Bibliography **139**

Introduction

Hydrogen fuel cells are more and more present in the industry, as a high capacity storage solution. Large size fuel cells, indeed, enable the storage of wind energy or photovoltaic energy. Smaller size fuel cells are also starting to be used in the car industry, for example BMW has produced a hybrid car powered partly with hydrogen, IKEA is planing to develop the use of forklifts powered with hydrogen in warehouses. Some laboratories are also currently studying processes to produce hydrogen from biomass (CEA, KIT..). Hydrogen is then not only a vector of energy but also a source of energy.

Nevertheless the use of hydrogen suffers from many inconveniences. The first of them is that a mixture of hydrogen and air is highly flammable when the volume concentration of hydrogen is between 4 up to 75 % of the mixture. The mixture might deflagrate or detonate causing severe damages to the surroundings (high pressure, high temperature, etc.). Burning hydrogen is not visible for the eyes (transparent flame), therefore a burning leakage is difficult to detect. Last but not least, in most of the applications using hydrogen, it is stored at high pressure in bottles. The pressure might be as high as 700 bars for the newly developed technologies. In case of strong damage to the storage, the pressure increase alone in the surroundings might be very destructive even without any combustion.

Motivations CEA has not only been involved in many French projects (ANR, OSEO) but also European projects (FPI, JTI) to investigate means to mitigate the risks to end up with a flammable hydrogen-air mixture, with the use of forced ventilation, passive vents, etc.. The present work has been initiated during the involvement of CEA in DimitrHy ANR project. One of the main objectives of CEA was to study experimentally the dispersion of helium (as a replacement for hydrogen) injected vertically in a cubic cavity - called GAMELAN - through nozzles of 5, 10 and 20 mm diameter. Different regimes of injection, from 1 Nl/min up to 360 Nl/min were carried out. Vertical distribution of helium concentration was measured with katharometers and comparisons of the results were achieved with Worster and Huppert (1983) model for closed cavities.

Cariteau and Tkatschenko (2012) observed a good agreement between the theoretical models and the experimental results. However for almost pure plumes, strong discrepancies were found, when using a 5 mm diameter nozzle. A linear distribution of concentration was measured whereas models predict a parabolic profile. The model of Worster and Huppert (1983) is essentially based on the properties of the entrainment coefficient α, assumed to be constant in the plume whereas many publications indicate that it might vary up to a factor 2 along the vertical position in the plume. It has been decided to investigate the velocity structure in the jet, through CFD simulations to have a better understanding of the mixing process. A benchmark has been organized in the DimitrHy project (BERNARD-MICHEL *et al.* 2012) but results produced with $k-\epsilon$ models and 2D-LES were unsatisfactory.

The present work aims at producing accurate modeling of the flow for almost pure plumes, in order to reproduce the experimental results obtained on GAME-

LAN. It will be a starting base to understand and to extend the existing simplified models.

Developing a numerical model One of our effort has been the implementation in the LIMSI CNRS code - developed by Patrick Le Quéré - of a low Mach solver for multi-species flows. The development first started with incompressible fluids, and was followed by helium-air mixture.

The code is highly optimized for fast resolution on large grids to be able to achieve DNS simulations.

The process of validation of the code and then its use to simulate reference experiments took too much time to be able to reach the step of a 3D calculation. Only 2D plane and 2D axisymmetric calculations are shown in this document. Nevertheless, all the processes that are documented in this manuscript can easily be extended to the 3D.

The study of laminar plumes First, we interests ourselves in the simulations of axisymmetric laminar starting plumes, which have been thoroughly investigated experimentally (Roger and Moris 2009, Kaminski and Jaupart 2003). We simulate the experiments published by (Roger and Moris 2009) in order to validate our numerical models and code implementation. A process to extract the shape of the head and its top vertical position is validated. Extensive convergence analysis is made in order to achieve an accuracy of the results around 1 %.

We reproduce with a very good accuracy the velocities measured by (Roger and Moris 2009). One of our main result is the proposal of a new correlation for the ascending velocity as a strong improvement over the correlation proposed by (Roger and Moris 2009).

A parametric numerical study is also achieved for a 2D laminar plane plume in order to understand the structure of the plume and to validate successfully its behavior against theoretical models.

The study of turbulent round plumes We present three different kinds of results. First of all, we compare the Worster and Hupper 1983 model to our simulations for the GAMELAN box scaled down at 1/5, 2/5, 3/5 and 5/5 of its original dimension. That parametric study mainly allowed us to optimize progressively the simulation of the full scale box, this calculation having a high computational cost. The same discrepancies were observed compared to the Worster's model as it was the case in some of Cariteau and Tkatschenko (2012) experiments.

A comparison with CEA 2D axisymmetric finite element calculation is done for the 3/5 cavity. The two simulations are very close in terms of modeling while the main difference is that CEA has an upwind scheme for advection. It is therefore a good way to validate both codes by inter-comparisons. Results are quite close but some differences are observed at long simulated times, showing the probable influence of grid discretization. Indeed, our grid is a lot finer (a 100 times approximately), and we capture more turbulent instabilities (although very attenuated by the axisymmetry) than cast3m simulations. We believe it to be the main reason why our results are approximately 5 to 10 % lower for the helium concentration at the top of the cavity, and higher at the bottom of the cavity.

At last comparisons with GAMELAN experiment and CFD calculations (BERNARD-MICHEL *et al.* (2013)) are done on the full scale box. Results produced by our simulations exhibit higher values of helium concentrations at the top of the cavity than in the experiments. It seems that the axisymmetrical approach blocks the turbulent oscillations in the plume and therefore turbulent diffusivity is strongly underestimated. It confirms the need to produce 3D calculations. CFD codes base on turbulence RANS model are, on the other hand, strongly underestimating the helium concentration at the top of the cavity, due to an overestimated turbulent diffusivity.

Organization of the document In the first chapter, we are reviewing the models and validation experiments for laminar and turbulent plumes. We are covering plane plumes and round plumes and also the transition criteria describing the change from laminar to turbulent plumes. In the chapter 2, we describe the physical models of the studied flows, which is followed by chapter 3 where we describe our numerical models. In chapter 4, the study of 2D plane turbulent starting plumes as well as laminar axisymmetric plumes is presented, as well as comparisons with a reference experiment (Roger and Moris 2009). In chapter 5, we present the round plumes simulations as well as comparisons with GAMELAN's results (Cariteau and Tkatschenko 2012).

Chapter 1

State of the art

1.1 Buoyant convection from isolated sources

By definition of [Turner, 1973], buoyant convection from isolated sources is motion produced under gravity by a density contrast between source fluid and environment. This motion occupies a limited region below or above the source and there exists a sharp interface with the non-buoyant region.

Buoyant convection can be found extensively in nature, from small size like smoke from a cigarette or smoke from chimneys to huge volcanic eruption (Fig. 1.1). Its applications are also found in a vast range of domains, some of which can be listed here: atmospheric, oceanic, cloud convection, air pollution, waste disposal, magma chambers, the Earth's mantle, etc.

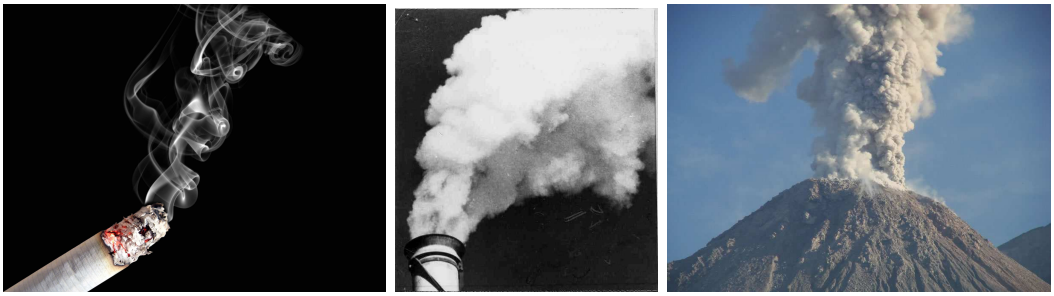

Figure 1.1: Examples of buoyant convection in nature. Source: Internet

According to [Turner, 1973], models of buoyant convection can be divided mainly in two types: plumes and thermals (see Fig. 1.2). Plumes are produced when buoyancy is supplied steadily from the source. The buoyant region is vertically continuous from the source. Thermals are produced when buoyancy is only supplied in a short time and when the buoyancy supply is finished, the buoyant region loses its connection with the source as it rises. A starting plume is defined as a plume at its early stage of emergence and it has some features in common of both plumes and thermals (see Fig. 1.2). We note that a pure plume (or simply a plume) has zero momentum at the source. A pure jet (or simply a jet) has negligible effect of buoyancy at the source. Otherwise, a forced plume or buoyant jet is produced. A buoyant jet eventually becomes a plume at a certain distance away from the source ([Chen and Rodi, 1980]). Therefore, studying plumes is essential to understand the behavior of buoyant jets.

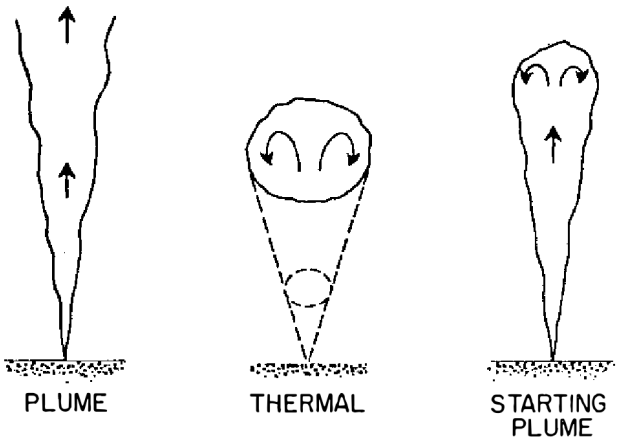

Figure 1.2: Sketches of various convection phenomena: plumes, thermals and starting plumes. Source: [Turner, 1969]

Buoyant convection is interesting for research because it provides a situation that can be studied both experimentally and theoretically. In a plume or a thermal, the distribution of velocity and temperature/density are interdependent. The nonlinearity of the coupled equations of motion makes it a very difficult problem and very few exact mathematical solutions exist. Mathematically, problems of free convection are among the most intractable in fluid dynamics ([Batchelor, 1954]).

1.2 Vertical steady plumes in a uniform unconfined environment

Steady plumes are buoyant convection flows which are produced by a steady supply of buoyancy and which are considered disregard of their formation stage. In these plumes, the distribution of velocity and temperature/density is of interest. The case of fully developed buoyant plumes in an unbounded space is well documented in the literature, both for a plume originating from a point source and a plane plume generated by a line source.

We restrict ourselves here to considering only plumes created by a heat or mass source that rise vertically upward in a uniform environment. The coordinates and velocity variables are defined in Fig. 1.3. x and z are horizontal and vertical coordinates, and u and w are horizontal and vertical velocity components, respectively. The steady plume covers a limited region spreading from the centerline to a certain extend in the x-direction and this is the domain the we are concerned with. The source that creates the plume is characterized by a density ρ_0, a temperature t_0 (if it is a heat source) or a density of species 1 $\rho_{1,0}$ (if it is a mass source that contains a different composition from the ambient fluid). The far field is characterized by a density ρ_∞, a temperature t_∞ or a density of species 1 $\rho_{1,\infty}$.

The approach to deal with a free plume presented in this section is taken from

[Gebhart et al., 1988].

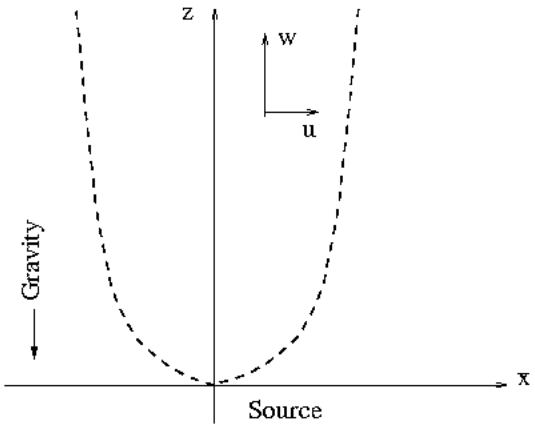

Figure 1.3: Geometry and velocity variables of a steady plume (modification of Fig. 1 [Gebhart et al., 1970])

1.2.1 Laminar plane plumes

The problem of natural convection flow resulting from an infinitely long horizontal line source is considered as a two dimensional laminar, steady flow. Similar to a thermal plume (Fig. 1.4), a plume created above a horizontal line source of mass occupies a small region which, separating from the vincinity of the source, is similar to a boundary layer.

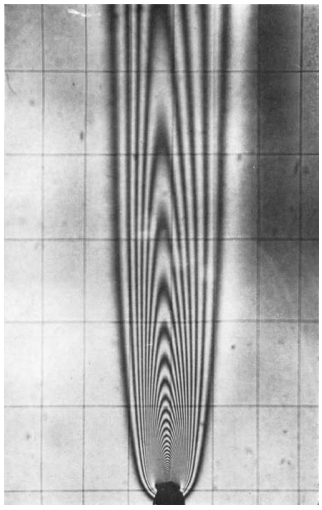

Figure 1.4: Interferogram of a plume formed above a heated wire in air. Source: [Gebhart et al., 1970]

Boundary layer equations The momentum, continuity and energy equations governing the transport of a thermal plume are simplified by the Boussinesq approximation and by boundary layer assumptions to the following form, assuming constant dynamic viscosity μ and thermal diffusivity κ.

$$\rho\left(w\frac{\partial w}{\partial z}+u\frac{\partial w}{\partial x}\right)=\mu\frac{\partial^2 w}{\partial x^2}+g\beta(t-t_\infty) \tag{1.1}$$

$$w\frac{\partial t}{\partial z}+u\frac{\partial t}{\partial x}=\kappa\frac{\partial^2 t}{\partial x^2} \tag{1.2}$$

$$\frac{\partial w}{\partial z}+\frac{\partial u}{\partial x}=0 \tag{1.3}$$

t is the temperature and t_∞ temperature in the ambient fluid.

Boundary conditions The velocity and temperature must be symmetrical with z-axis, which implies

$$\frac{\partial t}{\partial x}(0,z)=0,\quad \frac{\partial w}{\partial x}(0,z)=0,\quad u(0,z)=0 \tag{1.4}$$

The vertical velocity and temperature at the far field are not affected by the source, i.e.

$$w(x,\infty)=0,\quad t(x,\infty)=t_\infty \tag{1.5}$$

Similarity assumption We introduce the two-dimensional stream function ψ such that

$$\frac{\partial \psi}{\partial x}=w,\quad \frac{\partial \psi}{\partial z}=-u \tag{1.6}$$

The similarity method can be employed to study buoyant plumes. [Zeldovich, 1937] has described the natural convection plumes arising from a point and from a horizontal line source of heat. This method was used by [Tollmien, 1926] to solve the velocity field for the turbulent plane and axisymmetric jets. It was also used by [Schlichting, 1933] to solve the laminar velocity field. The problem was then extensively studied by various authors both analytically and experimentally and a summary of the previous work was given in [Gebhart et al., 1970]. A general treatment for both line and point sources and for both plumes created by thermal diffusion and mass diffusion is presented by [Gebhart et al., 1988]. By similarity, we assume that the vertical velocity w and the temperature difference $t-t_\infty$ take a similar form at all height, i.e.

$$\eta(x,z)=b(z)x,\quad \Psi(x,z)=\nu c(z)f(x,z),\quad t-t_\infty=d(z)\phi(x,z) \tag{1.7}$$

where $d(z)=t(0,z)-t_\infty$. Similarity solution exist if $b(z)$, $c(z)$ and $d(z)$ can be found such that ϕ and f will depend only on η while simultaneously satisfying all conditions of the transport, Eqs. (1.1), (1.2), (1.3) and Eqs. (1.4) and (1.5).

Using the requirement that similar solutions exist, equations (1.1) and (1.2) are transformed into

$$f'''+\frac{12}{5}ff''-\frac{4}{5}f'^2+\phi=0 \tag{1.8}$$

$$\phi'' + \frac{12}{5} Pr (f\phi)' = 0 \tag{1.9}$$

where $Pr = \dfrac{\nu}{\kappa}$ is the Prandlt number. Boundary conditions (1.4) and (1.5) are transformed into

$$\phi'(0) = 0, \quad f(0) = 0, \quad f'(0) = 0 \tag{1.10}$$

$$f'(\infty) = 0, \quad \phi(\infty) = 0 \tag{1.11}$$

Closed-form solutions of (1.8) and (1.9) were given only for $Pr = \dfrac{5}{9}$ and $Pr = 2$ by [Humphreys et al., 1952]. For an arbitrary value of the Prandtl number, a numerical procedure has to be carried out to calculate f' and Φ. The calculated values of f' and Φ for various Prandtl numbers are presented in Fig. 1.5

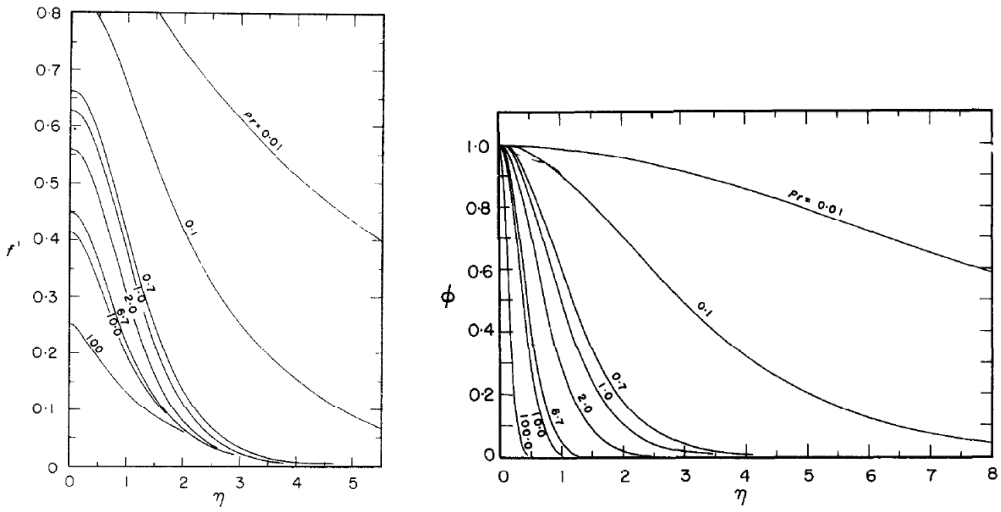

Figure 1.5: Computed dimensionless velocity f' and temperature ϕ profiles for various values of Pr for a plane plume. Source: [Gebhart et al., 1970]

By defining

$$I(Pr) = \int_{-\infty}^{\infty} f'\phi \mathrm{d}\eta \tag{1.12}$$

the similarity solutions to the equations (1.8) and (1.9) are the following

$$w = \left(\frac{4}{\nu}\right)^{1/5} \left(\frac{g\beta Q}{C_p I\sqrt{\mu\rho}}\right)^{2/5} z^{1/5} f'(\eta) \tag{1.13}$$

$$t - t_\infty = \left(\frac{Q^4}{4^3 g\beta C_p^4 \rho^2 \nu^2 I^4}\right)^{1/5} z^{-3/5} \phi(\eta) \tag{1.14}$$

$$\eta = \sqrt[5]{\frac{g\beta Q}{4^2 \nu^{5/2} C_p I\sqrt{\mu\rho}}} z^{-2/5} x \tag{1.15}$$

where Q is the total heat transfer across any horizontal plane. In a plume Q is constant and is defined as

$$Q = \int_{-\infty}^{\infty} C_p(t - t_\infty)\rho w \mathrm{d}x \tag{1.16}$$

Equation (1.13) implies that the peak velocity in the plane plume increases with the one-fifth power of the height above the source, while from Eq. (1.14) the peak temperature difference decreases with the three-fifths power of the height above the source.

Validation of the model During the same period, many experiments were conducted in air, water, silicone fluid and spindle oil and discrepancies are found compared to theoretical predictions (1.13) and (1.14). [Brodowics and Kierkus, 1966] measured velocity and temperature distributions in air above a wire having a length-to-diameter ratio L/D of 3330. Temperature were measured in air above a wire of L/D=250 by [Forstrom and Sparrow, 1967]. Temperature were determined by [Gebhart et al., 1970] in an interferometric study of a plume in a light silicone oil ($Pr = 6.7$) above a wire of 1.27×10^{-4} m diameter and 0.1524 m length, L/D=1200. The data of all three investigations indicated the maximum temperatures in the plumes were 15-20 percent lower than the theoretical predictions in the whole range of Grashof number. More accurate numerical solutions were presented by [Fujii et al., 1973] for several Prandtl numbers. Their experimental results in air also showed lower temperature levels, while those in water and spindle oil were in good agreement with the theoretical predictions for $Gr_x < 10^6$. Laser Doppler measurements downstream in water by [H. J. Nawoj, 1977] showed 20-25 per cent deficiencies in velocity level.

There are many ingredients that can lead to the discrepancies between analytical and experimental results and each ingredient may contribute a part to these discrepancies. One of which is the fact that the source in most experiments has finite dimension and that is why the concept of virtual line source was introduced by [Forstrom and Sparrow, 1967], [Lyakhov, 1970]. Applying this new concept helps reducing but not removing entirely the big differences between experimental results and theory. Neither end-conduction effects nor the decrease of the plume velocity near both ends of the line source could account for them. The convection motion below the line source was found to be one of the reason of the discrepancy by [Lyakhov, 1970]. Finally, by bounding the space below the line source with an impermeable insulating plate, [Lyakhov, 1970] found only a slight difference between their measurements in air and water and analytical results. This is consistent with the boundary layer theory because in this theory convection motion below the line source is not taken into account.

Similarity solution for plumes originating from a source of mass Solutions to plumes originating from a source of mass can be deduced in a similar way to those of plumes originating from a heat source. The governing momentum, continuity and transport equation of species 1 for a binary mixture flow are simplified by the Boussinesq approximation and by boundary layer assumptions to the following

form, assuming constant dynamic viscosity μ and mass diffusivity D.

$$\rho\left(w\frac{\partial w}{\partial z}+u\frac{\partial w}{\partial x}\right)=\mu\frac{\partial^2 w}{\partial x^2}+g(\epsilon_M-1)(\rho_1-\rho_{1,\infty}) \tag{1.17}$$

$$w\frac{\partial \rho_1}{\partial z}+u\frac{\partial \rho_1}{\partial x}=D\frac{\partial^2 \rho_1}{\partial x^2} \tag{1.18}$$

$$\frac{\partial w}{\partial z}+\frac{\partial u}{\partial x}=0 \tag{1.19}$$

The equations governing a binary mixture and the definition of ρ_1 will be given in detail in Chapter 2. The boundary conditions are as follows

$$\frac{\partial \rho_1}{\partial x}(0,z)=0,\quad \frac{\partial w}{\partial x}(0,z)=0,\quad u(0,z)=0 \tag{1.20}$$

$$w(x,\infty)=0,\quad \rho_1(x,\infty)=\rho_1,\infty \tag{1.21}$$

The same similarity analysis as applied previously on thermal plume may be used for mass plume. It just introduces in equations a Schmidt number ($Sc=\frac{\nu}{D}$) instead of the Prandtl number (Pr). Then the similarity solutions to the equations (1.8) and (1.9) reads:

$$w=\left(\frac{4}{\nu}\right)^{1/5}\left(\frac{(\epsilon_M-1)B}{I}\right)^{2/5}z^{1/5}f^{'}(\eta) \tag{1.22}$$

$$\rho_1-\rho_{1,\infty}=\left(\frac{B^4}{4^3g^5(\epsilon_M-1)\nu^2I^4}\right)^{1/5}z^{-3/5}\phi(\eta) \tag{1.23}$$

$$\eta=\sqrt[5]{\frac{B(\epsilon_M-1)}{4^2\nu^3I}}z^{-2/5}x \tag{1.24}$$

where

$$I(Sc)=\int_{-\infty}^{\infty}f^{'}\phi \mathrm{d}\eta \tag{1.25}$$

and B is the buoyancy flux across any horizontal plane. In a plume B is constant and is defined as

$$B=\int_{-\infty}^{\infty}g(\rho_1-\rho_{1,\infty})w\mathrm{d}x \tag{1.26}$$

1.2.2 Laminar round plumes

A round plume originating from a point heat source can also be treated by similarity method discussed in section 1.2.1. More details can be found in [Gebhart et al., 1988].

The conservation equations and boundary conditions (eq. (1.1) to eq. (1.5)) are now expressed in a cylindrical coordinates.

Using the requirement that similar solutions exist, equations (1.1) and (1.2) are transformed into

$$f''' + (f-1)\left(\frac{f'}{\eta}\right)' + \eta\phi = 0 \tag{1.27}$$

$$(\eta\phi')' + Pr(f\phi)' = 0 \tag{1.28}$$

with

$$\phi'(0) = 0, \quad f(0) = 0, \quad f'(0) = 0 \tag{1.29}$$

$$\frac{f'}{\eta}(\infty) = 0\,, \quad \phi(\infty) = 0 \tag{1.30}$$

Closed-form solutions of (1.27) and (1.28) were given only for $Pr = 1$ and $Pr = 2$ by [Humphreys et al., 1952], [Fujii, 1963]. For an arbitrary value of the Prandtl number, a numerical procedure has to be carried out to calculate $\frac{f'}{\eta}$ and Φ. The calculated values of f'/η and ϕ for various Prandtl numbers are presented in Fig. 1.6

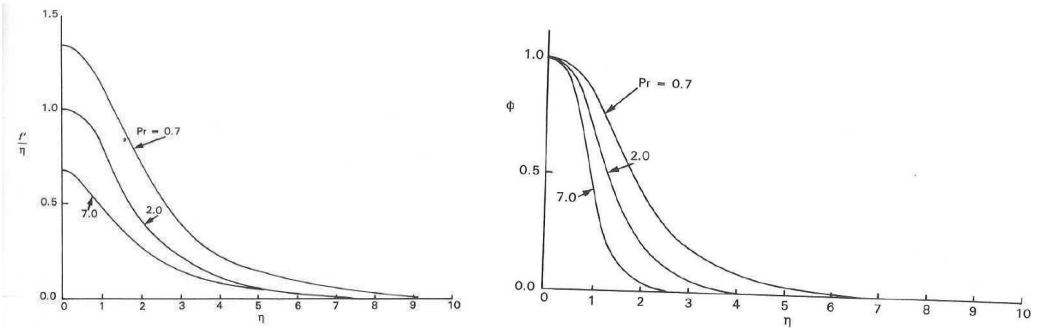

Figure 1.6: Computed dimensionless velocity f'/η and temperture ϕ profiles for various values of Pr for a plane plume. Source: [Gebhart et al., 1988]

By defining

$$I(Pr) = \int_0^\infty f'\phi \mathrm{d}\eta \tag{1.31}$$

the similarity solutions to the equations (1.8) and (1.9) are the following

$$w = \sqrt{\frac{g\beta Q}{2\pi\rho C_p \nu I}}\frac{f'(\eta)}{\eta} \tag{1.32}$$

$$t - t_\infty = \frac{Q}{2\pi\rho C_p \nu} z^{-1}\phi(\eta) \tag{1.33}$$

$$\eta = \sqrt[4]{\frac{g\beta(t_0 - t_\infty)}{\nu^2}} x z^{-1/4} \tag{1.34}$$

where Q is the total heat transfer across any horizontal plane. In a plume Q is constant and is defined as

$$Q = \int_0^\infty \rho C_p (t - t_\infty) w 2\pi x \mathrm{d}x \tag{1.35}$$

Equation (1.32) implies that the peak velocity in the laminar plume is constant with the height above the source, while from Eq. (1.33) the peak temperature difference decreases inversely to the height above the source.

Validation of the model The two-dimensional laminar plume has been studied in considerably more detail than the axisymmetric case, since it has been difficult to generate and measure the temperature distribution of axisymmetric laminar plumes ([Shlien and Boxman, 1979]). A temperature field measurement of an axisymmetric laminar plume was carried out by [Shlien and Boxman, 1979] in water. The heat source is an electrode which has a finite dimension. The results agree well with the analytical solution (1.33) if the virtual source concept is used. It was also found that the virtual source location is 4.7 times the diameter of the electrode and above the electrode. It was further found in [Shlien and Boxman, 1979] that for heights above the real source larger than ten electrode diameters, the calculated temperature distribution is not critically dependent on the virtual source location.

1.2.3 Transition from laminar to turbulent plumes

Very few plumes in nature are laminar. When fluid viscosity is large, plumes are produced that can remain laminar for a considerable height. At a certain height above the source, laminar plumes eventually become turbulent. The transition from a laminar to a turbulent state is marked by critical values of the Grashof number

$$Gr_{Q,z} = \frac{gz^3}{\nu^2} \frac{\beta Q}{\rho c_P \kappa} \tag{1.36}$$

where Q is the heat flux input at the source.

- Transition of **plane plumes** has been investigated experimentally by [Forstrom and Sparrow, 1967] and [Bill and Gebhart, 1975]. [Bill and Gebhart, 1975] measured the beginning of transition to occur at $Gr_{Q,z} = 11.2 \times 10^8$ and the end of the transition to occur at $Gr_{Q,z} = 7.9 \times 10^9$ (see Fig. 1.7). The corresponding values in the experiment of [Forstrom and Sparrow, 1967] were measured to be $Gr_{Q,z} = 5 \times 10^8$ and $Gr_{Q,z} = 5 \times 10^9$, respectively. The data of [Forstrom and Sparrow, 1967] were based on optical observations while the data of [Bill and Gebhart, 1975] were obtained from hot-wire measurements of the turbulent bursts. Also, the end of the transition in the data of [Forstrom and Sparrow, 1967] was marked by only one data point. Therefore, we consider the data of [Bill and Gebhart, 1975] to be more accurate. Converting $Gr_{Q,z}$ into Gr_z where

$$Gr_z = \frac{g\beta z^3 (t_0 - t_\infty)}{\nu^2} \tag{1.37}$$

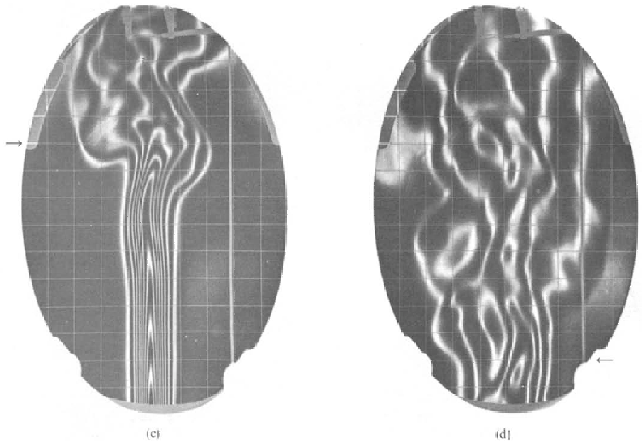

Figure 1.7: Interferograms, $L = 10in.$. Source: [Bill and Gebhart, 1975]

we obtain $Gr_z = 6.4 \times 10^7$ and $Gr_z = 2.95 \times 10^8$ for the beginning and the end of the transition, respectively.

- For **round plumes**, a value $Gr_{Q,z} = 1.8 \times 10^{10}$ was reported by [Railston, 1954] from Schlieren observations for the end of the transition.

1.2.4 Turbulent plumes

Plumes eventually become fully turbulent in the far field. The mechanisms of these turbulent flows are very complicated. Most past modeling efforts are based on greatly simplifying assumptions and approximations ([Gebhart et al., 1988]). There are two common approaches. The first approach deals with the detailed structure of the flow such as the local Reynolds stress tensor and the deformation tensor of the flow. The second approach only quantifies the overall behavior of the flow. The objective is to determine the trajectory of the discharge fluid In the second approach, integral method is used, the profiles of temperature and velocity are assumed as well as the magnitude and dependence of the downstream entrainment of the ambient fluid. We report in the following the second approach using integral method ([Gebhart et al., 1988]).

Before deriving the governing equations of a turbulent plume, the following assumptions are made

- The flow is fully turbulent. Molecular diffusion is neglected compared to turbulent transport
- Streamwise turbulent transport is negligible compared to convective transport
- The density variation is small, so that the Boussinesq approximation is valid
- The variation of physical properties of the fluid is small so that they can be taken constant

- The pressure is hydrostatic throughout the flow field

Time-averaged governing equations Under the above assumptions, the governing equations for a quasi-steady vertical axisymmetric turbulent plume in a quiescent ambient can be written as

$$\frac{\partial}{\partial z}(\rho\overline{w}x) + \frac{\partial}{\partial x}(\rho\overline{u}x) = 0 \tag{1.38}$$

$$\frac{\partial}{\partial z}(\rho\overline{w}^2x) + \frac{\partial}{\partial x}(\rho\overline{u}\overline{w}x) = -g(\rho-\rho_\infty)x - \frac{\partial}{\partial x}(x\rho\overline{u'w'}) \tag{1.39}$$

$$\frac{\partial}{\partial z}(\rho\overline{w}\bar{t}x) + \frac{\partial}{\partial x}(\rho\overline{u}\bar{t}x) = -\frac{\partial}{\partial x}(x\rho\overline{u't'}) \tag{1.40}$$

where $\overline{u(x,z)}$ and $\overline{w(x,z)}$ are the time-averaged velocity components in the x and z direction, respectively, $u^{'}$ and $w^{'}$ are the velocity fluctuating components, $\bar{t}$ is the time-averaged temperature and $t^{'}$ is the thermal fluctuation.

Experimental measurements of several authors indicated that the time-averaged profiles of turbulent plumes are similar and approximately Gaussian. For axisymmetric plumes the profiles for the time-averaged vertical velocity ($\overline{w(x,z)}$) and the density deficiency ($g\frac{\rho(x,z)-\rho_\infty}{\rho_\infty}$) are given by [Humphreys et al., 1952] as

$$\overline{w} = k_1 B_0^{1/3} z^{-1/3} exp\left(-96\frac{x^2}{z^2}\right) \tag{1.41}$$

$$g\frac{\rho-\rho_\infty}{\rho_\infty} = 11 B_0^{2/3} z^{-5/3} exp\left(-71\frac{x^2}{z^2}\right) \tag{1.42}$$

where

$$B_0 = 2\pi\int_0^\infty \overline{w} g\frac{\rho-\rho_0}{\rho_0} x dx \tag{1.43}$$

is the buoyancy flux at the source. The coefficient $k_1 = 4.7$ was reported by [Humphreys et al., 1952]. [Nakagome and Hirata, 1976] and [Jr. et al., 1977] reported values for k_1 in the range $3.4 - 3.9$.

The entrainment hypothesis and the "top-hat" assumption By observing that the plume thickness is increasing linearly, [Morton et al., 1956] pointed out that the horizontal entrainment velocity of the ambient fluid $\overline{u}$ must be proportional to the mean local upward velocity. This entrainment hypothesis was invoked to find similar solutions (i.e. for flows where velocity and density profiles have the same shape at different height z) and 'top-hat' profiles were assumed: the vertical velocity $\overline{w_T(z)}$ and the buoyancy force are supposed to be constant from the axis to the plume width $b_T(z)$ and equal to zero outside. In the following, the subscript T refers to top hat profile.

It can be deduced from these two hypotheses an estimation of the mass of fluid $E(z)$ which is entrained at the height z into the plume from the ambient:

$$E(z) = 2\pi b_T \rho_0 \alpha_T \overline{w_T}$$

where α_T is called the entrainment coefficient, ρ_0 is the density at the source and $2\pi b_T$ represents the perimeter of the plume. α_T has to be determined experimentally.

The entrainment coefficient α_T is an important parameter appearing in the determination of every integral quantity. However, its value can vary significantly between measurements. For a top-hat profile of the plumes, the measured value of α ranges from 0.10 to 0.16 in plumes and from 0.065 to 0.080 in jets ([Carazzo et al., 2006]).

The integral analysis To confirm the previous scaling laws, an integral method can be used to solve the set of equations (eq.1.38 to eq.1.40). It consists on the integration of these equations over the horizontal cross section, which introduces $E(z)$ in mass conservation equation. The integrating equations reads as:

$$\frac{d}{dz}\int_0^\infty \rho\overline{w}x dx = E(z) \tag{1.44}$$

$$\frac{d}{dz}\int_0^\infty \rho\overline{w}^2 x dx = g\int_0^\infty (\rho_\infty - \rho)x dx \tag{1.45}$$

$$\frac{d}{dz}\int_0^\infty \rho\overline{w}(t - t_\infty)x dx = -\frac{dt_\infty}{dz}\int_0^\infty \rho\overline{w}x dx \tag{1.46}$$

Assuming "top-hat" profiles for the vertical velocity and the buoyancy force, these equations become

$$\frac{d}{dz}(\pi\rho b_T^2 \overline{w}_T) = 2\pi b_T \rho_0 \alpha_T \overline{w_T} \tag{1.47}$$

$$\frac{d}{dz}(\pi b_T^2 \overline{w}_T^2 \rho) = \pi b_T^2 g(\rho - \rho_\infty) \tag{1.48}$$

$$\frac{d}{dz}\left[\pi b_T^2 \overline{w}_T(\rho_0 - \rho)\right] = 2\pi b_T \alpha_T \overline{w}_T(\rho_0 - \rho_\infty) \tag{1.49}$$

For small density variations the system of equations, becomes

$$\frac{d}{dz}(b_T^2 \overline{w}_T) = 2\alpha_T b_T \overline{w}_T \tag{1.50}$$

$$\frac{d}{dz}(b_T^2 \overline{w}_T^2) = b_T^2 g\frac{\rho_\infty - \rho}{\rho_0} \tag{1.51}$$

$$\frac{d}{dz}\left[b_T^2 \overline{w}_T g\frac{rho_\infty - \rho}{\rho_0}\right] = b_T^2 \overline{w}_T \frac{g}{\rho_0}\frac{d\rho_\infty}{dz} \tag{1.52}$$

For ρ_∞ constant, the last term in Eq. (1.52) is equal to zero. Integration of this equation then gives $b_T^2 \overline{w}_T g \dfrac{\rho_\infty - \rho}{\rho_0} = \text{const}$, which means that the buoyancy flux is conserved.

Integrating equations (1.50), (1.51) and (1.52) for constant ρ yields

$$\overline{w}_T = \frac{5}{6\alpha_T} \left(\frac{9}{10} \alpha_T B_0 \right)^{-1/3} z^{-1/3} \tag{1.53}$$

$$g \left(\frac{\rho_0 - \rho}{\rho_0} \right) = \frac{5 B_0}{6 \alpha_T} \left(\frac{9}{10} \alpha_T B_0 \right)^{-1/3} z^{-5/3} \tag{1.54}$$

$$b_T = \frac{6}{5} \alpha_T z \tag{1.55}$$

It can be noticed that that the same z dependence is obtained as deduced from dimensional analysis in eq. 1.41 and eq. 1.42.

1.3 Laminar starting plumes

Ascent velocity of the head One interesting feature of a starting plume is the advancing velocity of the head. Turner (1962) studied the motion of turbulent axisymmetric starting plumes. He considered that a starting plume consists of a thermal cap and a steady plume tail and derived the governing equations for the bulk motion of starting plumes from conservation considerations. Following the idea of [Turner, 1962], [Shlien, 1976] investigated laminar starting plumes and found that the advancing velocity of the head w_h was constant after the plume has risen to a certain height (Fig. 1.8). To find the scaling of the head velocity, [Shlien, 1976]

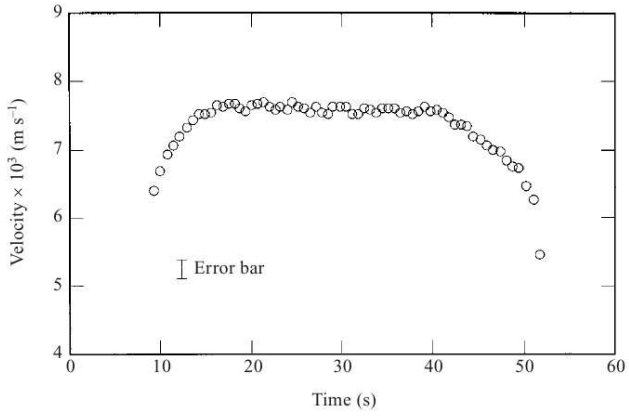

Figure 1.8: Ascent velocity of a laminar starting plume as a function of height.Source: [Kaminski and Jaupart, 2003]

modeled starting plume head as a buoyant vortex ring whose buoyancy increases

at a constant rate and by arguments pointed out that the head velocity w_h is proportional to the square root of the input heat flux Q ($J\ s^{-1}$)

$$w_h \propto \sqrt{Q} \tag{1.56}$$

This result is confirmed later by [Moses et al., 1993], who, in their experiment, measured the rising velocity of the head and found that it is constant in time and scales with input heat flux Q and viscosity ν

$$w_h = (0.23 \pm 0.05) \left(\frac{g\alpha Q}{\rho_a \nu_a C_p} \right)^{1/2} \tag{1.57}$$

The experiment in [Moses et al., 1993] was performed using four different fluids: water, methanol, pump oil and silicon with Prandtl number ranging from 6.2 to 5.7×10^3. In fact, the fitting error of their data to this relationship is quite large and [Kaminski and Jaupart, 2003] carried out another experimental work to confirm their hypothesis that these errors indicate a Prandtl dependence of the proportional coefficient in (eq. 1.57). The experiment in [Kaminski and Jaupart, 2003] was done in water and silicone oils with Prandtl numbers ranging from 7.16 to 1.03×10^4 and it was found that the head velocity w_h is increasing with increasing Prandtl number. The empirical correlation to evaluate w_h is

$$w_h = (0.57 \pm 0.02) \left(\frac{\ln \epsilon^{-2}}{2\pi} \right)^{1/2} \left(\frac{g\alpha Q}{\rho_a \nu_a C_p} \right)^{1/2} \tag{1.58}$$

where ϵ is again the solution of

$$\epsilon^4 \ln \epsilon^{-2} = Pr^{-1} \tag{1.59}$$

In fact (eq. 4.1) is a generalization of (eq. 1.57) taking into account the effect of the Prandtl number. The value of w_h measured in water in the experiment of [Kaminski and Jaupart, 2003] is almost identical to the value calculated by Eq. (1.57) proposed by [Moses et al., 1993].

An experiment on laminar starting forced plumes was carried out by [Rogers and Morris, 2009] with glycerol-water solutions. It was also found that the rising velocity of the head, after passing a starting period, is constant over a wide range of injection condition from buoyancy-driven plumes and momentum-driven jets. This result is predictable since forced plumes (or buoyant jet) eventually become plumes at a certain height away from the source. The rising velocity of the head is given by

$$w_h = (0.63 \pm 0.02) \left(\frac{g(\rho_a - \rho_i)Q}{\rho_a \nu_i} \right)^{1/2} \tag{1.60}$$

The shape of the head Another feature of interest in a starting plume is the head. In practical situations the relevant structure is the conduit. However, there are certain areas such as turbulent convection, in which the heads become the dominant structures in the flow field ([Chu and Goldstein, 1973, Solomon and Gollub, 1990, Zocchi et al., 1990]). The head of a turbulent plume was treated

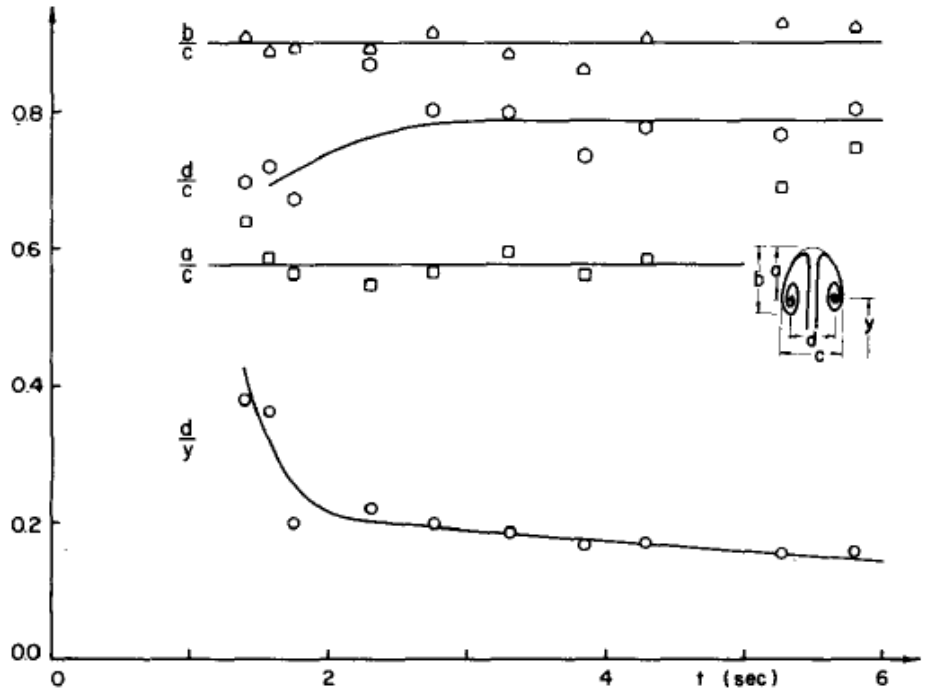

Figure 1.9: Shape of a laminar starting plume. Source: [Shlien, 1976]

theoretically by [Turner, 1962] and it was found that the head width was increasing linearly with height. The laminar plume head was studied experimentally by [Shlien, 1976] who found that its shape is self-similar (Fig. 1.9). The transition from a laminar head to a turbulent head was investigated in an experiment of axisymmetric plumes of [Shlien, 1978] and a criterion for predicting this transition has been proposed. A model to describe the shape of the head was developed in [Moses et al., 1993], from which a correlation was derived to estimate the width of the head. [Rogers and Morris, 2009] in their experiment of laminar starting forced plumes found two types of plume heads: confined heads and dispersed heads. They are different in that the fluid comprising confined heads remains compact during the entire evolution of the plume while in dispersed heads instabilities in the head front develop. In confined heads, the ratio head width/head length is a constant (Fig. 1.10). A criterion to distinguish these two kinds of head was established experimentally.

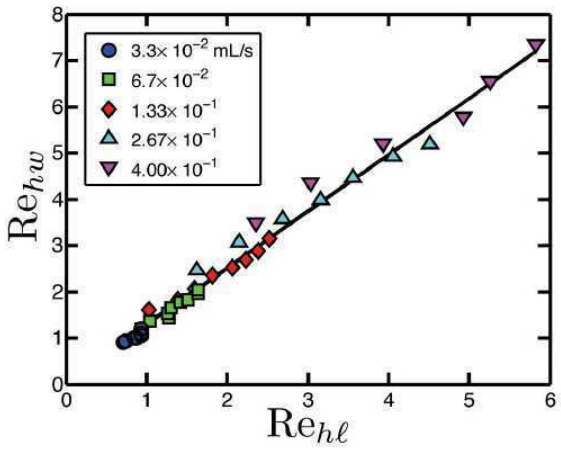

Figure 1.10: Relation between two parameters Re_{hl} and Re_{hw} based on the head length and head width for a confined head of a laminar starting forced plume. The ratio Re_{hl}/Re_{hw} is equal to head length/head width. Source: [Rogers and Morris, 2009]

1.4 Plumes in confined environment

Although a lot of research efforts have been devoted to the study of self-similar solutions of plumes rising in free space, the laboratory experiments to produce these plumes were carried out in confined spaces. The bounded wall creates the recirculating flow along sidewalls and the entrainment of underlying fluid. Despite the contributions of the past experimental studies, much remains to be learned about the interaction of the plume motion with its surrounding. The dynamics of a continuous buoyant release in a volume of limited extent are very different to that of a release in a free space. In a confined region the environment is increasingly

modified as the flow continues and the behavior of the source is also affected by this modified environment.

1.4.1 Theoretical models

In nominally unventilated enclosures, the majority of theoretical research on buoyant releases has been based on the filling-box model, the name given by [Turner, 1973] to the theory of [Baines and Turner, 1969]. In the theoretical work of [Baines and Turner, 1969] it is assumed that the flow, after colliding with the top surface, spreads out laterally and form a homogeneous layer at the top of the enclosure, separated with the underlying ambient fluid by what is called the filling front (Fig. 1.11). This layer descends in time and a stable vertical stratification is formed. [Baines and

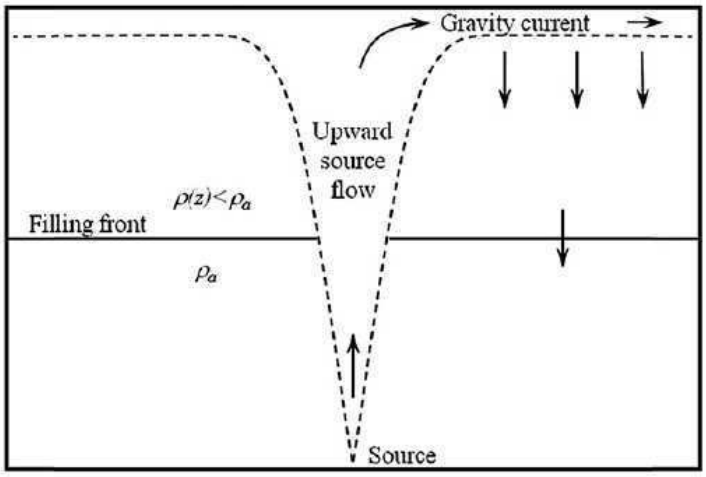

Figure 1.11: Schematic representation of the flow in an enclosure with a plume source and without overturning. Source: [Cariteau and Tkatschenko, 2012]

Turner, 1969] gave an analytical description of the velocity of the filling front and the final density profile once the front has reached the floor. The model of [Baines and Turner, 1969] was extended by [Worster and Huppert, 1983] to describe the time evolution of the vertical density profile during the first stage of descending of the first front. The length, time and density are normalized respectively by

$$z = H\zeta, \quad t = t^*\tau, \quad g\frac{\rho - \rho_a}{\rho_a} = \frac{B_0^{2/3}}{4\alpha^{4/3}H^{5/3}}\delta \tag{1.61}$$

where $t^* = \frac{A}{4\pi^{2/3}\alpha^{4/3}H^{2/3}B_0^{1/3}}$, ρ is the mixture density, A is the cross-section and H is the height of the cavity, α is the entrainment coefficient and B_0 is the source buoyancy flux given by

$$B_0 = g\frac{\rho_a - \rho_i}{\rho_a}Q_0 \tag{1.62}$$

For a pure plume a value of 0.1 was taken in [Baines and Turner, 1969]. However, its value can vary down to 0.05 (see for examples [Cariteau and Tkatschenko, 2012], [Papanicolaou and List, 1988], [Cleaver et al., 1994], [Germeles, 1975], [Lowesmith et al., 2009], [Venetsanos et al., 2010]). At constant temperature and pressure the volume fraction of the injected fluid is calculated as

$$X = \frac{\rho_a - \rho}{\rho_a - \rho_i} \tag{1.63}$$

where X is the volume fraction of the injected fluid. From this the normalized density is related to the volume fraction X by

$$X = X^*(-\delta) \tag{1.64}$$

where $X^* = \frac{B_0^{2/3}}{4\alpha^{4/3}H^{5/3}g\frac{\rho_a-\rho_i}{\rho_a}}$. The normalized position of the first front ζ_0 and density δ are given respectively by

$$\zeta_0(\tau) = \left(1 + \frac{1}{5}\left(\frac{18}{5}\right)^{\frac{1}{3}}\tau\right)^{-\frac{3}{2}} \tag{1.65}$$

and

$$\delta(\zeta,\tau) = \frac{1-\zeta^{\frac{5}{3}}}{1-\zeta}\,5(\frac{5}{18})^{\frac{1}{3}}\zeta^{-\frac{2}{3}}\left[1 - \frac{10}{39}\zeta - \frac{155}{8112}\zeta^2\right] - c(\tau) \tag{1.66}$$

where

$$c(\tau) = 5(\frac{5}{18})^{\frac{1}{3}}\left[\frac{\zeta_0^{-\frac{2}{3}}-1}{1-\zeta_0} + 3\frac{1-\zeta_0^{\frac{5}{3}}}{1-\zeta_0}\left(\frac{1-\zeta_0^{\frac{1}{3}}}{1-\zeta_0} - \frac{5}{78}\frac{1-\zeta_0^{\frac{4}{3}}}{1-\zeta_0} - \frac{155}{56784}\frac{1-\zeta_0^{\frac{7}{3}}}{1-\zeta_0}\right)\right] \tag{1.67}$$

[Baines and Turner, 1969] has noticed that under certain geometrical conditions, the plume may lead to a recirculation zone near the vertical sides of the enclosure. This overturning causes the formation of a layer of constant density near the ceiling. [Cleaver et al., 1994] studied the mixing process and build-up of gas concentration in an enclosure when the source is a buoyant jet. A three-layer model was proposed in which the upper layer is well-mixed, the second layer below it where the concentration decreases linearly and its height is increasing and the bottom layer has a concentration equal to that of the ambient fluid. A formula to estimate the thickness of the well-mixed layer was proposed by [Cleaver et al., 1994] which gave reasonable results in the case of an under-expanded sonic jet at the source. The geometrical condition which leads to overturning proposed by [Cleaver et al., 1994] is close to that proposed by [Baines and Turner, 1969]. An entrainment coefficient α is present in the model [Baines and Turner, 1969] and its value was taken equal to 0.1 to give best fit to the experiment performed by [Baines and Turner, 1969].

1.4.2 Validation of the models

The experimental study of [Cariteau and Tkatschenko, 2012] of helium/helium-air releases in a nominally unventilated enclosure has shown the validity and the limitation of the model of [Worster and Huppert, 1983]. The enclosure used in [Cariteau

and Tkatschenko, 2012] satisfy the geometrical conditions given by both [Baines and Turner, 1969] and [Cleaver et al., 1994] for the existence of overturning. However, three distinct filling regimes have been found: stratified without homogeneous layer, stratified with homogeneous layer and homogeneous. The criterion to differentiate those regimes is the volume Richardson number Ri_v (Eq. (2.66) in chapter 2). For stratified regime without homogeneous layer, two profiles of concentration were actually found by [Cariteau and Tkatschenko, 2012]. The parabolic concentration profile was in agreement with the model of [Worster and Huppert, 1983] (Fig. 1.12a). Compared to the value of 0.1 taken by [Baines and Turner, 1969] for a pure plume, the entrainment coefficient α of [Cariteau and Tkatschenko, 2012] is smaller. However, the trend of adjustment is consistent with experimental data documented in the literature, where α varies from 0.05 to 0.15 for pure jets to pure plumes ([Cariteau and Tkatschenko, 2012]). The model of [Worster and Huppert, 1983] failed to predict the linear profile produced by a source of smaller radius in the experiment of [Cariteau and Tkatschenko, 2012] (Fig. 1.12b). No satisfying explanation had been found but one possibility is that the entrainment coefficient α varies with height.

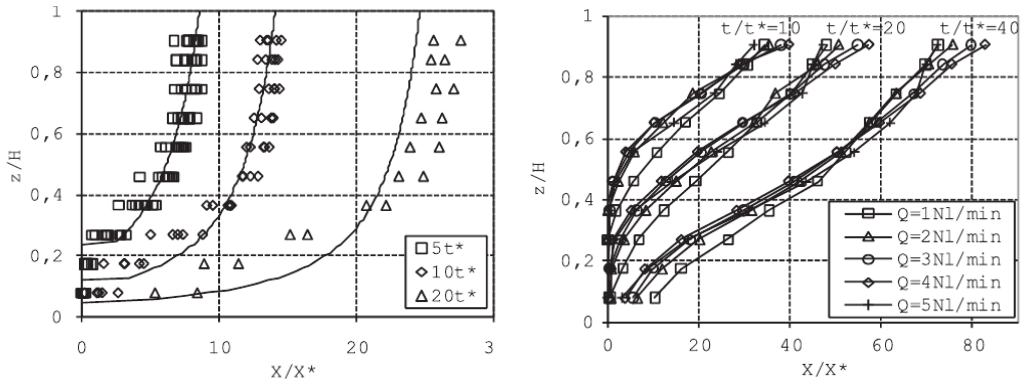

(a) (b)

Figure 1.12: Two concentration profiles of the stratified regime without homogeneous layer: a) Parabolic profile, b) Linear profile. Source: [Cariteau and Tkatschenko, 2012]

The experimental study of [Cariteau and Tkatschenko, 2012] also showed the validity and the limitation of the models of [Cleaver et al., 1994]. The model of [Cleaver et al., 1994] only gives good prediction of the thickness of the homogeneous layer for $0.01 < Ri_v < 3$. For higher value of Ri_v the actual layer thickness is highly underestimated by the model of [Cleaver et al., 1994] (Fig. 1.13). The critical volume Richardson number for the homogeneous regime predicted by [Cleaver et al., 1994] is 0.0032, which is quite near to three values of 0.0038, 0.0035 and 0.0023 found by [Cariteau and Tkatschenko, 2012] for 60 %, 80 % and 100 % volume fraction of helium in the injected fluid. However, the value of the critical volume Richardson number seems to decrease with increasing helium volume fraction at the injection.

From the comparison of the experimental study of [Cariteau and Tkatschenko,

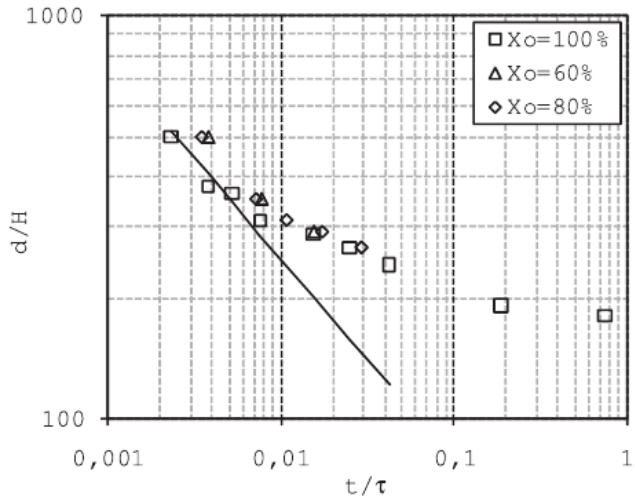

Figure 1.13: Comparison of the layer thickness predicted by the model of [Cleaver et al., 1994] (solid line) and the experimental results of [Cariteau and Tkatschenko, 2012] (symbols). The horizontal axis is the volume Richardson number Ri_v. Source: [Cariteau and Tkatschenko, 2012]

2012] and the models of [Worster and Huppert, 1983] and [Cleaver et al., 1994] we can see that there are certain situations where these models do not give satisfying results. The first situation is the linear profile in the stratified regime without homogeneous layer which contradicts the model of [Worster and Huppert, 1983]. The second situation is the stratified regime with a homogeneous layer in which the thickness of the homogeneous layer is underestimated for $0.01 < Ri_v < 3$. The explanation for these situation must rely on numerical modeling.

1.5 Numerical study of plumes

Numerical study of laminar starting plumes Numerical models can be tested by comparing with laboratory experiments of laminar starting plumes. [van Keken, 1997] used a numerical model to reproduce the laboratory experiment of [Griffiths and Campbell, 1990] on thermal plumes in glucose syrup and found similar results to [Griffiths and Campbell, 1990] regarding the time evolution, the size and the shape of the plume head. The volume of the plume head predicted is, within error, identical to that of the laboratory experiment. The numerical model of [van Keken, 1997] is then used to study more realistic mantle conditions. [Vatteville et al., 2009] compared finite element numerical results to a laboratory experiment of thermal plumes starting in a nearly isoviscous silicone oil. The time evolution of the temperature fields are found in good agreement between the two models (Fig. 1.14). The conduit velocity is found in excellent agreement near the heater but minor

systematic shifts are found in the top half of the plume conduit. The difference of more than 10 % between the conduit velocity produced by numerical results with constant viscosity and experimental results shows that even for this nearly isoviscous fluid, it is not accurate to assume that the fluid viscosity is constant. In a recently published paper of [Keken et al., 2013] the work of [Vatteville et al., 2009] was continued and the influence of boundary conditions on the flow was analyzed.

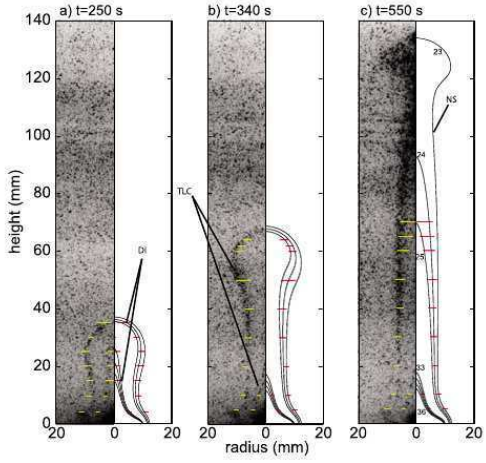

Figure 1.14: Comparison of temperature evolution of a plume in silicone oil between numerical results (right) and laboratory experiment (left) in each snapshot. Source: [Vatteville et al., 2009]

Numerical study of plumes in a confined cavity Some numerical results regarded the structure of the flow and the transition to turbulence in a air-filled confined cavity have been reported by [Desrayaud and Lauriat, 1993] and [Bastiaans et al., 2000]. Two-dimensional time-dependent buoyancy-induced flows above a horizontal line heat source inside an rectangular vessels, with adiabatic sidewalls and top and bottom wall studied by Direct Numerical Simulation (DNS) have been reported by [Desrayaud and Lauriat, 1993]. They found the critical Rayleigh number below which the flow is steady, to be $Ra = 3 \times 10^7$ where

$$Ra = \frac{g\rho Q d_i^3}{\lambda \nu \kappa} = Pr \cdot Gr_{Q,d_i} \tag{1.68}$$

where d_i is the size of the source, λ is the thermal conductivity. [Bastiaans et al., 2000] carried out direct and large-eddy simulation of the transition of two- and three-dimensional plane plumes in a confined enclosure. Their critical Rayleigh number was estimated to be 2.8×10^7, which is very close to the result of [Desrayaud and Lauriat, 1993]. [Bastiaans et al., 2000] also compared the results of the 2D simulation with those obtained from laminar theory and close agreement has been obtained.

Concerning the build-up of concentration when a light gas is injected in an enclosure, a benchmark on helium dispersion ([Bernard-Michel et al., 2012]) has been proposed in a simple geometrical configuration to assess and improve numerical modeling of this flow. Helium dispersion in a confined cavity results in a flow that is highly complex, which makes the prediction of the concentration of helium in the cavity a difficult task. Different teams using either LES or $k-\epsilon$ turbulence model have tried to simulate the flow. It has been shown in [Bernard-Michel et al., 2012] that in the case of high injection, satisfactory results were found by all the teams. However, when the injection is slow, the difference between experimental data and numerical results are significant (Fig. 1.15). The helium volume fraction is either underestimated or overestimated up to 100 % by the numerical results. Moreover, the slopes of the numerical curves in Fig. 1.15 are quite similar but they are significantly different from the the slope of the experimental data.

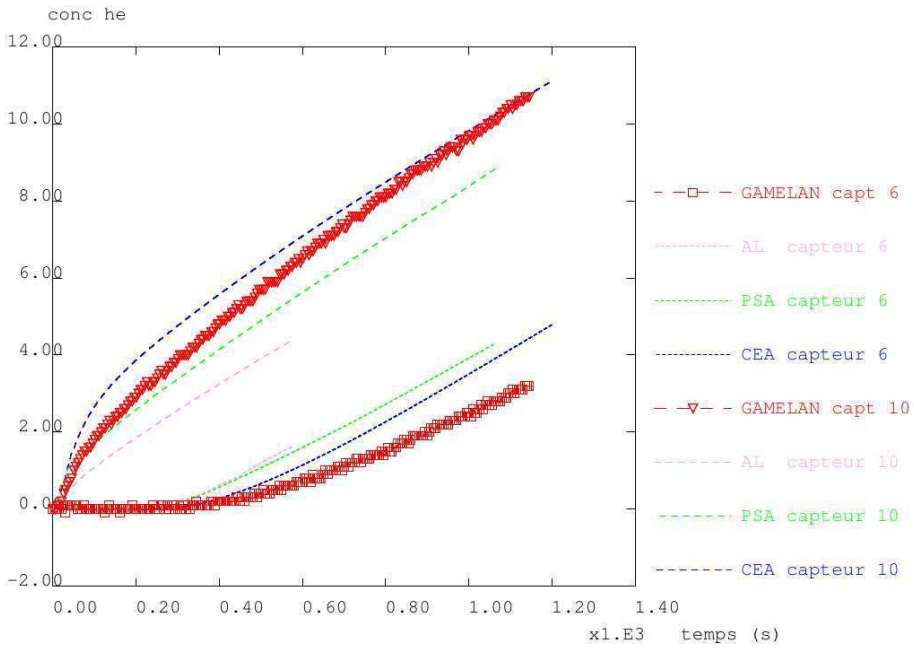

Figure 1.15: The time evolution of helium volume fraction at different positions: comparison between experimental data (symbols) and various numerical results (dashed curves). Source: [Bernard-Michel et al., 2012]

1.6 Motivation

We have seen that in bounded space the interaction between the plumes and the enclosure makes it very difficult to study the flow by theoretical method. Theoretical models like those of [Baines and Turner, 1969], [Worster and Huppert, 1983] and [Cleaver et al., 1994] have shown their limitations especially in the case of helium-air

mixture when compared with experimental data even in simple configurations.

One of the key points may be the entrainment coefficient. However its measurement necessitates the knowledge of the velocity field. Up to date it does not exist any experimental data concerning the velocity field published in the literature. That is the reason why a benchmark focusing on the helium dispersion in a bounded space has been proposed in [Bernard-Michel et al., 2012]. However large discrepancies between experimental data and numerical results obtained with commercial codes have been observed specifically in the case of small injection flow rate and the use of turbulence models.

Consequently the goal of this work is to develop a laboratory code to provide numerical results without any turbulence model, in order to clearly define all the physical and numerical parameters of the computations, and to get insight into the physics of the dispersion of helium in an air-filled cavity for a configuration close to the benchmark [Bernard-Michel et al., 2012].

This purpose is carried out in several steps

- Step 1: A suitable physical model is chosen to describe the flow.
- Step 2: A numerical method that can give sufficiently accurate solution is employed
- Step 3: The numerical code is shown to be capable of reproducing laboratory experiment of plumes in classical cases
- Step 4: The numerical code is shown to be capable of reproducing theoretical results of plumes
- Step 5: The numerical code is used to simulate the benchmark [Bernard-Michel et al., 2012] where the flow is assumed to be axisymmetric. This step has a role of simplified the complex flow to be studied with the limited time and computational resources and to identify the impact of the axisymmetric hypothesis on the structure of the flow.

These steps lead to the organization of the manuscript as follows

In chapter 2, the equations describing the flow of a binary mixture at constant temperature and pressure are developed. The laws for the variation of physical properties are described. The equations and variation laws are given for two cases: a glycerol-water mixture and a gas mixture.

In chapter 3, we describe the way the equations are discretized in time and space and how the discretized equations are solved. The treatment of the boundary conditions is different for a glycerol-water mixture and a gas mixture and is also discussed in this chapter.

In chapter 4, the numerical code is used to reproduce a laboratory experiment on laminar starting plumes of glycerol-water. A modified correlation for calculating the head ascent velocity is proposed.

In chapter 5, the numerical code is used to simulate plane plumes of helium-air mixture and the solution of the laminar conduit is compared to the analytical solution of steady plume. Then it is used to simulate the benchmark [Bernard-Michel et al., 2012] with an assumption that the plume is axisymmetric. The

numerical results obtained from this simulations are compared against experimental data and other numerical results.

In the last chapter, we present main conclusions of the work and give directions for future study.

Chapter 2

Physical modeling

Nomenclature

- D $[m^2\ s^{-1}]$: diffusion coefficient; D_{ij}: binary diffusion coefficient of gas i in gas j
- g $[m\ s^{-2}]$: gravitational acceleration
- $k = 1.3806503 \times 10^{-23}$ $[m^2\ kg\ s^{-2}\ K^{-1}]$: Boltzmann's constant
- m $[kg]$: mass of the mixture; m_i : mass of component i
- M $[kg/mol]$: molar mass of the mixture; M_i: molar mass of component i
- p $[Pa]$: driving pressure
- P $[Pa]$: dynamic pressure
- $\overline{P}$ $[Pa]$: thermodynamics pressure of the mixture; P_i : partial thermodynamics pressure of component i
- $\dot{r}$ $[kg\ m^{-3}\ s^{-1}]$: rate of production or destruction of component i
- $R = 8.314472\ [J\ K^{-1}\ mol^{-1}]$: ideal gas constant
- t $[s]$: time
- T $[K]$: absolute temperature
- $\mathbf{u}$ $[m\ s^{-1}]$: mass-averaged velocity vector; $\mathbf{u}_i$: absolute velocity vector of component i;
- V $[m^3]$: mixture volume; V_i: partial volume of component i
- $\mathbf{j}_i$ $[kgm^{-2}s^{-1}]$: mass diffusion flux of component i
- $\mathbf{n}_t$ $[kgm^{-2}s^{-1}]$: total mass flux; $\mathbf{n}_i$: mass flux of component i
- Y_i $[-]$: mass fraction of component i
- ϵ $[m^2\ kg\ s^{-2}]$: molecular energy parameter of the mixture
- ϵ_M^{ji} $[-]$: molar mass fraction of component j to component j

- μ $[kg\ m^{-1}\ s^{-1}]$: dynamic viscosity of the mixture; μ_i : dynamic viscosity of component i
- Ω_D $[-]$: diffusion collision integral
- ρ $[kg\ m^{-3}]$: mass density of the mixture; ρ_i : partial mass density of component i with respect to mixture volume
- ρ^0 $[kg\ m^{-3}]$: mass density at the initial state
- $\overline{\rho_i}$ $[kg\ m^{-3}]$: mass density of pure component i
- σ [Å]: characteristic length of the mixture

2.1 Governing equations for a binary mixture fluid flow at constant pressure and temperature ([Taylor and Krishna, 1993])

Let us discuss a very common approach to deal with binary mixtures issue proposed by [Taylor and Krishna, 1993]. Only a mixture of 2 species is considered. Taking an arbitrary infinitesimally small fluid element of volume V $[m^3]$ and of mass m $[kg]$ in the mixture, this element consists of one part of mass m_1 and volume V_1 of component 1 and the other part of mass m_2 and volume V_2 of component 2, which gives

$$m = m_1 + m_2 \tag{2.1}$$

and

$$V = V_1 + V_2 \tag{2.2}$$

We define the partial mass density ρ_i $[kg\ m^{-3}]$ of component i (i = 1,2) with respect to the mixture volume V, by

$$\rho_i = \frac{m_i}{V} \tag{2.3}$$

The mixture mass density is defined by

$$\rho = \frac{m}{V} \tag{2.4}$$

It leads to the relation

$$\rho = \rho_1 + \rho_2 \tag{2.5}$$

In this work we only deal with mass density. So as not to confuse the readers, the term "density" is understood as the mass density.

The mass fraction Y_i $[-]$ of component i is defined by

$$Y_i = \frac{m_i}{m} = \frac{\rho_i}{\rho} \tag{2.6}$$

From definition, the value range of each Y_i is between 0 and 1 and the sum over two components gives

$$Y_1 + Y_2 = 1 \tag{2.7}$$

2.1.1 Mass transport equation

Now we deduce the equations that govern the motion of a fluid flow comprising of two species. The transport equation for component i is written as

$$\frac{\partial \rho_i}{\partial t} + \nabla.(\rho_i \mathbf{u}_i) = \dot{r} \tag{2.8}$$

where $\mathbf{u}_i$ $[m\ s^{-1}]$ denotes the absolute velocity vector of component i with respect to a laboratory frame of reference, $\dot{r}$ $[kg\ m^{-3}\ s^{-1}]$ is the rate of production component i per unit volume of bulk phase by chemical reaction. We only consider non-reacting species, thus $\dot{r} = 0$.

We define a single new velocity that represents for the mixture. There exists several different ways to do this. The new velocity that we define is based on the conservation of the total mass flux and is called the mass average velocity $\mathbf{u}$ $[m\ s^{-1}]$. It is defined so that

$$\mathbf{n}_t = \rho \mathbf{u} \tag{2.9}$$

where $\mathbf{n}_t$ $[kgm^{-2}s^{-1}]$ is the total mass flux and is obtained by summing over the component mass flux $\mathbf{n}_i$, which is given by

$$\mathbf{n}_i = \rho_i \mathbf{u}_i \tag{2.10}$$

From definition (2.9), the mass average velocity $\mathbf{u}$ is related to the component absolute velocity $\mathbf{u_i}$ by

$$\mathbf{u} = \sum_{i=1}^{2} Y_i \mathbf{u_i} \tag{2.11}$$

To account for the difference between the mass average velocity $\mathbf{u}$ and the component absolute velocity $\mathbf{u}_i$, the mass diffusion flux $\mathbf{j}_i$ $[kgm^{-2}s^{-1}]$ of component i with respect to the mass average velocity is defined as

$$\mathbf{j}_i = \rho_i(\mathbf{u_i} - \mathbf{u}) \tag{2.12}$$

It implies from definition (2.12) that

$$\sum_{i=1}^{2} \mathbf{j}_i = 0. \tag{2.13}$$

Replacing the component velocity $\mathbf{u}_i$ by the mass average velocity $\mathbf{u}$ in equation (2.8) leads to

$$\frac{\partial \rho_i}{\partial t} + \nabla.(\rho_i \mathbf{u}) = -\nabla.\mathbf{j}_i \tag{2.14}$$

For a binary mixture, the mass diffusion flux of component 1 is modeled by Fick's first law as

$$\mathbf{j}_1 = -D_{12}\rho \nabla Y_1 \tag{2.15}$$

where D_{12} $[m^2/s]$ is the Fick diffusion coefficient of component 1 in component 2. An analogous relation is applied for component 2

$$\mathbf{j}_2 = -D_{21}\rho \nabla Y_2 \tag{2.16}$$

where D_{21} is the Fick diffusion coefficient of component 2 in component 1. Since $\mathbf{j}_1 + \mathbf{j}_2 = 0$ and $Y_1 + Y_2 = 1$, it can be deduced from Eqs. (2.15) and (2.16) that $D_{12} = D_{21}$ and we denote them by a unique diffusion coefficient D.

The evolution equation for component i can now be rewritten in the following form

$$\frac{\partial \rho Y_i}{\partial t} + \nabla.(\rho Y_i \mathbf{u}) = \nabla.(D\rho\nabla Y_i) \tag{2.17}$$

Summing equation (2.17) over two components results in the conservation equation for the total mass of the mixture

$$\frac{\partial \rho}{\partial t} + \nabla.(\rho \mathbf{u}) = 0 \tag{2.18}$$

To describe the motion of a binary mixture one needs two equations for two components and it gives rise to possibilities: either we use two equations like (2.17) for two components or we use equation (2.17) for one component and equation (2.18) for the mixture. In our work, we make the second choice.

2.1.2 Momentum equation

The momentum equation for a mixture is of the form very similar to the one for a single species but now the velocity corresponds to the mass average velocity $\mathbf{u}$ and the physical properties are for the mixture. It takes the form

$$\frac{\partial}{\partial t}(\rho \mathbf{u}) + \nabla.(\rho \mathbf{u} \otimes \mathbf{u}) = -\nabla P + \nabla.\underline{\underline{\tau}} + \rho \mathbf{g}, \tag{2.19}$$

where P $[Pa]$ is the total pressure. For a Newtonian fluid the viscous stress tensor $\underline{\underline{\tau}}$ is given by

$$\underline{\underline{\tau}} = \mu \left((\nabla \mathbf{u} + \nabla^T \mathbf{u}) - \frac{2}{3} \nabla.\mathbf{u}.\underline{\underline{I}} \right) \tag{2.20}$$

where $\underline{\underline{I}}$ is the identity matrix.

2.1.3 Equation relating the density and the mass fraction

In addition to the equations we have presented another equation relating the density and the mass fraction is needed. This equation is different for a gas mixture and a liquid mixture. In the case of helium-air mixture, helium is denoted by species 1 and air is denoted by species 2. In the case of glycerol-water mixture, species 1 (respectively species 2) represents glycerol (respectively water).

A gas mixture For a mixture of gases, an equation of state is chosen which takes the form

$$P = \rho R T \left(\frac{Y_1}{M_1} + \frac{Y_2}{M_2} \right) \tag{2.21}$$

where R $[J\ kg^{-1}\ mol^{-1}]$ is the ideal gas constant, T $[K]$ is the absolute temperature and M_1, M_2 $[g\ mol^{-1}]$ are the molar mass of the two gases in the mixture. Written in terms of Y_1, Eq. (2.21) becomes

$$P = \frac{\rho RT}{M_2}\left((\epsilon_M^{21} - 1)Y_1 + 1\right) \tag{2.22}$$

where $\epsilon_M^{21} = \frac{M_2}{M_1}$ is the molar mass fraction of gas 2 to gas 1.

A glycerol-water mixture ([Cheng, 2008]) For a glycerol-water mixture, the following formula was proposed to calculate the mixture density

$$\rho = \overline{\rho_1}Y_1 + \overline{\rho_2}Y_2 \tag{2.23}$$

where Y_i is the mass fraction of component i, which can be either glycerol or water; $\overline{\rho_i}$ is the density of pure component i at the same temperature as the mixture density ρ and is defined by

$$\overline{\rho_i} = \rho_i(Y_i = 1) \tag{2.24}$$

Written Eq. (2.23) in terms of Y_1 gives

$$\rho = \overline{\rho_2} + (\overline{\rho_1} - \overline{\rho_2})Y_1 \tag{2.25}$$

The densities of pure water, $\overline{\rho_2}$, and pure glycerol, $\overline{\rho_1}$, depend only on the temperature at which they are calculated and are estimated by [Cheng, 2008], in $[kg\ m^{-3}]$, as

$$\overline{\rho_2} = 1000\left(1 - \left|\frac{T - 277.15}{622}\right|^{1.7}\right) \tag{2.26}$$

$$\overline{\rho_1} = 1277 - 0.654(T - 273.15) \tag{2.27}$$

where T $[K]$ is the absolute temperature.

2.1.4 Low Mach approximation

For a flow in which the characteristic velocity is small compared to the velocity of sound, a low Mach approximation applies. In this approximation the pressure P can be decoupled into two parts

$$P(\mathbf{x}, t) = p(\mathbf{x}, t) + \overline{P}(t) \tag{2.28}$$

where p is the dynamic pressure and $\overline{P}$ is the thermodynamics pressure which is uniform in space. Using this approximation, the momentum equation and the equation of state for a gas mixture are written as

$$\frac{\partial}{\partial t}(\rho\mathbf{u}) + \nabla.(\rho\mathbf{u} \otimes \mathbf{u}) = -\nabla p + \nabla.\underline{\underline{\tau}} + \rho\mathbf{g}, \tag{2.29}$$

$$\overline{P} = \frac{\rho RT}{M_2}\left((\epsilon_M^{21} - 1)Y_1 + 1\right) \tag{2.30}$$

2.2 Estimation of the physical properties

The diffusion coefficient and the dynamic viscosity of a mixture can be calculated via the component diffusion coefficients and dynamic viscosities, and component mass fractions. We give their estimations for the case of a gas mixture and a glycerol-water mixture. We repeat here that in the case of helium-air mixture, helium is denoted by species 1 and air is denoted by species 2. In the case of glycerol-water mixture, glycerol is denoted by species 1 and water is denoted by species 2.

2.2.1 The case of a gas mixture

Estimation of the diffusion coefficient D ([Bird et al., 2001]) For non-polar molecules, Lennard-Jones potentials provide a basis for computing diffusion coefficients of binary gas mixtures. The binary diffusion coefficient D is given by the Chapman-Enskog's formula as

$$D = 0.018583 T^{3/2} \frac{\sqrt{\frac{1}{M_1} + \frac{1}{M_2}}}{P \sigma_{12}^2 \Omega_{D,12}} \tag{2.31}$$

where

D = diffusion coefficient $[m^2\ s^{-1}]$

T = absolute temperature $[K]$

M_i = molar mass of component i $[g\ mol^{-1}]$

P = pressure $[Pa]$

σ_{12} = Lennard-Jones force constant for the mixture [Å]

Ω_D = collision integral $[-]$

The following formula containing eight parameters proposed by [Neufeld et al., 1972] is used to calculate Ω_D

$$\Omega_D = \frac{1.06036}{(T^*)^{0.15610}} + \frac{0.19300}{e^{0.47635 T^*}} + \frac{1.03587}{e^{1.52996 T^*}} + \frac{1.76474}{e^{3.89411 T^*}} \tag{2.32}$$

where $T^* = kT/\epsilon_{12}$ and k is the Boltzmann constant equal to $1.38 \times 10^{-23} m^2 kg s^{-2} K^{-1}$. For nonpolar, nonreacting molecular pairs, fairly satisfactory estimates can be made for ϵ_{12}/k and σ_{12} by combining the Lennard-Jones parameters of species 1 and 2 empirically. Their values are evaluated as

$$\sigma_{12} = \frac{\sigma_1 + \sigma_2}{2} \tag{2.33}$$

$$\frac{\epsilon_{12}}{k} = \sqrt{\frac{\epsilon_1}{k} \times \frac{\epsilon_2}{k}} \tag{2.34}$$

The values of ϵ/k, σ and M for helium and air are given in Table 2.1. Eq. (2.31) gives a value of 6.91×10^{-5} $[m^2\ s^{-1}]$ for D at $20^o C$.

Parameters	Helium	Air
σ [Å]	2.576	3.617
M $[g\ mol^{-1}]$	4.003	28.97
ϵ/k $[K]$	10.2	97
μ $[kg\ m^{-1}\ s^{-1}]$	1.918×10^{-5}	1.792×10^{-5}

Table 2.1: Parameters in the Chapman-Enskog's formula for helium and air ([Bird et al., 2001]) and dynamic viscosities of helium and air at 20^oC.

Estimation of the dynamic viscosity μ ([Wilke, 1950] The value of μ depends on the properties of the two gases and their concentrations in the mixture and is evaluated using the semiempirical formula of [Wilke, 1950] as

$$\mu = \frac{\mu_1}{1 + \dfrac{\dfrac{Y_2}{Y_1}\dfrac{M_1}{M_2}\left(1 + \left(\dfrac{\mu_1}{\mu_2}\right)^{1/2}\left(\dfrac{M_2}{M_1}\right)^{1/4}\right)^2}{2\sqrt{2}\left(1 + \dfrac{M_1}{M_2}\right)^{1/2}}} + \frac{\mu_2}{1 + \dfrac{\dfrac{Y_1}{Y_2}\dfrac{M_2}{M_1}\left(1 + \left(\dfrac{\mu_2}{\mu_1}\right)^{1/2}\left(\dfrac{M_1}{M_2}\right)^{1/4}\right)^2}{2\sqrt{2}\left(1 + \dfrac{M_2}{M_1}\right)^{1/2}}} \tag{2.35}$$

where μ_1 and μ_2 are dynamic viscosities of gas 1 and gas 2 at the same temperature as the gas mixture. Their values for air and helium at 20 ^oC are given in Table 2.1.

We present in Fig. 2.1 the variations of the calculated kinematic viscosity ν for a helium-air mixture with the helium mass fraction. ν is the ratio of the dynamic viscosity μ estimated from Eq. (2.35) to the density ρ estimated from Eq. (2.22). The kinematic viscosity is increasing with increasing helium mass fraction almost linearly.

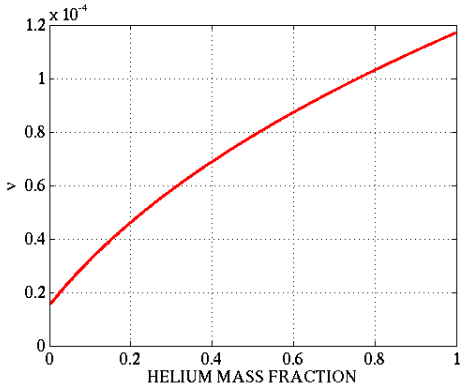

Figure 2.1: Variation of the kinematic viscosity ν in $[m^2\ s^{-1}]$ of a helium-air mixture with helium mass fraction Y_1 at 20 ^oC.

2.2.2 The case of a glycerol-water mixture

Estimation of the diffusion coefficient D ([He et al., 2006]) The mutual diffusion coefficient D of an aqueous solution of glycerol in $[m^2\ s^{-1}]$ can be evaluated using the formula

$$D = D_2 \frac{1 + W + X_2(W-1)}{1 + W - X_2(W-1)} \tag{2.36}$$

where X_2 is the volume fraction of water. It is linked to the mass fraction of water Y_2 by

$$X_2 = \frac{1}{1 + \frac{\overline{\rho_2}}{\overline{\rho_1}} \frac{1 - Y_2}{Y_2}} \tag{2.37}$$

D_2 is water self-diffusion coefficient in the aqueous solution of glycerol and is calculated in $[m^2\ s^{-1}]$ using the free volume model as

$$D_2 = D_0 exp\left(\frac{-\Delta E}{RT}\right) exp\left[\frac{-(Y_2\hat{V}_2^* + \xi Y_1 \hat{V}_1^*)}{Y_2(K_{22}/\gamma)(K_{12} - T_{12} + T) + Y_1(K_{21}/\gamma)(K_{11} - T_{11} + T)}\right] \tag{2.38}$$

where T is the temperature measured in $[K]$ and $R = 8.314\ [J\ kg^{-1}\ mol^{-1}]$ is the universal gas constant. The remaining parameters consisting of ΔE, the activation energy for a water molecule to overcome the attractive forces from the surrounding molecules; D_0, the pre-exponential factor; ξ, the ratio of the molar volume of the jumping unit of water to that of a cryo-/lyoprotectant; K_{21}/γ and K_{11}, two free volume parameters for glycerol; K_{12} and K_{22}/γ, two free volume parameters for water; $\hat{V}_2^*$ and $\hat{V}_1^*$, two critical volumes; T_{12} and T_{11}, the glass transition temperatures are given in Tables 2.2 and 2.3. The remaining parameter W is defined by

$$W = \left(\frac{D_1}{D_2}\right)_{Z_2 \to 1} \tag{2.39}$$

where $(D_2)_{Z_2 \to 1}$ is calculated by Eq. (2.38) and $(D_1)_{Z_2 \to 1}$ is the self-diffusion coefficient of glycerol in an infinitely dilute solution. For the temperature range from 0^oC to 60^oC, W is taken equal to 1.025×10^{-9} $[m^2\ s^{-1}]$ which was reported by [Errico et al., 2004].

Estimation of the dynamic viscosity μ ([Cheng, 2008]) An exponential formula was developed by [Cheng, 2008] in his study to calculate the dynamic viscosity of a glycerol-water mixture. The derived formula is applied for glycerol mass concentration in the range of 0-100 % and temperature varying from 0^oC to 100^oC. The dynamic viscosity of the mixture μ was calculated using the formula

$$\mu = \mu_2^{\alpha} \mu_1^{1-\alpha} \tag{2.40}$$

where α is the weighting factor varying from 0 to 1. It is associated with the mass fraction of glycerol, Y_1, by

$$\alpha = 1 - Y_1 + \frac{abY_1(1 - Y_1)}{aY_1 + b(1 - Y_1)} \tag{2.41}$$

Parameters	Values
T_{12} $[K]$	136
$\hat{V}_2^*$ $[ml/g]$	0.91
K_{22}/γ $[ml\ g^{-1}\ K^{-1}]$	1.945×10^{-3}
K_{12} $[K]$	-19.73
D_0 $[m^2\ s^{-1}]$	1.39×10^{-7}
ΔE $[J\ mol^{-1}]$	1.98×10^3

Table 2.2: Parameters in the free volume models for pure water ([He et al., 2006]).

Parameters	Values
T_{11} $[K]$	192.15
V_1^* $[ml\ g^{-1}]$	0.716
K_{11} $[K]$	30.12
K_{21}/γ $[ml\ g^{-1}\ K^{-1}]$	5.93×10^{-4}

Table 2.3: Parameters in the free volume models for aqueous solution of glycerol ([He et al., 2006]).

where the approximations of a and b to the temperature, T $[K]$, are given by

$$a = 0.705 - 0.0017\tilde{T} \ , b = (4.9 + 0.036\tilde{T})a^{2.5} \tag{2.42}$$

where $\tilde{T} = T - 273.15$. The dynamic viscosities of water, μ_2, and glycerol, μ_1, are dependent on the temperature and are calculated, in $[kg\ m^{-1}\ s^{-1}]$, by the following equations

$$\mu_2 = 1.790 \times 10^{-3} \exp\left(\frac{(-1230 - \tilde{T})\tilde{T}}{36100 + 360\tilde{T}}\right) \tag{2.43}$$

$$\mu_1 = 12.1 \ \exp\left(\frac{(-1233 + \tilde{T})\tilde{T}}{9900 + 70\tilde{T}}\right) \tag{2.44}$$

We present in Fig. 2.2 the variations of the calculated diffusion coefficient D and the calculated kinematic viscosity ν for a glycerol-water solution with the glycerol mass fraction. The diffusion coefficient D is decreasing with increasing glycerol mass fraction almost linearly, while the mixture kinematic viscosity ν is increasing with increasing glycerol mass fraction almost exponentially.

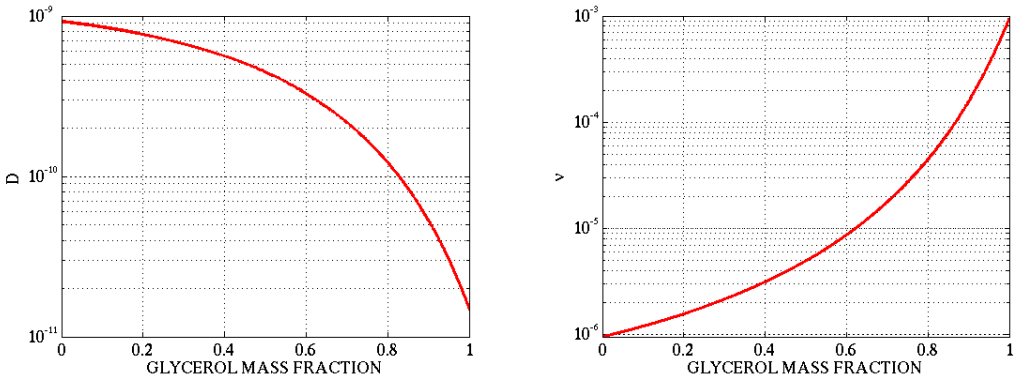

Figure 2.2: Variation of the diffusion coefficient D and kinematic viscosity ν in $[m^2\ s^{-1}]$ of a glycerol-water solution with glycerol mass fraction Y_1 at 22 ^oC.

2.3 The complete set of governing equations in dimensionless form

By introducing reference quantities, the dimensionless quantities and differential operators are defined as follows

$$x^* = \frac{x}{L_r};\quad \nabla^* = \frac{\nabla}{L_r};\quad t^* = \frac{t}{L_r/U_r};\quad \frac{\partial}{\partial t^*} = \frac{L_r}{U_r}\frac{\partial}{\partial t}$$
$$\rho^* = \frac{\rho}{\rho_r};\quad \mu^* = \frac{\mu}{\mu_r};\quad \nu^* = \frac{\nu}{\nu_r};\quad D^* = \frac{D}{D_r}$$
$$T^* = \frac{T}{T_r};\quad \overline{P}^* = \frac{\overline{P}}{P_r};\quad \mathbf{u}^* = \frac{\mathbf{u}}{U_r};\quad \pi^* = \frac{\pi}{\pi_r}$$

In a problem where a fluid is injected in an ambient confined domain, the reference length L_r is chosen as the height of the domain. P_r and T_r take the actual value of the pressure and temperature in the system, respectively. The choice of the reference velocity U_r is not unique and will be specified later in each problem. Other reference thermodynamics properties take the values of the ambient fluid at the system state P_r and T_r. The reference driving pressure π_r is taken as $\rho_r U_r$. We note that the temperature and pressure are constant in our problem and the reference temperature and pressure are taken equal to those constant values. Introducing the dimensionless quantities and differential operators into the governing equations (2.18), (2.17), (2.29), (2.30) and (2.25) gives

- Conservation equation of the mixture mass

$$\frac{\partial \rho^*}{\partial t^*} + \nabla^*.(\rho^* \mathbf{u}^*) = 0 \tag{2.45}$$

- Transport equation for species 1

$$\frac{\partial \rho^* Y_1}{\partial t^*} + \nabla^*.(\rho^* Y_1 \mathbf{u}^*) = \frac{1}{ReSc}\nabla^*.(D^* \rho^* \nabla^* Y_1) \tag{2.46}$$

- Momentum equation

$$\frac{\partial \rho^* \mathbf{u}^*}{\partial t^*} + \nabla^*.(\rho^* \mathbf{u}^* \otimes \mathbf{u}^*) = -\nabla^* \pi^* + \frac{1}{Re}\nabla^*.\underline{\underline{\tau}}^* + \frac{1}{Fr}(\rho^* - \rho^{0*})\mathbf{z} \tag{2.47}$$

- Equation relating density and mass fraction, which is either

$$\rho^* = \frac{1}{1 + (\epsilon_M^{21} - 1)Y_1} \tag{2.48}$$

for a gas mixture, or,

$$\rho^* = 1 + (\frac{\overline{\rho_1}}{\overline{\rho_2}} - 1)Y_1 \tag{2.49}$$

for a glycerol-water mixture.

The similarity parameters appearing in the dimensionless equations are defined as

Reynolds number Re

$$Re = \frac{U_r L_r}{\nu_r}$$

Froude number Fr

$$Fr = \frac{U_r^2}{g L_r}$$

The ratio of molar mass ϵ_M^{21}

$$\epsilon_M^{21} = \frac{M_2}{M_1}$$

The Schmidt number Sc

$$Sc = \frac{\nu_r}{D_r}$$

In a pressure-correction method, it is a divergence constraint on the velocity which is relevant rather than the conservation equation for the mixture mass. For a mixture of two incompressible miscible liquids such as glycerol and water, the divergence of the velocity is calculated by [Joseph et al., 1996] as

$$\nabla^*.\mathbf{u}^* = \frac{1}{ReSc}\frac{\overline{\rho_1} - \overline{\rho_2}}{\overline{\rho_1}}\nabla.\left[D^*\nabla X_1\right] \tag{2.50}$$

where X_1 is the volume fraction of glycerol. In our case Sc is of the order 10^4 so (2.50) can be approximated by

$$\nabla^*.\mathbf{u}^* = 0 \tag{2.51}$$

For a gas mixture we use Eqs. (2.49), (2.45) and (2.46) to deduce a divergence constraint on the velocity field. Multiplying Eq. (2.46) by $(\epsilon_M^{21} - 1)$ and then adding the result to Eq. (2.45) gives

$$\begin{aligned}\frac{\partial}{\partial t^*}\left((\epsilon_M^{21}-1)\rho^* Y_1 + \rho^*\right) + \nabla^*.\left(\left((\epsilon_M^{21}-1)\rho^* Y_1 + \rho^*\right)\mathbf{u}^*\right) \\ = (\epsilon_M^{21}-1)\nabla^*.(D^*\rho^*\nabla^* Y_1)\end{aligned} \tag{2.52}$$

Using the equation of state (2.48) in Eq. (2.52) gives

$$\nabla^*.\mathbf{u}^* = \frac{(\epsilon_M^{21}-1)}{ReSc}\nabla^*.(D^*\rho^*\nabla^* Y_1) \tag{2.53}$$

To simplify the notation, the "*" superscript of the dimensionless quantities will be omitted from now on. The complete set of equations to solve reads

- Glycerol-water mixture

$$\nabla.\mathbf{u} = 0 \tag{2.54}$$

$$\frac{\partial \rho Y_1}{\partial t} + \nabla.(\rho Y_1 \mathbf{u}) = \frac{1}{ReSc}\nabla.(D\rho\nabla Y_1) \tag{2.55}$$

$$\frac{\partial \rho \mathbf{u}}{\partial t} + \nabla.(\rho \mathbf{u} \otimes \mathbf{u}) = -\nabla \pi + \frac{1}{Re} \nabla . \underline{\underline{\tau}} + \frac{1}{Fr}(\rho - \rho^0)\mathbf{z} \tag{2.56}$$

$$\rho = 1 + (\frac{\overline{\rho_1}}{\overline{\rho_2}} - 1)Y_1 \tag{2.57}$$

- Helium-air mixture

$$\nabla . \mathbf{u} = \frac{(\epsilon_M^{21} - 1)}{ReSc} \nabla . (D\rho \nabla Y_1) \tag{2.58}$$

$$\frac{\partial \rho Y_1}{\partial t} + \nabla . (\rho Y_1 \mathbf{u}) = \frac{1}{ReSc} \nabla . (D\rho \nabla Y_1) \tag{2.59}$$

$$\frac{\partial \rho \mathbf{u}}{\partial t} + \nabla . (\rho \mathbf{u} \otimes \mathbf{u}) = -\nabla \pi + \frac{1}{Re} \nabla . \underline{\underline{\tau}} + \frac{1}{Fr}(\rho - \rho^0)\mathbf{z} \tag{2.60}$$

$$\rho = \frac{1}{1 + (\epsilon_M^{21} - 1)Y_1} \tag{2.61}$$

2.4 Dimensionless parameters

In this section some dimensionless parameters that are necessary to characterize our problem are introduced. We consider the injection of a fluid of density ρ_i in an enclosure filled by an ambient fluid of different density ρ_a. The ratio of density difference between injection and ambient fluids is defined as

$$\frac{\Delta \rho}{\rho_a} = \frac{\rho_a - \rho_i}{\rho_a} \tag{2.62}$$

The enclosure has a height H and a volume V. The source is characterized by a diameter d_i and an average velocity $\overline{w_i}$, calculated by dividing the volume flux Q by the injection surface

$$\overline{w_i} = \frac{4Q}{\pi d_i^2} \tag{2.63}$$

At the source the flow may be laminar or turbulent depending on the injection Reynolds number

$$Re_i = \frac{\overline{w_i} d_i}{\nu_i} \tag{2.64}$$

where ν_i is the kinematic viscosity of the injected fluid. This number gives a measure of the ratio of inertial forces to viscous forces at the source.

A parameter which expresses the ratio of potential to kinetic energy at the source is the injection Richardson number

$$Ri_i = \frac{1}{2} g \frac{\rho_a - \rho_i}{\rho_i} \frac{d_i}{\overline{w_i}^2} \tag{2.65}$$

where g is the gravitational acceleration. If $Ri_i \gg 1$ buoyancy is dominant and if $Ri_i \ll 1$ buoyancy is unimportant at the source.

To characterize different regimes of the build-up of concentration in an enclosed cavity, [Cleaver et al., 1994] proposed a volume Richardson defined by

$$Ri_v = g\frac{\rho_a - \rho_i}{\rho_i}\frac{V^{1/3}}{\overline{w_i}^2} \tag{2.66}$$

For high values of this number compared to unity, a stable density stratification is developed in the enclosure during the injection. Otherwise overturning can occur and the cavity can become partially or entirely homogeneous in density.

Schmidt number defines the ratio of viscosity and mass diffusivity, and is used to characterize fluid flows in which there are simultaneous momentum and mass diffusion convection processes.

$$Sc_i = \frac{\nu_i}{D_i} \tag{2.67}$$

where D_i is the mass diffusivity at the source. An analogous number is defined for the ambient flow

$$Sc_a = \frac{\nu_a}{D_a} \tag{2.68}$$

In natural convection the Grashof number approximates the ratio of the buoyancy to viscous force acting on a fluid

$$Gr = g\frac{\rho_a - \rho_i}{\rho_a}\frac{H^3}{\nu_a^2} \tag{2.69}$$

A local Grashof number is also defined as

$$Gr_z = g\frac{\rho_a - \rho}{\rho_a}\frac{z^3}{\nu_a^2} \tag{2.70}$$

where z is the vertical position and ρ is the density at that position.

Chapter 3

Numerical methods

We make use of the code developed in LIMSI for the differentially heated cavity and adapt it to our problem. The numerical resolution of the Navier-Stokes equations in this code is presented in the context of a finite volume method. First of all, the temporal and spatial discretization, and the handling of the pressure-velocity coupling are presented. After that, the algorithm is described together with inlet and outlet boundary conditions. Finally, solvers used for linear problems are introduced. The algorithm is demonstrated on the governing equations of a gas mixture but it is also applicable to equations of a glycerol-water mixture.

We present the numerical resolution of Navier-Stokes equations in cylindrical coordinates. The adimensionalized Navier-Stokes equations governing the fluid flow of a binary gas mixture at constant temperature and pressure condition from the previous chapter are recalled. They are the time-dependent conservation equation for the mass fraction Y_1, the conservation equation for the velocity $\mathbf{u}$ and the divergence constraint on the velocity

$$\frac{\partial \rho Y_1}{\partial t} + \nabla.(\rho Y_1 \mathbf{u}) = \frac{1}{ReSc}\nabla.(D\rho\nabla Y_1) \tag{3.1}$$

$$\frac{\partial \rho \mathbf{u}}{\partial t} + \nabla.(\rho \mathbf{u} \otimes \mathbf{u}) = -\nabla\pi + \frac{1}{Re}\nabla.\underline{\underline{\tau}} + \frac{1}{Fr}(\rho - \rho^0)\mathbf{z} \tag{3.2}$$

$$\nabla.\mathbf{u} = \frac{1}{ReSc}(\epsilon_M^{21} - 1)\nabla.(D\rho\nabla Y_1) \tag{3.3}$$

This is a system of coupled partial differential equations which consists of six variables: ρ, Y_1, $\mathbf{u}$, μ, D, π. Together with three Eqs. (3.1), (3.2) and (3.3) there are three more equations describing the variation of ρ, μ and D with Y_1 (Eqs. (2.57), (2.35) and (2.31)). These six equations are then completed by suitable boundary conditions. For time-dependent problems, initial conditions have also to be supplied. The system is first discretized in time (section 3.2) to obtain a semi-discretized system and the velocity-pressure coupling is handled by a pressure-correction method (section 3.3). From the initial condition, the fully-discretized equations obtained after spatial discretization (section 3.1) are integrated in time using a time-marching method to obtain a time-accurate solution. At each time level, the systems are solved in a sequential way. It means that one equation is solved after another and the variables that are not yet updated are approximated by their values at previous time levels. In our algorithm, the following order is taken

- The species transport equation (3.1) is solved.

- The new physical properties ρ, D, μ are calculated by Eqs. (2.57), (2.35) and (2.31).
- The pressure and velocity are calculated by the pressure-correction method

We make a hypothesis that the flow is axisymmetric, and that there is no motion in angular direction. Denoting the cylindrical coordinates by ($\mathbf{e}_r$,$\mathbf{e}_z$) in which $\mathbf{e}_z$ points upward against gravity $\mathbf{g}$ and u and w are velocity components in $\mathbf{e}_r$ and $\mathbf{e}_z$ directions, respectively, the governing equations (3.1)-(3.3) are written as

$$\frac{\partial(\rho Y_1)}{\partial t}+\frac{\partial(w\rho Y_1)}{\partial z}+\frac{1}{r}\frac{\partial(ru\rho Y_i)}{\partial r}=\frac{1}{ReSc}\left[\frac{\partial}{\partial z}\left(\rho D\frac{\partial Y_1}{\partial z}\right)+\frac{1}{r}\frac{\partial}{\partial r}\left(r\rho D\frac{\partial Y_1}{\partial r}\right)\right] \tag{3.4}$$

$$\begin{aligned}\frac{\partial(\rho u)}{\partial t}+\frac{\partial(\rho w u)}{\partial z}+\frac{1}{r}\frac{\partial(r\rho u^2)}{\partial r}=&-\frac{\partial \pi}{\partial r}+\frac{1}{Re}\left\{\frac{\partial}{\partial z}\left[\mu\left(\frac{\partial u}{\partial z}+\frac{\partial w}{\partial r}\right)\right]\right.\\&\left.+\frac{1}{r}\frac{\partial}{\partial r}\left[r\mu\left(2\frac{\partial u}{\partial r}-\frac{2}{3}\nabla.\mathbf{u}\right)\right]-2\mu\frac{u}{r^2}+\frac{2}{3}\frac{\mu}{r}\nabla.\mathbf{u}\right\}\end{aligned} \tag{3.5}$$

$$\begin{aligned}\frac{\partial(\rho w)}{\partial t}+\frac{\partial(\rho w^2)}{\partial z}+\frac{1}{r}\frac{\partial(r\rho u w)}{\partial r}=&-\frac{\partial \pi}{\partial z}+\frac{1}{Re}\left\{\frac{\partial}{\partial z}\left[\mu\left(2\frac{\partial w}{\partial z}-\frac{2}{3}\nabla.\mathbf{u}\right)\right]\right.\\&\left.+\frac{1}{r}\frac{\partial}{\partial r}\left[r\mu\left(\frac{\partial w}{\partial r}+\frac{\partial u}{\partial z}\right)\right]\right\}-\frac{1}{Fr}(\rho-\rho^0)\end{aligned} \tag{3.6}$$

$$\nabla.\mathbf{u}=\frac{\partial w}{\partial z}+\frac{1}{r}\frac{\partial(ru)}{\partial r}=\frac{1}{ReSc}(\epsilon_M^{21}-1)\nabla.(D\rho\nabla Y_1) \tag{3.7}$$

Boundary conditions We are only interested in the behavior of the flow in the enclosure, hence we only model the enclosure and treat its interaction with the remaining environment via boundary conditions. We divide the domain boundary $\partial\Omega$ into four types: solid surface $\partial\Omega_w$, inflow boundary $\partial\Omega_i$, outflow boundary or free surface $\partial\Omega_o$ and symmetry boundary $\partial\Omega_s$.

$$\Omega=\partial\Omega_w\cup\partial\Omega_i\cup\partial\Omega_o\cup\partial\Omega_s \tag{3.8}$$

We treat here the case in which the symmetry boundary is vertical and the inflow and outflow boundaries are horizontal. A sketch of the domain boundary is given in Fig. 3.1.

Solid surfaces are impermeable to fluid and fluid particles stick to them. Hence, there is no slip and no penetration and the fluid on a stationary solid surface has zero velocity. The boundary conditions on solid surfaces read

$$u=0;\quad w=0;\quad \frac{\partial Y_1}{\partial \mathbf{n}}=0;\quad \frac{\partial \rho}{\partial \mathbf{n}}=0 \tag{3.9}$$

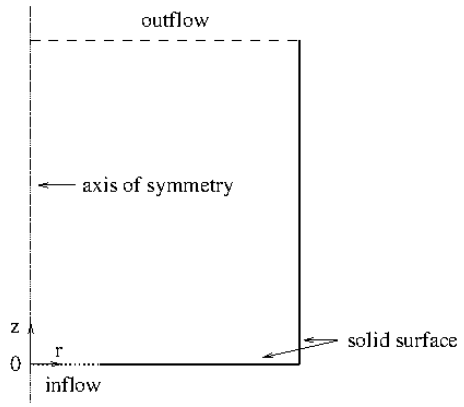

Figure 3.1: The domain boundary consists of four parts: solid boundary $\partial\Omega_w$, inflow boundary $\partial\Omega_i$, outflow boundary $\partial\Omega_o$ and symmetry boundary $\partial\Omega_s$.

Symmetry boundary conditions are used when the physical domain of interest has a mirror symmetry. There is no convective flux and no diffusion flux across a symmetry plane. The normal velocity component is zero and the normal gradients of all flow variables across at symmetry plane, which read

$$u = 0; \quad \frac{\partial w}{\partial z} = 0; \quad \frac{\partial Y_1}{\partial \mathbf{n}} = 0; \quad \frac{\partial \rho}{\partial \mathbf{n}} = 0 \tag{3.10}$$

At the inflow boundary, the velocity and mass fraction profiles are specified which read

$$u = 0; \quad w = w_i(r,t); \quad Y_1 = Y_{1i}(r,t); \quad \rho = \rho_i(r,t) \tag{3.11}$$

The inflow profiles $w_i(r,t)$ and $Y_1 = Y_{1i}(r,t)$ will be described in section 3.4.

If the outflow boundary is large relative to the domain of interest such as in the glycerol-water case, the outflow boundary conditions consist of specifying a zero diffusion flux for all flow variables and making an overall mass balance correction. The overall mass balance correction is described in section 3.3. The outflow boundary condition read

$$\frac{\partial u}{\partial z} = 0; \quad \frac{\partial w}{\partial z} = 0; \quad \frac{\partial Y_1}{\partial \mathbf{n}} = 0; \quad \frac{\partial \rho}{\partial \mathbf{n}} = 0 \tag{3.12}$$

If the outflow boundary is small such as in the helium-air case, the tangential velocity is set to zero and a zero diffusion flux for all flow variables are specified

$$u = 0; \quad \frac{\partial w}{\partial z} = 0; \quad \frac{\partial Y_1}{\partial \mathbf{n}} = 0; \quad \frac{\partial \rho}{\partial \mathbf{n}} = 0 \tag{3.13}$$

3.1 Spatial discretization

The set of equations (3.1)-(3.3) are solved numerically with the help of a finite volume method. The spatial discretization is performed on a staggered grid. In this grid all the variables are defined at different geometrical positions. The scalar

variables (pressure, density, mass fraction etc.) are defined at the center of a control volume whereas the velocity components are defined on the faces of the control volume. This is different from a collocated grid, where all variables are defined in the same grid position. A visualization of a two-dimensional grid is shown in Fig. 3.2. Ghost cells are created outside the domain boundary to facilitate the treatment of the boundary conditions.

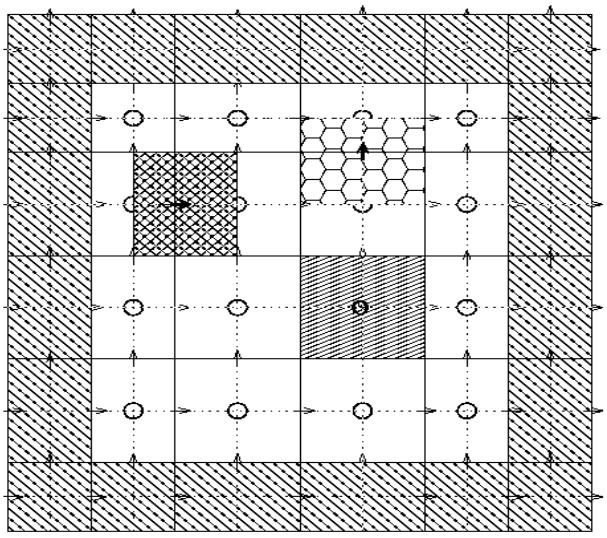

Figure 3.2: Staggered location for scalar and vector quantities: $\rightarrow = u$, $\uparrow = w$, $o = p$, Y_1 and examples of their corresponding control volumes. Velocities are defined at cell boundaries while scalars are defined at cell centers. Dashed cells correspond to cells out of the computational domains.

Using a staggered grid is a simple way to avoid obtaining checkerboard pattern solutions, which can occur from the spatial discretization using collocated grid (see [Patankar, 1980], chapter 6). In collocated grid the discretized equations make use of variable values at alternate grid points and not adjacent ones, hence a checkerboard solution do satisfy the discretized equations equally as a uniform solution. By placing variables differently, in staggered grid the discretized equations make use of variable values at adjacent grid points and hence a checkerboard solution is no longer felt as a uniform solution. The staggered grid was first used by [Harlow and Welch, 1965] in their Marker And Cell (MAC) method to solve time-dependent motion of a viscous, incompressible fluid in two-dimensional Cartesian coordinates.

In discretizing the different terms in the governing equations, various schemes can be used. These schemes are different in the way the face value of a variable and its derivatives are approximated. We report here two schemes that will be used in our numerical calculation: centered scheme and Quick scheme. The difference between them is the way the interface values are approximated by cell-centered values.

Denoting by ϕ_C the averaged value of a variable ϕ in the cell considered, ϕ_R, ϕ_L

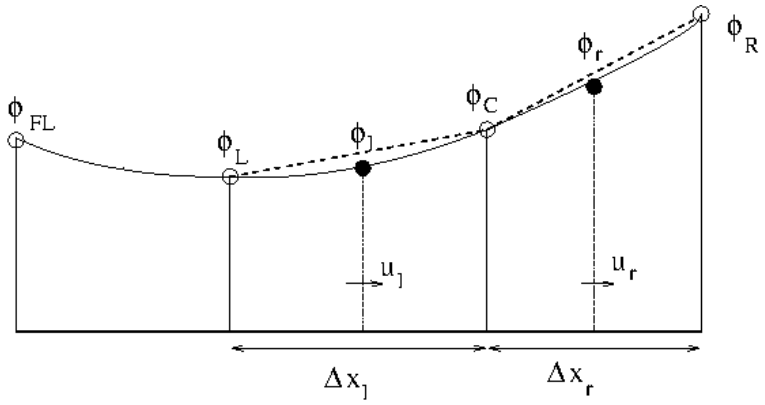

Figure 3.3: Quadratic upstream interpolation for ϕ_l, $\left(\frac{\partial\phi}{\partial x}\right)_l$, ϕ_r and $\left(\frac{\partial\phi}{\partial x}\right)_r$ ([Leonard, 1979]).

and ϕ_{FL} the averaged value of ϕ in the adjacent cells as are depicted in Fig. 3.3. The velocity is defined at the interface and we suppose that it has the direction as shown in Fig. 3.3. In developing the discretization of the governing equation, the face values ϕ_l, ϕ_r, $\left(\frac{\partial\phi}{\partial x}\right)_l$ and $\left(\frac{\partial\phi}{\partial x}\right)_r$ have to be defined based on the cell values of ϕ. A second-order approximation which is called the centered scheme gives

$$\phi_r = \frac{1}{2}(\phi_C + \phi_R) + O(\Delta x^2) \tag{3.14}$$

$$\left(\frac{\partial\phi}{\partial x}\right)_r = \frac{\phi_R - \phi_C}{\Delta x_r} + O(\Delta x^2) \tag{3.15}$$

$$\phi_l = \frac{1}{2}(\phi_L + \phi_C) + O(\Delta x^2) \tag{3.16}$$

$$\left(\frac{\partial\phi}{\partial x}\right)_l = \frac{\phi_C - \phi_L}{\Delta x_l} + O(\Delta x^2) \tag{3.17}$$

The centered scheme has some instability problem if the local Peclet number is too large (see [Patankar, 1980], chapter 5). Upwind scheme, although possessing good stability properties, suffers from severe inaccuracies due to numerical diffusion and its low convergence of order 1. [Leonard, 1979] developed a third-order scheme called Quadratic Upstream Interpolation for Convective Kinematics (QUICK scheme). This is an interpolation scheme which possesses good accuracy and the directional properties associated with stable convective sensibility of the upwind scheme. The gradients at the interfaces are approximated exactly the same as in the centered scheme and the face values are approximated as follows

$$\phi_r = \frac{1}{2}(\phi_C + \phi_R) - \frac{1}{8}(\phi_L + \phi_R - 2\phi_C) + O(\Delta x^3) \tag{3.18}$$

$$\phi_l = \frac{1}{2}(\phi_L + \phi_C) - \frac{1}{8}(\phi_{FL} + \phi_C - 2\phi_L) + O(\Delta x^3) \tag{3.19}$$

At the boundary, these approximations are reduced to those of the centered scheme. QUICK scheme will be used for simulating glycerol-water plumes in chapter 4 to reduce numerical oscillation at the interface due to large Schmidt number.

3.2 Temporal discretization

By regrouping the pressure gradient and the body force in a source term S, the linear terms in L and the nonlinear terms in NL, Eqs. (3.4), (3.5) and (3.6) can be written as

$$\frac{\partial(\rho f)}{\partial t} = L(f) + NL(f) + PG(f) + S(f) \tag{3.20}$$

where f can be either Y_1 or u or w; $L(f)$ is the linear part; $NL(f)$ is the nonlinear part, $PG(f)$ is the pressure gradient and $S(f)$ is the source term. At time level $n+1$ these parts read

- In the conservation equation for Y_1

$$L^{n+1}(Y_1) = \frac{1}{ReSc}\left[\frac{\partial}{\partial z}\left(\rho^{n+1}D^{n+1}\frac{\partial Y_1^{n+1}}{\partial z}\right) + \frac{1}{r}\frac{\partial}{\partial r}\left(r\rho^{n+1}D^{n+1}\frac{\partial Y_1^{n+1}}{\partial r}\right)\right] \tag{3.21}$$

$$NL^{n+1}(Y_1) = -\frac{\partial(w^{n+1}\rho^{n+1}Y_1^{n+1})}{\partial z} - \frac{1}{r}\frac{\partial(ru^{n+1}\rho^{n+1}Y_1^{n+1})}{\partial r} \tag{3.22}$$

$$PG^{n+1}(Y_1) = 0 \tag{3.23}$$

$$S^{n+1}(Y_1) = 0 \tag{3.24}$$

- In the equation for u

$$L^{n+1}(u) = \frac{1}{Re}\left[\frac{\partial}{\partial z}\left(\mu^{n+1}\frac{\partial u^{n+1}}{\partial z}\right) + \frac{2}{r}\frac{\partial}{\partial r}\left(r\mu^{n+1}\frac{\partial u^{n+1}}{\partial r}\right) - 2\mu^{n+1}\frac{u^{n+1}}{r^2}\right] \tag{3.25}$$

$$NL^{n+1}(u) = -\frac{\partial(\rho^{n+1}w^{n+1}u^{n+1})}{\partial z} - \frac{1}{r}\frac{\partial(r\rho^{n+1}u^{n+1}u^{n+1})}{\partial r} \tag{3.26}$$

$$PG^{n+1}(u) = -\frac{\partial\pi^{n+1}}{\partial r} \tag{3.27}$$

$$S^{n+1}(u) = \frac{1}{Re}\left[\frac{\partial}{\partial z}\left(\mu^{n+1}\frac{\partial w^{n+1}}{\partial r}\right) - \frac{1}{r}\frac{\partial}{\partial r}\left(\frac{2}{3}r\mu^{n+1}\nabla.\mathbf{u}^{n+1}\right) + \frac{2}{3}\frac{\mu^{n+1}}{r}\nabla.\mathbf{u}^{n+1}\right] \tag{3.28}$$

- In the equation for w

$$L^{n+1}(w) = \frac{1}{Re}\left[2\frac{\partial}{\partial z}\left(\mu^{n+1}\frac{\partial w^{n+1}}{\partial z}\right) + \frac{1}{r}\frac{\partial}{\partial r}\left(r\mu^{n+1}\frac{\partial w^{n+1}}{\partial r}\right)\right] \tag{3.29}$$

$$NL^{n+1}(w) = -\frac{\partial(\rho^{n+1}w^{n+1}w^{n+1})}{\partial z} - \frac{1}{r}\frac{\partial(r\rho^{n+1}u^{n+1}w^{n+1})}{\partial r} \tag{3.30}$$

$$PG^{n+1}(w) = -\frac{\partial \pi^{n+1}}{\partial z} \tag{3.31}$$

$$S^{n+1}(w) = \frac{1}{Re}\left[-\frac{\partial}{\partial z}\left(\frac{2}{3}\mu^{n+1}\nabla.\mathbf{u}^{n+1}\right) + \frac{1}{r}\frac{\partial}{\partial r}\left(r\mu^{n+1}\frac{\partial u^{n+1}}{\partial z}\right)\right] - \frac{1}{Fr}(\rho^{n+1} - \rho^0) \tag{3.32}$$

The temporal discretization is carried out in the following classical way using a second-order backward Euler scheme (BDF2) with a constant time step δt. This method, when applied to Eq. (3.20) at time level $n+1$, gives

$$\frac{3\rho^{n+1}f^{n+1} - 4\rho^n f^n + \rho^{n-1}f^{n-1}}{2\delta t} = L^{n+1}(f) + NL^{n+1}(f) + PG^{n+1}(f) + S^{n+1}(f) + O(\delta t^2) \tag{3.33}$$

The nonlinear part is treated explicitly by using the second-order Adams-Bashforth approximation

$$NL^{n+1}(f) = 2NL^n(f) - NL^{n-1}(f) + O(\delta t^2) \tag{3.34}$$

The conservation equation for Y_1 has zero source term and pressure gradient, so it becomes

$$L^{n+1}(Y_1) - \frac{3\rho^{n+1}}{2\delta t}Y_1^{n+1} = \frac{-4\rho^n Y_1^n + \rho^{n-1}Y_1^{n-1}}{2\delta t} + 2NL^n(Y_1) - NL^{n-1}(Y_1) \tag{3.35}$$

Eq. (3.35) is solved first. Since at this instant the physical properties ρ^{n+1} and D^{n+1} are not known, they are approximated by the Adams-Bashforth scheme as

$$\rho^{n+1} = 2\rho^n - \rho^{n-1} + O(\delta t^2), \quad D^{n+1} = 2D^n - D^{n-1} + O(\delta t^2) \tag{3.36}$$

In the equations for velocity components, the source term is composed of the body force S_b^{n+1} and additional terms on the velocity $S_{\mathbf{u}}^{n+1}$

$$S^{n+1}(f) = S_b^{n+1}(f) + S_{\mathbf{u}}^{n+1}(f) \tag{3.37}$$

Once the mass fraction Y_1^{n+1} is calculated the source term $S_b^{n+1}(f)$ is known. The remaning source term $S_{\mathbf{u}}^{n+1}(f)$ is approximated by $S_{\mathbf{u}}^n(f)$. The equations for velocity components read

$$L^{n+1}(u) - \frac{3\rho^{n+1}}{2\delta t}u^{n+1} = \frac{-4u^n f^n + \rho^{n-1}u^{n-1}}{2\delta t} + 2NL^n(u) - NL^{n-1}(u) + PG(u)^{n+1} + S_{\mathbf{u}}^n(u) \tag{3.38}$$

$$L^{n+1}(w) - \frac{3\rho^{n+1}}{2\delta t} w^{n+1} = \frac{-4\rho^n w^n + \rho^{n-1} w^{n-1}}{2\delta t} + 2NL^n(w) - NL^{n-1}(w) + PG^{n+1}(w) + S_b^{n+1}(w) + S_{\mathbf{u}}^n(w) \tag{3.39}$$

Eqs. (3.38) and (3.39) will be solved together with the divergence constraint on **u** by a projection method that will be described in section 3.3.

Stability condition for the time integration As the convection terms NL are treated explicitly the time step must stay below a certain value beyond which the algorithm becomes unstable. For the advection-diffusion equation in one dimension

$$U_t = aU_x + \nu U_x x \tag{3.40}$$

where a and ν are constants, $\nu > 0$, [Ascher et al., 1995] have shown that the second-order BDF2 scheme applied for the implicit diffusion part together with the second-order Adams-Bashforth scheme applied for the explicit convection part is stable for all $\nu \geq 0$, provided that the Courant-Friedrichs-Lewy (CFL) condition is satisfied, i.e.

$$a\frac{\delta t}{\delta x} < 1 \tag{3.41}$$

Applying the result of [Ascher et al., 1995] for our problem in two dimensions yields the stability condition

$$CFL = \frac{\mid u \mid \delta t}{\delta x} + \frac{\mid w \mid \delta t}{\delta z} < 1 \tag{3.42}$$

3.3 Velocity-pressure coupling: fractional-step projection method

The velocity-pressure coupling is handled by a fractional-step projection method. The projection method was first introduced by [Chorin, 1968] to solve the time-dependent Navier-Stokes equations for an incompressible fluid. In each time level the method is composed of two sub-steps. In the first sub-step the pressure is treated explicitly or ignored and a provisional velocity field is calculated. In the second sub-step the pressure is corrected by projecting the provisional velocity onto the space of divergence-free vectors. The method of [Chorin, 1968] is called the non-incremental form since the pressure is ignored in the first sub-step and the new pressure is calculated in the second sub-step. [Kan, 1986] proposed a second-order incremental pressure-correction scheme in which the pressure is treated explicitly and a pressure increment is solved in the second step. We make use of the incremental formulation in our numerical method.

- Prediction step: a provisional velocity field $\tilde{\mathbf{u}}^{n+1}$ is calculated from

$$\begin{cases} L^{n+1}(\tilde{u}) - \dfrac{3\rho^{n+1}}{2\delta t}\tilde{u}^{n+1} & = \dfrac{-4\rho^n u^n + \rho^{n-1}u^{n-1}}{2\delta t} - 2NL^n(u) + NL^{n-1}(u) \\ & \quad + \dfrac{\partial \pi^n}{\partial r} + S^n_{\mathbf{u}}(u) \\ L^{n+1}(\tilde{w}) - \dfrac{3\rho^{n+1}}{2\delta t}\tilde{w}^{n+1} & = \dfrac{-4\rho^n w^n + \rho^{n-1}w^{n-1}}{2\delta t} - 2NL^n(w) + NL^{n-1}(w) \\ & \quad + \dfrac{\partial \pi^n}{\partial z} + S^n_{\mathbf{u}}(w) + S^{n+1}_b(w) \end{cases} \tag{3.43}$$

The Alternating Direction Implicit (ADI) method used to solve Eqs. (3.43) will be described in section 3.5. Subtracting the first and second equations of (3.43) from (3.38) and (3.39), respectively, and multiplying the results by $\lambda = \dfrac{2\delta t}{3\rho^{n+1}}$ gives

$$\begin{cases} \lambda\left(L^{n+1}(u) - L^{n+1}(\tilde{u})\right) - (u^{n+1} - \tilde{u}^{n+1}) & = \lambda\dfrac{\partial}{\partial r}(\pi^{n+1} - \pi^n) \\ \lambda\left(L^{n+1}(w) - L^{n+1}(\tilde{w})\right) - (w^{n+1} - \tilde{w}^{n+1}) & = \lambda\dfrac{\partial}{\partial z}(\pi^{n+1} - \pi^n) \end{cases} \tag{3.44}$$

Expanding the linear terms in (3.44) gives

$$\begin{aligned} \frac{\lambda}{Re}\left[\frac{\partial}{\partial z}\left(\mu^{n+1}\frac{\partial(u^{n+1} - \tilde{u})}{\partial z}\right) + \frac{2}{r}\frac{\partial}{\partial r}\left(r\mu^{n+1}\frac{\partial(u^{n+1} - \tilde{u})}{\partial r}\right)\right] \\ - \left(1 + \frac{2\lambda\mu^{n+1}}{Re\, r^2}\right)(u^{n+1} - \tilde{u}^{n+1}) = \lambda\frac{\partial}{\partial r}(\pi^{n+1} - \pi^n) \end{aligned} \tag{3.45}$$

$$\begin{aligned} \frac{\lambda}{Re}\left[2\frac{\partial}{\partial z}\left(\mu^{n+1}\frac{\partial(w^{n+1} - \tilde{w})}{\partial z}\right) + \frac{1}{r}\frac{\partial}{\partial r}\left(r\mu^{n+1}\frac{\partial(w^{n+1} - \tilde{w})}{\partial r}\right)\right] \\ - \left(1 + \frac{2\lambda\mu^{n+1}}{Re\, r^2}\right)(w^{n+1} - \tilde{w}^{n+1}) = \lambda\frac{\partial}{\partial z}(\pi^{n+1} - \pi^n) \end{aligned} \tag{3.46}$$

When Re and δt are small, the first term in the left hand side of (3.45) and (3.46) are negligible, so Eqs. (3.45) and (3.46) become

$$-\left(1 + \frac{2\lambda\mu^{n+1}}{Re\, r^2}\right)(u^{n+1} - \tilde{u}^{n+1}) = \lambda\frac{\partial}{\partial r}(\pi^{n+1} - \pi^n) \tag{3.47}$$

$$-\left(1 + \frac{2\lambda\mu^{n+1}}{Re\, r^2}\right)(w^{n+1} - \tilde{w}^{n+1}) = \lambda\frac{\partial}{\partial z}(\pi^{n+1} - \pi^n) \tag{3.48}$$

Taking r-partial derivative of (3.47) and z-partial derivative of (3.48) and summing up the results gives

$$-\left(1 + \frac{2\lambda\mu^{n+1}}{Re\, r^2}\right)(\nabla.\mathbf{u}^{n+1} - \nabla.\tilde{\mathbf{u}}^{n+1}) = \frac{\partial}{\partial r}\left(\lambda\frac{\partial}{\partial r}(\pi^{n+1} - \pi^n)\right) + \frac{\partial}{\partial z}\left(\lambda\frac{\partial}{\partial z}(\pi^{n+1} - \pi^n)\right) \tag{3.49}$$

We come to the second sub-step:

- Correction step: a pressure increment $\Phi = \pi^{n+1} - \pi^n$ is calculated from (3.49). After the solution for Φ has been obtained, the new pressure and velocity are calculated from

$$\begin{cases} \pi^{n+1} = \pi^n + \Phi \\ u^{n+1} = \tilde{u}^{n+1} - \dfrac{Re\, r^2 \lambda}{Re\, r^2 + 2\lambda\mu^{n+1}} \dfrac{\partial \Phi}{\partial r} \\ w^{n+1} = \tilde{w}^{n+1} - \dfrac{Re\, r^2 \lambda}{Re\, r^2 + 2\lambda\mu^{n+1}} \dfrac{\partial \Phi}{\partial z} \end{cases} \tag{3.50}$$

The remaining task is to define proper boundary conditions for (3.43) and (3.49). The relation between boundary conditions of these two systems can be seen if we take the integral of (3.49) over the whole domain Ω which reads

$$\int_\Omega \left(\frac{\partial}{\partial r} \left(\frac{1}{\rho^{n+1}} \frac{\partial \Phi}{\partial r} \right) + \frac{\partial}{\partial z} \left(\frac{1}{\rho^{n+1}} \frac{\partial \Phi}{\partial z} \right) \right) dV = \left(1 + \frac{2\lambda\mu^{n+1}}{3Re\, r^2} \right) \int_{\partial\Omega} (\tilde{\mathbf{u}}^{n+1} - \mathbf{u}^{n+1}) \mathbf{n}\, d\Gamma = 0 \tag{3.51}$$

We consider firstly the case in which a Dirichlet boundary condition is specified for $\mathbf{u}^{n+1}$ on the whole domain

$$\mathbf{u}^{n+1} = \mathbf{g}^{n+1} \quad \text{on} \quad \partial\Omega \tag{3.52}$$

A natural choice is to employ the same boundary condition for $\tilde{\mathbf{u}}^{n+1}$ as for $\mathbf{u}^{n+1}$, i.e.

$$\tilde{\mathbf{u}}^{n+1} = \mathbf{u}^{n+1} \quad \text{on} \quad \partial\Omega \tag{3.53}$$

A Neumann boundary condition on Φ is a choice which is compatible with condition (3.53) and (3.51)

$$\frac{\partial \Phi}{\partial \mathbf{n}} = 0 \quad \text{on} \quad \partial\Omega, \tag{3.54}$$

Modification of the projection method for domains with openings We have described the projection method in which a Dirichlet condition is specified for $\mathbf{u}$ on the whole boundary. When other boundary conditions are applied for $\mathbf{u}$, such as in the case where openings are present, the projection method needs to be modified. The boundary conditions for $\mathbf{u}$ can be divided into two types: Neumann condition at the outflow boundary and Dirichlet condition at the remaining boundary. We suppose here without the lost of generality that the outflow boundary is horizontal.

$$\begin{aligned} \mathbf{u}^{n+1} &= \mathbf{g}^{n+1} \quad \text{on} \quad \partial\Omega_w \cup \partial\Omega_i \cup \partial\Omega_s \\ \frac{\partial w^{n+1}}{\partial z} &= 0 \quad \text{on} \quad \partial\Omega_o \end{aligned} \tag{3.55}$$

The first sub-step of the projection method is the same as in the case of Dirichlet condition, except that now the Neumann condition is applied for $\tilde{w}^{n+1}$ at the outflow

boundary

$$\begin{aligned} \tilde{\mathbf{u}}^{n+1} &= \mathbf{g}^{n+1} \quad \text{on} \quad \partial\Omega_w \cup \partial\Omega_i \cup \partial\Omega_s \\ \frac{\partial \tilde{w}^{n+1}}{\partial z} &= 0 \quad \text{on} \quad \partial\Omega_o \end{aligned} \tag{3.56}$$

At the second sub-step we solve Eq. (3.49). The problem is that if we specified the Neumann condition for Φ as in (3.54) and the condition for $\tilde{\mathbf{u}}^{n+1}$ as in (3.53) which satisfies the condition (3.51), another condition may be violated. It is the integral of (3.3) on the whole domain which indicates the overall mass balance

$$\int_{\partial\Omega} \mathbf{u}^{n+1}\mathbf{n}\, d\Gamma = \frac{(\epsilon_M^{21} - 1)}{ReSc} \int_{\partial\Omega} \left(D^{n+1}\rho^{n+1}\nabla Y_1^{n+1} \right) \mathbf{n}\, d\Gamma \tag{3.57}$$

Now we will correct the value of $\tilde{\mathbf{u}}^{n+1}$ at the outflow boundary and denote the corrected value by $\tilde{\mathbf{u}}_*^{n+1}$ so that it satisfies

$$\int_{\partial\Omega} \tilde{\mathbf{u}}_*^{n+1}\mathbf{n}\, d\Gamma = \frac{(\epsilon_M^{21} - 1)}{ReSc} \int_{\partial\Omega} \left(D^{n+1}\rho^{n+1}\nabla Y_1^{n+1} \right) \mathbf{n}\, d\Gamma \tag{3.58}$$

Denoting by M the right-hand-side of (3.57) and N the following quantity

$$N = \int_{\partial\Omega} \tilde{\mathbf{u}}^{n+1}\mathbf{n}\, d\Gamma \tag{3.59}$$

which can be different from M. The value $\tilde{\mathbf{u}}_*^{n+1}$ is the same as $\tilde{\mathbf{u}}^{n+1}$ on the whole domain except that at the outflow boundary it is calculated as

$$\tilde{w}_*^{n+1} = \tilde{w}^{n+1} + \frac{M - N}{l(\partial\Omega_o)} \quad \text{on} \quad \partial\Omega_o \tag{3.60}$$

where $l(\partial\Omega_o)$ is the area of the outlet boundary.

Applying the condition

$$\mathbf{u}^{n+1} = \tilde{\mathbf{u}}_*^{n+1} \quad \text{on} \quad \partial\Omega \tag{3.61}$$

and $\mathbf{u}^{n+1}$ satisfies (3.57).

3.4 Determination of the inflow boundary condition

At the inflow boundary the velocity $w_i(r,t)$ and concentration profile $Y_{1i}(r,t)$ have to be specified. First of all, let us consider a laboratory experiment of fluid injection in an enclosure. Before reaching the inflow boundary, the injected mass has to go from a source of mass S_m through an injection tube as is depicted in Fig. 3.4. Only the mass flux at the source is controlled where an averaged velocity $\overline{w}$ and a mass fraction $\overline{Y_1}$ are specified. However, in the computation the injection tube is not modeled and we have to specify the velocity and the mass fraction profiles at the inflow so that the total mass flux injected in the system is exactly what has been injected at the mass source.

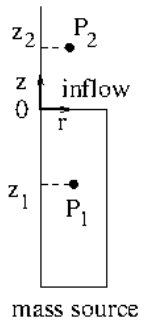

Figure 3.4: The injection tube connecting the mass source S_m and the inflow boundary $\partial\Omega_i$.

The total mass flux F_t going in the enclosure through the inflow boundary is composed of convective flux F_c and diffusive flux F_d

$$F_t = F_c + F_d \tag{3.62}$$

where the convective flux is calculated as

$$F_c = \int_{\partial\Omega_i} (\rho Y_1 w)\, d\Gamma \tag{3.63}$$

and the diffusive flux is calculated as

$$F_d = -\frac{(\epsilon_M^{21} - 1)}{ReSc} \int_{\partial\Omega_i} \left(D\rho \frac{\partial Y_1}{\partial z} \right)\, d\Gamma \tag{3.64}$$

The diffusive flux can be negligible (in the glycerol-water case) or significant (in the helium-air case). We treat both cases in the following.

Negligible diffusive flux If at the mass source there is no diffusion the total flux can be approximated by the convective flux. The same is applied at the inflow boundary if diffusive flux is very small compared to convective flux, as in glycerol-water case where the Schmidt number Sc is very large. The boundary condition at the source can be specified as follows

- Y_1, flat profile
$$Y_{1i}(r,t) = \overline{Y_1} \tag{3.65}$$
- w, flat profile
$$w_i^f = \overline{w} \tag{3.66}$$
- w, parabolic profile
$$w_i^p(r) = w_i^f \left(-\frac{8r^2}{d_i^2} + 2 \right), \quad 0 \le r \le \frac{d_i}{2} \tag{3.67}$$

However, when the diffusive flux is not negligible a process to calculate $w_i(r,t)$ and $Y_{1i}(r,t)$ has to be carried out.

Significant diffusive flux In helium-air case the flow rate is small and the mass fraction gradient is large at the inflow, so the diffusive flux is not negligible. This is illustrated in Fig. 3.5 for a helium-air plume if the boundary conditions like (3.65) and (3.67) are applied at the inflow boundary. When the injection velocity is small, the resulting diffusive flux is much larger than the convective flux. We have to take into account this diffusion flux in calculating the inflow velocity and mass fraction.

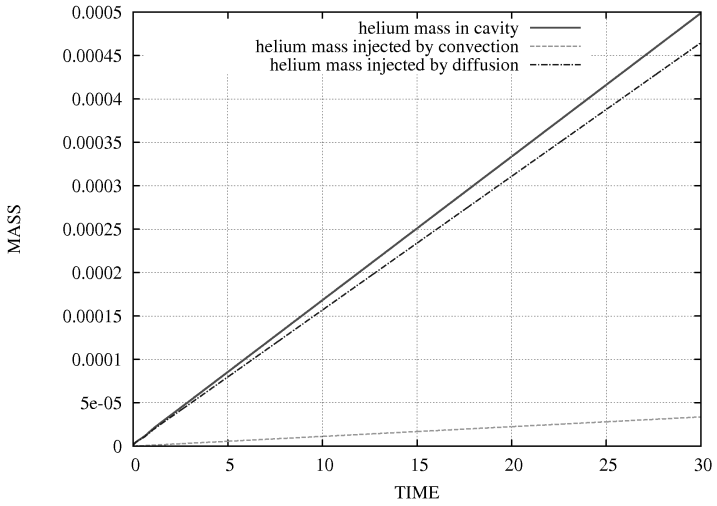

Figure 3.5: Comparison between the diffusive flux and convective flux of helium at the inflow boundary for a helium-air plume.

Integrating Eq. (3.3) over the injection tube gives

$$\int_{\partial\Omega_i} w \, d\Gamma - \int_{S_m} w \, d\Gamma = \frac{(\epsilon_M^{21} - 1)}{ReSc} \left(\int_{\partial\Omega_i} D\rho \frac{\partial Y_1}{\partial z} \, d\Gamma - \int_{S_m} D\rho \frac{\partial Y_1}{\partial z} \, d\Gamma \right) \tag{3.68}$$

The diffusion flux at the source of mass is zero, so it implies that

$$\int_{\partial\Omega_i} w \, d\Gamma = l(S_m)\overline{w} + \frac{(\epsilon_M^{21} - 1)}{ReSc} \int_{\partial\Omega_i} D\rho \frac{\partial Y_1}{\partial z} \, d\Gamma \tag{3.69}$$

where $l(S_m)$ is the surface of the mass source. Supposing that $l(S_m) = l(\partial\Omega_i)$, the flat and parabolic profiles of w at the injection at the inflow boundary are calculated as

- Flat profile

$$w_i^f(t) = \overline{w} + \frac{1}{l(\Omega_i)} \frac{(\epsilon_M^{21} - 1)}{ReSc} \int_{\partial\Omega_i} D\rho \frac{\partial Y_1}{\partial z} \, d\Gamma \tag{3.70}$$

- Parabolic profile

$$w_i^p(r,t) = w_i^f(t) \left(-\frac{8r^2}{d_i^2} + 2 \right), \quad 0 \le r \le \frac{d_i}{2} \tag{3.71}$$

where d_i is the diameter of the injection.

Now we determine the profile of Y_1 at the inflow boundary. Denoting by P_1 a point below the inflow boundary at which the mass fraction is equal to $\overline{Y_1}$ after a delay time t_c and P_2 the point above and nearest to the inflow boundary (on a certain computational grid). They are at vertical positions z_1 and z_2, respectively. The value of Y_1 at P_2 is taken from the computational results at the previous time level. The value of Y_1 at P_1 is increasing linearly from 0 to 1 after a time t_c and is constant after that

$$Y_1^{n+1}(z_1) = \begin{cases} \dfrac{(n+1)\delta t}{t_c}\overline{Y_1} & \text{if} \quad (n+1)\delta t \le t_c \\ \overline{Y_1} & \text{if} \quad (n+1)\delta t > t_c \end{cases} \tag{3.72}$$

where the delay time t_c is dependent on the source velocity $\overline{w}_i$. It is large if $\overline{w}_i$ is small and vice versa. z_1 is chosen near the injection if the source velocity $\overline{w}$ is large and far the injection if $\overline{w}$ is small. The purpose is to ensure that $w_i(r,t)$ is always positive. The choice of t_c and z_1 will be given corresponding to $\overline{w}_i$ in later chapters.

Finally, the inflow value of the mass fraction is interpolated from their values at P_1 and P_2

$$Y_{1_i}^{n+1}(r) = \frac{z_2}{z_1 - z_2} Y_1^{n+1}(z_1) - \frac{z_1}{z_1 - z_2} Y_1^n(r, z_2) \tag{3.73}$$

3.5 Solution of the algebraic equations

3.5.1 Alternating Direction Implicit (ADI) method

To demonstrate the ADI method we replace two semi-discretized equations in (3.43) by a simplified differential form

$$\frac{\partial^2 f^{n+1}}{\partial r^2} + \frac{\partial^2 f^{n+1}}{\partial z^2} - \frac{\partial f^{n+1}}{\partial t} = S \tag{3.74}$$

where S is a known source term. Eq. (3.74) can be discretized implicit method as follows

$$\frac{f_{i-1,j}^{n+1} - 2f_{i,j}^{n+1} + f_{i+1,j}^{n+1}}{(\delta r)^2} + \frac{f_{i,j-1}^{n+1} - 2f_{i,j}^{n+1} + f_{i,j+1}^{n+1}}{(\delta z)^2} - \frac{1}{\delta t}(f_{i,j}^{n+1} - f_{i,j}^{n}) = S \tag{3.75}$$

The implicit method is stable for any time step size δt. However, it leads to large sets of N^2 linear simultaneous equations with N^2 unknown

$$\frac{f_{i-1,j}^{n+1}}{(\delta r)^2} + \frac{f_{i+1,j}^{n+1}}{(\delta r)^2} + \frac{f_{i,j-1}^{n+1}}{(\delta z)^2} + \frac{f_{i,j+1}^{n+1}}{(\delta z)^2} - \left(\frac{1}{(\delta r)^2} + \frac{1}{(\delta z)^2} + \frac{1}{\delta t}\right) f_{i,j}^{n+1} = S - \frac{1}{\delta t} f_{i,j}^{n} \tag{3.76}$$

where N^2 is the number discrete points in the computational domain. The Alternating Direction Implicit (ADI) method is an efficient method to solve (3.74) which avoids the solution of N^2 simultaneous equations like (3.76). It was introduced by [Peaceman and Rachford, 1955] to solve heat flow equation in two space dimensions. At time level $n+1$, the method is carried out in two sub-steps with the same time step size δt.

- In the first sub-step, only one second derivative in one direction, say z, is replaced by the difference approximation of the unknown at time level $n+1/2$. The second derivative in r-direction is replaced by the difference approximation of the unknown at time level n. It means that only z-direction is implicit.

$$\frac{f^{n}_{i-1,j} - 2f^{n}_{i,j} + f^{n}_{i+1,j}}{(\delta r)^2} + \frac{f^{n+1/2}_{i,j-1} - 2f^{n+1/2}_{i,j} + f^{n+1/2}_{i,j+1}}{(\delta z)^2} - \frac{1}{\delta t}(f^{n+1/2}_{i,j} - f^{n}_{i,j}) = S \tag{3.77}$$

which is rearranged in the following form for calculation

$$\frac{f^{n+1/2}_{i,j-1}}{(\delta z)^2} + \frac{f^{n+1/2}_{i,j+1}}{(\delta z)^2} - \left(\frac{2}{(\delta z)^2} + \frac{1}{\delta t}\right) f^{n+1/2}_{i,j} = S - \frac{f^{n}_{i-1,j} - 2f^{n}_{i,j} + f^{n}_{i+1,j}}{(\delta r)^2} - \frac{1}{\delta t} f^{n}_{i,j} \tag{3.78}$$

- In the second sub-step, r-direction is implicit and the second derivative in z-direction is replaced by the difference approximation of the newly calculated unknown at the first sub-step.

$$\frac{f^{n+1}_{i-1,j} - 2f^{n+1}_{i,j} + f^{n+1}_{i+1,j}}{(\delta r)^2} + \frac{f^{n+1/2}_{i,j-1} - 2f^{n+1/2}_{i,j} + f^{n+1/2}_{i,j+1}}{(\delta z)^2} - \frac{1}{\delta t}(f^{n+1}_{i,j} - f^{n+1/2}_{i,j}) = S \tag{3.79}$$

which is rearranged in the following form for calculation

$$\frac{f^{n+1}_{i-1,j}}{(\delta r)^2} + \frac{f^{n+1}_{i+1,j}}{(\delta r)^2} - \left(\frac{2}{(\delta r)^2} + \frac{1}{\delta t}\right) f^{n+1}_{i,j} = S - \frac{f^{n+1/2}_{i,j-1} - 2f^{n+1/2}_{i,j} + f^{n+1/2}_{i,j+1}}{(\delta z)^2} - \frac{1}{\delta t} f^{n+1/2}_{i,j} \tag{3.80}$$

Eqs. (3.78) and (3.80) are tridiagonal and can be solved by Tridiagonal Matrix Algorithm (TDMA) of [Thomas, 1949]. ADI method has been proved in [Peaceman and Rachford, 1955] in the case of unsteady heat equation to be stable for any δt. ADI has to perform only $9N^2$ operations per time step compared to $35N^2$ operations of the most efficient iterative method, extrapolated Liebmann method, and requires a relatively small increase in storage capacity over this method. (see, for example, [Briggs et al., 2000])

3.5.2 Multigrid method

In the second sub-step of the fractional-step projection method we need to solve the discretized elliptic equation (3.49) for the pressure increment. In each time level, this step consumes the most calculation time (average 80 % in our case), so it is essential to have an efficient method in this step and a multigrid method has been chosen. Multigrid has proved to be a powerful method in solving elliptic problems which offers the possibility of solving problems with N unknowns with $O(N)$ work and storage. We describe in the following the multigrid method implemented in of calculation code.

Suppose that the linear problem to be solved is denoted by

$$A\mathbf{u} = \mathbf{f} \tag{3.81}$$

where $\mathbf{u}$ is the vector of unknowns, A is a matrix and $\mathbf{f}$ is a vector of given value. In multidimensional applications, A is large and sparse and the non-zero entries have a regular structure. Therefore, iterative methods are favored in solving (3.81). However, in most basic iterative methods (Jacobi, Gauss-Seidel, successive over-relaxation, etc.) the rate of convergence deteriorates as the mesh size decreases. Fourier analysis of the error has shown that this is because short wavelength modes of the error are reduced rapidly, while long wavelength modes decay slowly. The essential principle of multigrid algorithm is that: the long wavelength part of the error is approximated on coarser grids and the short wavelength modes are reduced with a basic iterative method on fine grids.

Multigrid algorithm Let us denote by $\{G^k, k = 1, 2, .., K\}$ a sequence of increasingly finer grids. The mesh size of the coarser grid is double the mesh size of the fine grid next to it. We denote by $\mathbf{U}^k$ the set of functions defined on G^k. On each grid a prolongation operator $P^k : \mathbf{U}^k \to \mathbf{U}^{k+1}$ and a restriction operator $R^k : \mathbf{U}^k \to \mathbf{U}^{k-1}$ are defined.

Problem (3.81) is defined on G^k as

$$A^k \mathbf{u}^k = \mathbf{f}^k \tag{3.82}$$

The coarse grid approximation is done as follows. On G^k let us denote the error

$$\mathbf{e}^k = \hat{\mathbf{u}}^k - \mathbf{u}^k \tag{3.83}$$

where $\hat{\mathbf{u}}^k$ is the approximation to $\mathbf{u}^k$. The residual is computed as

$$A^k \mathbf{e}^k = -\mathbf{r}^k = A^k \hat{\mathbf{u}}^k - \mathbf{f}^k \tag{3.84}$$

The coarse grid approximation $\mathbf{e}^{k-1}$ of $\mathbf{e}^k$ satisfies

$$A^{k-1} \mathbf{e}^{k-1} = R^k(-\mathbf{r}^k) \tag{3.85}$$

Assuming that (3.85) is solved exactly, the coarse grid correction to be added to $\hat{\mathbf{u}}^k$ is $P^k \mathbf{e}^k$

$$\hat{\mathbf{u}}^k := \hat{\mathbf{u}}^k + P^k \mathbf{e}^k \tag{3.86}$$

The multigrid algorithm for linear problem consists of smoothing on the fine grids, approximation of the required correction on the coarser grids, prolongation of the coarse grid correction to the fine grids and smoothing again on the fine grids. We go from the finest grid to the coarsest and then back to the finest grid in a V pattern, so it is called a V cycle. A multigrid algorithm can contain several successive V cycles until a desired tolerance is achieved. The algorithm is illustrated as follows

Multigrid algorithm

Initialize $\mathbf{u}_0^K$
For $ncy := 1$ to ncy_{max} do

- Relaxation on the finest grid: $\mathbf{u}^K := S(\mathbf{u}_0^K, A^K, \mathbf{f}^K, n_1)$

- Compute the residual on the finest grid: $\mathbf{r}^K := \mathbf{f}^K - A^K\mathbf{u}^K$
- Going successively to coarser grid:

  For $j := K-1$ to 2 do
  - $\mathbf{e}^j := S(0, A^j, R^{j+1}\mathbf{r}^{j+1}, n_1)$
  - $\mathbf{r}^j := R^{j+1}\mathbf{r}^{j+1} - A^j\mathbf{e}^j$
- Relaxation on the coarest grid: $\mathbf{e}^1 := S(0, A^1, R^2\mathbf{r}^2, n_2)$
- Going successively to finer grid:

  For $j := 2$ to $K-1$ do
  - $\mathbf{e}^j := \mathbf{e}^j + P^{j-1}\mathbf{e}^{j-1}$
  - $\mathbf{e}^j := S(\mathbf{e}^j, A^j, r^j, n_3)$
- Compute the new solution on the finest grid: $\mathbf{u}^K := \mathbf{u}^K + P^{K-1}\mathbf{e}^{K-1}$
- Relaxation on the finest grid:$\mathbf{u}^K := S(\mathbf{u}^K, A^K, \mathbf{f}^K, n_3)$

The number of V-cycles performed is ncy_{max}. $S(\mathbf{u}_0^K, A^K, \mathbf{f}^K, n_1)$ stands for n_1 smoothing iterations, for example with the SOR method in our code, applied to $A^K\mathbf{u}^K = \mathbf{f}^K$, starting with $\mathbf{u}_0^K$.

Restriction and prolongation operators In 2D case the definition of the restriction operator $R^{k+1} : \mathbf{U}^{k+1} \to \mathbf{U}^k$ and the prolongation operator $P^k : \mathbf{U}^k \to \mathbf{U}^{k+1}$ are illustrated for a part of the grid. Denoting by small filled circles the cell-centers of the control volumes of fine grid G^{k+1} and big open circles those of the control volumes of coarse grid G^k, the control volumes are labeled as in Fig. (3.6).

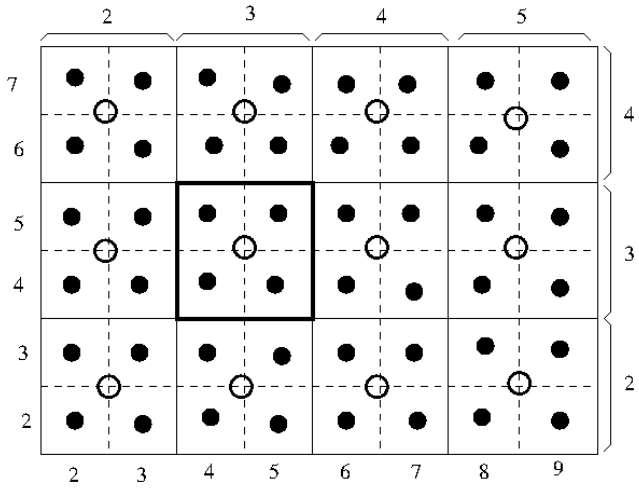

Figure 3.6: Control volumes corresponding to fine and coarse grids in multigrid method.

Case	Number of cells	CPU time for 10000 δt (δt=10^{-4})	CPU time/δt/cell
Glycerol-water	514x2498	115 h	3.2×10^{-5} s
Helium-air	322x642	2.1 h	3.7×10^{-6} s

Table 3.1: Performance of the code on Linux platform Intel (R) Xeon (R) CPU X5675 @3.07 GHz.

The value of $\mathbf{u}^k$ in cell $(3,3)$ of G^k is the weighted average of four cells defined on grid G^{k+1} included in it.

$$\mathbf{u}^k(3,3) = \frac{1}{4}\left(\mathbf{u}^{k+1}(4,4) + \mathbf{u}^{k+1}(4,5) + \mathbf{u}^{k+1}(5,4) + \mathbf{u}^{k+1}(5,5)\right) \tag{3.87}$$

The values of $\mathbf{u}^{k+1}$ in four cells $(4,4)$, $(4,5)$, $(5,4)$, $(5,5)$ on grid G^{k+1} are calculated as follows

$$\mathbf{u}^{k+1}(4,4) = \frac{1}{16}\left(9\mathbf{u}^k(3,3) + 3\mathbf{u}^k(3,2) + 3\mathbf{u}^k(2,3) + \mathbf{u}^k(2,2)\right) \tag{3.88}$$

$$\mathbf{u}^{k+1}(4,5) = \frac{1}{16}\left(9\mathbf{u}^k(3,3) + 3\mathbf{u}^k(3,4) + 3\mathbf{u}^k(2,3) + \mathbf{u}^k(2,4)\right) \tag{3.89}$$

$$\mathbf{u}^{k+1}(5,4) = \frac{1}{16}\left(9\mathbf{u}^k(3,3) + 3\mathbf{u}^k(2,3) + 3\mathbf{u}^k(4,3) + \mathbf{u}^k(4,2)\right) \tag{3.90}$$

$$\mathbf{u}^{k+1}(5,5) = \frac{1}{16}\left(9\mathbf{u}^k(3,3) + 3\mathbf{u}^k(3,4) + 3\mathbf{u}^k(4,3) + \mathbf{u}^k(4,4)\right) \tag{3.91}$$

3.6 Implementation of the numerical method, code performance

The numerical method described in this chapter has been implemented in a 2D sequential code written in FORTRAN language. Two versions of the code have been developed corresponding to the glycerol-water case where the divergence is zero and the helium-air case where the divergence is different from zero. The code is run on a Linux platform. Its performance in the two cases mentioned above is reported in Table 3.1. We can see that the CPU time for glycerol-water case is approximately ten times the CPU time for helium-water case. This is because the Schmidt number in glycerol-water case is very large and the multigrid solver requires more cycles to converge to the same residual (10^{-12}) in this case (17 cycles for glycerol-water case compared to 3 cycles for helium-air case).

3.7 Conclusion

In this chapter the detailed numerical method has been presented. We can summarize the main points as follows

- The governing equations are discretized in time using a semi-implicit scheme of order 2 in which the diffusion parts are treated implicitly and the convection parts are approximated by a second-order Adams-Bashforth scheme. The pressure-velocity coupling is treated by a pressure-correction method.
- A finite volume method is used for the spatial discretization. Second-order center scheme is used for the diffusion terms. The convection terms are discretized using either second-order center scheme or third-order QUICK scheme.
- At each time level the governing equations are solved in a sequential way: the species transport equation is solved first, then the momentum equations are solved together with the divergence constraint.
- The pressure-correction method has been modified to take into account the inlet and outlet boundaries.
- Special treatment has been done for the inflow boundary condition in the helium-air case where the diffusion flux is significant.
- The numerical method has been implemented in a Fortran code and is run on a Linux platform.

The next chapter is devoted to the validation of the numerical method implemented.

Chapter 4

Laminar starting forced plumes at high Schmidt numbers: validation with experimental data

4.1 Introduction

When a plume rises in a confined environment, in the starting period when the impact of the confinement is not significant, it behaves like a starting plume in an unbounded environment.

Starting round plumes in an unbounded environment have been studied extensively. A laminar starting plume has two parts: a conduit which is similar to a steady plume and a well-defined, evolving head which can be considered as a thermal with increasing buoyancy ([Shlien, 1976]). Experimental results established that the ascent velocity of the upper front of the head, which is called the ascent velocity of the head w_h, is constant in time and is equal to a constant ratio of the centerline vertical velocity of a steady plume. Several empirical formulae have been proposed ([Shlien, 1976], [Moses et al., 1993], [Kaminski and Jaupart, 2003]) and a complete formula, in which the dependence on the Prandtl number is taken into account, was proposed by [Kaminski and Jaupart, 2003]

$$w_h = (0.57 \pm 0.02) \left(\frac{\ln \epsilon^{-2}}{2\pi} \right)^{1/2} \left(\frac{g\beta P}{\rho_a \nu_a C_p} \right)^{1/2} \tag{4.1}$$

where ϵ is the solution of

$$\epsilon^4 \ln \epsilon^{-2} = Pr^{-1} \tag{4.2}$$

The definitions of the notations are given in Table 4.1. The ratio of this velocity to the centerline velocity of a steady plume w_c is 0.57 ([Kaminski and Jaupart, 2003]).

For plumes created by compositional differences, [Rogers and Morris, 2009] has carried out experiments on several forced plumes and a formula for w_h has been

Symbol	Variable	Dimensions
D	mass diffusivity	$[m^2 s^{-1}]$
β	Thermal expansion coefficient	$[K^{-1}]$
κ	Thermal diffusivity	$[m^2 s^{-1}]$
ρ	Density	$[kg\ m^{-3}]$
ρ_a	Density of ambient fluid	$[kg\ m^{-3}]$
ρ_i	Density of injected fluid	$[kg\ m^{-3}]$
μ	Viscosity	$[Pa\ s]$
$\nu = \mu/\rho$	Kinematic viscosity	$[m^2 s^{-1}]$
ν_i	Viscosity of injected fluid	$[m^2 s^{-1}]$
ν_a	Viscosity of ambient fluid	$[m^2 s^{-1}]$
Y_1	Glycerol mass fraction	[-]
Y_{1i}	Glycerol mass fraction of injected fluid	[-]
Y_{1a}	Glycerol mass fraction of ambient fluid	[-]
C_p	Specific heat	$[JK^{-1}kg^{-1}]$
g	Gravitational acceleration	$[m\ s^{-2}]$
P	Heat flux	$[J\ s^{-1}]$
Q	Volume flux	$[m^3\ s^{-1}]$
$Pr = \nu/\kappa$	Prandtl number	[-]
$Sc = \nu/D$	Schmidt number	[-]

Table 4.1: Notations

proposed

$$w_h = (0.54 \pm 0.01) \left(\frac{g(\rho_a - \rho_i)Q}{\rho_a \nu_i} \right)^{1/2} \tag{4.3}$$

This formula is similar to that of a thermal plume, in which the buoyancy thermal flux $\frac{g\beta P}{\rho_a C_p}$ has been replaced by the densimetric compositional buoyancy flux $g\frac{\rho_a - \rho_i}{\rho_a}Q$. However, the viscosity in Eq. (4.3) is that of the injection fluid while in Eq. (4.1) it is the viscosity of the ambient fluid. When the ratio of these two viscosities is nearly 1, using either of them would yield the same results. However, when this ratio is far from 1 the results would be quite different.

In this chapter we carry out simulations on several glycerol-water plumes in the experiment of [Rogers and Morris, 2009] and make a comparison with their experimental data. Our purpose is twofold. Firstly, the direct comparison of numerical model with laboratory model will provide essential validation and verification of independent approaches. We are also provided with a means to estimate the magnitude of the errors by the assumptions made in the numerical modeling. Secondly, the influence of the viscosity in formula (4.3) is investigated.

The organization of this chapter is as follows. The description of the experiment of [Rogers and Morris, 2009] is given in section 4.2. The numerical set up for the simulations and the method to analyze the results are introduced in section 4.3. In section 4.5 several parameters that can influence the numerical simulations are investigated. Finally, section 4.6 is devoted to the comparison of the numerical results with the experimental data of [Rogers and Morris, 2009].

4.2 Description of the experiment of [Rogers and Morris, 2009]

The experiments of [Rogers and Morris, 2009] were performed in two tanks, one of which is larger than the other. Since two tanks gave the same conclusions for the overall results, only test cases in the larger tank are simulated numerically. The larger tank (Fig. 4.1) has a base of $13.4 \times 13.4\ cm^2$ and is $50.2\ cm$ high. The tank is open with a hole of $6\ cm$ diameter in the center of the ceiling, so the pressure remains constant during the injection. A homogeneous glycerol-water solution fills the tank up to $10\ cm$ from its ceiling.

The temperature of $22\ ^oC$ and the atmospheric pressure of $1\ atm$ are maintained during the experiment.

A glycerol-water solution slightly less dense than the ambient solution is injected in the tank through a round inlet at the center of the base, which has a diameter $d_i = 3.0mm$. The injection volume flow rate Q was varied in the range of 3.3×10^{-8} m^3/s to $6.67 \times 10^{-7}\ m^3/s$, which covers the transition from buoyancy-dominated regime to momentum-dominated regime.

The difference between the injected fluid density, ρ_i, and the ambient fluid density, ρ_a, is not more than 1%. The dimensionless ratio of their kinematic viscosities, ν_i and ν_a, was typically close to unity.

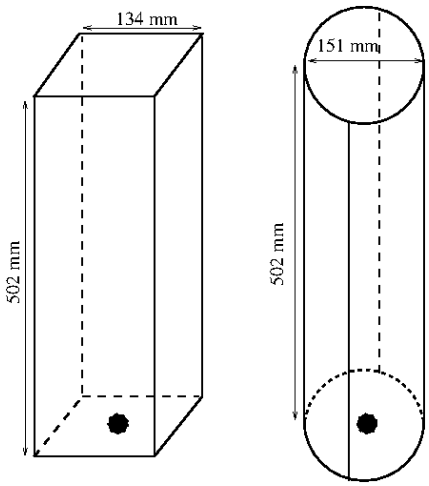

Figure 4.1: Geometry of the glycerol-water plume experiment of [Rogers and Morris, 2009] (left) and the computational domain (right).

The diffusion coefficient, D, is of the order $10^{-10}m^2/s$, which is very small compared to the kinematic viscosity, ν. Therefore, the Schmidt number Sc_a, defined by (2.68), is in the range $1 \times 10^3 \leq Sc \leq 2 \times 10^6$.

4.3 Numerical set up

In this section the parameters and conditions for the numerical simulations of glycerol-water starting plumes are presented in section 4.3.1. Then we describe the general structure of the plume in section 4.4.

4.3.1 Numerical set up

We present in this section the physical parameters and conditions for the numerical simulations of glycerol-water plumes.

We performed simulations on 13 forced plumes which allow a detailed comparison with the experiments in a total of 34 forced plumes of [Rogers and Morris, 2009]. The test cases that we performed together with their physical properties and dimensionless parameters are presented in Tables 4.2 and 4.3. The name of the test cases are taken the same as in [Rogers and Morris, 2009].

The temperature is 22^oC, which is the same as the experiment.

In table 4.2, ρ_i and $\frac{\rho_a - \rho_i}{\rho_a}$ are taken from the experimental data while ρ_a is calculated from these two quantities. The glycerol mass fractions Y_{1i} and Y_{1a} are calculated from ρ_i and ρ_a, respectively, via Eqs. (2.27)-(2.25).

In order to take into account the variation of the viscosity in the numerical simulation, a law for the dependence of viscosity on the glycerol mass fraction given by Eqs. (2.40)-(2.44) was used. By adjusting mass fraction, we reproduced the viscosities within 4 % different with the experimental data.

Case	ρ_i	Y_{1i}	ρ_a	Y_{1a}	$\frac{\rho_a-\rho_i}{\rho_a}$	ν_i	ν_a	$\frac{\nu_i}{\nu_a}$	Gr	Sc_a
D1	1174.5	0.6656	1177.54	0.6771	0.00258	14.19	15.47	0.917	1.3×10^7	64128
D2	1175.2	0.6683	1179.7	0.6852	0.00381	14.47	16.48	0.878	1.7×10^7	70976
D4	1204.5	0.7786	1215.95	0.8218	0.00942	37.87	60.32	0.628	2.8×10^6	592574
D5	1213.5	0.8125	1216.055	0.8222	0.00210	54.32	60.59	0.896	8.2×10^5	597078

Table 4.2: Physical properties of the simulated test cases of glycerol-water forced plumes: ρ_a and ρ_i are in $[kg\ m^{-3}]$, ν_a and ν_i are in 10^{-6} $[m^2\ s^{-1}]$.

Case	Q (m^3/s)	Re_i	Ri_i
D1,1	3.3×10^{-8}	0.987	1.746
D1,2	6.7×10^{-8}	2.004	0.424
D1,3	1.67×10^{-7}	4.995	0.068
D1,4	2.67×10^{-7}	7.986	0.027
D1,5	4.0×10^{-7}	11.964	0.012
D5,1	1.33×10^{-7}	1.039	0.088
D5,2	2.0×10^{-7}	1.563	0.039

Case	Q (m^3/s)	Re_i	Ri_i
D4,1	3.3×10^{-8}	0.370	6.420
D4,2	6.7×10^{-8}	0.751	1.558
D4,3	1.33×10^{-7}	1.491	0.395
D4,4	2.67×10^{-7}	2.992	0.098
D4,5	4.0×10^{-7}	4.483	0.044
D2	2.67×10^{-7}	7.831	0.039

Table 4.3: Injection volume flux and dimensionless parameters of the simulated test cases of glycerol-water forced plumes

The diffusion coefficient D is calculated via Eqs. (2.36)-(2.38). The definitions of the dimensionless parameters can be found in section 2.4.

The governing equations are solved in axisymmetric form. For parametric study of the numerical simulations in section 4.5, we model a cylindrical tank whose height is the same as the experimental tank (Fig. 4.1). The diameter of the computational domain is taken equal to the tank width in the experiment, which is 13.4 cm. This configuration is only used to study the dependence of the flow on different parameters of the numerical simulation. To compare with experimental results, a cylindrical of 151 mm diameter is used to conserve the volume of the experimental tank (Fig. 4.1). All the calculated quantities are dimensionless. The reference length is the height of the cavity and the reference velocity is the average injection velocity $\overline{w_i}$ calculated by Eq. (2.63).

When the tank is supplied continuously with the injection fluid, the fluid level in it increases. In the experiments of [Rogers and Morris, 2009] the increase of the fluid level in the tank is 1 mm for the largest flow rate $Q = 4.0 \times 10^{-7} m^3/s$ during the injection time of 35 seconds. This increase is negligible compared with 502 mm the height of the tank. Therefore, it is neglected in the numerical model without affecting the numerical results.

The boundary conditions are described in chapter 3.

At the initial state, the ambient fluid is quiescent and of constant density ρ_a.

4.4 General plume characteristics

In this section we present the general structure of a glycerol-water plume. This general structure includes the outer shape (i.e how we see the plume by our eyes) and the internal structure which is represented by the velocity field.

4.4.1 Plume outer shape

The time evolution of the plume is represented by glycerol mass fraction field in Fig. 4.2. These 3D figures are obtained by superimposing the original mass fraction field Y_1 which is the solution of the governing equations (2.54), (2.55), (2.56) and (2.57). This procedure is similar to putting a camera in front of the plume and taking a picture of it.

Over the course of its evolution, the plume develops a thin column of fluid called the "conduit" and a well-defined, evolving "head" (or "stem" and "cap", respectively, in [Moses et al., 1993]). The conduit has an almost constant radius along its height and shrinks slightly as the head is approached. The head is fed by the fluid from the conduit and grows in size. The injected fluid concentrates in a thin layer of the head edge surrounding the conduit. Between this layer and the conduit is the ambient fluid which occupies most of the volume of the head.

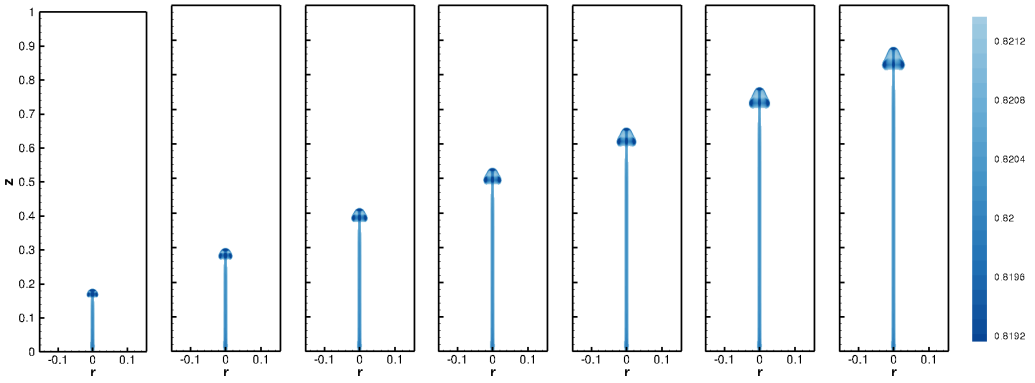

Figure 4.2: Case D4,5: time evolution of the plume presented by glycerol mass fraction field from $t = 0.1$ to $t = 4.0$. The time interval between two consecutive images is 0.5. The reference time is $t_r = 8.9s$

We use the mass fraction field to define the outer shape of a plume by the front between the fluid in the plume with the ambient fluid. This front is quite difficult to define since there are oscillations in the glycerol mass fraction field where the injected fluid meets the ambient fluid. We see in Fig. 4.3 that Y_1 passes through large oscillations and changes abruptly from the injected value to the ambient value of 0.8218 at $z = 0.85$. These oscillations can be seen more clearly in the insert to

Fig. 4.3 which is the zoom of the curve at $t = 3.2$. This is the front of the head interface with the ambient fluid. These are numerical oscillations due to large local gradients of the mass fraction near this interface. Since the Schmidt numbers for these flows are very large, this interface is quite sharp and the centered scheme for the convective term, which possesses some dispersive error, can not resolve all the oscillations with the present resolutions (up to 898 cells in x-direction and up to 3746 cells in z-direction, see more in section 4.5.4). However, we will see in section 4.5.3 that QUICK scheme for the mass fraction equation helps decrease these oscillations.

We use an identification coefficient $id = \frac{Y_{1a}-Y_1}{Y_{1a}-Y_{1i}}$ for defining this interface. A point is in the plume if id is greater than some threshold ϵ.

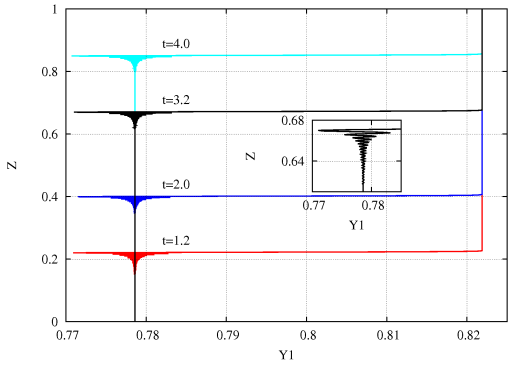

Figure 4.3: Mass fraction of glycerol along the centerline in case D4,5.

Several values for ϵ from 0.05 to 0.4 were tested and the comparison is presented in Fig. 4.4a for case D4,5 at $t = 4.0$. For $\epsilon = 0.4$ a part is lost in the plume head. The plume conduit is not well-defined for ϵ of 0.05 and 0.1. The plume interface defined with ϵ equal to 0.2 and 0.3 are almost identical and it is plotted in Fig. 4.4b for $\epsilon = 0.2$. We can see clearly from this figure a plume with a well-defined head and a conduit part with an almost constant diameter, which shrinks a little when the head is approached.

From the plume outer shape, the following quantities are measured characterize the plume

- The plume height h
- Conduit diameter d_c: the diameter of the conduit measured at half of the plume height h.
- Head diameter d_h: the largest diameter of the head.
- Head length l_h: the distance between the vertical position at which h is defined and the vertical position below and nearest to it at which the diameter of the plume goes below d_c.
- Aspect ratio of the head RF_h=$\frac{d_h}{l_h}$.

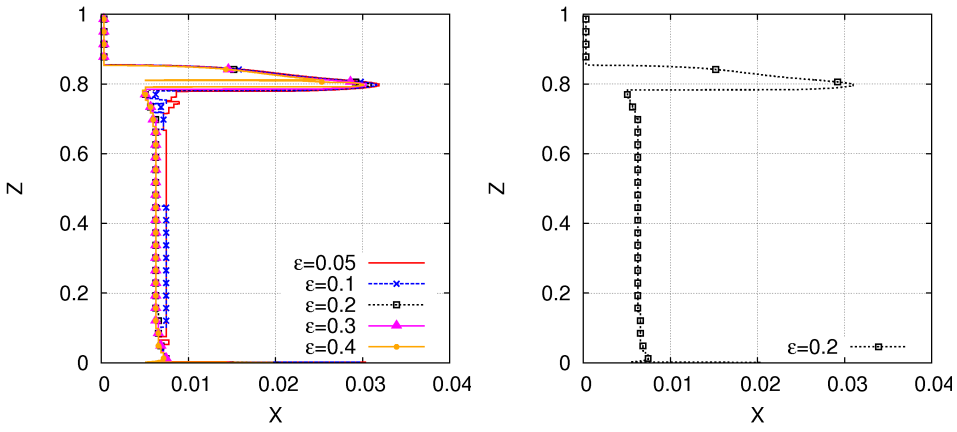

(a) (b)

Figure 4.4: The shape of the plume at $t = 4.0$ in case D4,5: a) for different values of the threshold ϵ for the identification factor id. A point (x, y) is defined to be in the plume if $id = \frac{Y_{1a} - Y_1(x,z)}{Y_{1a} - Y_{1i}} > \epsilon$. b) for $\epsilon = 0.2$.

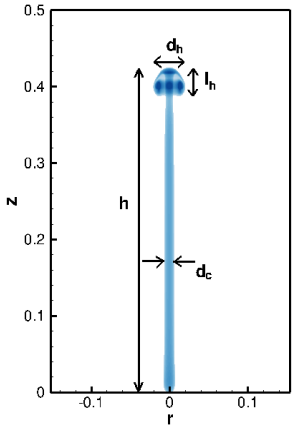

Figure 4.5: The main characteristics of a plume.

ϵ	h	d_c	l_h	d_h	RF_h
0.05	0.8540	0.0143	0.0757	0.0632	0.83
0.1	0.8540	0.0119	0.0739	0.0626	0.85
0.2	0.8534	0.0119	0.0709	0.0614	0.87
0.3	0.8528	0.0119	0.0685	0.0602	0.88

Table 4.4: Results of case D4,5: Plume characteristics at $t = 4.0$ for different values of ϵ.

These quantities are illustrated in Fig. 4.5

The plume characteristics are calculated and listed in Table 4.4 for ϵ from 0.05 to 0.3. From $\epsilon = 0.05$ to $\epsilon = 0.3$ the plume height h decreases by only 0.14% while the head diameter d_h decreases by 5% and the head length l_h decreases by 10.5 %. The conduit diameter d_c keeps the same values for ϵ from 0.1. Therefore, the method to define the plume interface is proved to be reliable and a value of 0.2 for ϵ is used for the other plumes from now on.

4.4.2 Plume ascent velocity

The ascent velocity of the plume can be estimated from the time evolution of the plume height by a second-order formula as

$$w_h(t) = \frac{dh}{dt}(t) = \frac{h(t+\delta t) - h(t-\delta t)}{2\delta t} \tag{4.4}$$

For the plume being considered, the plume height is recorded every $\delta t = 0.02$ and is plotted in Fig. 4.6a. The velocity is calculated using Eq. (4.4) and is plotted in Fig. 4.6b. We can see clearly that at the beginning the plume velocity decreases very fast and then increases until it reaches a constant state. The steps in Fig. 4.6b is due to numerical error of the approximation (4.4). From $t = 0.75$ w_h only oscillates between two values 0.21 and 0.24. The ascent velocity is then defined as the average value of 0.21 and 0.24, which is 0.225, with an error band of 0.015. We denoted as follows

$$w_h = 0.225 \pm 0.015 \tag{4.5}$$

4.4.3 Plume internal structure

Centerline velocity The vertical velocity w along the centerline at four different times are presented in Fig. 4.7.

In Fig. 4.7 each curve representing the vertical velocity w is divided into two parts. Taking the profile at $t = 4.0$ as an example.

- First part ($z = 0$ to $z = 0.7$) in the plume conduit: the forced plume behaves like a jet when the buoyancy effect is small compared to the viscous effect and w decreases very fast from a value of 1.0 to about 0.23, then it increases

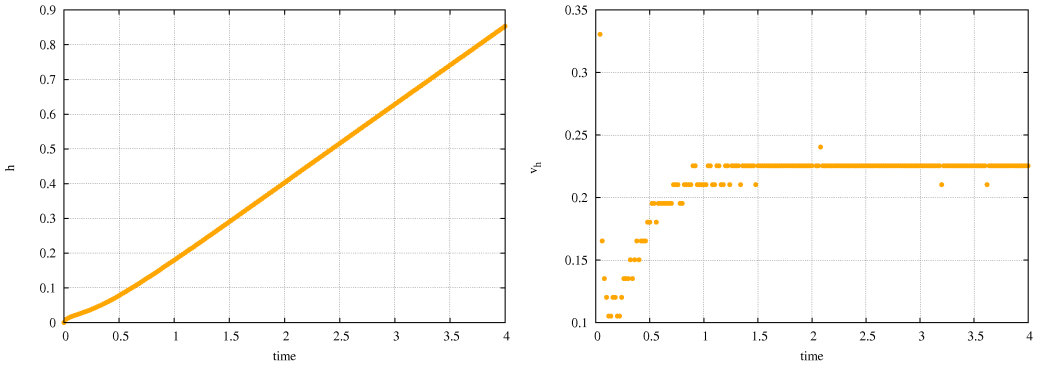

(a) (b)

Figure 4.6: Case D4,5: a) Time evolution of the plume's elevation above the source, b) Time evolution of the plume ascent velocity.

when the buoyancy effect is dominant. Then the buoyancy effect is balanced with the viscous effect and w has a constant value of 0.28. This constant is called the centerline velocity of the conduit and is denoted by w_c. From four curves in Fig. 4.7 it is clear that the velocity structure in the conduit achieves a steady-state structure as soon as it is built, which is independent of the dynamics of the ascending head above.

- Second part (from $z = 0.7$): when the plume head is approached, w accelerates a little above w_c. Then it decelerates and accelarates again in the middle of the plume head. This creates a valley of w in the plume head.

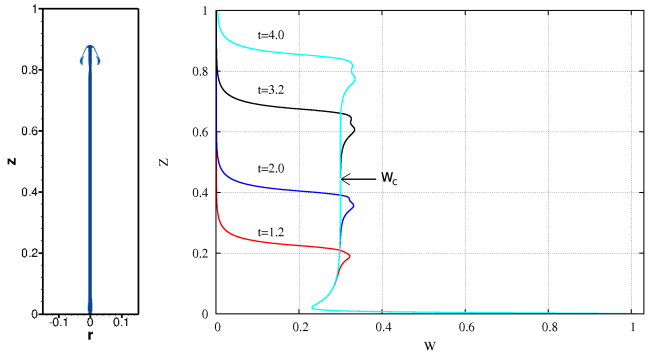

(a) (b)

Figure 4.7: a) The plume at $t = 4.0$, b) vertical velocity along the centerline in case D4,5.

Streamlines and velocity vector field The streamlines on top of the mass fraction and vorticity fields are presented in Fig. 4.8. The ascent of the plume happens together with the descent of the ambient fluid surrounding it. Two centers of rotation (C_R) are visible outside the plume head near its lower part. In Fig. 4.8-b the local extrema of the vorticity are found in the lower part of the head.

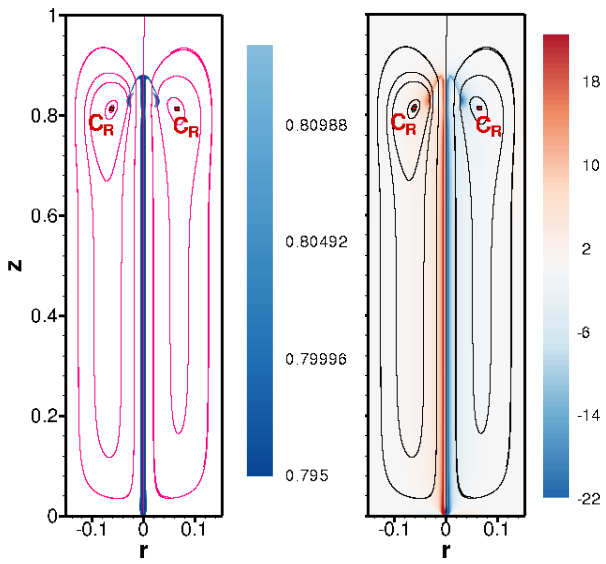

(a) (b)

Figure 4.8: Streamlines on top of a) mass fraction field, b) vorticity field at $t = 4.0$ in case D4,5.

Radial profiles of velocity The radial profiles of the velocity components at different heights are presented in Fig. 4.9 and Fig. 4.10.

In Fig. 4.9 the radial profile of w is presented. At $z = 0$, $w = 1.0$ within the injection and $w = 0$ elsewhere. This uniform profile is spread out when the injected fluid penetrates into the domain. At $z = 0.1$ the profile of w has a peak of 0.3 and a radius of 0.06. In the plume conduit from $z = 0.1$ to $z = 0.6$ the profile of w keeps the same shape. For $x < 0.06$, $w > 0$ corresponding to the ascending of the plume and for $x > 0.06$, $w < 0$ corresponding to the descending of the ambient fluid. At $z = 0.7$, w at the centerline increases when the head is approached. At $z = 0.8$ the profile of w has two peaks: one corresponding to the centerline value and the other corresponding to the lobe of the head. The upper limit of the head is at $z = 0.85$ where the centerline value decreases to 0.26, smaller than the centerline value of 3.0 in the conduit. The velocity profile at the surface is presented in the insert to Fig. 4.9 which shows a positive part from $x = 0$ to $x = 0.09$ and a negative part from $x = 0.09$. Since the plume has risen up to 4/5 of the height of the cavity, the descending effect of the ambient fluid is visible at this surface.

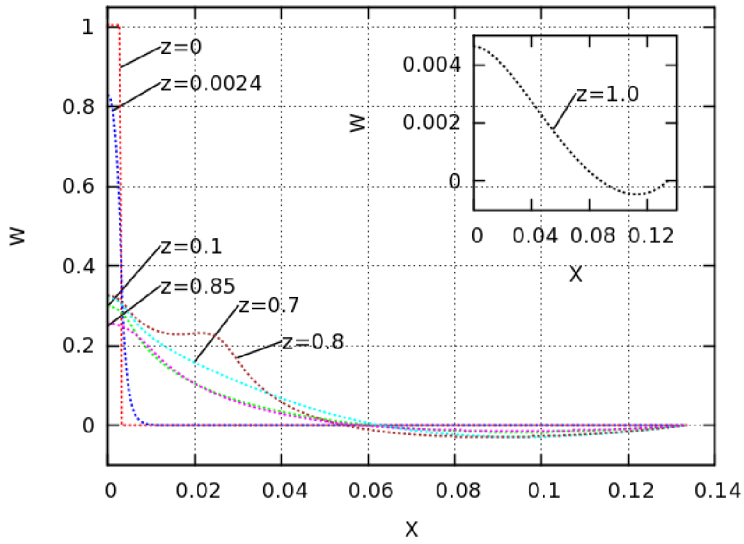

Figure 4.9: Case D4,5: Radial profile of vertical velocity at $t = 4.0$ at different z-positions.

The radial profile of the horizontal velocity is presented in Fig. 4.10. At $z = 0$ it is uniformly equal to 0 but just above the injection, at $z = 0.0024$ it attains a much higher value of 0.18 due to the spreading of the injected fluid. From $z = 0.1$ ot $z = 0.6$ the horizontal velocity has a value of almost 0 which shows that there is no spreading of the plume conduit. As the head is approached at $z = 0.7$ there is a shrinkage of the plume conduit, which is demonstrated by the negative value of the horizontal velocity. From $z = 0.8$ to $z = 0.85$ u comes back to positive values, which shows the spreading of the plume head.

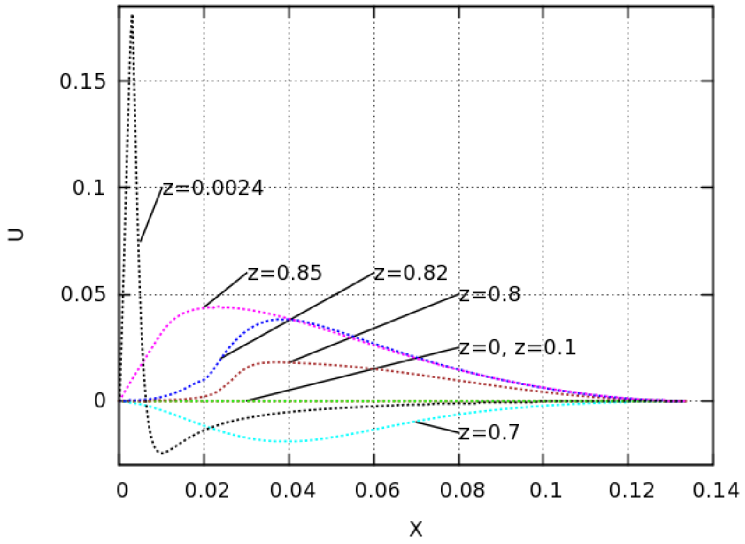

Figure 4.10: Case D4,5: radial profile of horizontal velocity at $t = 4.0$ at different z-positions.

All the plume characteristics have been defined. Their dependence on different parameters of the numerical simulations will be analyzed in the next section.

4.5 Parametric study for the numerical simulation

In a numerical simulation there are many parameters that can have major or minor influences on the solution. Their effects are analyzed in this section on steady and transient properties of the plumes. For steady properties we mean the ascent velocity of the plume w_h, the centerline velocity of the conduit w_c and the diameter of the conduit d_c. For transient properties we mean the plume height h, the head length l_h, the head width d_h and the head aspect ratio RF_h. In the following, the time step is calculated corresponding to $CFL = 0.9$ (CFL number is calculated in 3.2).

4.5.1 Influence of variable viscosity

Firstly, we investigate the influence of the viscosity on the numerical results. We present in Fig. 4.11 the results obtained with constant viscosity model (the viscosity is taken equal to that of the ambient at the beginning of the simulation) and variable viscosity model (the viscosity is calculated using Eqs. (2.40)-(2.44)) in case D4,5 where the viscosity ratio between the ambient and injected fluids is largest ($\frac{\nu_i}{\nu_a}$=0.628). The centerline velocity in the conduit w_c is 7.8 % higher when the variable viscosity model is employed. The plume height with the variable viscosity model is also higher but the difference with constant viscosity model is only less than 1 %.

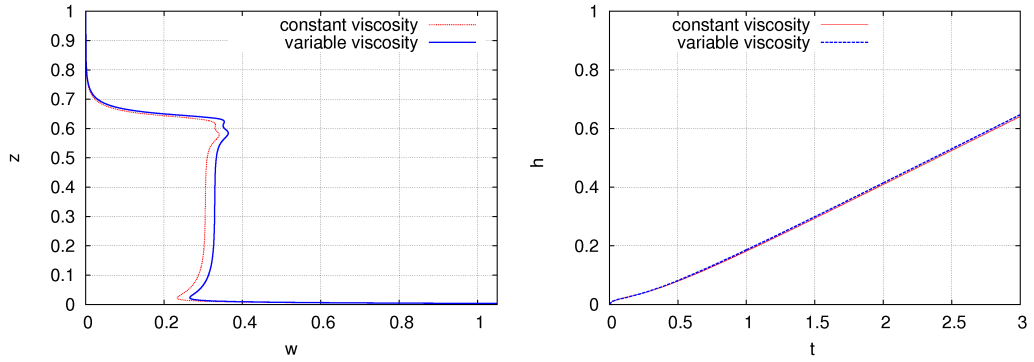

(a) (b)

Figure 4.11: Comparison of constant viscosty model and variable viscosity model for case D4,5: a) Vertical velocity along the centerline at $t = 3.0$, b) Time evolution of the plume height above the source

4.5.2 Influence of the inlet velocity profile

The simulations of case D4,5 with uniform and parabolic inlet velocity profiles defined in section 3.4 are compared. Except the maximum velocity at the inlet of the parabolic profile which is twice that of the uniform profile, no differences in the plume height and vertical velocity along the centerline are found.

4.5.3 Influence of the convection schemes

We investigate in this section the influence of CENTER and QUICK schemes on the solution. Those convection schemes have been described in chapter 3. We carried out four simulations on case D4,5 with the combinations of CENTER and QUICK schemes as follows:

- 1. CENTER scheme for both the equation for $Y1$ and momentum equation

- 2. CENTER scheme for the equation for $Y1$ and QUICK schem for momentum equation
- 3. QUICK scheme for the equation for $Y1$ and CENTER schem for momentum equation
- 4. QUICK scheme for both the equation for $Y1$ and momentum equation

Combinations 1 and 2 give the same results. Combinations 3 and 4 give the same results which are different from those of combinations 1 and 2. We conclude that in this case QUICK scheme, when applied for the momentum equation, gives the same results as CENTER scheme. When QUICK scheme is applied for the equation for Y_1 it gives less oscillations than CENTER scheme, as is illustrated in Fig. 4.12a. This shows the preference of using QUICK scheme for the scalar equation in this case because the accumulation of numerical errors can decrease the quality of the solutions.

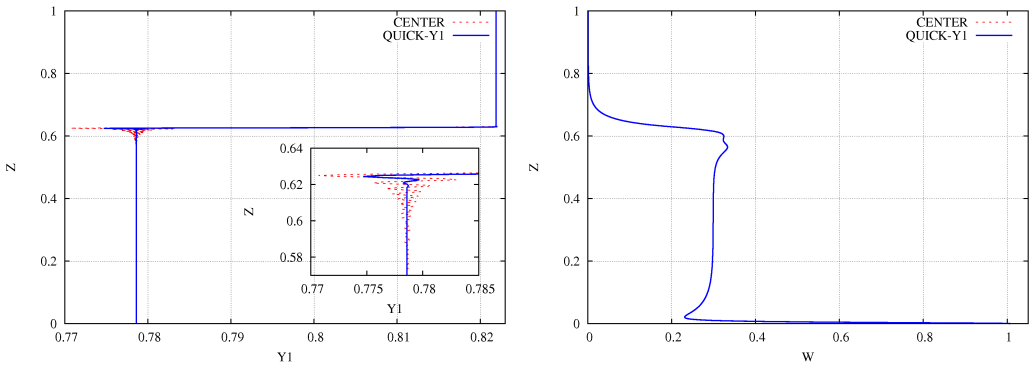

(a) (b)

Figure 4.12: Comparison of CENTER scheme and QUICK scheme for the convection term in the equation for Y_1 for case D4,5: a) Vertical velocity along the centerline at $t = 3.0$, b) Glycerol mass fraction along the centerline at $t = 3.0$

4.5.4 Influence of the spatial resolution

In this section the influence of the mesh size is investigated. The grid convergence study are carried out in both r and z-directions with 6 grids:

- Finer in the radial direction: 226x1666, 450x1666, 898x1666
- Finer in the vertical direction: 226x1666, 226x2496, 226x3746
- Finer in both directions: 226x1666, 450x2498

for test cases D4,5 (corresponding to confined heads) and D2 (corresponding to dispersed heads). The definitions of those kinds of head are given in section 4.6.3. We recall that the investigation in this section is performed in a cavity with 134 mm diameter. The results are presented below.

Case D4,5-centerline profiles We present in Fig. 4.13a the mass fraction of glycerol Y_1 along the centerline for 3 grids 226x1666, 450x1666 and 898x1666. In this figure we see that for two grids 450x1666 and 898x1666 the amplitudes of the oscillations visible in the plume head are comparable and are smaller than those for 226x1666 grid.

The influence of the resolution in z-direction are presented for three grids: 226x1666, 226x2498 and 226x3746 in Fig. 4.13b. Again, the finer resolution gives smaller amplitudes of the oscillation in the plume head.

We have mentioned before that these are numerical oscillations due to the large mass fraction gradient at the interface which can not be resolved by the numerical scheme. The fact that numerical errors amplify the physical instabilities of the plume should be kept in mind. Therefore, finer grid in both directions are needed to decrease the amplitudes of the numerical oscillations.

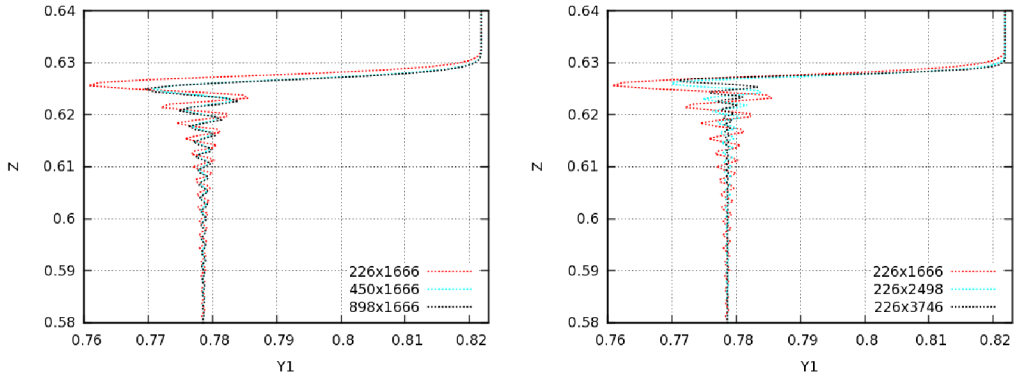

(a) (b)

Figure 4.13: Case D4,5: Mass fraction of glycerol Y_1 along the centerline at $t = 3.0$ with different grids.

Case D4,5-horizonal velocity The time evolution of the maximum horizontal velocity u for 6 resolutions presented in Fig. 4.14 shows that the grid refinement in either direction increases the maximum horizontal velocity. The refinement in the z-direction increases this maximum value stronger than the refinement in the x-direction.

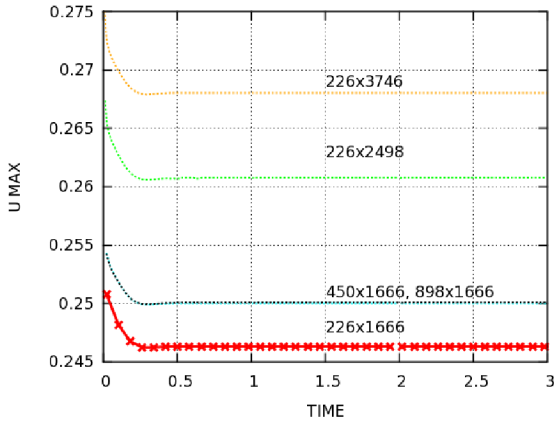

Figure 4.14: Case D4,5: Time evolution of the maximum horizontal velocity.

Grid	w_h	w_c	d_c
226x1666	0.225 ± 0.015	0.299	0.0119
450x1666	0.225 ± 0.015	0.299	0.0119
898x1666	0.225 ± 0.015	0.299	0.0119
226x2498	0.220 ± 0.020	0.299	0.0119
450x2498	0.220 ± 0.020	0.299	0.0119
226x3746	0.217 ± 0.017	0.299	0.0119

Table 4.5: Case D4,5: Comparison of steady properties for 6 grids.

Grid	h	d_h	l_h	RF_h
226x1666	0.6292	0.0536	0.0565	0.95
450x1666	0.6286	0.0542	0.0559	0.97
898x1666	0.6280	0.0539	0.0553	0.98

(a)

Grid	h	d_h	l_h	RF_h
226x1666	0.6292	0.0536	0.0565	0.95
226x2498	0.6286	0.0536	0.0545	0.98
226x3746	0.6287	0.0536	0.0545	0.98

(b)

Grid	h	d_h	l_h	RF_h
450x1666	0.6286	0.0542	0.0559	0.97
450x2498	0.6286	0.0536	0.0541	0.99

(c)

Table 4.6: Case D4,5: Comparison of transient properties at $t = 3.0$ for 6 grids.

Case D4,5-steady properties The steady properties of the plume for 6 grids are presented in Tables 4.5.

The centerline velocity of the conduit w_c and the conduit diameter d_c are identical for 6 grids. The ascent velocity is decreasing with increasing vertical resolution with the difference between the finest vertical resolution and coarsest one 3.7 %.

Case D4,5-transient properties The transient properties at $t = 3.0$ for 6 grids are compared in Table 4.6. We see that the refinement in either x-direction or z-direction has the effect of decreasing the head length l_h. The refinement in x-direction also has the effect of decreasing the plume height h. The effects of refinement in other properties are not seen clearly. The overall differences are within 0.2 % for the plume height h, 1.1 % for the head width d_h, 4.4 % for the head length l_h and 4.2 % for the head aspect ratio. The results could be considered as satisfactory for 450x2498 grid, where the difference with the finest resolution in both directions 898x1666 and 226x3746 is within 2 % for all the transient and steady properties. Largest head aspect ratio is also obtained with 450x2498.

Case D4,5-plume head The confined heads of case D4,5 for 6 grids are presented in Fig. 4.15, which shows more clearly the differences we have seen in Table

4.6. Comparing the plume heads at different resolutions shows that with higher resolutions the head is less diffusive than with lower resolutions, which is represented by smaller head lengths. The heads are almost identical between the resolutions 450x1666 and 898x1666, as well as between the resolutions 226x2498 and 226x3746.

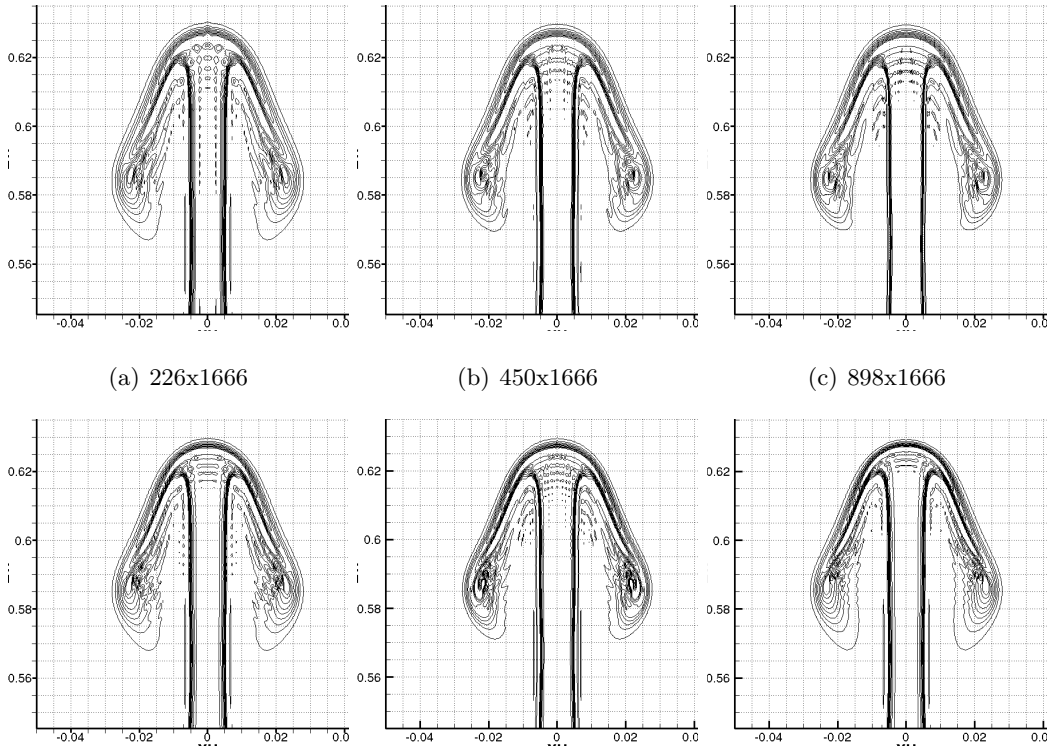

(a) 226x1666 (b) 450x1666 (c) 898x1666

(d) 226x2498 (e) 450x2498 (f) 226x3746

Figure 4.15: Case D4,5: Plume head represented by the glycerol mass fraction Y_1 at $t = 3.0$ with 6 grids. Contour levels [0.78:0.005:0.82]

The grid convergence study for case D2 is carried out similarly.

Case D2-steady properties The steady and properties of the plume for 6 grids are presented in Tables 4.7. They are almost identical for 6 grids.

The transient properties at $t = 3.0$ for 6 grids are presented in Table 4.8. We see that the refinement in either x-direction or z-direction has the effect of decreasing the head length l_h. The refinement in x-direction also has the effect of decreasing the plume height h. The effects of refinement in other properties are not seen clearly. The overall differences are within 0.3 % for the plume height, 1.7 % for the head diameter, 7.4 % for the head length, 6.6 % for the head aspect ratio. The results could be considered as satisfactory for 450x2498 grid, where the difference with the finest resolution in both directions 898x1666 and 226x3746 is within 6 %

Grid	w_h	w_c	d_c
226x1666	0.300 ± 0.031	0.460	0.0095
450x1666	0.300 ± 0.031	0.460	0.0095
898x1666	0.300 ± 0.031	0.460	0.0095
226x2498	0.301 ± 0.021	0.460	0.0095
450x2498	0.301 ± 0.021	0.460	0.0095
226x3746	0.300 ± 0.034	0.460	0.0095

Table 4.7: Case D2: Comparison of steady properties for 6 grids.

Grid	h	d_h	l_h	RF_h
226x1666	0.8612	0.0643	0.1046	0.61
450x1666	0.8582	0.0637	0.1004	0.63
898x1666	0.8582	0.0637	0.0998	0.64

(a)

Grid	h	d_h	l_h	RF_h
226x1666	0.8612	0.0643	0.1046	0.61
226x2498	0.8590	0.0643	0.1022	0.63
226x3746	0.8590	0.0643	0.1018	0.63

(b)

Grid	h	d_h	l_h	RF_h
450x1666	0.8582	0.0637	0.1004	0.63
450x2498	0.8594	0.0632	0.0974	0.65

c)

Table 4.8: Case D2: Comparison of transient properties at $t = 3.0$ for 6 grids.

for all the transient and steady properties. Largest aspect ratio is also obtained with 450x2498 grid.

Case D2-plume head The dispersed heads of case D2 for 6 grids are presented in Figures 4.16. Comparing the plume head at different resolutions shows that with higher resolutions the head is less diffusive, which is represented by smaller head length. The heads are almost identical between the resolutions 450x1666 and 898x1666, as well as between the resolutions 226x2498 and 226x3746.

In summary, we have analyzed the grid convergence in both directions for case D4 (confined head) and case D2 (dispersed heads). The results obtained with finer grids are less diffusive and have smaller amplitudes of the oscillations in the mass fraction field. The steady properties display very minor differences between the grids analyzed. The transient properties show larger differences between the grids analyzed, espeically in the case of dispersed heads. We conclude that from the resolution of 450x2498 the results can be considered convergent and further refinement does not change the results significantly.

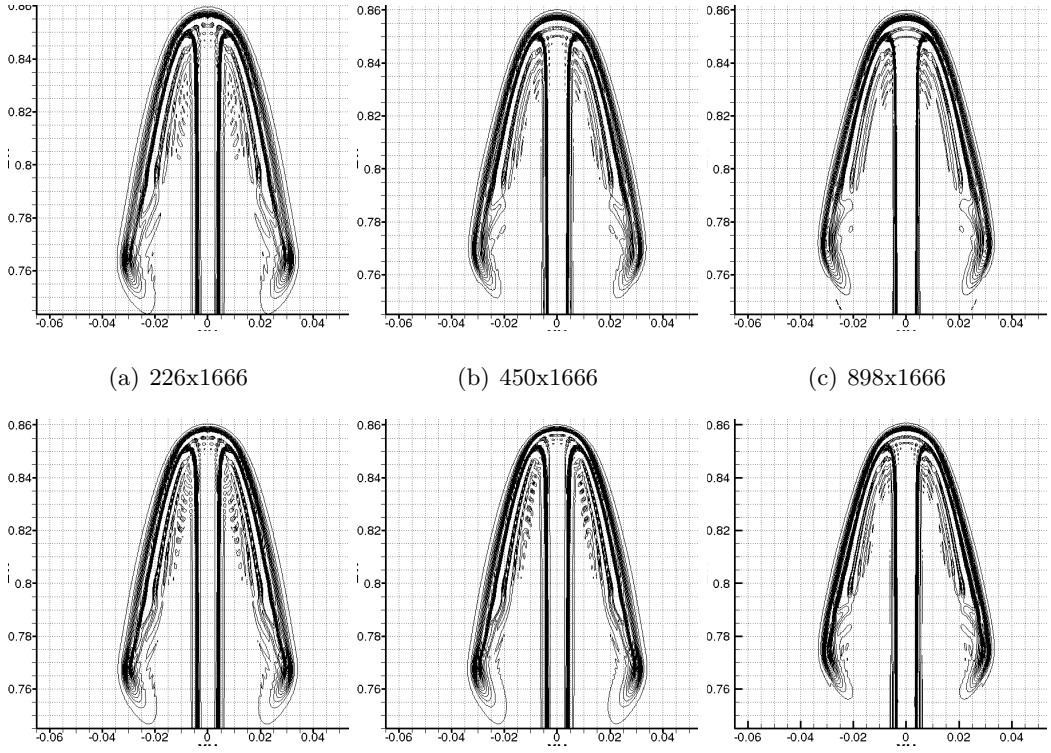

(a) 226x1666 (b) 450x1666 (c) 898x1666

(d) 226x2498 (e) 226x3746 (f) 450x2498

Figure 4.16: Case D2: Plume head represented by the glycerol mass fraction Y_1 at $t = 3.0$ with 6 grids. Contour levels [0.669:0.001:0.685]

4.6 Comparison with the experiment of [Rogers and Morris, 2009]

Now we will proceed to compare the numerical results with the experimental data of [Rogers and Morris, 2009]. All the numerical results in this section are simulated in a cavity of 502 mm height and 151 mm diameter with 514x2498 regular grid, $\Delta t = 0.0001$. CENTER scheme is used for the convective terms in momentum equation and QUICK scheme for the convective term in the equation for Y_1. The inlet velocity profile is parabolic.

The comparison with the experimental data is carried out in three aspects. The general plume shape is compared in section 4.6.1. The ascent velocity is compared in section 4.6.2 and finally the plume head is compared in section 4.6.3.

4.6.1 General plume shape

First of all, the plume shape in case D5,1 is compared with Fig. 1 of [Rogers and Morris, 2009] in Fig. 4.17. The shape of the conduit agree well with the

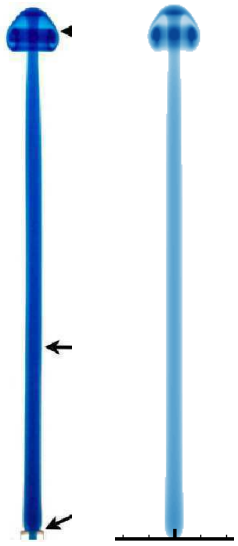

(a) (b)

Figure 4.17: a) The plume shape in case D5,1 in Fig. 1 of [Rogers and Morris, 2009], b) The numerical result at $t = 58.7s$: $h = 19.23cm$, $d_h = 1.97cm$, $l_h = 1.72cm$ and $d_c = 0.66cm$.

experimental result. It is largest near the injection, then it shrinks a little and becomes constant along the plume height until it shrinks a little more when the

head is approached. The head shape is also very similar with a vortex ring inside the head. Quantitatively, the plume height, head diameter, head length and conduit diameter of the numerical solution are $h = 19.2cm$, $d_h = 2.0cm$, $l_h = 1.7cm$ and $d_c = 0.7cm$, respectively. Compared with $h = 19.3cm$, $d_h = 1.9cm$, $l_h = 1.6cm$ and $d_c = 0.6cm$ of the experimental data, the difference is very minor. Since the error bars of experimental data were not given, it is not possible to have a more accurate comparison with our results.

4.6.2 Ascent velocity

The ascent velocity is calculated as in section 4.4. The numerical results show that the ascent velocity w_h is constant in time for each plume in total of 13 plumes that we simulated. This is consistent with the experimental findings of [Rogers and Morris, 2009]. Now we compare quantitatively our results with experimental data of [Rogers and Morris, 2009].

Comparison with Fig. 2 in [Rogers and Morris, 2009] In Fig. 2 of [Rogers and Morris, 2009] the time evolution of the plume height for five plumes in case D4 is presented. The experimental data in this figure are reconstructed and are plotted in Fig. 4.18 using lines with points. The corresponding numerical results are plotted using the same colors with the experimental data using plain solid lines. We can see that each curve, both experimental and numerical results, consists of

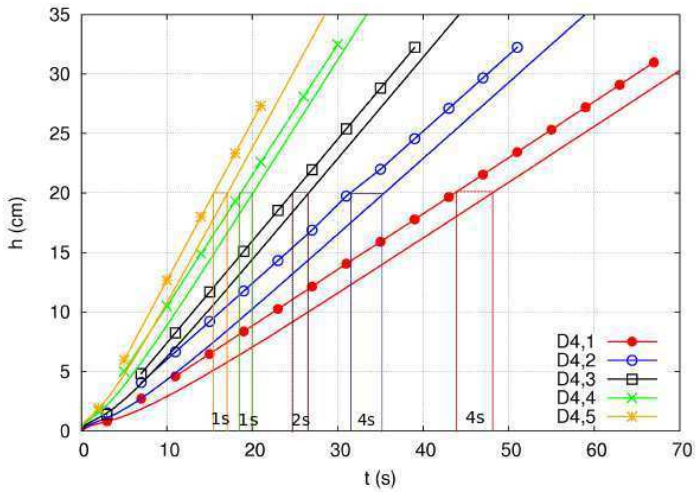

Figure 4.18: Time evolution of the plume height for five plumes in case D4. Lines with points are for the experimental data ([Rogers and Morris, 2009]) and plain solid lines with the same colors are for the corresponding numerical results. The slope of a plain solid line is the constant ascent velocity w_h of each plume.

a transient period where the ascent velocity w_h is increasing following by a linear period where the ascent velocity w_h is constant. In the linear period, the numerical

Case	Re_i	Time shift
D4,1	0.370	4.0 s
D4,2	0.751	3.5 s
D4,3	1.491	2 s
D4,4	2.992	1.4 s
D4,5	4.483	1.4 s

Table 4.9: Case D4 of glycerol-water plumes: Time shift between experimental data and numerical results.

results are almost parallel to the corresponding experimental data. However, there is a time shift between experimental data and numerical results and the value of the time shift is decreasing with increasing injection flow rates, as indicated in Table 4.9

A possible explanation for this time shift is as follows. In the experiment of [Rogers and Morris, 2009] glycerol-water is injected through a capillary tube below the tank base (Fig. 4.19a) while in the numerical simulation the fluid is injected right at the tank base. Therefore, the time at which the injected fluid from the tube arrives at the tank base in the experiment is different from that in the numerical simulation by a time shift. This time shift depends on the velocity of the injected fluid and is smaller if the injection velocity is large, which is consistent with Table 4.9. If we shift the numerical results according to this table they superimpose the corresponding experimental data, as in Fig. 4.19b. This implies that the ascent velocities of the numerical results are very close to those of experimental data.

The ascent velocities for both results are measured and compared in Table 4.10. The numerical result is denoted by w_h and the experimental data by w_h^e. Once again, we see that their values are very close with the largest discrepancy being 3 % for the largest flow rate.

Comparison with the empirical formula (4.3) To have a single correlation describing the ascent velocities of all the plumes, [Rogers and Morris, 2009] examined that relation between the head Richardson number Ri_h and the injection Reynolds number Re_i. These numbers are defined as

$$Ri_h = \frac{g(\rho_a - \rho_i)d_i}{\rho_a w_h^2} \tag{4.6}$$

$$Re_i = \frac{d_i \overline{w_i}}{\nu_i} \tag{4.7}$$

We recall here that $\overline{w_i}$ is the average velocity at the injection, calculated by dividing the volume flow rate Q by the surface of injection $\pi\frac{d_i^2}{4}$. The best fitting of all experimental data gave the relation

$$Ri_h = (4.3 \pm 0.2) Re_i^{-0.96\pm0.05} \tag{4.8}$$

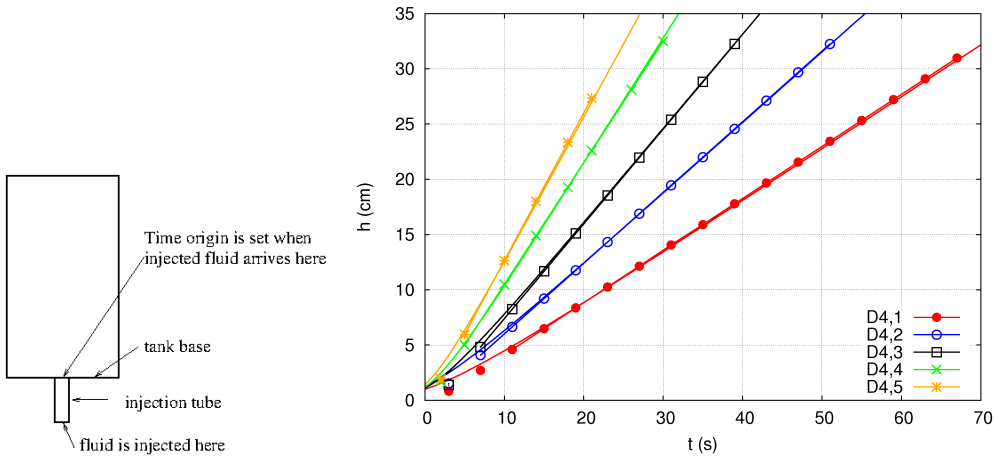

(a) (b)

Figure 4.19: a) Experimental apparatus, b) Figure 4.18 after shifting numerical results according to Table 4.9.

which is plotted as a solid line in Fig. 3 of [Rogers and Morris, 2009]. By re-examining Fig. 3 of [Rogers and Morris, 2009], we discovered that the data points corresponding to cases D4,1 to D4,5 actually represent the relation between Ri_h and Re_i^*, where

$$Re_i^* = \frac{d_i \overline{w_i}}{\nu_a} \tag{4.9}$$

However, the data points corresponding to cases D2, D5,1, D1,2 to D1,4 represent the relation between Ri_h and Re_i. Replacing Re_i by Re_i^* causes big differences only in case D4 where ν_i is quite different from ν_a. In other cases, the ratio $\frac{\nu_i}{\nu_a}$ is nearly 1. Last but not least, the data points corresponding to case D5,2, D1,1 and D1,5 can not be found in Fig. 3 of [Rogers and Morris, 2009], although all cases have been plotted in this figure. Therefore we only keep equation 4.3 as a reference and find again the correlation for the ascent velocity based on our numerical data.

We examine numerical data using both relation between Ri_h and Re_i and that between Ri_h and Re_i^*.

The plot of the dependence of Ri_h on Re_i for all the numerical results is presented in Fig. 4.20a. We can see that the symbols do not align and, even those for case D4 for which we obtained very accurate results compared with the experimental data, are not superimposed by the dashed line whose equation is $Ri_h = 4.3 Re_i^{-0.96}$.

Now, if Re_i is now replaced by Re_i^* the symbols are more aligned. The black dashed line whose equation is

$$Ri_h = 3.74 Re_i^{*-0.78} \tag{4.10}$$

gives a better fit for the dependence of Ri_h on Re_i^* as in Fig. 4.20b.

Case	Re_i	w_h (cm/s)	w_h^e (cm/s)	w_h/w_h^e
D4,1	0.370	0.47	0.47	1.00
D4,2	0.751	0.64	0.64	1.0
D4,3	1.491	0.85	0.86	0.99
D4,4	2.992	1.10	1.10	1.00
D4,5	4.483	1.30	1.34	0.97

Table 4.10: Case D4 of glycerol-water plumes: Comparison of the ascent velocities obtained from numerical simulations (w_h) and data extraction from Fig. 2 in [Rogers and Morris, 2009] (w_h^e).

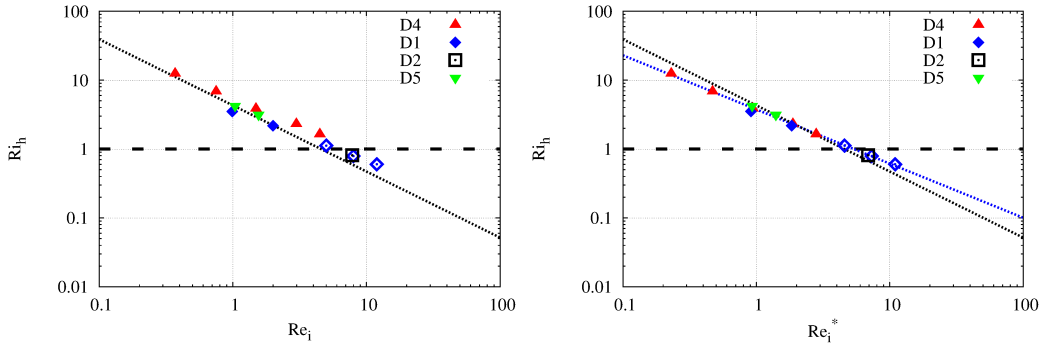

(a) (b)

Figure 4.20: The dependence of the head Richardson number Ri_h on the injection Reynolds number for the numerical results of 13 plumes. The black dotted lines are $Ri_h = 4.3Re_i^{-0.96}$ (a) and $Ri_h = 4.3Re_i^{*-0.96}$ (b). The blue dotted line is $Ri_h = 3.74Re_i^{*-0.78}$.

Side wall effects Now we generalize formula $Ri_h = 3.7Re_i^{*-0.78}$ for plumes in free environment. Supposing that we can keep the prefactor and only change the exponent from -0.78 to -1, the correlation to describe the ascent of plumes in free environment is

$$Ri_h = 3.74Re_i^{*-1} \tag{4.11}$$

This change will give larger ascent velocity, since in free environment the plume is not affected by the side wall effect as in a confined box. It implies that the ascent velocity is calculated by

$$w_h = 0.583 \left(\frac{g(\rho_a - \rho_i)Q}{\rho_a \nu_a} \right)^{1/2} \tag{4.12}$$

Now we examine numerically formula (4.12). We do the simulations of case D4,5 in cavities which have the same height $502mm$ and four diameters 151 mm,

Cavity diameter	v_h (cm/s)	$\frac{v_h}{v_h^f}$	$\frac{v_h}{v_h^r}$
151 mm	1.313	0.91	0.78
201 mm	1.358	0.94	0.81
268 mm	1.404	0.97	0.83
402 mm	1.443	1.00	0.85

Table 4.11: Case D4,5: Comparison of ascent velocity v_h with values predicted by formula (4.12)(v_h^f) and (**??**) (v_h^r) for cavities with a height of 502 mm and different diameters.

201 mm, 268 mm and 402 mm. In Fig. 4.21-a we compare the profiles of the vertical velocity w along the centerline at $t = 4.0$ for different cavity diameters. After entering the cavities, w is decreasing to the same minimum value for four cavities. Then it is increasing again and from here it is consistently higher both in the conduit and in the plume head for larger cavities. The difference between the two largest cavities is very little which means that the wall effect becomes less significant for cavity diameter from 402 mm. The ascent velocity w_h is plotted as a function of the cavity diameter in Fig. 4.21-b. We see that w_h converges to

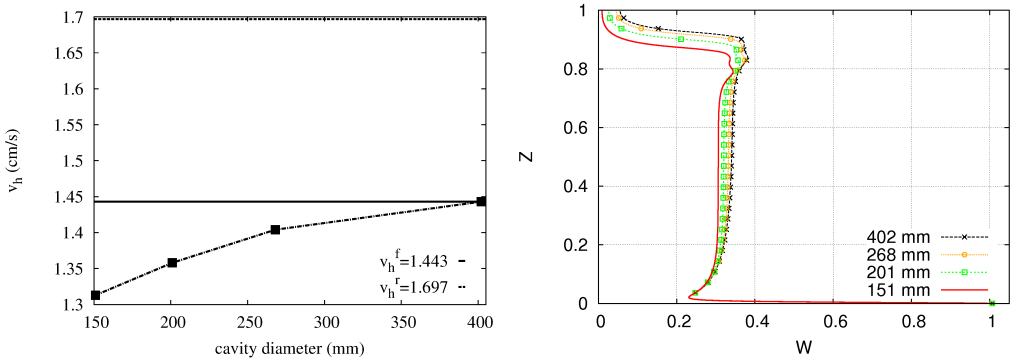

(a) (b)

Figure 4.21: a) Vertical velocity along the centerline in case D4,5 at $t = 4.0$ with different cavity diameters, b) Ascent velocity of case D4,5 as a function of cavity diameter. v_h^f is the value calculated from (4.12). v_h^r is the value calculated from (4.3).

the value calculated by formula (4.12), w_h^f. The comparison between w_h and w_h^f is made in Table 4.11. We see also in this table that for the largest cavity, the difference from v_h and v_h^r, the value calculated by equation (4.3), is 15 %. It seems that formula (4.12) is more suitable to describe the ascent velocity of plumes in free environment.

Now the morphology of the plume heads are compared with the experiment.

4.6.3 Morphology of the plume heads

In this section we first compare the shape of the plume heads with Fig. 2, Fig. 4 and Fig. 8 in [Rogers and Morris, 2009]. Then the criterion to distinguish confined heads and dispersed is discussed.

Comparison with Fig. 2 and Fig. 4 in [Rogers and Morris, 2009] We present in Figures 4.22, 4.23, 4.25 and 4.24 the plume heads of 12 cases simulated.

In the first line of Fig. 4.22 is the experimental result for case D5,2. Two stable vortex rings are clearly visible inside the head during its evolution and this property is typical for confined heads. The computed heads are are presented below the experimental heads of Fig. 2 in [Rogers and Morris, 2009] for comparison. They are taken at the same plume height h as the experimental heads. We see that the computed results capture very well not only the overall shape of the head but also the two vortex rings developing inside the head. The sizes ($l_h \times d_h$) of the first and the last heads in the experiment are 1.9 cm x 2.3 cm and 2.4 cm x 3.1 cm, respectively, while the corresponding numerical results are 2.0 cm x 2.3 cm and 2.6 cm x 2.8 cm. It means that the head width is 10% smaller than the experimental data for the last head and the head length is 5 % larger than the experimental data for the first head and 8 % for the last head.

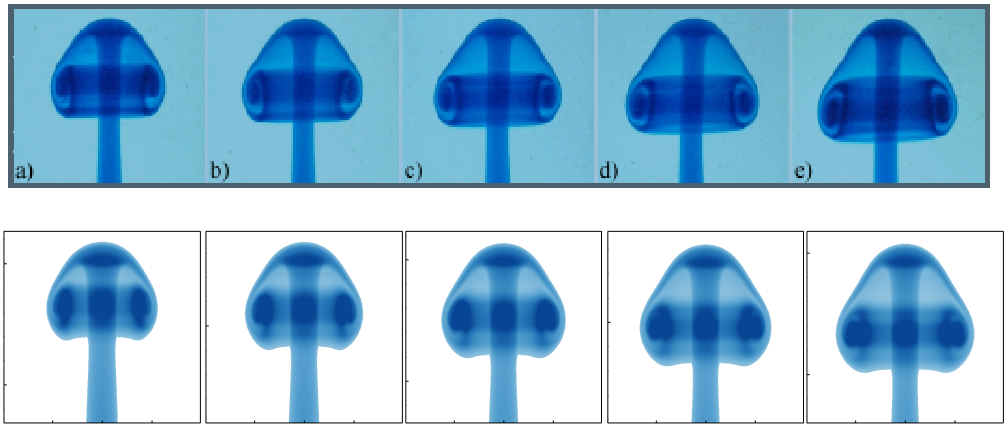

Figure 4.22: Confined heads in case D5,2. From the first to last image in the sequence, h increases from 20.5 cm to 35.2 cm. Top: experimental results: each image is 5 s apart. From the first to last image, the size of the head increases from 1.9cmx 2.3cm ($l_h \times d_h$) to 2.4cmx 3.1cm. Bottom: numerical simulation: each image is 8.3 s apart. From the first to last image, the size of the head increases from 2.0cmx 2.3cm to 2.6cmx 2.8cm.

In contrast to the confined heads where the fluid comprising it remains within a compact structure and the fluid in the head circulates around an axisymmetric vortex ring that remains localized near the top of the plume, dispersed heads do not remain compact and do not contain a stable vortex ring structure. The time evolution of a typical dispersed head is presented in Fig. 4.23 for case D2. The experimental data of Fig. 4 in [Rogers and Morris, 2009] are presented in the two

first lines followed by the numerical results for comparison. They are taken at the same plume height h. The computed results capture well the overall shape of the head except the instability developing at the edge of the head. This may due to the axisymmetric hypothesis that we made in solving the equations because dispersed heads are accompanied by small asymmetry visible in the experimental results. The hammer-shape structure, which is typical for dispersed heads, is also observed in the first two images of Fig. 4.23. The sizes of the first head in the experiment is 1.6 cm x 2.1 cm, while it is 1.6 cm x 1.9 cm in the numerical simulation. It means that at the beginning the head width is 10 % smaller than the experimental data.

Comparison of the criterion for confined heads and dispersed heads Now we discuss the criterion to distinguish confined heads and dispersed heads. The heads for case D4 are presented in Fig. 4.24. Both the sizes of the head and of the conduit are increasing with the injection flow rate. Although the stable vortex ring in the head is not as clearly seen as in case D5, all the heads in this case can be considered as confined heads.

The heads for case D1 are presented in Fig. 4.25. From case D1,3 it is clear that the heads are dispersed heads since the instability at the interface of the head is invisible. For the first two cases D1,1 and D1,2, the heads are more like confined heads although we observe that the hammer-shape structure, which is the onset of a dispersed head as recommended by [Rogers and Morris, 2009], is present in both cases.

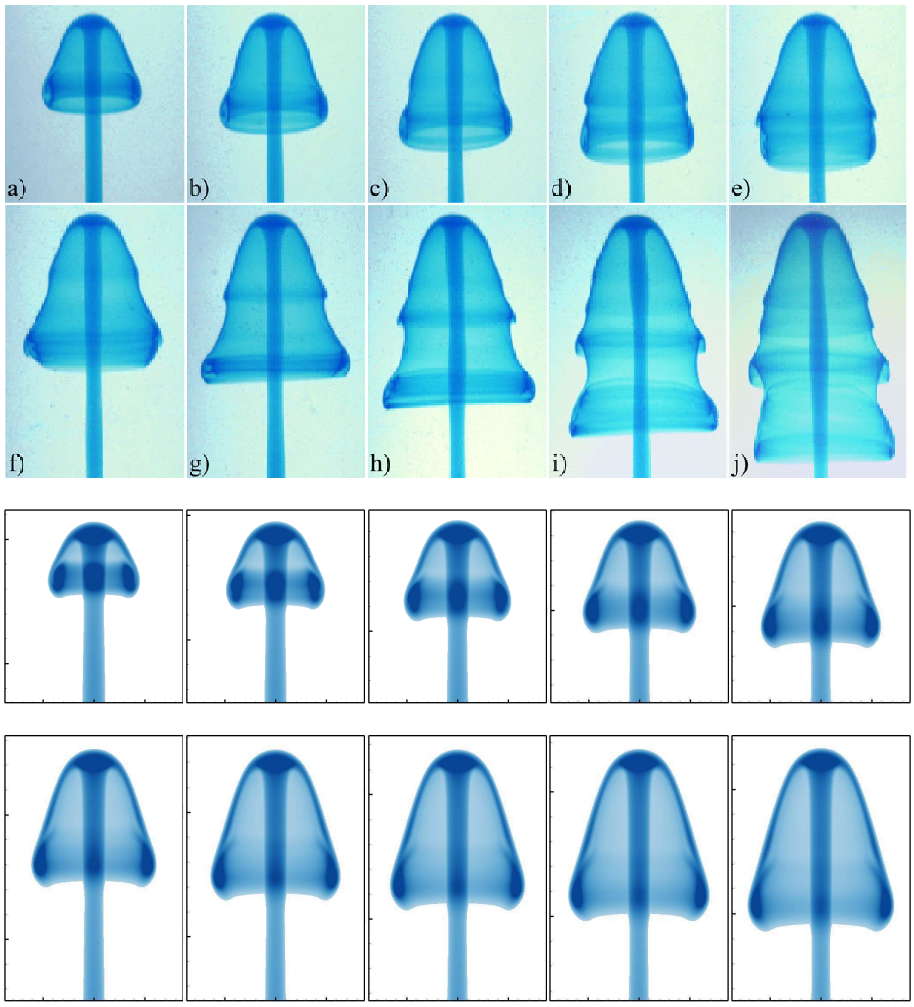

Figure 4.23: Dispersed heads in case D2. From the first to last image in the sequence, h increases from 10.4 cm to 31.0 cm. Top: experimental results: each image is 2 s apart. The size of the first image is l_h=1.6 cm and d_h=2.1 cm. Bottom: each image is 2 s apart. The size of the first image is l_h=1.6 cm and d_h=1.9 cm.

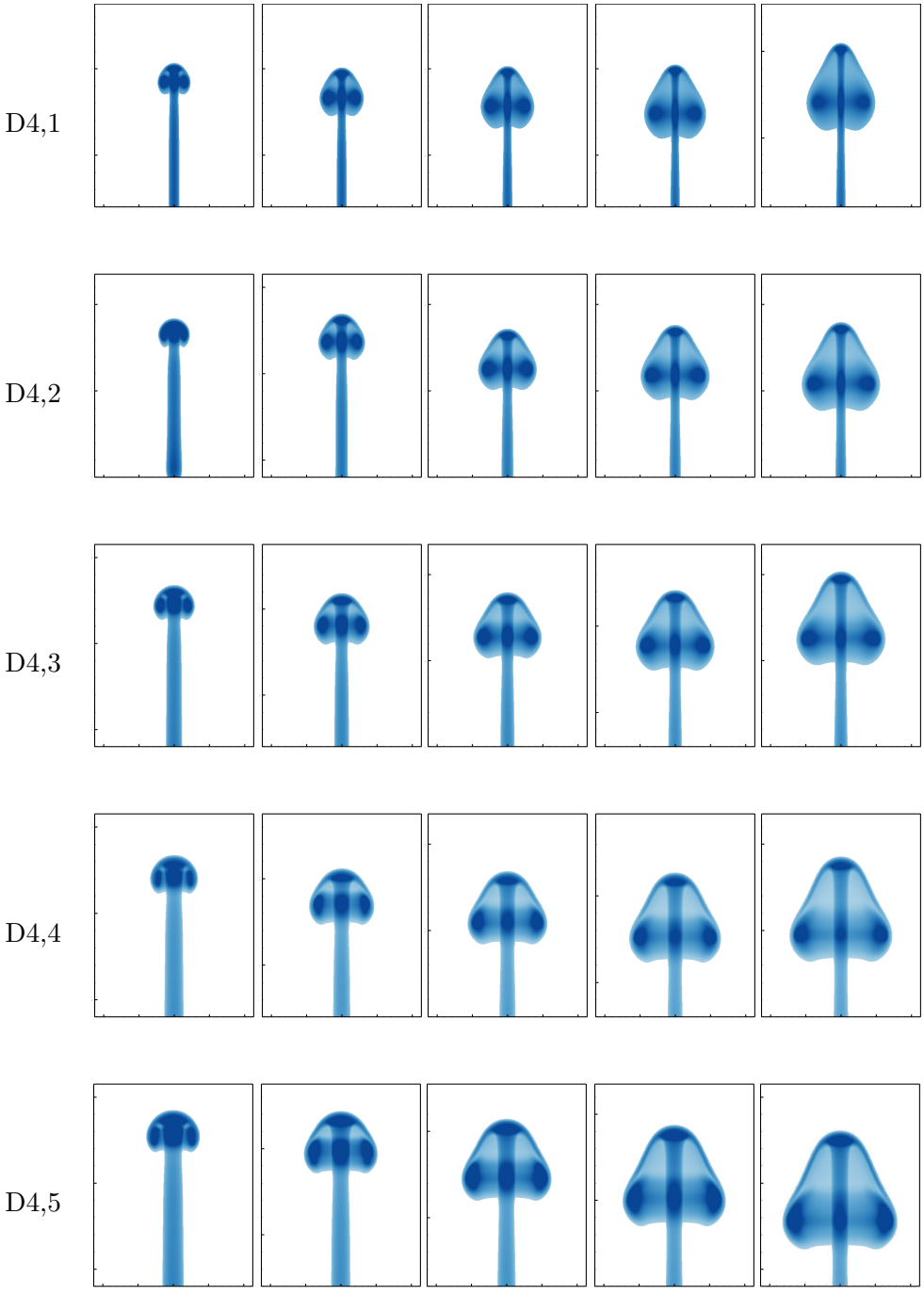

Figure 4.24: Time evolution of plume heads in case D4.

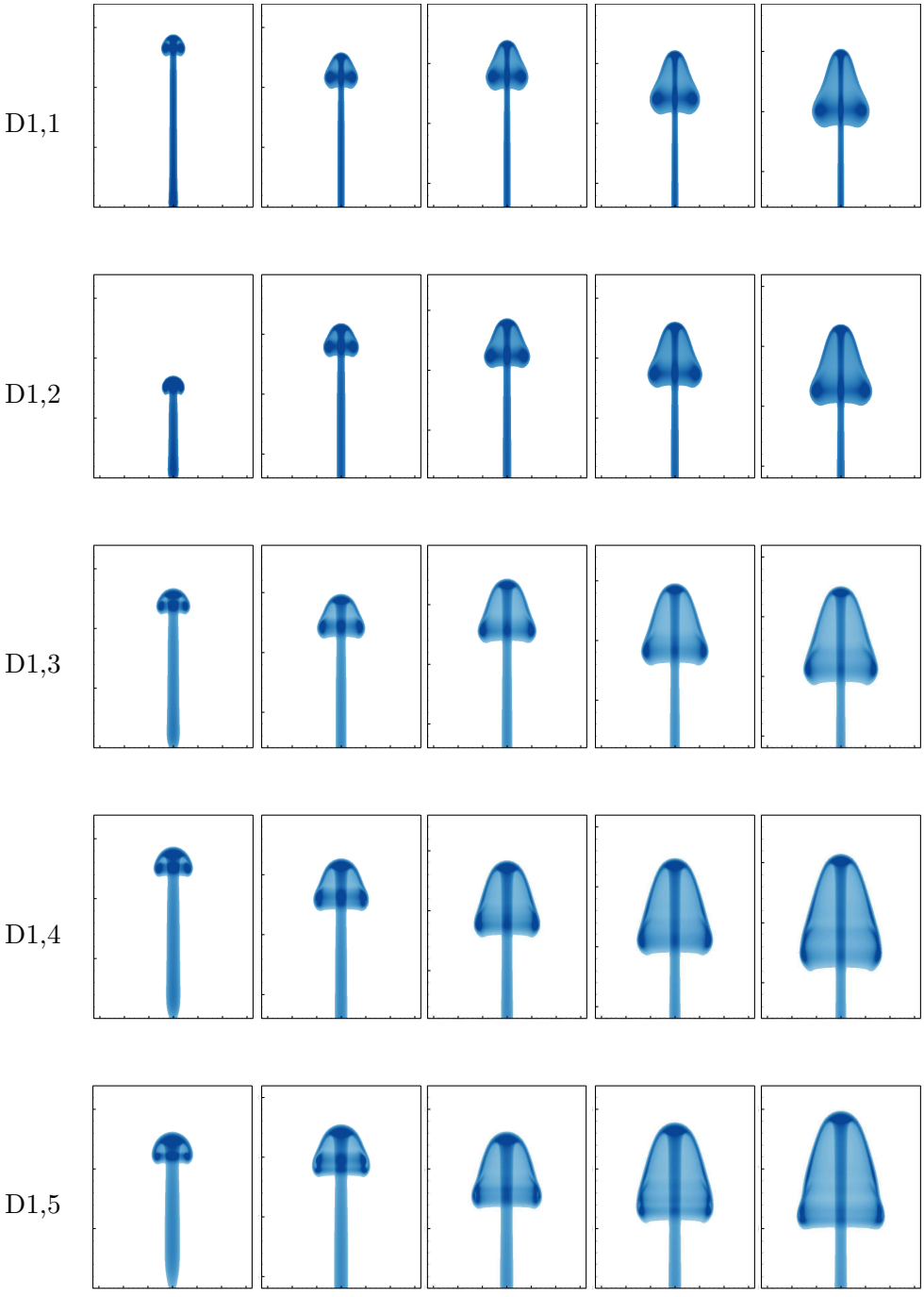

Figure 4.25: Time evolution of plume heads in case D1.

Case	Type of head	Ri_h
D1,1	confined	3.512
D1,2	confined	2.181
D1,3	dispersed	1.116
D1,4	dispersed	0.786
D1,5	dispersed	0.597
D5,1	confined	4.235
D5,2	confined	3.149

Case	Type of head	Ri_h
D4,1	confined	12.44
D4,2	confined	6.854
D4,3	confined	3.846
D4,4	confined	2.312
D4,5	confined	1.635
D2	dispersed	0.809

Table 4.12: Summary of the types of heads obtained with numerical simulations for 13 glycerol-water starting plumes.

The summary of the types of head in the numerical simulations of 13 plumes studied are presented in Table 4.12 together with the head Richardson numbers calculated by (4.6). It is clear that when $Ri_h < 1$ the heads are dispersed. When $Ri_h > 1$, however, we have dispersed heads in case D1,3. Except in case D2,2 in which the experimental data give dispersed heads but we consider our results as confined heads, the plume head type for the remaining cases agree well with the experimental data.

Head aspect ratio The head aspect ratio was suggested by [Rogers and Morris, 2009] as a criterion to distinguish confined heads and dispersed heads. Now we analyze the aspect ratio of the head in our numerical results.

In Fig. 4.26a we make a plot of the head width as a function of the head length for case D4, in which the head width d_h and head length l_h are nondimensionalized respectively by

$$Re_{hw} = \frac{d_h w_h}{\nu_i} \quad \text{and} \quad Re_{hl} = \frac{l_h w_h}{\nu_i} \tag{4.13}$$

This figure is in very good agreement with Fig. 5 in [Rogers and Morris, 2009] presented in Fig. 4.26b) and we can see that $Re_{hw} = 1.24 Re_{hl}$ is a good approximate description of the numerical data. However, we note that the numerical data plotted in this figure are at early stages in the development of the plume. The evolution of the head aspect ratio RF_h with the plume height h during the entire evolution of a plume is plotted in Fig. 4.27. In this figure we see that in each case, the maximum aspect ratio RF_h is increasing with the flow rate. The maximum value of the aspect ratio for the highest flow rate, case D4,5, is 1.25, approximately the constant value 1.24 found for confined heads by [Rogers and Morris, 2009]. During the plume's evolution, RF_h is decreasing and the rate of decreasing is greater for greater flow rates Q.

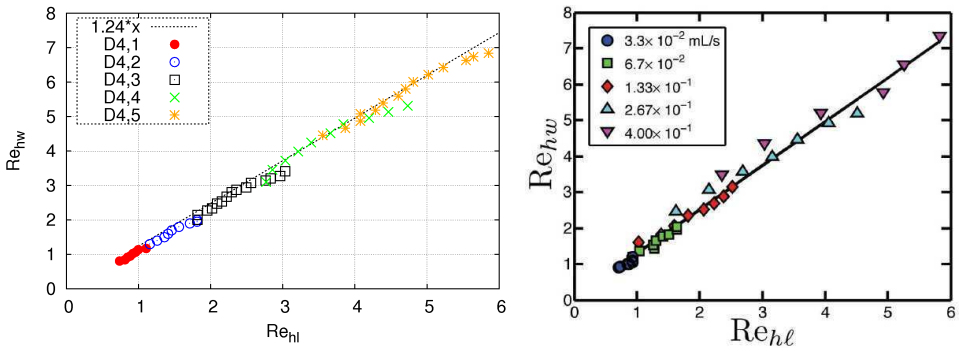

(a) (b)

Figure 4.26: Head width as a function of head length for D4 set of plumes : a) Numerical results, b) Fig. 5 of [Rogers and Morris, 2009].

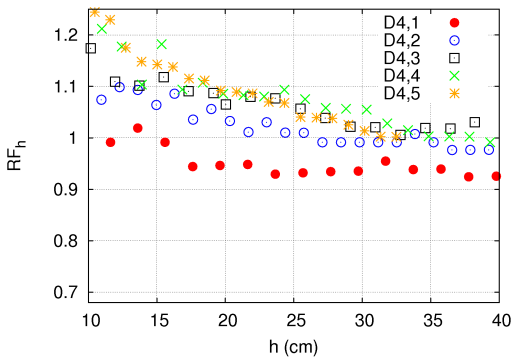

(a)

Figure 4.27: D4 set of plumes: Evolution of the head aspect ratio with the plume height.

A plot of the head width as a function of the head length for case D1 is presented in Fig. 4.28a. Compared with Fig. 7 in [Rogers and Morris, 2009] presented in Fig. 4.28b) the agreement is not very good for three largest flow rates. At the same value of Re_{hw} we have smaller value of Re_{hl} compared with the experimental data. This may be because the axisymmetric hypothesis that we use has reduced the development of instability in the head and hence shortened the head length.

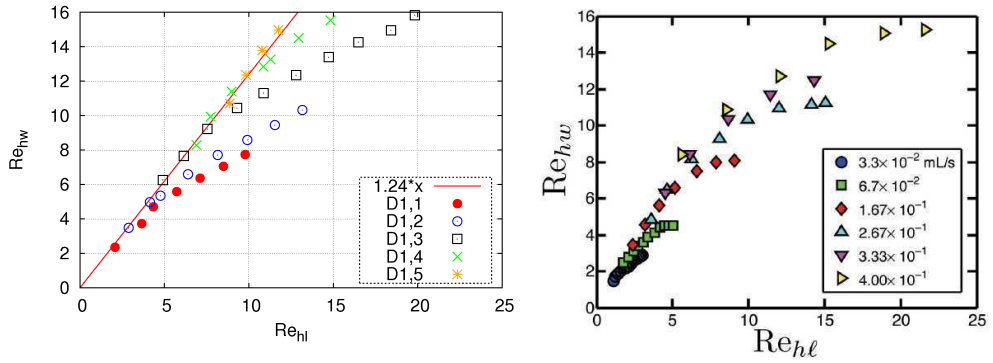

(a) (b)

Figure 4.28: Head width as a function of head length for D1 set of plumes: a) Numerical results, b) Fig. 7 of [Rogers and Morris, 2009]

The evolution of the head aspect ratio with the plume height during the entire evolution of a plume is plotted in Fig. 4.29. Again, RF_h is decreasing and the rate of decreasing is greater for greater flow rates Q. Also, the rate of decreasing is greater for dispersed heads than for confined heads.

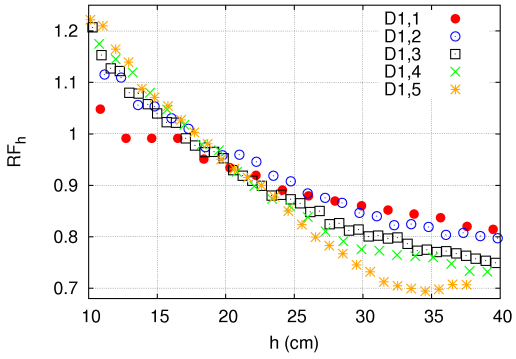

(a)

Figure 4.29: D1 set of plumes: Evolution of the head aspect ratio with the plume height

The evolution of RF_h for case D2 and D5 is presented in Fig. 4.30. For dispersed

heads in case D2, RF_h decreases from 1.2 to 0.7. For confined heads in case D5,1 and D5,2, RF_h only decreases from 1.2 to 1. These behaviors are similar to those observed in Fig. 4.26b and Fig. 4.28b.

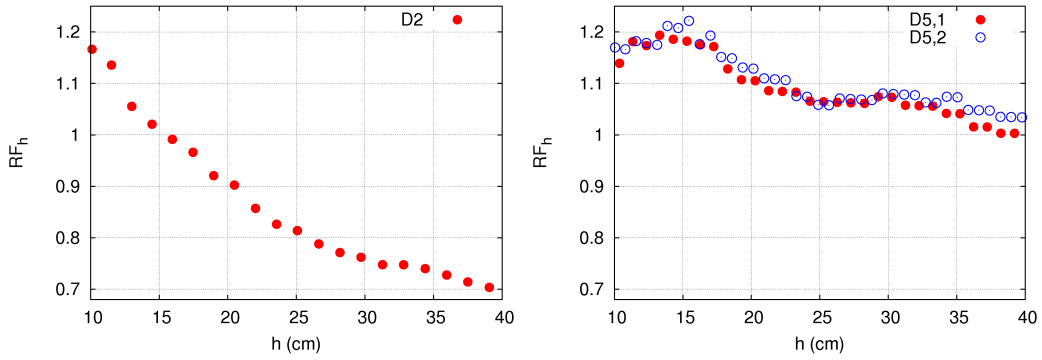

(a) (b)

Figure 4.30: Evolution of the head aspect ratio with the plume height for a) Case D2, b) Case D5

We wonder if the increase of the cavity diameter has influences on the head aspect ratio. In Fig. 4.31 the evolution of the head aspect ratio RF_h with the plume height h with four cavity diameters: 151 mm, 201 mm, 268 mm and 402 mm is presented. We can see that RF_h is slightly larger for larger cavity but the difference is not significant. The decreasing trend is the same for four diameters. It is concluded that the increase of the cavity diameter does not affect the head ratio.

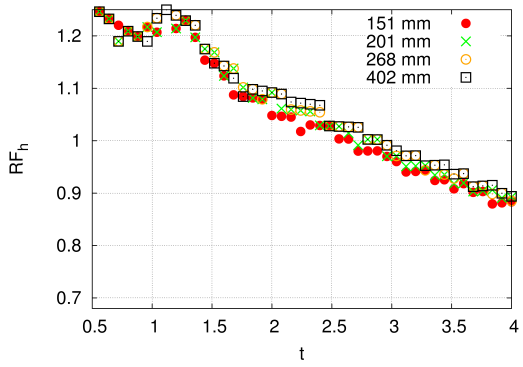

Figure 4.31: Resutls for case D4, $Q = 4.0 \times 10^{-7} m^3/s$: Evolution of the head aspect ratio RF_h with the plume height with different cavity diameters.

4.7 Conclusions

We have simulated 13 forced plumes in total of 34 forced plumes in the experiment of [Rogers and Morris, 2009]. The results have been proven to be independent of the mesh size. Different parameters that can have influences on the development of the plumes have been analyzed and the configuration chosen for all the final results is a cylindrical cavity with a diameter of 151 mm, which gives the same volume as the rectangular cavity used in the experiment of [Rogers and Morris, 2009]. A spatial resolution of 514x2498 is used. Parabolic velocity profile is imposed at the inlet. Centered scheme is used the convection term in the momentum equation and QUICK scheme in the mass fraction equation.

The numerical results are compared against the experimental data for the ascent velocity of the head and good agreement has been achieved.

- Numerical simulations give constant ascent velocities for 13 forced plumes studied, which is consistent with experimental measurements of [Rogers and Morris, 2009].
- Compared with the figures from [Rogers and Morris, 2009] we have very accurate ascent velocity in one case where the data on the time evolution of the plume height is provided. The numerical results for the plume height are consistently lower than the experimental results by approximately 2 cm in this case and this can be explained by the possibly different time origins between the experiment and numerical simulation.
- In the other two cases where only snapshots with the plume height and the time interval are provided, we get very good agreement in one case and poor agreement in the other. The poor agreement remains unexplained.
- The formula for calculating the ascent velocity proposed by [Rogers and Morris, 2009] is shown to have poor agreement with the numerical results and is not consistent with past formulae proposed by [Moses et al., 1993] and [Kaminski and Jaupart, 2003] for thermal starting plumes. A modified formula is proposed which gives better agreement with the experimental data.
- The discrepancies between the ascent velocity calculated by the new formula and the numerical results are small when the flow rate is small and is increasing with increasing flow rate.
- The modified formula results from scaling argument for plumes in unbounded environment and these discrepancies can be explained partly by the wall effect on the plume. The wall effect is larger on plumes with larger injection flow rate and hence the discrepancy with the formula is larger. We have showed in one case that the simulation in a larger cavity has increased the ascent velocity and its difference with the formula has decreased from 17 % to 6 %.

The plume heads are well reproduced numerically for 13 plumes studied.

- The types of the heads are consistent with the experimental data, except in one case (D2,2) the numerical results give confined heads while experimental data give dispersed heads.

- The types of the head can be distinguished based on the head Richardson number Ri_h proposed by [Rogers and Morris, 2009]. When Ri_h is less than 1 dispersed heads are obtained. When Ri_h is greater than 1 in one case we have dispersed heads, while in the other cases the heads are confined.

- Concerning the size of the head there are some discrepancies between the experimental data and the numerical results. [Rogers and Morris, 2009] proposed that for confined heads the aspect ratio is always a constant in time and is equal to 1.24. In the numerical results, the head aspect ratio is not a constant for every confined head and not a constant in time. The maximum aspect ratio obtained in the numerical results is 1.25 in case D4,5 which is close to 1.24. However, it is smaller than 1.24 in other cases and is decreasing in time and the decreasing rate is greater for higher flow rates.

- For dispersed heads we obtain smaller head length than in the experiment. This may caused by the axisymmetric assumption that we have made since it is visible from the experimental data that some asymmetry develops in dispersed heads. The failure to simulate this asymmetry may prevent the head length to develop.

- The rate of decreasing of the head aspect ratio is larger for dispersed heads than for confined heads.

- The wall effect has shown to have very little effect on the head ratio.

Chapter 5

Buoyant jets of helium-air mixture or helium in a partially confined air-filled cavity

5.1 Introduction

When a light fluid is injected in an enclosure filled by a heavy fluid, a starting plume is created. Before this starting plume interacts with the walls of the enclosure, it behaves like a starting plume in an unconfined environment. Plumes in unconfined environments have been extensively studied while studies about plumes in confined spaces are still limited. The interaction of a plume with an enclosure is very complex and is difficult to predict.

A problem of interest in a nominally unventilated enclosure is how to predict the distribution of the lighter fluid inside the enclosure. Theoretical models such as those of [Baines and Turner, 1969] and [Worster and Huppert, 1983] predict the short term and long term distribution of the injected fluid when overturning does not happen and a vertical density stratification is produced. When overturning happens, [Cleaver et al., 1994] developed a model to predict the depth of the homogeneous layer. In all these models, the entrainment coefficient is assumed constant. When compared with the experimental data (GAMELAN) of [Cariteau and Tkatschenko, 2012] on the dispersion of helium in air in a nearly cubic cavity at low flow rates, those models give good agreement for an injection diameter of 20 mm. However, they failed to predict the distribution of helium inside the cavity with an injection diameter of 5 mm. A linear structure of vertical density stratification is found in the experiment, while the model of [Worster and Huppert, 1983] gave a parabolic structure.

The failure of the model to predict the experimental data, even in the simple geometry of the experiment of [Cariteau and Tkatschenko, 2012] may be due to the hypothesis of constant entrainment coefficient. To have a good model of entrainment coefficient we must have access to the velocity fluctuations in the plumes. However, in the mean time it is very difficult to measure those quantities and often only concentrations are measured. Therefore, we must seek the help from computational fluid dynamics (CFD).

The results from CFD must prove to be reliable before they can be used for further study. In the benchmark [Bernard-Michel et al., 2012] on helium dispersion based on the experiment of [Cariteau and Tkatschenko, 2012], the discrepancies between CFD results and experimental data were found to be significant in a case of low injection flow rate. The maximum concentration is underestimated at least by 25 % which fails to be a reliable result for safety prediction. The discrepancies may due to the turbulence models used in the CFD models. Therefore, improving turbulence modeling in CFD is an essential requirement. This task relies greatly on Direct numerical simulation results (DNS) since they give access to every quantities of the flow.

In this chapter, we use a DNS code to simulation helium dispersion in an air-filled cavity. First of all the code is used to simulate a plane plume and the results are compared with the theory of steady plane plume. Then simulations on GAMELAN experiment in a case of low injection flow rate are carried out. During the injection the vertical volume fraction profile in the cavity far from the plume axis is almost one-dimensional. Therefore, we make an assumption that the flow is axisymmetric. We will evaluate the effects of this assumption on the flow.

The structure of this chapter is as follows. Plane plumes are simulated in section 5.2 and the comparison with theoretical model of steady laminar plane plumes ([Gebhart et al., 1988]) is made. In section 5.3 GAMELAN experiment is simulated with the axisymmetric assumption and the numerical results are compared with the experimental data of GAMELAN and several other numerical results. The general conclusions are discussed in section 5.4.

5.2 Plane plume simulations

In this chapter we simulate plane plumes of helium-air mixture and helium. The physical configuration and numerical treatment are given in section 5.2.1. The transition to unsteadiness is discussed in section 5.2.3. The flow structure is described in section 5.2.2. Section 5.2.4 is devoted to the comparison with the theory of steady laminar plane plumes ([Gebhart et al., 1988]).

5.2.1 Physical configuration and numerical set-up

Physical configuration The enclosure is a square cavity of 1m width (W) and 1m height (H) filled with air (Fig. 5.1). The inlet has a width of 20 mm (d_i) and is located in the center of the bottom of the domain. An opening of 20mm width (d_o) is located at the foot of a side wall for depressurization.

The lighter gas injected can be helium or a mixture of helium and air. Three injection situations are considered depending on the percentage of helium in the injected mixture, characterized by helium mass fraction Y_1. We recall that helium is denoted as species 1 and air as species 2. The injection velocity $\overline{w_i}$ is fixed at $1.51 \times 10^{-3}\ m/s$ in three cases which gives the volume flux of $3 \times 10^{-5}\ m^2/s$. The physical parameters of three injection situations are given in Table 5.1. The first two cases correspond to the injection of a helium-air mixture and the last case corresponds to the injection of pure helium. The density ρ_a and dynamic

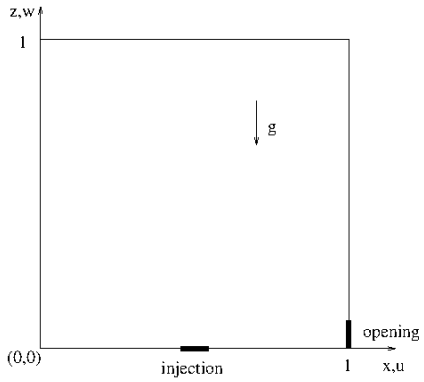

Figure 5.1: A 2D square cavity with a small opening for depressurization.

Y_{1i}	ρ_i (kg/m^3)	$\frac{\Delta\rho}{\rho_a}$	$\nu_i \times 10^6 (m^2/s)$	$\frac{\nu_i}{\nu_a}$
0.01	1.117	0.059	16.98	1.124
0.1	0.731	0.394	32.04	2.136
1.0	0.164	0.862	117.0	7.748

Table 5.1: Physical properties of three injection situations of helium-air plumes.

viscosity μ_a of air (the ambient fluid) at 20 ^oC and 1 atm are 1.1839 (kg/m^3) and 15.1×10^{-6} (m^2/s), respectively. The molar mass ratio of air to helium is $\epsilon_M^{21} = 7.24$.

Dimensionless parameters The dimensionless parameters were already defined in section 2.4 and are given in Table 5.2

Numerical set-up The scaling for the velocity is based on the characteristic velocity used for natural convection flows

$$U_r = \sqrt{g \frac{\rho_a - \rho_i}{\rho_a} H}, \tag{5.1}$$

Y_{1i}	Re_i	Ri_i	Sc_i	Gr
0.01	1.778	4.1	0.245	2.53×10^9
0.1	0.942	42.2	0.463	1.65×10^{10}
1.0	0.258	406	1.689	3.71×10^{10}

Table 5.2: Parameters of three injection situations of helium-air plumes.

The uniform profile is used for both veritcal velocity w and helium mass fraction Y_1 at the inflow boundary (section 3.4). The open boundary condition is used at the outflow boundary with zero normal fluxes of fraction and velocity. Regular grids up to 1536x1536 were used depending on the case. The timestep was chosen so that the CFL condition 3.42 is satisfied.

5.2.2 Flow description

We present in Fig. 5.2 a typical flow field for $Y_{1i} = 0.01$ before and after the collision of the plume with the top wall. When the lighter fluid is injected in the cavity, a dipolar structure which is called the plume head develops on top of a steady conduit. As time increases, if the plume is still stable the dipolar structure collides with the top of the enclosure. After the collision, the dipole splits into two mono-pole vortices. When a mono-pole vortex rebounds from the top wall another vortex of the opposite sign is created and a new dipole is formed. This kind of behavior is typical of the collision of a dipole with a no-slip wall and was found experimentally by [van Heijst and Flor, 1989] and numerically by [Orlandi, 1990]. These new dipolar structures penetrate into the fluid below them in the enclosure. This leads to a large scale recirculating flow in the upper part of the cavity on both sides of the plume. After some time this large scale motion results in oscillating motion of the plume.

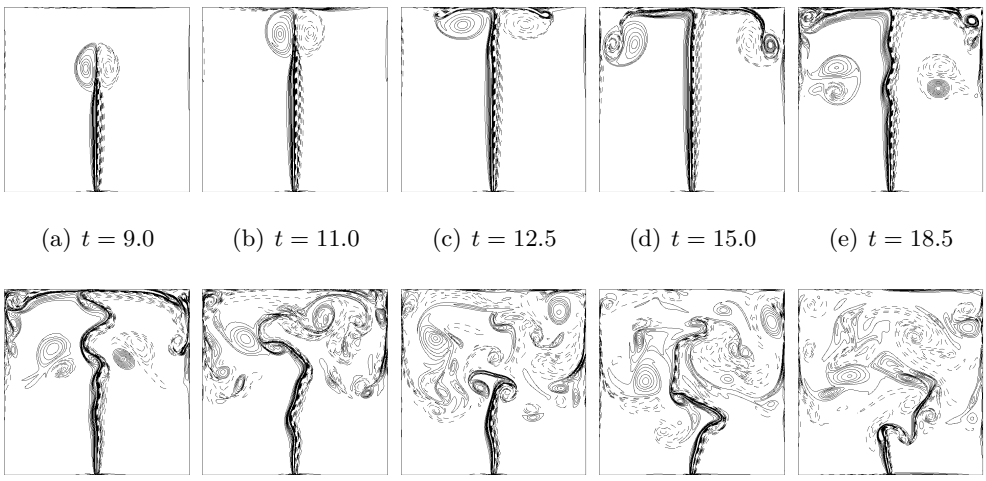

(a) $t = 9.0$ (b) $t = 11.0$ (c) $t = 12.5$ (d) $t = 15.0$ (e) $t = 18.5$

(f) $t = 20.0$ (g) $t = 24.5$ (h) $t = 28.5$ (i) $t = 32.5$ (j) $t = 35.5$

Figure 5.2: Case $Y_{1i} = 0.01$ with 512x512 grid: Time evolution of vorticity distribution. Contour levels of ω [-10:0.5:10]

Now the transition to unsteadiness corresponding with three cases of Y_{1i} is discussed.

5.2.3 Transition to unsteadiness

Case $Y_{1i} = 0.01$ In an open space a plume becomes unstable at a certain elevation z above the source and finally becomes turbulent. The local Grashof number

$$Gr_z = g\frac{\rho_a - \rho}{\rho_a}\frac{z^3}{\nu^2} \tag{5.2}$$

at which the transition begins and ends were found experimentally by [Bill and Gebhart, 1975] to be $Gr_z^1 = 6.4 \times 10^7$ and $Gr_z^2 = 2.95 \times 10^8$, respectively.

If we take $\nu = \nu_a$ and $\rho = \rho_i$ in Eq. (5.2) the values of z corresponding to Gr_z^1 and Gr_z^2 are $z_1 = 0.293m$ and $z_2 = 0.425m$. Above the source $\nu > \nu_a$ and $\rho > \rho_i$ so the exact values of z calculated from (5.2) for Gr_z^1 and Gr_z^2 would be larger. Fig. 5.3 presents the plume for case $Y_{1i} = 0.01$ with three resolutions. For the coarsest grid the plume becomes unstable at about $z = 0.5m$ while it remains stable until it impacts the top wall for the two finer grids.

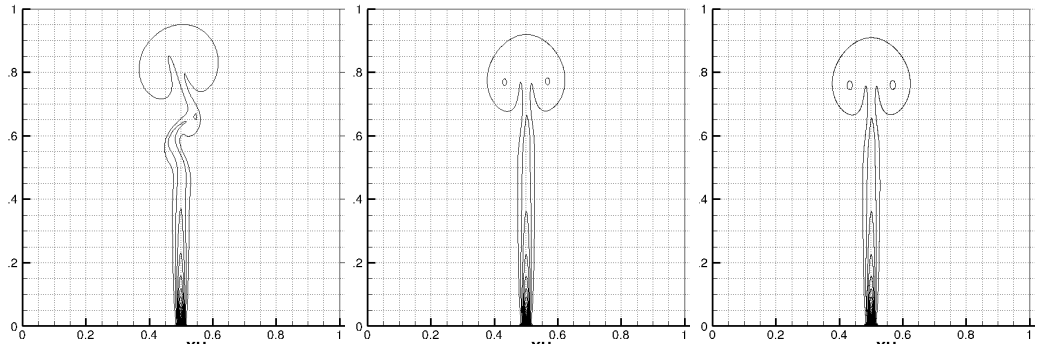

(a) $w = 0.2850(z - 0.0236)^{1/5}$ (b) $w = 0.2844(z - 0.0115)^{1/5}$ (c) $w = 0.2835(z - 0.0077)^{1/5}$

Figure 5.3: $Y_{1i} = 0.01$: Density distribution at $t = 10.0$ with three grids: a) 256x256, b) 512x512, c) 1024x1024. Contour levels of ρ [0.94:0.00125:1.0]

Case $Y_{1i} = 0.1$ For $Y_{1i} = 0.1$ the values of z_1 and z_2 are $0.156m$ and $0.26m$, respectively. In Fig. 5.4 the position at which it becomes unstable is very near the injection for the coarsest grid while for two finer grids it is about $z = 0.45$.

Case $Y_{1i} = 1$ When pure helium is injected, i.e. $Y_{1i} = 1$ the buoyancy force acting on the flow is very large and the plume becomes unstable very near the injection, as can be seen in Fig. 5.5 for the finest grid. In this case the values calculated for z_1 and z_2 are $0.12m$ and $0.2m$, respectively.

We have seen that for $Y_{1i} = 0.01$ and $Y_{1i} = 0.1$ the plumes remain stable for a considerable height above the source. The vertical and horizontal profiles of the

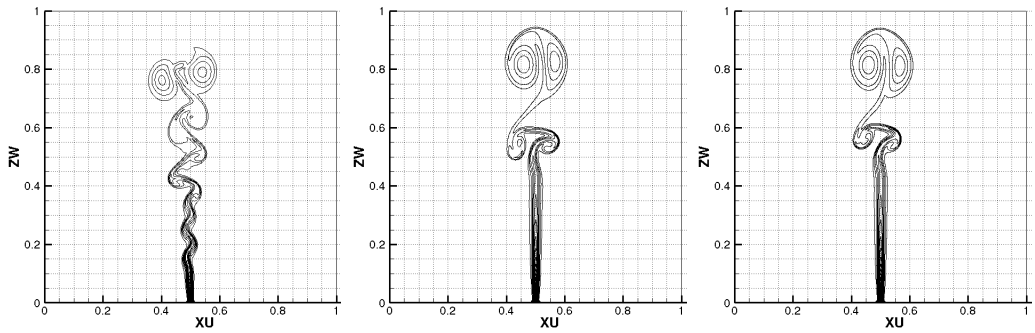

(a) 512x512 (b) 1024x1024 (c) 1536x1536

Figure 5.4: $Y_{1i} = 0.1$: Density distribution at $t = 10.0$ with 3 grids: a) 512x512, b) 1024x1024 and c) 1536x1536. Contour levels of ρ [0.62:0.005:1.0]

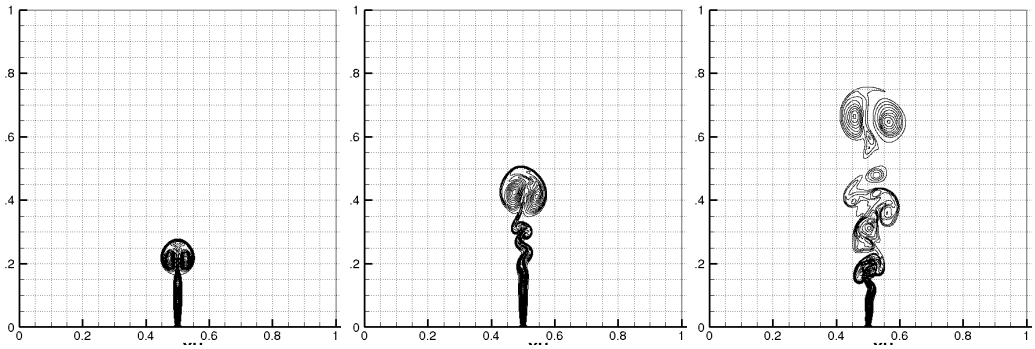

(a) $t = 3.5$ (b) $t = 5.5$ (c) $t = 8.0$

Figure 5.5: $Y_{1i} = 1$: Density distribution at different times with 1536x1536 grid: . Contour levels [0.14:0.01:1.0]

vertical velocity w and density difference $\rho_a - \rho$ of the steady conduit are now compared to the theory of steady laminar plane plumes ([Gebhart et al., 1988]).

5.2.4 Comparison with scaling laws and similarity theory of laminar plane plumes

In this section we verify the decay laws of the vertical velocity and density difference along the centerline, $w_c(z)$ and $(\rho_a - \rho_c)(z)$, respectively. We also verify that the horizontal profiles $w(x, z)$ and $(\rho_a - \rho)(x, z)$ are self-similar. These properties of a steady laminar plane plume was described in section 1.2.1. We recall here that in a plane plume the vertical velocity along the centerline $w_c(z)$ increases as $z^{1/5}$ (Eq. (1.22)) and the density difference along the centerline $(\rho_a - \rho_c)(z)$ decreases as $z^{-3/5}$

(Eq. (1.23)). Also, the horizontal profiles $\frac{w(x,z)}{w_c(z)}$ with the radius scaled with $z^{-2/5}$ have similar forms for all x (Eq. 1.24). The same result applies for the horizontal profiles $\frac{(\rho_a-\rho_c)(x,z)}{(\rho_a-\rho_c)(z)}$. The verification is carried out for two cases $Y_{1i}=0.01$ and $Y_{1i}=0.1$.

Case $Y_{1i}=0.01$ First of all, we investigate the decay law of $w_c(z)$ and $(\rho_a-\rho_c)(z)$.

The profiles of the vertical velocity w along the centerline are presented in Fig. 5.6a at four different times before the plume collides with the top wall until $t=12.0$.

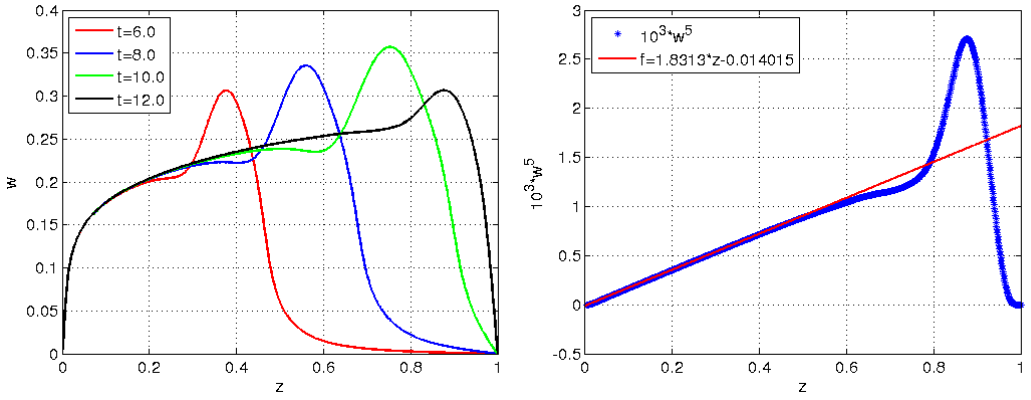

(a) (b)

Figure 5.6: Case $Y_{1i}=0.01$ with 1024x1024 grid: a) Vertical velocity profile along the centerline at 4 different times: $t=6.0$, $t=8.0$, $t=10.0$, $t=12.0$ and b) at $t=12.0$.

Each curve is divided sequentially into three parts from $z=0$: the first part of smoothly increasing velocity corresponding to the lower part of the plume or the conduit, the second part of slightly decreasing velocity corresponding to the part just below the plume head and the third part of substantial increasing velocity corresponding to the plume head.

The lower parts of the four curves in Fig. 5.6a collapse on the same curve, which shows a steady behavior of the conduit. The conduit part from $z=0$ to $z=0.5$ is taken from the curve at $t=12.0$ and a linear fitting of this part (Fig. 5.6b) gives

$$10^3 w_c^5 = 1.8313z - 0.014 \tag{5.3}$$

which implies

$$w_c = 0.2835\overline{z}_w^{1/5} \tag{5.4}$$

where $\overline{z}_w = z - 0.0077$.

It is shown that w_c is proportional to z^5 if the source is placed at $z=0.0077$ above the source. The notion of a virtual source appeared in the literature when the theory of plumes originating from an infinitely thin line source is compared with

the experiment. A virtual source is a notion to account for the finite dimension of the source in laboratory experiments. [Shlien and Boxman, 1979] compared the temperature measurement in an axisymmetric plume and the agreement with the theory of laminar round plume was obtained if the virtual source location is 4.7 times the diameter of the source and above source.

The profiles of $\rho_a - \rho$ along the centerline are presented in Fig. 5.7a.

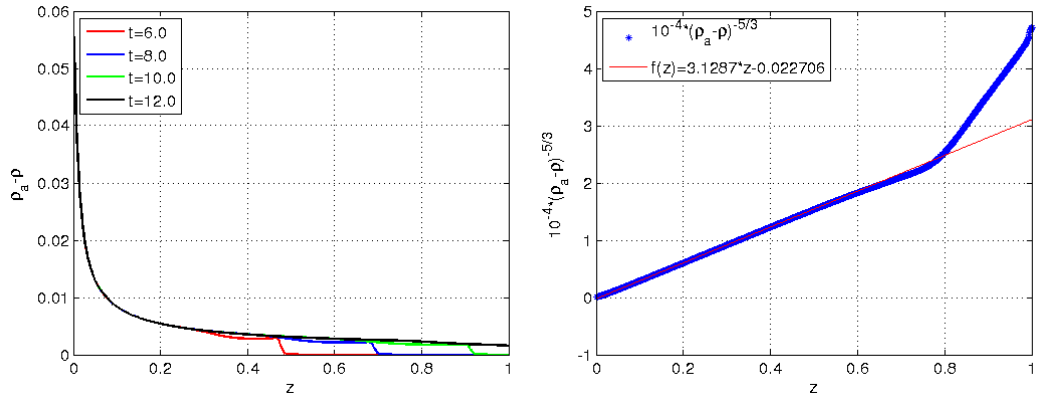

(a) (b)

Figure 5.7: Case $Y_{1i} = 0.01$ with 1024x1024 grid: a) Profile of density difference along the centerline at 4 different times: $t = 6.0$, $t = 8.0$, $t = 10.0$, $t = 12.0$ and b) at $t = 12.0$.

The lower parts of the four curves in Fig. 5.7a superimpose each other. The conduit part from $z = 0$ to $z = 0.5$ is taken from the curve at $t = 12.0$ and a linear fitting of this part (Fig. 5.7b) gives

$$10^{-4}(\rho_a - \rho_c)^{-5/3} = 3.1287z - 0.0227 \tag{5.5}$$

which implies

$$\rho_a - \rho_c(z) = 0.0020\overline{z}_\rho^{-3/5} \tag{5.6}$$

where $\overline{z}_\rho = z - 0.0073$. A virtual source is found at $z_0 = 0.0073$, a little higher than the virtual source found for w at $z = 0.0077$.

Now we show that $w(x, z)$ and $\rho_a - \rho(x, z)$ has self-similar forms.

The horizontal profiles of w at $t = 10.0$ at different z-positions plotted in Fig. 5.8a show that the curves below $z = 0.5$, which correspond to the plume conduit, display similar behavior.

To show that the curves below $z = 0.5$ in Fig. 5.8a are self-similar, we rescale $w(x, z)$ according to the decay rate of w_c. Then we rescale the radius of the plume by creating a new variable $\eta_w = x(z - 0.0077)^{-2/5}$. Plotting $w(x, z)(z - 0.0077)^{1/5}$ as a function of η_w, all the curves below $z = 0.5$ collapse on one curve in the region

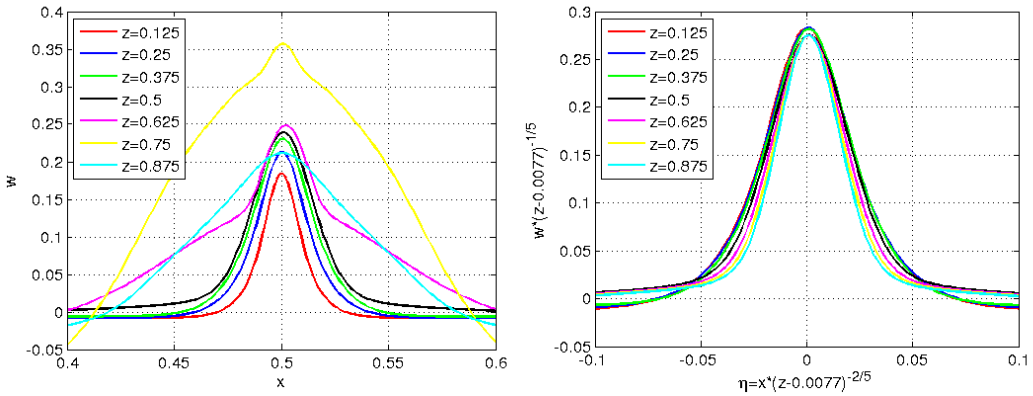

(a) (b)

Figure 5.8: $Y_{1i} = 0.01$ with 1024x1024 grid: a) Horizontal profile of vertical velocity at different heights at $t = 10.0$; b) The curves in a) with a change of variables: $w.(z - 0.0077)^{-1/5}$ is plotted as a function of $\eta = x.(z - 0.0077)^{-2/5}$

$-0.05 \leq \eta_w \leq 0.05$, as observed in Fig. 5.8b. Denoting this curve by $f(\eta_w)$ the horizontal profile of w below $z = 0.5$ satisfies

$$w(x, z)(z - 0.0077)^{1/5} = f(\eta_w) \tag{5.7}$$

Using relation (5.4) in equation(5.7) gives the following similarity form for w

$$w(x, z) = 3.5273 w_c(z) f(\eta_w) \tag{5.8}$$

Similarly, the horizontal profiles of $\rho_a - \rho(x, z)$ at $t = 10.0$ at different z-positions are plotted in Fig. 5.9a.

In Fig. 5.9b $(\rho_a - \rho(x, z))(z - 0.0073)^{3/5}$ is plotted as a function of $\eta_\rho = x(z - 0.0073)^{-2/5}$ and all the curves below $z = 0.5$ collapse on one curve in the region $-0.05 \leq \eta_\rho \leq 0.05$. Denoting this curve by $g(\eta_w)$ the horizontal profile of $\rho_a - \rho(x, z)$ below $z = 0.5$ satisfies

$$(\rho_a - \rho(x, z))(z - 0.0073)^{3/5} = g(\eta_\rho) \tag{5.9}$$

Using relation (5.6) in equation (5.9) gives the following similarity form for $\rho_a - \rho$

$$(\rho_a - \rho(x, z)) = 500(\rho_a - \rho_c(z)) g(\eta_\rho) \tag{5.10}$$

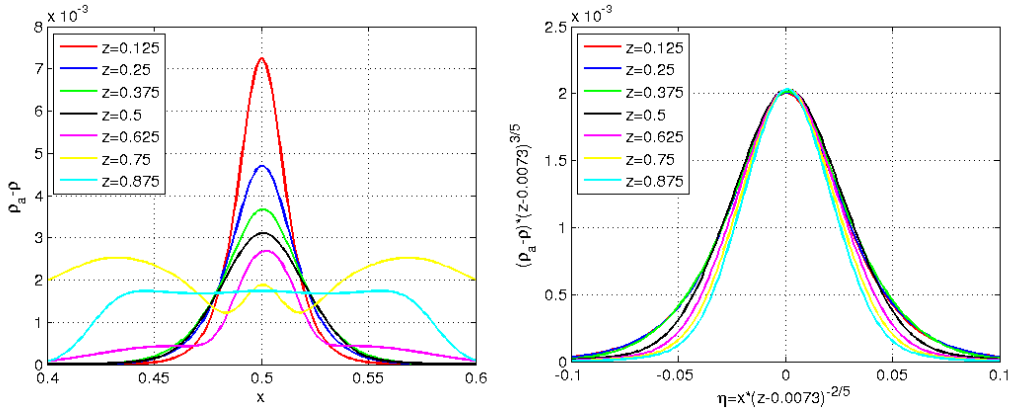

(a) (b)

Figure 5.9: $Y_{1i} = 0.01$ with 1024x1024 grid: a) Horizontal profile of density difference at different heights at $t = 10.0$; b) The curves in a) with a change of variables: $(\rho_a - \rho).(z - 0.0073)^{3/5}$ is plotted as a function of $\eta = x.(z - 0.0073)^{-2/5}$.

Case $Y_{1i} = 0.1$ We carry out similarly to the case $Y_{1i} = 0.01$. First of all, we investigate the decay law of $w_c(z)$ and $(\rho_a - \rho_c)(z)$.

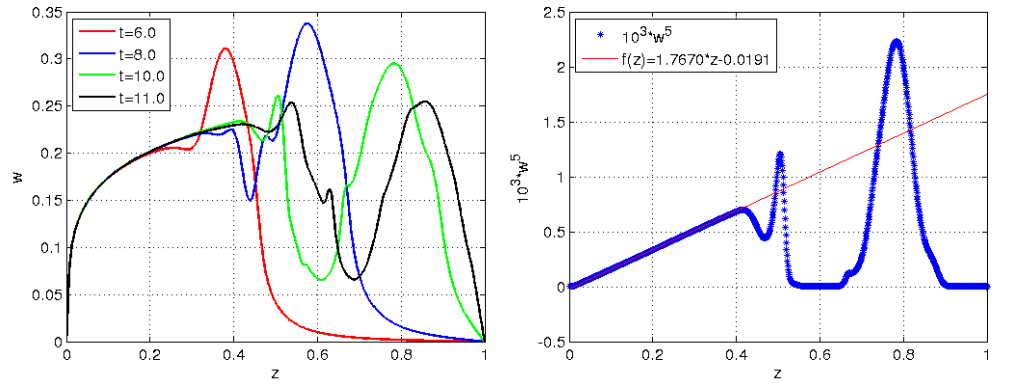

(a) (b)

Figure 5.10: $Y_{1i} = 0.1$ with 1024x1024 grid: a) Vertical velocity profile along the centerline at 4 different times: $t = 6.0$, $t = 8.0$, $t = 10.0$, $t = 11.0$ and b) at $t = 10.0$

In Fig. 5.10a the vertical profiles of w along the centerline at different times are presented. At $t = 6.0$ the plume is stable while at $t = 8.0$ an instability develops just above $z = 0.4$. At $t = 10.0$ this instability is advected downstream and develops in the head part of the plume and at $t = 11.0$ it begins to affect the conduit. The

conduit part form $z = 0$ to $z = 0.4$ is taken from the curve at $t = 10.0$ and a linear fitting of this part gives

$$10^3 w_c^5 = 1.7670z - 0.0191 \tag{5.11}$$

which implies

$$w_c(z) = 0.2815\overline{z}_w^{1/5} \tag{5.12}$$

where $\overline{z}_w = z - 0.0108$.

In Fig. 5.11a the profiles of $\rho_a - \rho$ along the centerline at different times are presented.

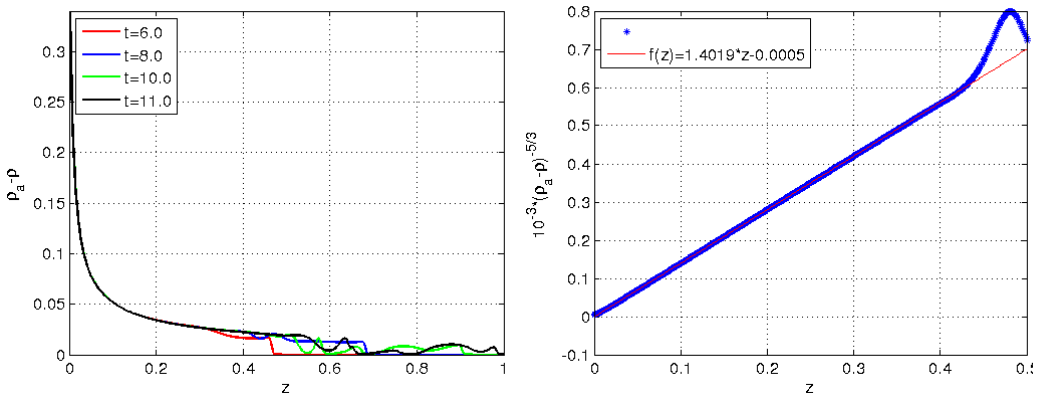

Figure 5.11: $Y_{1i} = 0.1$ with 1024x1024 grid: a) Profile of density difference along the centerline at 4 different times: $t = 6.0$, $t = 8.0$, $t = 10.0$, $t = 11.0$ and b) at $t = 10.0$.

The conduit part form $z = 0$ to $z = 0.4$ is taken from the curve at $t = 10.0$ and a linear fitting of this part gives

$$10^{-3}(\rho_a - \rho_c)^{-5/3} = 1.4019z - 0.0005 \tag{5.13}$$

which implies

$$\rho_a - \rho_c(z) = 0.0129\overline{z}_\rho^{-3/5} \tag{5.14}$$

where $\overline{z}_\rho = z - 0.0004$.

Now we show that $w(x, z)$ and $\rho_a - \rho(x, z)$ has self-similar forms.

The horizontal profiles of $w(x, z)$ at $t = 10.0$ at different z-positions plotted in Fig. 5.12a show that the curves below $z = 0.4$ display similar behavior. Plotting $w(x, z)(z - 0.0108)^{1/5}$ as a function of $\eta_w = x(z - 0.0108)^{-2/5}$, all the curves below $z = 0.4$ collapse on one curve in the region $-0.05 \leq \eta_w \leq 0.05$, as observed in Fig. 5.12b. Denoting this curve by $f(\eta_w)$ the horizontal profile of $w(x, z)$ below $z = 0.4$ satisfies

$$w(x, z)(z - 0.0108)^{1/5} = f(\eta_w) \tag{5.15}$$

Using relation (5.12) in equation (5.15) gives the following similarity form for $w(x, z)$

$$w(x, z) = 3.5524 w_c(z) f(\eta_w) \tag{5.16}$$

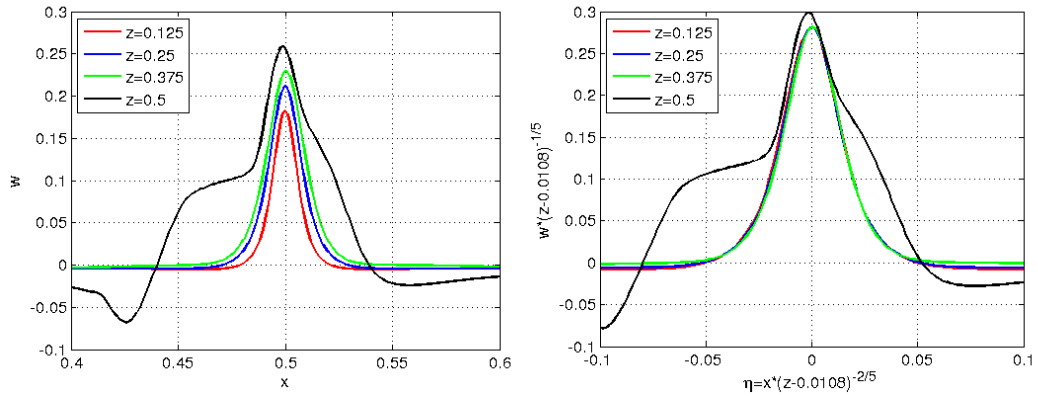

Figure 5.12: $Y_{1i} = 0.1$ with 1024x1024 grid: a) Horizontal profile of vertical velocity at different heights at $t = 10.0$; b) The curves in a) with a change of variables: $w.(z - 0.0108)^{-1/5}$ is plotted as a function of $\eta = x.(z - 0.0108)^{-2/5}$.

The horizontal profiles of $\rho_a - \rho(x, z)$ at $t = 10.0$ at different z-positions are plotted in Fig. 5.13a.

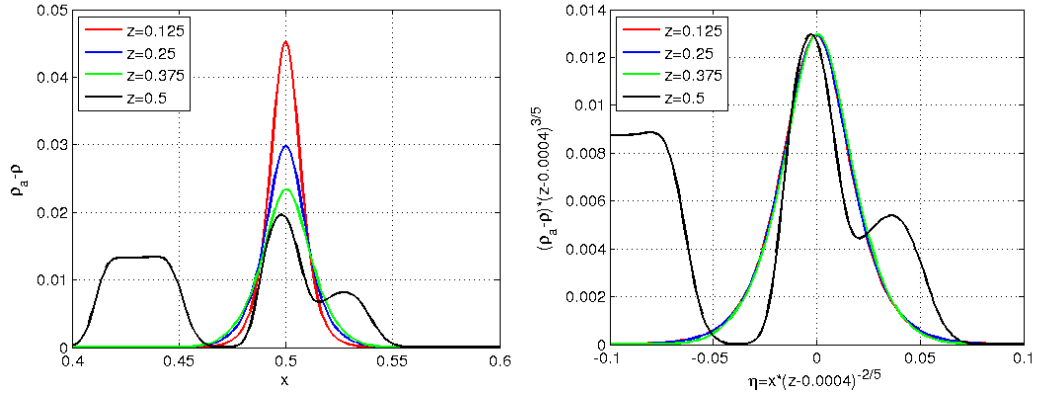

Figure 5.13: $Y_{1i} = 0.1$ with 1024x1024 grid: a) Horizontal profile of density difference at different heights at $t = 10.0$; b) The curves in a) with a change of variables: $(\rho_a - \rho).(z - 0.0004)^{3/5}$ is plotted as a function of $\eta = x.(z - 0.0004)^{-2/5}$.

Plotting $(\rho_a - \rho)(z - 0.0004)^{3/5}$ as a function of $\eta_\rho = x(z - 0.0004)^{-2/5}$ in Fig. 5.13, all the curves below $z = 0.4$ collapse on one curve in the region $-0.05 \leq \eta_\rho \leq 0.05$. Denoting this curve by $g(\eta_w)$ the horizontal profile of $\rho_a - \rho(x, z)$ below $z = 0.4$ satisfies

$$(\rho_a - \rho(x, z))(z - 0.0004)^{3/5} = g(\eta_\rho) \tag{5.17}$$

Using relation (5.14) in equation (5.17) gives the following similarity form for $\rho_a - \rho$

$$\rho_a - \rho(x,z) = 77.52(\rho_a - \rho_c(z))g(\eta_\rho) \tag{5.18}$$

In this section we have verified that before the plumes become unstable, their conduits behave like steady laminar plane plumes. The vertical velocity along the centerline $w_c(z)$ increases as $z^{1/5}$ and the density difference along the centerline $(\rho_a - \rho_c)(z)$ decreases as $z^{-3/5}$. We have also shown that the horizontal profiles $w(x,z)$ and $(\rho_a - \rho_c)(x,z)$ are self-similar.

In the next section we carry out the simulation on round plumes, assuming that the flow is axisymmetric.

5.3 Axisymmetric plume simulation

In this section we carry out simulations on round plumes, assuming that they are axisymmetric. In section 5.3.1 the description of GAMELAN experiment and the test cases followed from this experiment are given. In section 5.3.2 the flow structure obtained with the axisymmetric assumption is investigated. The comparison with a finite element simulation is carried out for a small-scale cavity in section 5.3.3. The comparison with the experimental results of GAMELAN and other numerical results are presented in section 5.3.4. In the last section 5.3.5 we compare the numerical results with the theoretical model of [Worster and Huppert, 1983].

5.3.1 Description of the test cases

Description of GAMELAN experiment ([Cariteau and Tkatschenko, 2012]) GAMELAN is a set of experiments to study the dispersion properties of the light gas helium in air. Its description is given as follows.

Geometry: The experiments were carried out in a parallelepiped cavity with a dimension of HxLxW. The cavity can be closed or vented. Only the closed configuration is presented here in which the cavity is closed except for a small opening of diameter d_o in the middle of one side wall, at a height h_o from the floor for depressurization, since it will be the configuration for numerical simulations. Helium or helium-air mixture is injected through a vertical tube of diameter d_i placed upward in the center of the bottom wall. The exit is at a height h_i from the bottom. Those geometry parameters are given in Table 5.3.

H	L	W	d_i	h_i	d_o	h_o
0.126	0.93	0.93	0.02/0.005	0.21	0.01	0.01

Table 5.3: Geometry parameters (in *meter*) of GAMELAN experiment ([Cariteau and Tkatschenko, 2012]).

Working fluids: The cavity is initially filled with air at rest. The light fluid injected in the cavity at a constant rate can contain 60 %, 80 % or 100 % volume of helium.

Method of concentration measurement: Measurements of helium concentration is done by placing mini-Katharometers (sensors) at 10 different heights along 2 vertical lines away from the source and are recorded in time. The experimental set-up is presented in Fig. 5.14. The positions of 10 thermocouples are listed in Table 5.4

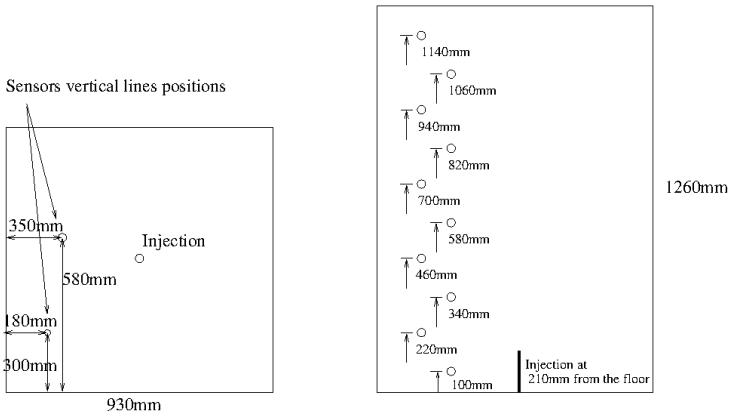

Figure 5.14: The experimental set-up of GAMELAN experiment : top view (left) and side view (center) ([Cariteau and Tkatschenko, 2012]).

Test cases for axisymmetric plume We consider the injection of helium in an air-filled cavity at constant temperature and pressure. The configuration is based on the experimental set-up of GAMELAN ([Cariteau and Tkatschenko, 2012]) whose results we want to reproduce. The experimental results show that

Sensor number	r_{out} (m)	z (m)
1	0.35	0.1
2	0.35	0.34
3	0.35	0.58
4	0.35	0.82
5	0.35	1.06

Sensor number	r (m)	z (m)
6	0.18	0.22
7	0.18	0.46
8	0.18	0.70
9	0.18	0.94
10	0.18	1.14

Table 5.4: Positions of ten thermocouples (sensors) in GAMELAN experiment ([Cariteau and Tkatschenko, 2012]): r_{out} is the distance between thermocouples and the vertical wall nearest to them, z is the distance from the thermocouples to the floor.

the helium volume fraction profiles far from the source are dependent only on the vertical position. Therefore, we choose to mimic the experimental apparatus by a cylindrical cavity.

Geometry: The full cylindrical cavity is depicted in Fig. 5.15. This cavity has a diameter $d = 1050\ mm$, which gives the same cross-sectional area A as the cavity of GAMELAN. The height of the cylindrical cavity spreads from the exit of the injection tube to the top of GAMELAN experiment and the portion below the exit of the injection tube is not modeled. Therefore, the height of the cylindrical is equal to

$$L_z = H - h_i \tag{5.19}$$

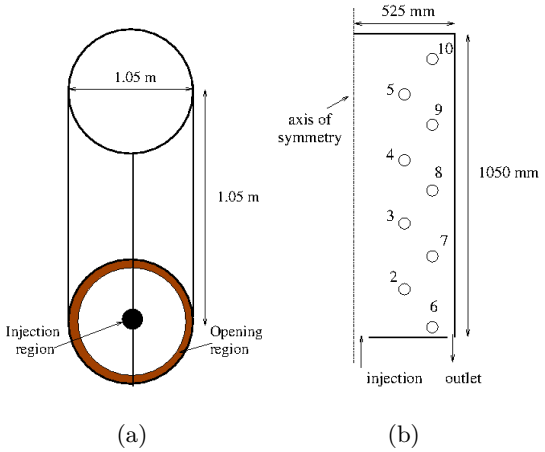

Figure 5.15: The full cavity of numerical simulation: a) The full shape, b) A plane of axisymmetry with positions of sensors.

The opening has a donut shape placed at the bottom and near the vertical side wall with diameter equal to $d_i/2$. This configuration is called cavity 1. Sensor 1 is below the exit of the injection tube and thus is not modeled. Therefore, there are only nine sensors from 2 to 10 corresponding to GAMELAN experiment. The horizontal position r_{out} in Table 5.4 is modified according to the ratio of the diameter of the new cavity to the width of the experimental cavity. As a result, $r_{out} = 0.395m$ for sensors from 2 to 5 and $r_{out} = 0.203m$ for sensors from 6 to 10.

Working fluids: The physical properties of helium and air are listed in Table 5.5. The binary diffusion coefficient and the viscosity of a helium-air mixture are calculated using Eqs. (2.31) and (2.35) at 20 ^oC, the same temperature as GAMELAN experiment.

Smaller configurations: Four cavities of the same aspect ratio as cavity 1 and with smaller heights of 1/10, 1/5, 2/5, 3/5 of cavity 1 are also simulated. They are used to approach the simulation of cavity 1. Horizontal and vertical positions of sensors are also rescaled according to these size ratio.

Injection conditions: The injection has a diameter $d_i = 0.02m$ and a flow rate Q of 4 Nl/min (corresponding to $7.1 \times 10^{-5}\ m^3/s$) is used for 5 cavities. In

the benchmark [Bernard-Michel et al., 2012] this is the configuration that shows large discrepancies between experimental and numerical results. The corresponding injection Richardson number Ri_i of 11.6, defined by Eq. (2.65), indicates that at the source the flow is dominated by buoyancy. In all the cases Sc_a, defined by Eq. (2.68), is equal to 0.218.

Other dimensionless parameters are given in Table 5.6.

Numerical set-up The uniform profile is used for both vertical velocity w and helium mass fraction Y_1 at the inflow boundary. In this case the inflow boundary conditions have to be defined as in section 3.4 for significant diffusion flux. These conditions contain t_c in Eq. (3.72) and z_1 in Eq. (3.73) and their values for the problem being studied are listed in Table 5.6. These values ensure that the vertical velocity at the inflow is always positive. The open boundary condition, Eq. (3.13), is used at the outflow boundary.

The grid: Rectangular nonuniform grids with a hyperbolic tangential distribution in the r-direction is used which gives finer grid near the injection and the wall and a coarser one in the middle. The distance between the grid points are adjusted slightly near the injection so as to give exactly the injection area as in the experiment. Only 642 grid points have to be used in the vertical direction compared with 1024 grid points of 2D Cartesian simulation for the largest cavity since the axisymmetry assumption has the effect of stabilizing the flow.

The numerical results for round plume simulations are checked to ensure that the solutions are independent of the grid size and the grids chosen are listed in

ρ_i	Y_{1i}	ρ_a	Y_{1a}	$\frac{\Delta\rho}{\rho_a}$	ν_i	ν_a	D
$[kg/m^3]$	[-]	$[kg/m^3]$	[-]	[-]	$[m^2/s]$	$[m^2/s]$	$[m^2/s]$
0.164	1	1.184	0	0.862	11.7×10^{-5}	1.51×10^{-5}	6.93×10^{-5}

Table 5.5: Physical properties of the helium-air round plume simulations.

Cavity	Gr_r	d_i/d	Ri_v	Grid	Time step	t_c
1/10	4.3×10^7	0.19	0.15	74x146	min: 10^{-4}, max: 1.5×10^{-4}	0.09
1/5	3.4×10^8	0.1	1.16	98x194	min: 10^{-4}, max: 1.5×10^{-4}	0.54
2/5	2.7×10^9	0.05	9.28	146x290	min: 10^{-4}, max: 1.5×10^{-4}	3.2
3/5	9.3×10^9	0.03	31.3	218x434	min: 10^{-4}, max: 1.5×10^{-4}	9.0
1	3.7×10^{10}	0.02	145	322x642	min: 5×10^{-5}, max: 1.5×10^{-4}	33.3

Table 5.6: Helium-air axisymmetric plume simulations: dimensionless parameters, mesh size, time step and transitional time t_c for the inflow boundary conditions.

Table 5.6. With those grids the solutions are free of numerical oscillations and the difference with the solutions of finer grid is negligible. The detailed grid convergence study for all the cavities are given in Appendix A.

In the next section the description of the flow is given.

5.3.2 Description of the flow

We show in this section how the flow evolves with time and how the mass fraction distribution develops inside a cavity by investigating the vorticity fields and the mass fraction fields.

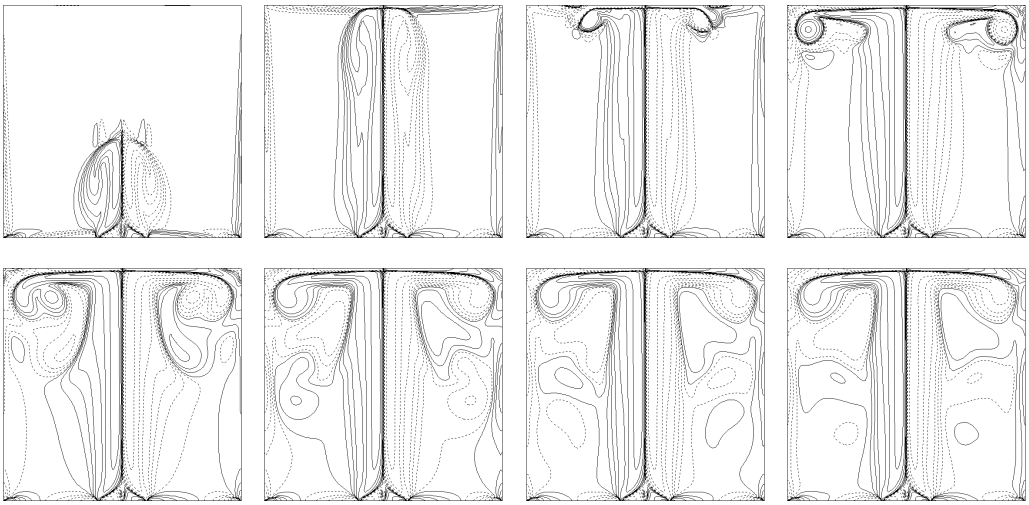

Figure 5.16: Vorticity isocontour respectively at t=1.5, 2.5, 3, 5.5, 10.5, 15.5, 20.5 and 25.5 for cavity 1/10 (from left to right, top to bottom).

Vorticity fields The vorticity fields of cavity 1/10 are presented in Fig. 5.16. The computational results are reflected through the vertical axis to obtain the whole field. It is shown that the plume carrying two stable vortices impact the top wall and spreads out horizontally to form a thin layer. This layer propagates downward due to the entrainment of the newly injected fluid. The motions are visible inside the plumes and in the top region where the fluid from the plume interact with the top wall and roll down at the two top corners. The vorticity fields of cavity 1 are presented in Fig. 5.17. The diameter of the injection is a small portion of the bottom wall, so the motions of the plume concentrate in a small portion of the domain. In the remaining region of the domain the flow is almost steady. Compared with Fig. 5.2 of plane plumes we see that the axisymmetric plume is much more stable. The oscillation of the plume about the centerline has been blocked by the axisymmetric assumption, so there is no strong interaction with the walls. The vorticity fields of other cavities have almost the same behaviors of cavity 1 and 1/10.

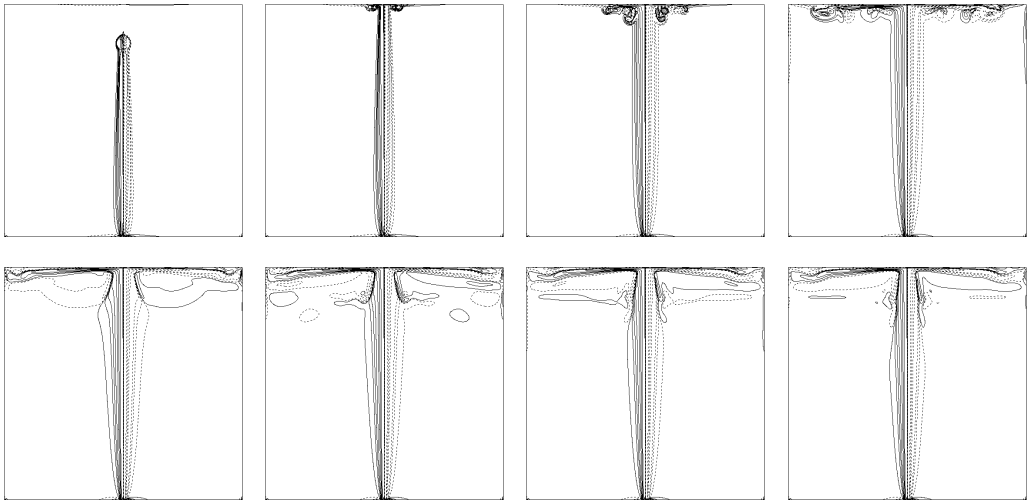

Figure 5.17: Vorticity isocontour respectively at t= 6.5, 7.75, 12.75, 25.25, 62.75, 125.25, 200.25 and 275.25 for cavity 1 (from left to right, top to bottom).

Helium mass fraction fields The snapshots of the mass fraction fields are shown in Fig. 5.18 for cavities from 1/10 and 1. Cavity 1/10 is quite small and the injection region is a considerable portion of the cavity so the mass fraction profile is affected by the developing plume and the side walls is not one-dimensional. For larger cavities the plume occupies only a small portion of the domain, so the helium volume fraction profile is nearly one-dimensional, as can be seen for cavity 1 in Fig. 5.18.

In the next section our numerical results for cavity 3/5 is compared with the finite element results of Gilles Bernard-Michel produced by Cast3m code of CEA.

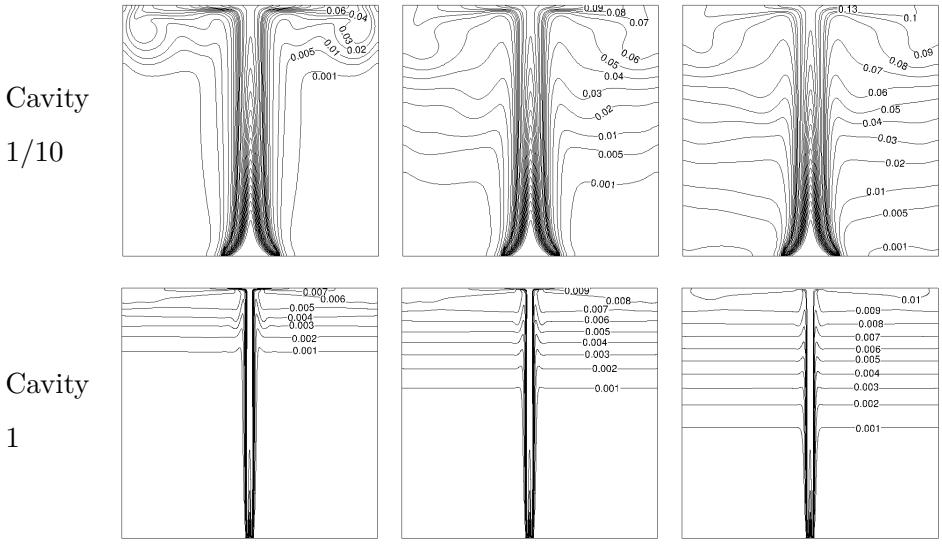

Figure 5.18: Helium mass fraction fields: Cavity 1/10 at $t = 5.5$, 15.5 and 25.5; Cavity 1/5 at t =10.5, 50.5 and 150.5; c) Cavity 2/5 at $t = 25.5$, 100.5 and 275.5; Cavity 3/5 at $t = 50.5$, 200.5 and 350.5; Cavity 1 at $t = 275.25$, 500.25 and 800.25 (from left to right).

5.3.3 Comparison with the finite element results for cavity 3/5

In this section we compare our numerical results for cavity 3/5 with the finite element results of Gilles Bernard-Michel.

The finite element results are obtained with Cast3m code of CEA. The equations in cylindrical coordinates with axisymmetric hypothesis are used. The equations are discretized by a cubic finite element method of order 3. The convection term in the momentum equation is discretized by an upwind scheme. Time discretization is performed using BDF2 scheme, implicit, with projection method. Internal iterations are used to reduce by 10^5 times the nonlinear residual. Irregular triangular mesh along both r and z-direction with 2500 elements are used, in which there are 10 nodes in the injection. The time step is fixed at 0.05 seconds. The parabolic velocity profile is used at the inflow boundary.

The comparison are made at ten points. Fives points are 6, 7, 8, 9 and 10 and five other points which we will denote by A6, A7, A8, A9, A10 on the axis at the same height levels, respectively.

Comparison of the velocity The comparison of the vertical velocity w on the axis at five points A6, A7, A8, A9, A10 are presented in Fig. 5.19. Except at point A6 the difference between DNS results and finite element results are quite large (16 %). At the four remaining points the two results are very close.

The differences at point A6 may be explained as follows. In DNS simulation a uniform fine grid with 434 cells are used in the z-direction while in the finite element simulation a coarser grid is used. Moreover, the grid in finite element simulation

is irregular with fine grids near the injection and the top and coarser grid in the middle. Another factor is that finite element simulation used upwind scheme for the momentum equation which is more diffusive in the coarse grid region and leads to lower value of w compared to DNS.

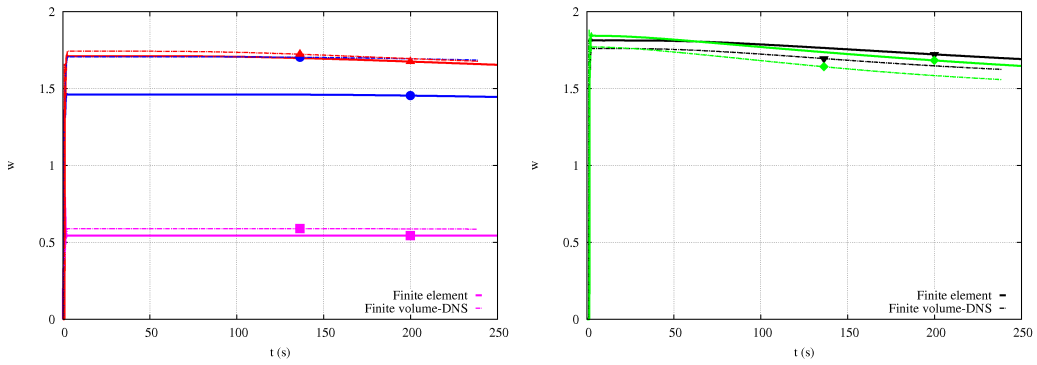

(a) (b)

Figure 5.19: Cavity 3/5: Time evolution of vertical velocity w at 5 points on the axis (a) A6 (square), A7 (circle), A8 (up triangle), (b) A9 (down triangle), A10 (diamond): comparison of DNS and finite element results. DNS results are denoted by dashed lines and finite element results by bold solid lines

Comparison of helium volume fraction Helium volume fraction at ten points are compared in Fig. 5.20. On the axis DNS results are consistently smaller than laminar results which means that DNS results are more diffusive on the axis. The the largest discrepancy being about 7 %. Off the axis, however, a change in behavior is observed in Fig. 5.20b. At the beginning the DNS results are consistently higher than finite element results. At approximately 60 s the finite element results begin to exceed DNS result at sensor 10, the highest sensor. Then at 100 s and 240 s finite element results exceed DNS results at sensor 9 and 8, respectively.

We can explain the observations in Fig. 5.20b as follows. At the beginning the turbulence has not developed yet in the flow, the DNS results are higher because they are less diffusive than finite element results. After a certain time when turbulence has developed, DNS results can capture the turbulence and mixing is promoted while finite element results with coarse grid does not capture well the turbulence and remain laminar. Therefore, DNS results are lower than finite element results when the time increases. Also, in axisymmetric plumes the turbulence motion develops from the top of the cavity where the plumes impact the ceiling. The turbulence motion is then promoted downward with the propagating front (Fig. 5.21). Therefore, finite element results exceed DNS results from the highest sensors to lower sensors.

In the next section we compare our DNS results with the GAMELAN experiment and other numerical results.

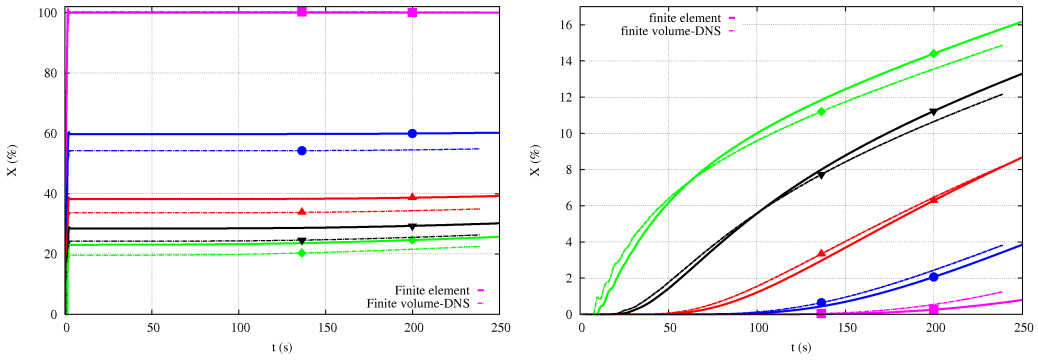

(a) (b)

Figure 5.20: Cavity 3/5: Time evolution of helium volume fraction Y_1 at (a) 5 points on the axis A6 (square), A7 (circle), A8 (up triangle), A9 (down triangle), A10 (diamond) and (b) 5 points 6 (square), 7 (circle), 8 (up triangle), 9 (down triangle), 10 (diamond) off the axis: comparison of DNS and finite element results. DNS results are denoted by dashed lines and finite element results by bold solid lines

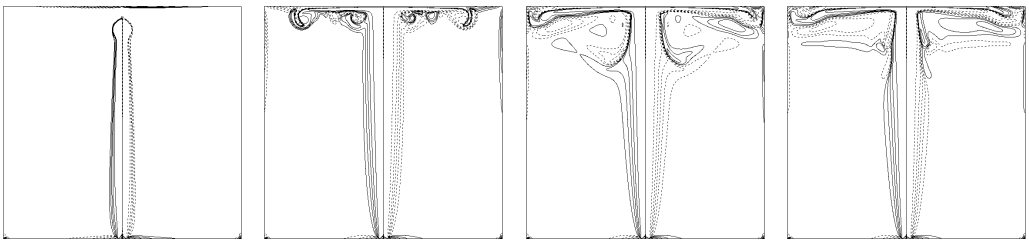

Figure 5.21: Vorticity isocontour respectively at t=4, 20, 46, 139 for cavity 3/5 (from left to right).

5.3.4 Comparison with GAMELAN experiment and other numerical results

We have seen in the previous section that DNS results of the present study for cavity 3/5 is quite close to the finite element results produced by Cast3m code. In this chapter we compare DNS results of the present study for the full cavity (cavity 1) with the experimental data of GAMELAN and other numerical results.

DNS results of the present study are compared with experimental data of GAMELAN for cavity 1 in Fig. 5.22. The time evolution of helium volume fraction at 9 sensors from 2 to 10 shows large discrepancies between numerical and experimental results. For the moment it is concluded that the helium volume fraction is overestimated at high sensors and underestimated at low sensors by DNS results.

The inter-comparison between experimental data of GAMELAN with several

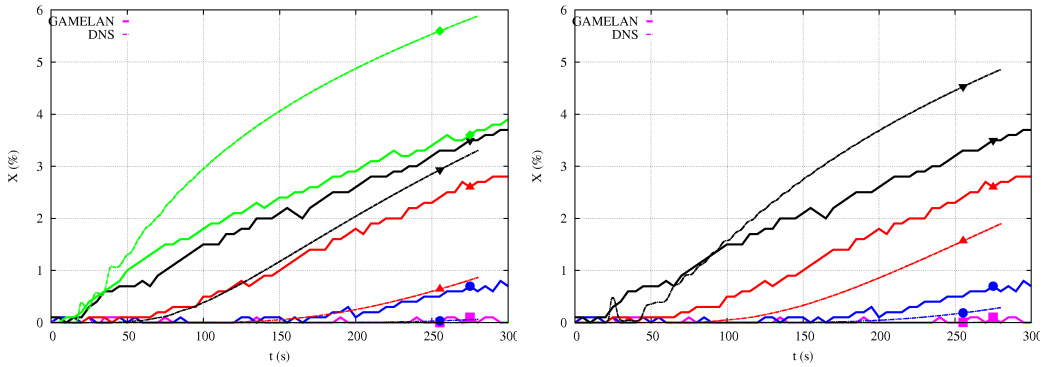

(a) (b)

Figure 5.22: Cavity 1: Time evolution of helium volume fraction at a) sensors 6 (square), 7(circle) , 8 (up triangle), 9 (down triangle), 10 (diamond), b) sensors 2 (square), 3 (circle), 4 (up triangle), 5 (down triangle) : comparison between DNS results (dashed lines) and experimental data of GAMELAN (bold solid lines).

numerical results (including the present study) are now presented. The details of the numerical simulations used in this comparison are presented in Table 5.7 ([Bernard-Michel, 2013]). There are three simulations without turbulence modeling (CEA DNS, JCR DNS, NCSRD DNS), one Large Eddy Simulation (CEA LES 2D), three $k-\epsilon$ models (NCSRD RNG, NCSRD $k-\epsilon$, AL $k-\epsilon$) and one $k-\omega$ model (JCR SST). The spatial discretization employs either finite element or finite volume method. Except for CEA DNS and CEA LES 2D simulations which are done in 2D axisymmetric configuration, other simulations are in 3D.

The vertical profiles of helium volume fraction at 115 s are compared in Fig. 5.23. The results obtained with 2D axisymmetric hypothesis show a linear behavior and are in close agreement with each other. However, helium volume fraction are highly overestimated at sensors near the top and underestimated at sensors near the bottom compared to experimental data.

The results obtained with 3D simulations are divided into two groups. The first group consisting of two $k-\epsilon$ models and RNG model give very similar results and they are very diffusive. They all show that the fluid at the upper half of the domain is well-mixed and become nearly homogeneous. As a result, the maximum volume fraction is highly underestimated compared to the experimental data. The second group consisting of two 3D-DNS simulations and a SST model seems to give results closest to experiment. However, the volume fraction at sensors near the top is still higher than experimental data.

The vertical profiles of helium volume fraction at 275 s are compared in Fig. 5.24. Similar to those at 115s, the results obtained with 2D axisymmetric hypothesis are very linear and close to each other. However, LES result is now more diffusive than DNS results.

The 3D results obtained with two $k-\epsilon$ models and RNG model are still very

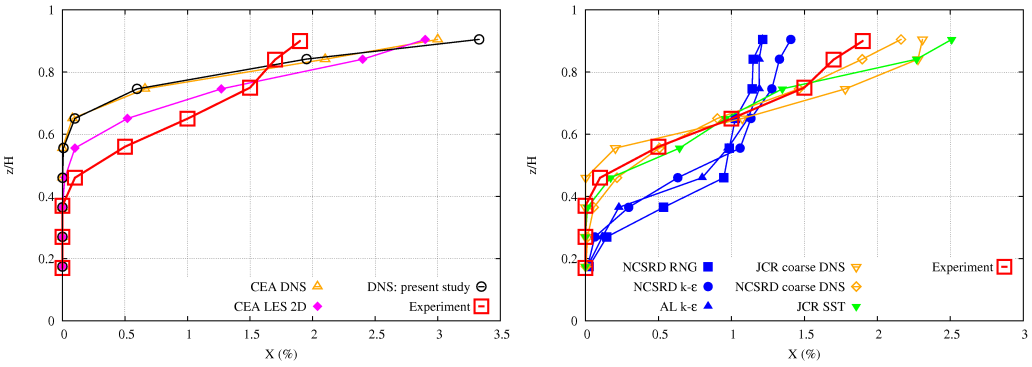

(a) With 2D axisymmetric hypothesis

(b) Without 2D axisymmetric hypothesis

Figure 5.23: Cavity 1: Vertical profiles of helium volume fraction at 115 s a) with axisymmetric hypothesis and b) without axisymmetric hypothesis (3D).

diffusive. 3D-DNS and SST results are the ones closest to experiment. However, some considerable discrepancies are observed at medium height of the cavity. In ad-

Numerical simulation	Turbulence model	Spatial discretization	Time discretization	Dimension
CEA DNS	none	3rd order finite element	BDF2, algebraic projection, implicit	2D axisymmetric
CEA LES 2D	Smagorinsky	3rd order finite element	BDF2, algebraic projection, implicit	2D axisymmetric
JCR SST	SST $k-\omega$	High resolution advection scheme	BDF2	3D
JCR DNS	none	High resolution advection scheme	BDF2	3D
NCSRD RNG	RNG $k-\epsilon$	not given	not given	3D
NCSRD DNS	none	not given	not given	3D
NCSRD $k-\epsilon$	Standard $k-\epsilon$	not given	not given	3D
AL $k-\epsilon$	Realizable $k-\epsilon$	2nd order finite volume	2nd order implicit	3D

Table 5.7: Details of other numerical simulations used for comparing with GAMELAN experimental results. ([Bernard-Michel, 2013])

dition, a thin homogeneous layer observed in the experimental data is not produced by none of these three results.

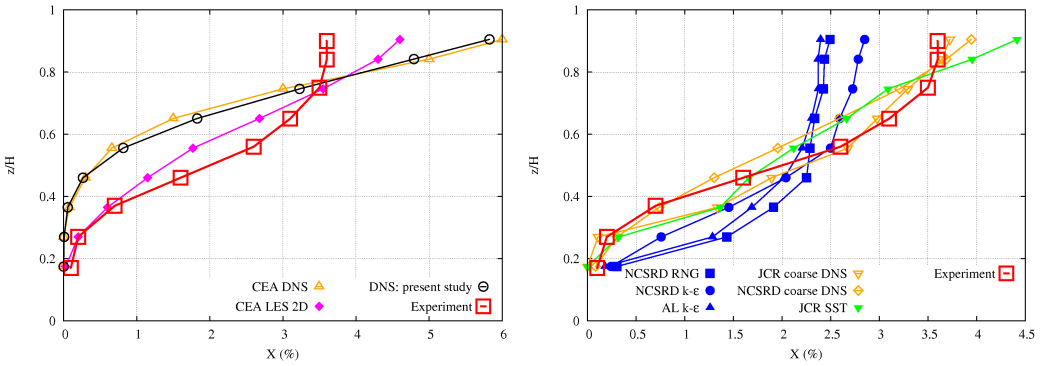

(a) With 2D axisymmetric hypothesis

(b) Without 2D axisymmetric hypothesis

Figure 5.24: Cavity 1: Vertical profiles of helium volume fraction at 275 s a) with axisymmetric hypothesis and b) without axisymmetric hypothesis (3D).

From the comparison above at 115 s and 275 s it has been shown that their is close agreement between results with axisymmetric hypothesis. By using DNS without axisymmetric hypothesis, the numerical results are improved greatly and are quite close to experimental data. We can conclude that the hypothesis of 2D axisymmetric is the origin of the linear profile and the big difference between numerical and experimental results.

5.3.5 Comparison with the model of [Worster and Huppert, 1983]

In this section we compare the DNS numerical results with the theoretical model of [Worster and Huppert, 1983] for the helium volume fraction profile during the descending fot the first front in Fig. 5.25. The time and helium volume fraction are normalized using Eqs. (1.61) and (1.64), respectively, and the normalized helium volume fraction is compared with $\delta(\zeta, \tau)$ in Eq. (1.66). Solid curves represent the helium volume fraction along the outer line passing through sensors 6 to 10. Some points are not on any curves since the helium fraction profile is not exactly one-dimensional in the cavity. This happens for the smallest cavity and for larger cavities at early times due to the instability in establishing the first front. However, when the front is well established all the points collapse on the corresponding curves. The entrainment coefficient in the normalization scheme was adjusted to give a reasonable fit of the data. It is decreasing from $\alpha = 0.17$ to $\alpha = 0.04$ for cavity 1/10 to 3/5.

In the model of Worster and Huppert [Worster and Huppert, 1983] the entrainment coefficient α is supposed to be independent of the distance from the source and is taken equal to 0.1. A review of literature in [Cariteau and Tkatschenko, 2012] shows that α vary from 0.05 to 0.1 for pure jets to pure plumes. Cariteau, in the comparison of experimental results [Cariteau and Tkatschenko, 2012] and the

model [Worster and Huppert, 1983], used α from 0.04 to 0.065. Our adjustment here is somewhat exceeding this limit. On the other hand, the trend of adjusting the entrainment coefficient α seems to contradict the literature. For cavity 1/10, the top wall is not far from the source and the buoyant jet behaves like a jet. However, $\alpha = 0.17$ is higher compared to $\alpha = 0.1$ normally taken for pure plumes in the literature. For cavity 3/5, the top wall is far from the source and the buoyant jet behaves like a plume. However, $\alpha = 0.04$ is smaller compared to $\alpha = 0.05$ normally taken for pure jets in the literature. We have not been able to explain this contradiction. Another observation is that even with the adjustment of the entrainment coefficient α, the numerical results do not seem to collapse on the theoretical curves. The profiles obtained in the numerical results are closer to linear. Our hypothesis of axisymmetric flow may be the key point of this behavior. Cariteau [Cariteau and Tkatschenko, 2012] also observed this linearity behavior in his experiment with 5 mm diameter source, while with 20 mm diameter source the solution is close to the model of [Worster and Huppert, 1983].

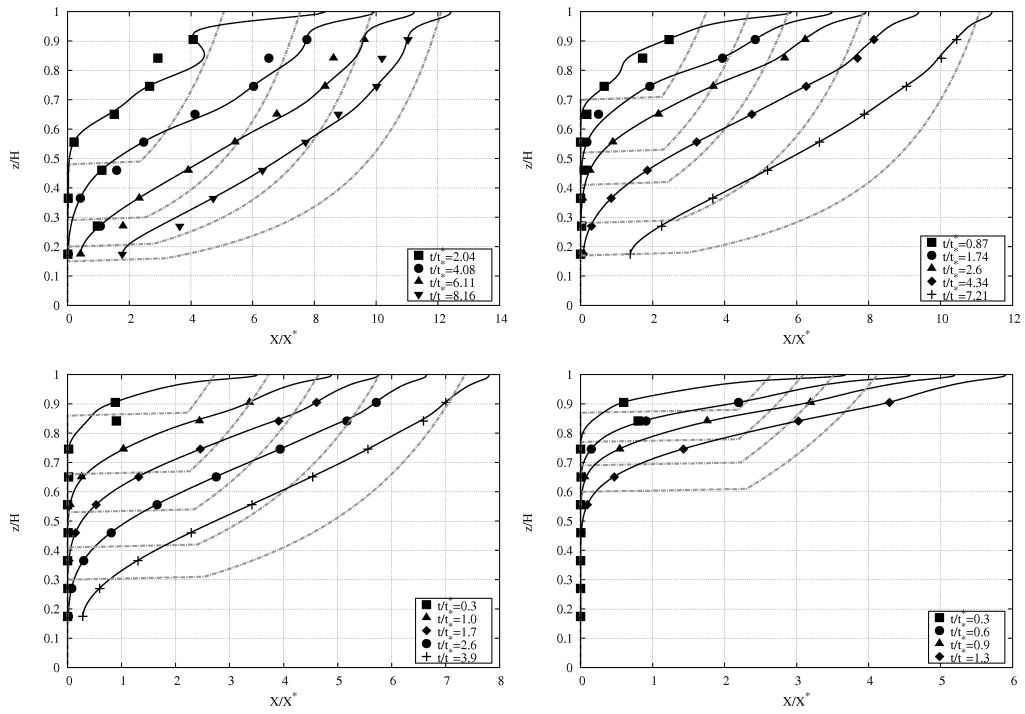

Figure 5.25: Normalized helium volume fraction variation with height, from top to bottom, left to right: cavity 1/10, $\alpha = 0.17$; cavity 1/5, $\alpha = 0.09$; cavity 2/5, $\alpha = 0.045$; cavity 3/5, $\alpha = 0.04$. Symbols represent for sensors from 2 to 10, solid curves for outer vertical lines passing through sensors 6 to 10 and dashed curves for model of Worster and Huppert [Worster and Huppert, 1983]

5.4 Conclusions

We have developed a numerical tool to simulate the mixing and dispersion of helium injected in an air-filled cavity. It is used to simulate helium-air plumes in 2D Cartesian coordinates and the scalings and similarity theory for steady laminar plane plumes have been reproduced. For the experimental configuration an assumption of axisymmetric flow has been made to reduce the dimension of the problem. Four cavities with the same aspect ratio and injection condition as the experimental set-up [Cariteau and Tkatschenko, 2012] have also been investigated.

The DNS results show almost one-dimensional profile of the helium volume fraction in the cavity, as found in the experimental results of [Cariteau and Tkatschenko, 2012]. The helium volume fraction at nine sensors have been compared with the experimental data for the full cavity and large discrepancies have been found. The maximum volume fraction at high sensors are highly overestimated. The vertical profiles of the volume fraction show that the experimental results are parabolic-like while the numerical results are close to linear. A comparison with a finite element simulation for cavity 3/5 have been made and similar results have been found. This shows that the hypothesis of axisymmetric flow which prevents the oscillation of the plume tends to laminarize the flow. In the case of full cavity, DNS results are compared with results obtained with other numerical models. It has been shown that the maximum volume fraction of the experimental data lies between those of numerical models using $k-\epsilon$ model and not using $k-\epsilon$ model. Results obtained with $k-\epsilon$ are too diffusive and homogeneous layer which extends over half of the domain is found. LES or results tend to give linear profiles. The results which are closest to experimental data were those produced by $k-\omega$ model.

The vertical helium volume fraction profiles during the descent of the initial front are compared with the model of [Worster and Huppert, 1983]. The entrainment coefficient has to be adjusted from 0.17 to 0.04. It is larger for smaller cavities and smaller for larger cavities. This seems to contradict the literature since near the source the buoyant jet behaves like a jet and α should be small, while far from the source the buoyant jet behaves like a plume and α should be larger. With the chosen α the fit with the model is not very good since the numerical profiles show a strong linearity which is not observed in the model of [Worster and Huppert, 1983]. However the linear profile of helium volume fraction has been observed in experimental results of [Cariteau and Tkatschenko, 2012] for the 5mm-diameter source.

The flow structure of different cavities sizes are investigated. It has been shown that even with the smallest cavity where $Ri_v = 0.15$ overturning does not occur and the vertical profiles of the volume fraction are close to linear. We account this linearity to the axisymmetric hypothesis we have made. It leads to the laminarization of the flow and in this case where Gr is large and the turbulent level may be important, the experimental data can not be reproduced.

Conclusion

Main results

Code development Our first results are numerical. One of the first objectives achieved within this work is the programming and the validation of a CFD code - inside Patrick Le Quéré CNRS LIMSI CFD code - in order to simulate 2D and 2D axisymetrical flows of multi-species low Mach flows. A strong effort has been made to validate the convergence of the simulations. Especially, extensive simulations have been done to test the influence of the choice of the Péclet and the CFL numbers on the calculated results.

A new and conservative treatment of the injection boundary conditions has been developed in order to prevent the apparition of numerical oscillations and to ensure conservation of the injected mass in the system. This model has been validated on references test cases.

Reference models In our process of thoroughly validating the code, we also highlighted an interesting 2D axisymetric reference case, based on Rogers and Morris (2009) experiments. Their well instrumented experiment has proven to be a good test for transient incompressible flows, with density variation. Furthermore, the Schmidt number was very high, so a stiff interface had to be modeled during the transient. Flow regime was described up to the point of instability apparition. Our numerical simulations proved to be very accurate since compared results for the ascending velocity show an agreement within the 3 % range. Our work shows that this might be used as a reference test case. Such benchmark cases remain pretty rare in the published literature.

Running parametric simulations around this experiment, we improved Rogers and Morris (2019) proposed model for the ascending velocity, exhibiting a better fitting.

On a second part, we studied 2D plane turbulent plumes with different injection regimes (flux, concentration at injection). We confirm the theoretical evolution laws of velocity versus vertical position and as well as other parameters. Turbulence is very well captured with the DNS approach.

Round turbulent plumes We simulated a round turbulent plume based on CEA GAMELAN experiments and compared the results with experiments and other CEA partners CFD calculations. The main results is that turbulence is not well capture for the 2D-axisymetric discretization. It appears that the symmetry is blocking the development of turbulent instability. Therefore, we obtain less diffusive results than those measured in the experiments.

Nevertheless, all the numerical process are in place to simulate a full 3D cavity. Only parallelization of code has to be completed in order to run such a simulation. The main interest of this phase of our work was to prepare all the tools to realize such a 3D simulation : convergence analysis, programming.

2D results are nonetheless not worse than those published with RANS models (BERNARD-MICHEL 2013) compared to the experiments. It is indeed better to overestimate the concentrations in safety calculations rather than underestimated them. Therefore the main conclusion of this section is that for the moment, only DNS (or may be LES) approach is accurate to simulate almost pure plumes in a cavity. It is advised to run axisymmetric DNS calculation rather than 3D (or 2D) RANS calculation in the perspectiveof safety calculations. The ultimate goal is to be able to achieve a 3D calculation.

Perspectives

2D plan results, for which no symmetry is applied on the axis, show strong fluctuation of the velocity and comparisons with published experimental results are excellent. One of our objective is to extend the code in order to achieve 3D calculations. It requires to extend the parallelization of the code to 3D, due to very time-consuming calculations.

The objective is to be able to extract from the velocity time-fluctuations the level of turbulence is the main area of interest : the plume, the impact location at the top wall, the impact location on the side walls, the stratified zones (to help understanding what is the mechanism of stratification in those flows).

A second objective would be to calculate, based on the time averaged velocity fields, the entrainment coefficient and its variation along the vertical axis of the plume. Correlations proposed by (CARAZZO 2008) are indeed not specifically validated yet, and based on broad past literature: fittings are accurate to roughly 25 % and are not given at distances closer that 10 diameters from the source.

If such a process proves to be successful, many other subjects of interest are at our hands: we only interested ourselves to closed cavity, but similar modeling approach still needs improvements in the field of one or multi openings cavities. The problem of the presence of obstacles and/or the problem of ventilation is hardly modeled yet. A robust method to study plumes in those situations would help to improve models.

List of Figures

1 Gémotrie de l'expérience eau-glycérol [Rogers et Morris, 2009] (figure de gauche) et du domaine de calcul (figure de droite) . . . . . .
2 Les caractéristiques principales d'un panache. . . . . .
3 a) Évolution en temps de la hauteur du panache dans le cas D4. b) a) Après translation temporelle des résultats numériques. . . . . .
4 La dépendence de Ri_h à Re_i ou à Re_i^* pour les résultats numériques. Les traits noirs et pointillés sont $Ri_h = 4.3Re_i^{-0.96}$ (a) et $Ri_h = 4.3Re_i^{*-0.96}$ (b). Le trait bleu et pointillé est $Ri_h = 3.74Re_i^{*-0.78}$. . . .
5 Vitesse ascendante du cas D4, 5 en fonction du diamètre de la cavité. v_h^f est la valeur calculée à partir de (15). v_h^r est la valeur calculée à partir d'équation 4 dans [Rogers and Morris, 2009]. . . . . .
6 Les têtes confinées pour le cas D5, 2. De la première à la dernière image de la séquence, h augmente de 20.5 cm à 35.2 cm. En haut: résultats expérimentaux: chaque image est de 5 s d'intervalle. De la première à la dernière image, la taille de la tête augmente de 1.9 cmx 2.3 cm ($l_h \times d_h$) à 2.4cmx 3.1cm. En bas: la simulation numérique: chaque image est de 8,3 s d'intervalle. De la première à la dernière image, la taille de la tÃªte augmente de 2.0cm x 2.3cm à 2.6cm x 2.8cm. . . . . .
7 Des têtes dispersées dans le cas D2. De la première à la dernière image de la séquence, h augmente de 10.4 cm à 31.0 cm. En haut: résultats expérimentaux: chaque image est de 2 s d'intervalle. La taille de la première image est $l_h = 1.6$ cm et $d_h = 2.1$ cm. En bas: chaque image est de 2 s d'intervalle. La taille de la première image est $l_h = 1.6$ cm et $d_h = 1.9$ cm . . . . . .
8 Une cavité carrée 2D avec une petite ouverture pour la dépressurisation.
9 Cas $Y_{1i} = 0.01$ avec 1024x1024 grille: a) profil de vitesse verticale le long de l'axe à $t = 6.0$, $t = 8.0$, $t = 10.0$ et $t = 12.0$ b) les profils horizontaux de densité différente à des hauteurs différentes à $t = 10.0$ avec un changement de variables:. $(\rho_a - \rho).(z - 0.0073)^{3/5}$ est tracée en fonction des $\eta = x.(z - 0.0073)^{-2/5}$. . . . . .
10 a) Installation de l'expérience de GAMELAN: vue de dessus et vue de côté ([Cariteau and Tkatschenko, 2012]) b) cavité cylindrique complet de la simulation numérique, c) Un plan axisymmétrique avec des positions de capteurs. . . . . .
11 Isocontour de tourbillon respectivement à t = 12.75, 25.25, 125.25 et 275.25 pour la cavité 1 (de gauche à droite, de haut en bas). . . . . .
12 champs de fraction de l'hélium de masse: cavité 1 à $t = 275{,}25$, 500,25 et 800,25 (de gauche à droite). . . . . .
13 Comparaison des DNS (courbes en pointillés) et éléments finis (courbes solides gras) résultats pour cavité 3/5: L'évolution temporelle du volume d'hélium fraction Y1 à (a) 5 points sur l'axe et (b) 5 points de retard sur l'axe. . . . . .

14 Cavité 1: profils verticaux de la fraction volumique d'hélium à 115 s a) avec l'hypothèse de révolution et b) sans hypothèse axisymétrique (3D) . . . .
15 Cavité 1: profils verticaux de la fraction volumique d'hélium à 275 s a) avec l'hypothèse de révolution et b) sans hypothèse axisymétrique (3D). . . . .

1.1 Examples of buoyant convection in nature. Source: Internet 5
1.2 Sketches of various convection phenomena: plumes, thermals and starting plumes. Source: [Turner, 1969] 6
1.3 Geometry and velocity variables of a steady plume (modification of Fig. 1 [Gebhart et al., 1970]) 7
1.4 Interferogram of a plume formed above a heated wire in air. Source: [Gebhart et al., 1970] 7
1.5 Computed dimensionless velocity $f^{'}$ and temperature ϕ profiles for various values of Pr for a plane plume. Source: [Gebhart et al., 1970] 9
1.6 Computed dimensionless velocity $f^{'}/\eta$ and temperture ϕ profiles for various values of Pr for a plane plume. Source: [Gebhart et al., 1988] 12
1.7 Interferograms, $L = 10in.$. Source: [Bill and Gebhart, 1975] 14
1.8 Ascent velocity of a laminar starting plume as a function of height.Source: [Kaminski and Jaupart, 2003] 17
1.9 Shape of a laminar starting plume. Source: [Shlien, 1976] 19
1.10 Relation between two parameters Re_{hl} and Re_{hw} based on the head length and head width for a confined head of a laminar starting forced plume. The ratio Re_{hl}/Re_{hw} is equal to head length/head width. Source: [Rogers and Morris, 2009] 20
1.11 Schematic representation of the flow in an enclosure with a plume source and without overturning. Source: [Cariteau and Tkatschenko, 2012] 21
1.12 Two concentration profiles of the stratified regime without homogeneous layer: a) Parabolic profile, b) Linear profile. Source: [Cariteau and Tkatschenko, 2012] 23
1.13 Comparison of the layer thickness predicted by the model of [Cleaver et al., 1994] (solid line) and the experimental results of [Cariteau and Tkatschenko, 2012] (symbols). The horizontal axis is the volume Richardson number Ri_v. Source: [Cariteau and Tkatschenko, 2012] . 24
1.14 Comparison of temperature evolution of a plume in silicone oil between numerical results (right) and laboratory experiment (left) in each snapshot. Source: [Vatteville et al., 2009] 25
1.15 The time evolution of helium volume fraction at different positions: comparison between experimental data (symbols) and various numerical results (dashed curves). Source: [Bernard-Michel et al., 2012] 26

2.1 Variation of the kinematic viscosity ν in $[m^2\ s^{-1}]$ of a helium-air mixture with helium mass fraction Y_1 at 20 ^oC. 35
2.2 Variation of the diffusion coefficient D and kinematic viscosity ν in $[m^2\ s^{-1}]$ of a glycerol-water solution with glycerol mass fraction Y_1 at 22 ^oC. 38

3.1 The domain boundary consists of four parts: solid boundary $\partial\Omega_w$, inflow boundary $\partial\Omega_i$, outflow boundary $\partial\Omega_o$ and symmetry boundary $\partial\Omega_s$. 45
3.2 Staggered location for scalar and vector quantities: $\rightarrow = u$, $\uparrow = w$, $o = p$, Y_1 and examples of their corresponding control volumes. Velocities are defined at cell boundaries while scalars are defined at cell centers. Dashed cells correspond to cells out of the computational domains. 46
3.3 Quadratic upstream interpolation for ϕ_l, $\left(\frac{\partial\phi}{\partial x}\right)_l$, ϕ_r and $\left(\frac{\partial\phi}{\partial x}\right)_r$ ([Leonard, 1979]). 47
3.4 The injection tube connecting the mass source S_m and the inflow boundary $\partial\Omega_i$. 54
3.5 Comparison between the diffusive flux and convective flux of helium at the inflow boundary for a helium-air plume. 55
3.6 Control volumes corresponding to fine and coarse grids in multigrid method. 59

4.1 Geometry of the glycerol-water plume experiment of [Rogers and Morris, 2009] (left) and the computational domain (right). 66
4.2 Case D4,5: time evolution of the plume presented by glycerol mass fraction field from $t = 0.1$ to $t = 4.0$. The time interval between two consecutive images is 0.5. The reference time is $t_r = 8.9s$ 68
4.3 Mass fraction of glycerol along the centerline in case D4,5. 69
4.4 The shape of the plume at $t = 4.0$ in case D4,5: a) for different values of the threshold ϵ for the identification factor id. A point (x, y) is defined to be in the plume if $id = \frac{Y_{1a} - Y_1(x,z)}{Y_{1a} - Y_{1i}} > \epsilon$. b) for $\epsilon = 0.2$. . . 70
4.5 The main characteristics of a plume. 70
4.6 Case D4,5: a) Time evolution of the plume's elevation above the source, b) Time evolution of the plume ascent velocity. 72
4.7 a) The plume at $t = 4.0$, b) vertical velocity along the centerline in case D4,5. 72
4.8 Streamlines on top of a) mass fraction field, b) vorticity field at $t = 4.0$ in case D4,5. 73
4.9 Case D4,5: Radial profile of vertical velocity at $t = 4.0$ at different z-positions. 74
4.10 Case D4,5: radial profile of horizontal velocity at $t = 4.0$ at different z-positions. 75
4.11 Comparison of constant viscosty model and variable viscosity model for case D4,5: a) Vertical velocity along the centerline at $t = 3.0$, b) Time evolution of the plume height above the source 76
4.12 Comparison of CENTER scheme and QUICK scheme for the convection term in the equation for Y_1 for case D4,5: a) Vertical velocity along the centerline at $t = 3.0$, b) Glycerol mass fraction along the centerline at $t = 3.0$ 77
4.13 Case D4,5: Mass fraction of glycerol Y_1 along the centerline at $t = 3.0$ with different grids. 78
4.14 Case D4,5: Time evolution of the maximum horizontal velocity. . . 79

4.15 Case D4,5: Plume head represented by the glycerol mass fraction Y_1 at $t = 3.0$ with 6 grids. Contour levels [0.78:0.005:0.82] 81
4.16 Case D2: Plume head represented by the glycerol mass fraction Y_1 at $t = 3.0$ with 6 grids. Contour levels [0.669:0.001:0.685] 83
4.17 a) The plume shape in case D5,1 in Fig. 1 of [Rogers and Morris, 2009], b) The numerical result at $t = 58.7s$: $h = 19.23cm$, $d_h = 1.97cm$, $l_h = 1.72cm$ and $d_c = 0.66cm$. 84
4.18 Time evolution of the plume height for five plumes in case D4. Lines with points are for the experimental data ([Rogers and Morris, 2009]) and plain solid lines with the same colors are for the corresponding numerical results. The slope of a plain solid line is the constant ascent velocity w_h of each plume. 85
4.19 a) Experimental apparatus, b) Figure 4.18 after shifting numerical results according to Table 4.9. 87
4.20 The dependence of the head Richardson number Ri_h on the injection Reynolds number for the numerical results of 13 plumes. The black dotted lines are $Ri_h = 4.3Re_i^{-0.96}$ (a) and $Ri_h = 4.3Re_i^{*-0.96}$ (b). The blue dotted line is $Ri_h = 3.74Re_i^{*-0.78}$. 88
4.21 a) Vertical velocity along the centerline in case D4,5 at $t = 4.0$ with different cavity diameters, b) Ascent velocity of case D4,5 as a function of cavity diameter. v_h^f is the value calculated from (4.12). v_h^r is the value calculated from (4.3). 89
4.22 Confined heads in case D5,2. From the first to last image in the sequence, h increases from 20.5 cm to 35.2 cm. Top: experimental results: each image is 5 s apart. From the first to last image, the size of the head increases from $1.9cm$x $2.3cm$ ($l_h \times d_h$) to $2.4cm$x $3.1cm$. Bottom: numerical simulation: each image is 8.3 s apart. From the first to last image, the size of the head increases from $2.0cm$x $2.3cm$ to $2.6cm$x $2.8cm$. 90
4.23 Dispersed heads in case D2. From the first to last image in the sequence, h increases from 10.4 cm to 31.0 cm. Top: experimental results: each image is 2 s apart. The size of the first image is l_h=1.6 cm and d_h=2.1 cm. Bottom: each image is 2 s apart. The size of the first image is l_h=1.6 cm and d_h=1.9 cm. 92
4.24 Time evolution of plume heads in case D4. 93
4.25 Time evolution of plume heads in case D1. 94
4.26 Head width as a function of head length for D4 set of plumes : a) Numerical results, b) Fig. 5 of [Rogers and Morris, 2009]. 96
4.27 D4 set of plumes: Evolution of the head aspect ratio with the plume height. 96
4.28 Head width as a function of head length for D1 set of plumes: a) Numerical results, b) Fig. 7 of [Rogers and Morris, 2009] 97
4.29 D1 set of plumes: Evolution of the head aspect ratio with the plume height 97
4.30 Evolution of the head aspect ratio with the plume height for a) Case D2, b) Case D5 98

4.31 Resutls for case D4, $Q = 4.0 \times 10^{-7} m^3/s$: Evolution of the head aspect ratio RF_h with the plume height with different cavity diameters. 98

5.1 A 2D square cavity with a small opening for depressurization. 103
5.2 Case $Y_{1i} = 0.01$ with 512x512 grid: Time evolution of vorticity distribution. Contour levels of ω [-10:0.5:10] 104
5.3 $Y_{1i} = 0.01$: Density distribution at $t = 10.0$ with three grids: a) 256x256, b) 512x512, c) 1024x1024. Contour levels of ρ [0.94:0.00125:1.0] 105
5.4 $Y_{1i} = 0.1$: Density distribution at $t = 10.0$ with 3 grids: a) 512x512, b) 1024x1024 and c) 1536x1536. Contour levels of ρ [0.62:0.005:1.0] . 106
5.5 $Y_{1i} = 1$: Density distribution at different times with 1536x1536 grid: . Contour levels [0.14:0.01:1.0] 106
5.6 Case $Y_{1i} = 0.01$ with 1024x1024 grid: a) Vertical velocity profile along the centerline at 4 different times: $t = 6.0$, $t = 8.0$, $t = 10.0$, $t = 12.0$ and b) at $t = 12.0$. 107
5.7 Case $Y_{1i} = 0.01$ with 1024x1024 grid: a) Profile of density difference along the centerline at 4 different times: $t = 6.0$, $t = 8.0$, $t = 10.0$, $t = 12.0$ and b) at $t = 12.0$. 108
5.8 $Y_{1i} = 0.01$ with 1024x1024 grid: a) Horizontal profile of vertical velocity at different heights at $t = 10.0$; b) The curves in a) with a change of variables: $w.(z - 0.0077)^{-1/5}$ is plotted as a function of $\eta = x.(z - 0.0077)^{-2/5}$ 109
5.9 $Y_{1i} = 0.01$ with 1024x1024 grid: a) Horizontal profile of density difference at different heights at $t = 10.0$; b) The curves in a) with a change of variables: $(\rho_a - \rho).(z - 0.0073)^{3/5}$ is plotted as a function of $\eta = x.(z - 0.0073)^{-2/5}$. 110
5.10 $Y_{1i} = 0.1$ with 1024x1024 grid: a) Vertical velocity profile along the centerline at 4 different times: $t = 6.0$, $t = 8.0$, $t = 10.0$, $t = 11.0$ and b) at $t = 10.0$ 110
5.11 $Y_{1i} = 0.1$ with 1024x1024 grid: a) Profile of density difference along the centerline at 4 different times: $t = 6.0$, $t = 8.0$, $t = 10.0$, $t = 11.0$ and b) at $t = 10.0$. 111
5.12 $Y_{1i} = 0.1$ with 1024x1024 grid: a) Horizontal profile of vertical velocity at different heights at $t = 10.0$; b) The curves in a) with a change of variables: $w.(z - 0.0108)^{-1/5}$ is plotted as a function of $\eta = x.(z - 0.0108)^{-2/5}$. 112
5.13 $Y_{1i} = 0.1$ with 1024x1024 grid: a) Horizontal profile of density difference at different heights at $t = 10.0$; b) The curves in a) with a change of variables: $(\rho_a - \rho).(z - 0.0004)^{3/5}$ is plotted as a function of $\eta = x.(z - 0.0004)^{-2/5}$. 112
5.14 The experimental set-up of GAMELAN experiment : top view (left) and side view (center) ([Cariteau and Tkatschenko, 2012]). 114
5.15 The full cavity of numerical simulation: a) The full shape, b) A plane of axisymmetry with positions of sensors. 115
5.16 Vorticity isocontour respectively at t=1.5, 2.5, 3, 5.5, 10.5, 15.5, 20.5 and 25.5 for cavity 1/10 (from left to right, top to bottom). 117

5.17 Vorticity isocontour respectively at t= 6.5, 7.75, 12.75, 25.25, 62.75, 125.25, 200.25 and 275.25 for cavity 1 (from left to right, top to bottom). 118
5.18 Helium mass fraction fields: Cavity 1/10 at t = 5.5, 15.5 and 25.5; Cavity 1/5 at t =10.5, 50.5 and 150.5; c) Cavity 2/5 at t = 25.5, 100.5 and 275.5; Cavity 3/5 at t = 50.5, 200.5 and 350.5; Cavity 1 at t = 275.25, 500.25 and 800.25 (from left to right). 119
5.19 Cavity 3/5: Time evolution of vertical velocity w at 5 points on the axis (a) A6 (square), A7 (circle), A8 (up triangle), (b) A9 (down triangle), A10 (diamond): comparison of DNS and finite element results. DNS results are denoted by dashed lines and finite element results by bold solid lines 120
5.20 Cavity 3/5: Time evolution of helium volume fraction Y_1 at (a) 5 points on the axis A6 (square), A7 (circle), A8 (up triangle), A9 (down triangle), A10 (diamond) and (b) 5 points 6 (square), 7 (circle), 8 (up triangle), 9 (down triangle), 10 (diamond) off the axis: comparison of DNS and finite element results. DNS results are denoted by dashed lines and finite element results by bold solid lines . 121
5.21 Vorticity isocontour respectively at t=4, 20, 46, 139 for cavity 3/5 (from left to right). 121
5.22 Cavity 1: Time evolution of helium volume fraction at a) sensors 6 (square), 7(circle) , 8 (up triangle), 9 (down triangle), 10 (diamond), b) sensors 2 (square), 3 (circle), 4 (up triangle), 5 (down triangle) : comparison between DNS results (dashed lines) and experimental data of GAMELAN (bold solid lines). 122
5.23 Cavity 1: Vertical profiles of helium volume fraction at 115 s a) with axisymmetric hypothesis and b) without axisymmetric hypothesis (3D). 123
5.24 Cavity 1: Vertical profiles of helium volume fraction at 275 s a) with axisymmetric hypothesis and b) without axisymmetric hypothesis (3D). 124
5.25 Normalized helium volume fraction variation with height, from top to bottom, left to right: cavity 1/10, $\alpha = 0.17$; cavity 1/5, $\alpha = 0.09$; cavity 2/5, $\alpha = 0.045$; cavity 3/5, $\alpha = 0.04$. Symbols represent for sensors from 2 to 10, solid curves for outer vertical lines passing through sensors 6 to 10 and dashed curves for model of Worster and Huppert [Worster and Huppert, 1983] 125

A.1 Cavity 1/10: Time evolution of helium volume fraction at sensors 6 to 10 with 50x98, 74x146 and 110x218 grids at t =10, 20, 30, 40, 50, 60, 80, 90 and 100. 140
A.2 Cavity 1/5: Time evolution of helium volume fraction at sensors 6 to 10 with 66x130, 98x194 and 146x290 grids at t =25, 50, 75, 100, 125, 150, 175, 200, 225 and 250. 140
A.3 Cavity 2/5: Time evolution of helium volume fraction at sensors 6 to 10 with 98x194, 146x290 and 218x434 grids at t =50, 100, 150 and 200. 141

A.4 Cavity 3/5: Time evolution of helium volume fraction at sensors 6 to 10 with 146x290 and 218x434 grids at t = 49.5, 99.5, 149.5, 199.5, 274.3, 349.3 and 424.3. 141
A.5 Cavity 1: Time evolution of helium volume fraction at sensors 6 to 10 with 218x434 and 322x642 grids at t = 50, 100, 150, 200, 274.8, 349.8, 424.8 and 499.8. 142

List of Tables

1 Propriétés physiques des cas tests glycerol-eau du panache forcé: ρ_a et ρ_i sont en $[kg\ m^{-3}]$, ν_a et ν_i sont en 10^{-6} $[m^2\ s^{-1}]$. . . . . .
2 Débit volumique et paramètres adimensionnés des cas tests glycérol-eau du panache forcé. . . . . .
3 Types de têtes obtenues avec des simulations numériques pour 13 plumes glycérol-eau. . . . . .
4 Paramètres des trois situations d'injection des plumes hélium-air. . .
5 Propriétés physiques des simulations des panaches rondes d'hélium-air.

2.1 Parameters in the Chapman-Enskog's formula for helium and air ([Bird et al., 2001]) and dynamic viscosities of helium and air at 20^oC. 35
2.2 Parameters in the free volume models for pure water ([He et al., 2006]). 37
2.3 Parameters in the free volume models for aqueous solution of glycerol ([He et al., 2006]). 37

3.1 Performance of the code on Linux platform Intel (R) Xeon (R) CPU X5675 @3.07 GHz. 60

4.1 Notations 64
4.2 Physical properties of the simulated test cases of glycerol-water forced plumes: ρ_a and ρ_i are in $[kg\ m^{-3}]$, ν_a and ν_i are in 10^{-6} $[m^2\ s^{-1}]$. . 67
4.3 Injection volume flux and dimensionless parameters of the simulated test cases of glycerol-water forced plumes 67
4.4 Results of case D4,5: Plume characteristics at $t = 4.0$ for different values of ϵ. 71
4.5 Case D4,5: Comparison of steady properties for 6 grids. 80
4.6 Case D4,5: Comparison of transient properties at $t = 3.0$ for 6 grids. 80
4.7 Case D2: Comparison of steady properties for 6 grids. 82
4.8 Case D2: Comparison of transient properties at $t = 3.0$ for 6 grids. . 82
4.9 Case D4 of glycerol-water plumes: Time shift between experimental data and numerical results. 86
4.10 Case D4 of glycerol-water plumes: Comparison of the ascent velocities obtained from numerical simulations (w_h) and data extraction from Fig. 2 in [Rogers and Morris, 2009] (w_h^e). 88
4.11 Case D4,5: Comparison of ascent velocity v_h with values predicted by formula (4.12)(v_h^f) and (**??**) (v_h^r) for cavities with a height of 502 mm and different diameters. 89
4.12 Summary of the types of heads obtained with numerical simulations for 13 glycerol-water starting plumes. 95

5.1 Physical properties of three injection situations of helium-air plumes. 103
5.2 Parameters of three injection situations of helium-air plumes. 103

5.3 Geometry parameters (in *meter*) of GAMELAN experiment ([Cariteau and Tkatschenko, 2012]). 113
5.4 Positions of ten thermocouples (sensors) in GAMELAN experiment ([Cariteau and Tkatschenko, 2012]): r_{out} is the distance between thermocouples and the vertical wall nearest to them, z is the distance from the thermocouples to the floor. 114
5.5 Physical properties of the helium-air round plume simulations. . . . 116
5.6 Helium-air axisymmetric plume simulations: dimensionless parameters, mesh size, time step and transitional time t_c for the inflow boundary conditions. 116
5.7 Details of other numerical simulations used for comparing with GAMELAN experimental results. ([Bernard-Michel, 2013]) 123

A.1 Grids used for grid convergence study of helium-air round plume simulations. 139

Appendix A

Grid convergence study of helium-air round plume simulations

We investigate the influence of the grid size on helium volume fraction at sensors 6 to 10. From this the suitable grid size for each cavity is determined. For cavities 1/10, 1/5, 2/5 three grids are used. For cavities 3/5 and 1 only 2 grids are used due to the long time running the simulation. The grid sizes are listed in Table A.1.

The comparison of the solutions on different grids are presented in Figs. A.1-A.5. In all the situations, the difference between solutions of different grids is quite small and are mainly at the early time. It decreases when the time evolves. In some cases, small grids give rise to numerical oscillation in the solution. The grids chosen for each cavity ensure that the solution is free of any numerical oscillation and the differences with the solutions at larger grids are small.

Cavity	Grids used	Grid chosen	Time step
1/10	50x98, 74x146, 98x194	74x146	min: 10^{-4}, max: 1.5×10^{-4}
1/5	66x130, 98x194, 146x290	98x194	min: 10^{-4}, max: 1.5×10^{-4}
2/5	98x194, 146x290, 218x434	146x290	min: 10^{-4}, max: 1.5×10^{-4}
3/5	146x290, 218x434	218x434	min: 10^{-4}, max: 1.5×10^{-4}
1	218x434, 322x642	322x642	min: 5×10^{-5}, max: 1.5×10^{-4}

Table A.1: Grids used for grid convergence study of helium-air round plume simulations.

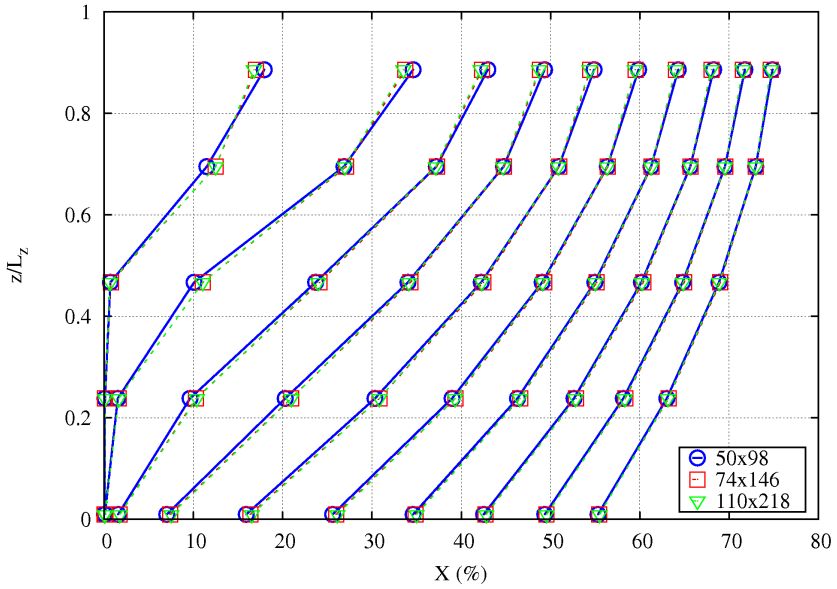

Figure A.1: Cavity 1/10: Time evolution of helium volume fraction at sensors 6 to 10 with 50x98, 74x146 and 110x218 grids at t =10, 20, 30, 40, 50, 60, 80, 90 and 100.

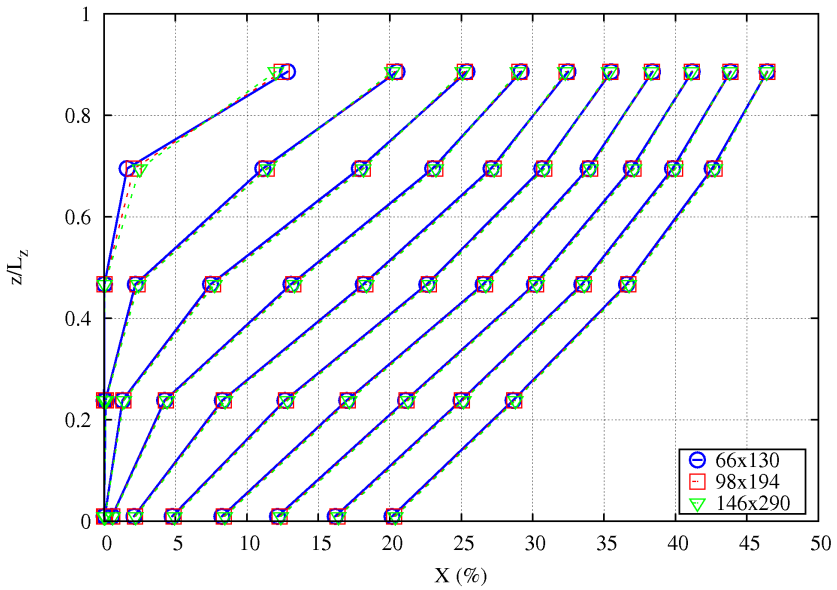

Figure A.2: Cavity 1/5: Time evolution of helium volume fraction at sensors 6 to 10 with 66x130, 98x194 and 146x290 grids at t =25, 50, 75, 100, 125, 150, 175, 200, 225 and 250.

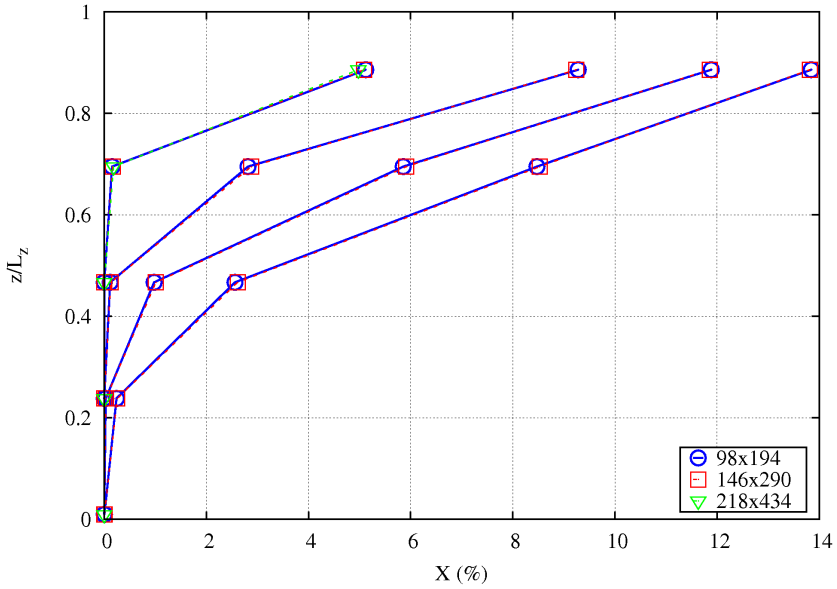

Figure A.3: Cavity 2/5: Time evolution of helium volume fraction at sensors 6 to 10 with 98x194, 146x290 and 218x434 grids at t =50, 100, 150 and 200.

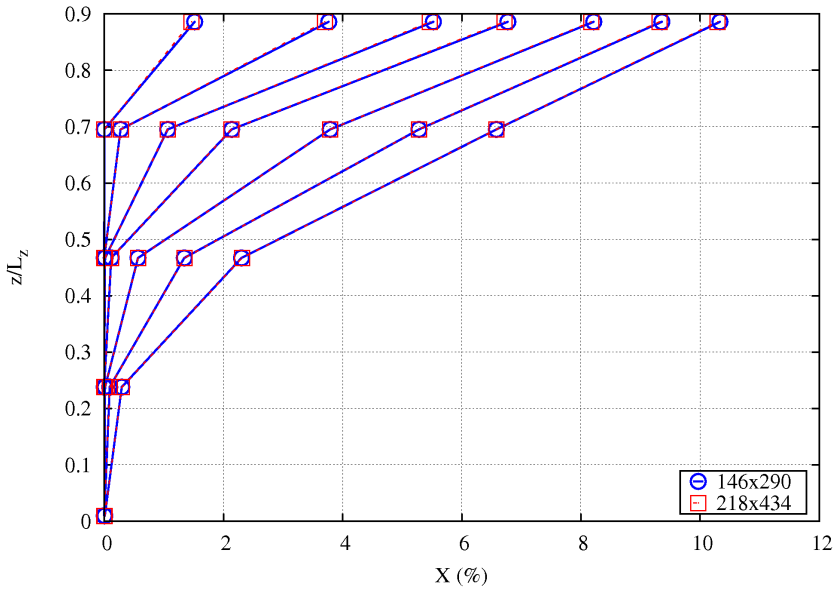

Figure A.4: Cavity 3/5: Time evolution of helium volume fraction at sensors 6 to 10 with 146x290 and 218x434 grids at t = 49.5, 99.5, 149.5, 199.5, 274.3, 349.3 and 424.3.

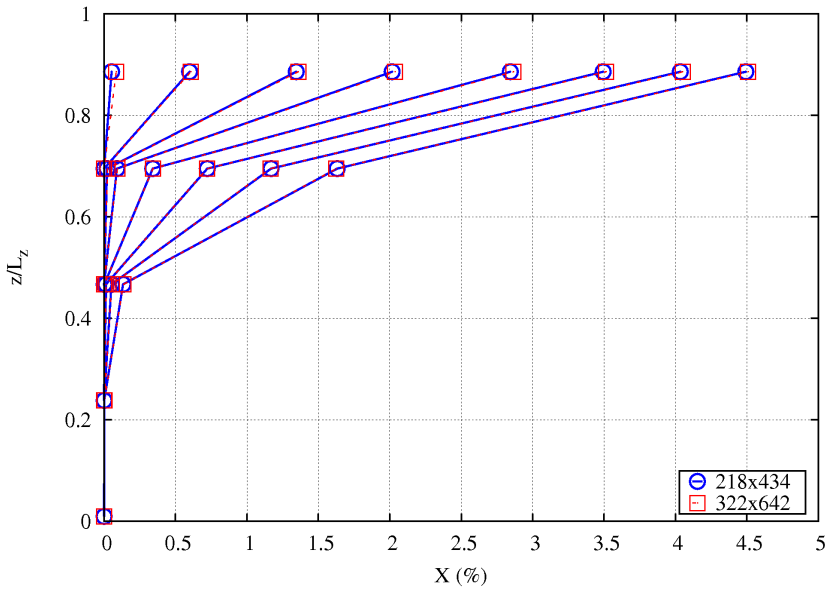

Figure A.5: Cavity 1: Time evolution of helium volume fraction at sensors 6 to 10 with 218x434 and 322x642 grids at t = 50, 100, 150, 200, 274.8, 349.8, 424.8 and 499.8.

Bibliography

[Ascher et al., 1995] Ascher, U. M., Ruuth, S. J., and Wetton, B. T. R. (1995). Implicit-explicit methods for time-dependent partial differential equations. *SIAM J. Numer. Anal.*, 32(3).

[Baines and Turner, 1969] Baines, W. D. and Turner, J. S. (1969). Turbulent buoyant convection from a source in confined regions. *J. Fluid Mech.*, 37.

[Bastiaans et al., 2000] Bastiaans, R. J. M., Rindt, C. C. M., Nieuwstadt, F. M. T., and van Steenhoven, A. A. (2000). Direct and large-eddy simulation of the transition of two- and three-dimensional plane plumes in a confined enclosure. *Int. J. Heat Mass Transfer*, 43.

[Batchelor, 1954] Batchelor, G. K. (1954). Heat convection and buoyancy effects in fluids. *Quarterly Journal of the Royal Meteorological Society*, 80(345):339–358.

[Bernard-Michel, 2013] Bernard-Michel, G. (2013). Personal communication. in print for ichs5 conference. *ICHS5*.

[Bernard-Michel et al., 2012] Bernard-Michel, G., Trochon, J., Vyazmina, E., and Gentilhomme, O. (2012). Resultat du benchmark ventilation sur 3 essais gamelan dans le cadre du projet anr dimitrhy. Technical Report DEN/DANS/DM2S/STMF/LIEFT/RT/12/020/A., CEA Saclay DEN/DANS/DM2S/STMF/LIEFT.

[Bill and Gebhart, 1975] Bill, R. G. and Gebhart, B. (1975). The transition of plane plumes. *Int. J. Heat Mass Transfer*, 18.

[Bird et al., 2001] Bird, R. B., Stewart, W. E., and Lightfoot, E. N. (2001). *Transport phenomena*. John Wiley & Sons.

[Briggs et al., 2000] Briggs, W. L., McCormick, S., and Henson, V. (2000). *A Multigrid Tutorial*. SIAM, second edition.

[Brodowics and Kierkus, 1966] Brodowics, K. and Kierkus, W. T. (1966). Experimental investigation of laminar free-convection flow in air above horizontal wire with constant heat flux. *Int. J. Heat Mass Transfer*, 9.

[Carazzo et al., 2006] Carazzo, G., Kaminski, E., and Tait, S. (2006). The route to self-similarity in turbulent jets and plumes. *Journal of Fluid Mechanics*, 547.

[Cariteau and Tkatschenko, 2012] Cariteau, B. and Tkatschenko, I. (2012). Experimental study of the concentration build-up regimes in an enclosure without ventilation. *International Journal of Hydrogen Energy*, 37.

[Chen and Rodi, 1980] Chen, C. J. and Rodi, W. (1980). *Vertical turbulent buoyant jets: A review of experimental data*. London/Newyork: Pergamon.

[Cheng, 2008] Cheng, N. S. (2008). Formula for viscosity of glycerol-water mixture. *Engineering Chemistry Research*, 47.

[Chorin, 1968] Chorin, A. J. (1968). Numerical solution of the navier-stokes equations. *Math. Comp.*, 22:745–762.

[Chu and Goldstein, 1973] Chu, T. Y. and Goldstein, J. R. (1973). Turbulent convection in a horizontal layer of water. *Journal of Fluid Mechanics*, 60.

[Cleaver et al., 1994] Cleaver, R. P., Marshall, M. R., and Linden, P. F. (1994). The build-up of concentration within a single enclosed volume following a release of natural gas. *J. Hazard. Mater.*, 36.

[Desrayaud and Lauriat, 1993] Desrayaud, G. and Lauriat, G. (1993). Unsteady confined buoyant plumes. *Journal of Fluid Mech.*, 252.

[Errico et al., 2004] Errico, G. D., Ortona, O., Capuano, F., and Vitagliano, V. (2004). Diffusion coefficients for the binary system glycerol + water at 25oc. a velocity correlation study. *J. Chem. Eng. Data*, 49.

[Forstrom and Sparrow, 1967] Forstrom, R. J. and Sparrow, E. M. (1967). Experiments on the buoyant plumes above a heated horizontal wire. *Int. J. Heat Mass Transfer*, 10.

[Fujii, 1963] Fujii, T. (1963). Theory of the steady laminar natural convection above a horizontal line heat source and a point heat source. *Int. J. Heat Mass Transfer*, 6.

[Fujii et al., 1973] Fujii, T., Morioka, I., and Uehara, H. (1973). Buoyant plume above a horizontal line heat source. *Int. J. Heat Mass Transfer*, 16.

[Gebhart et al., 1988] Gebhart, B., Jaluria, Y., Mahajan, R. L., and Sammakia, B. (1988). *Buoyancy-induced flows and transport*. Hemisphere Publishing Corporation, New York.

[Gebhart et al., 1970] Gebhart, B., Pera, L., and Schorr, A. W. (1970). Steady laminar natural convection plumes above a horizontal line heat source. *Int. J. Heat Mass Transfer*, 13.

[Germeles, 1975] Germeles, A. E. (1975). Forced plumes and mixing of liquids in tanks. *J. Fluid Mech.*, 71:601–623.

[Griffiths and Campbell, 1990] Griffiths, R. W. and Campbell, I. H. (1990). Stirring and structure in mantle starting plumes. *Earth and Planetary Science Letters*, 99(1-2):66–78.

[H. J. Nawoj, 1977] H. J. Nawoj, R. S. H. (1977). An experimental investigation of the plume velocity field above a horizontal line heat source. *J. Heat Transfer*, 99(4).

[Harlow and Welch, 1965] Harlow, F. H. and Welch, J. E. (1965). Numerical calculation of time-dependent viscous incompressible flow of fluid with free surface. *Physics of Fluids*, 8(12):2182–2189.

[He et al., 2006] He, X., Fowler, A., and Toner, M. (2006). Water activity and mobility in solutions of glycerol and small molecular weight sugars: Implication for cryo- and lyopreservation. *J. Appl. Phys.*, 100(074702).

[Humphreys et al., 1952] Humphreys, H. W., Rousse, H., and Yih, C. S. (1952). Gravitational convection from a boundary source. *Tellus*, 4.

[Joseph et al., 1996] Joseph, D. D., Huang, A., and Hu, H. (1996). Non-solenoidal velocity effects and korteweg stresses in simple mixtures of incompressible liquids. *Physica D*, 97:104–125.

[Jr. et al., 1977] Jr., W. K. G., Alpert, R. L., and Tamanini, F. (1977). Turbulence measurements in an axisymmetric buoyant plume. *International Journal of Heat and Mass Transfer*, 20(11):1145 – 1154.

[Kaminski and Jaupart, 2003] Kaminski, E. and Jaupart, C. (2003). Laminar starting plumes in high-prandtl-number fluids. *Journal of Fluid Mechanics*, 478.

[Kan, 1986] Kan, J. V. (1986). A second-order accurate pressure-correction scheme for viscous incompressible flow. *SIAM J. Sci. Stat. Comput.*, 7(3).

[Keken et al., 2013] Keken, P., Davaille, A., and Vatteville, J. (2013). Dynamics of a laminar plume in a cavity: The influence of boundaries on the steady state stem structure. *Geochemistry, Geophysics, Geosystems*.

[Leonard, 1979] Leonard, B. (1979). A stable and accurate convective modelling procedure based on quadratic upstream interpolation. *Computer Methods in Applied Mechanics and Engineering*, 19(1):59 – 98.

[Lowesmith et al., 2009] Lowesmith, B. J., Hankinson, G., Spataru, C., and Stobbart, M. (2009). Gas build-up in a domestic property following releases of methane/hydrogen mixture. *Int. J. Hydrogen Energy*, 34.

[Lyakhov, 1970] Lyakhov, Y. N. (1970). Experimental investigation of free convection above a heated horizontal wire. *J. Appl. Mech. Tech. Phys.*, 11.

[Morton et al., 1956] Morton, B. R., Taylor, G., and Turner, J. S. (1956). Turbulent gravitational convection from maintained and instantaneous sources. *Proceedings of the Royal Society of London. Series A, Mathematical and Physical Sciences*, 234(1196).

[Moses et al., 1993] Moses, E., Zocchi, G., and Libchaber, A. (1993). An experimental study of laminar plumes. *J. Fluid Mech.*, 251.

[Nakagome and Hirata, 1976] Nakagome, H. and Hirata, M. (1976). The structure of turbulent diffusion in an axisymmetrical plume. *Proceeding ICHMT1976 Seminar on Turbulent Buoyant Convection.*, pages 361–372.

[Neufeld et al., 1972] Neufeld, P. D., Janzen, A. R., and Aziz, R. A. (1972). Empirical equations to calculate 16 of the transport collision integrals for the lennard-jones (12-6) potential. *J. Chem. Phys.*, 57:1100–1102.

[Orlandi, 1990] Orlandi, P. (1990). Vortex dipole rebound from a wall. *Phys. Fluids A*, 2(8).

[Papanicolaou and List, 1988] Papanicolaou, P. N. and List, E. J. (1988). Investigations of round vertical turbulent buoyant jets. *J. Fluid Mech.*, 195.

[Patankar, 1980] Patankar, S. V. (1980). *Numerical heat transfer and fluid flow.* Hemisphere Series on Computational methods in Mechanics and thermal science.

[Peaceman and Rachford, 1955] Peaceman, D. W. and Rachford, H. H., J. (1955). The numerical solution of parabolic and elliptic differential equations. *Journal of the Society for Industrial and Applied Mathematics*, 3(1):pp. 28–41.

[Railston, 1954] Railston, W. (1954). The temperature decay law of a naturally convected air stream. *Proc. Phys. Soc. B*, 67(1).

[Rogers and Morris, 2009] Rogers, M. C. and Morris, S. W. (2009). Natural versus forced convection in laminar starting plumes. *Physics of Fluids*, 21.

[Schlichting, 1933] Schlichting, H. (1933). Laminare strahlausbreitung. *Z. Angew. Math. Mech.*, 13.

[Shlien, 1976] Shlien, D. J. (1976). Some laminar thermal and plume experiments. *Physics of Fluids*, 19.

[Shlien, 1978] Shlien, D. J. (1978). Transition of the axisymmetric starting plume cap. *Physics of Fluids*, 21.

[Shlien and Boxman, 1979] Shlien, D. J. and Boxman, R. L. (1979). Temperature field measurement of an axisymmetric laminar plume. *Physics of Fluids*, 22.

[Solomon and Gollub, 1990] Solomon, T. H. and Gollub, J. P. (1990). Sheared boundary layers in turbulent rayleigh-bénard convection. *Phys. Rev. Lett.*, 64:3102–3102.

[Taylor and Krishna, 1993] Taylor, R. and Krishna, R. (1993). *Multicomponent mass transfer.* John Wiley & Sons.

[Thomas, 1949] Thomas, L. H. (1949). Elliptic Problems in Linear Differential Equations over a Network. Technical report, Columbia University.

[Tollmien, 1926] Tollmien, W. (1926). Berechnung turbulenter ausbreitungsvorgange. *Z. Angew. Math. Mech.*, 6.

[Turner, 1962] Turner, J. S. (1962). The starting plume in neutral surroundings. *J. Fluid Mech.*, 13:356–368.

[Turner, 1969] Turner, J. S. (1969). Buoyant plumes and thermals. *ANNUAL REVIEW OF FLUID MECHANICS*, 1:29–44.

[Turner, 1973] Turner, J. S. (1973). *Buoyancy effects in fluids.* Cambridge University Press.

[van Heijst and Flor, 1989] van Heijst, G. and Flor, J. (1989). Dipole formation and collisions in a stratified fluid. *Nature*, 340.

[van Keken, 1997] van Keken, P. (1997). Evolution of starting mantle plumes: a comparison between numerical and laboratory models. *Earth and Planetary Science Letters*, 148(1-2):1–11.

[Vatteville et al., 2009] Vatteville, J., van Keken, P. E., Limare, A., and Davaille, A. (2009). Starting laminar plumes: Comparison of laboratory and numerical modeling. *Geochemistry, Geophysics, Geosystems*, 10(12).

[Venetsanos et al., 2010] Venetsanos, A. G., Papanikolaou, E., Cariteau, B., Adams, P., and Bengaouer, A. (2010). Hydrogen permeation from cgh2 vehicles in garages: Cfd dispersion calculations and experimental validation. *Int. J. Hydrogen Energy*, 35.

[Wilke, 1950] Wilke, C. R. (1950). A viscosity equation for gas mixture. *The journal of chemical physics*, 18(4).

[Worster and Huppert, 1983] Worster, M. G. and Huppert, H. E. (1983). Time-dependent density profiles in a filling box. *J. Fluid Mech.*, 132.

[Zeldovich, 1937] Zeldovich, Y. B. (1937). The asymptotic laws of freely-ascending convective flows. *Zh. Eksp. Teor. Fiz.*, 7.

[Zocchi et al., 1990] Zocchi, G., Moses, E., and Libchaber, A. (1990). Coherent structures in turbulent convection, an experimental study. *Physica A: Statistical Mechanics and its Applications*, 166(3):387 – 407.

Huong-Lan TRAN

Numerical modeling of natural convection of binary mixtures: case of a helium buoyant jet in an air-filled enclosure

Résumé

Ce travail porte sur l'étude des mécanismes de mélange et dispersion d'un jet d'hélium dans une cavité semi-confinée remplie d'air. Ce phénomène est pris comme un cas modèle de l'injection d'un gaz léger dans un fluide lourd produisant un panache. Ce thème est en lien avec les questions de sécurité des systèmes basés sur l'hydrogène. Un modèle numérique a été développé combinant les conditions limites adéquates avec les équations de conservation de la masse (mélange et une espèce), de la quantité de mouvement, ainsi que la loi d'état et la variation des propriétés physiques en fonction du mélange. En premier lieu, le panache d'un mélange eau glycérol est considéré comme cas de validation par comparaison avec des résultats expérimentaux [Rogers & Morris 09]. Le développement d'un panache axisymétrique est modélisé pour de grands nombres de Grashof et petit nombres de Reynolds d'injection. Un bon accord est obtenu pour la vitesse d'ascension du panache ainsi que le type et la forme de la tête. Une loi d'échelle modifiée est proposée prenant en compte le ratio de viscosité des deux fluides. Dans le cas du mélange hélium-air, une cavité 2D est tout d'abord considérée. Les lois d'échelle auto-similaires pour des panaches plans stationnaires en milieu infini avant impact avec le plafond [Gebhart et al. 88] ont été reproduites numériquement pour les profils de vitesse verticale et de masse volumique sur l'axe. Puis une cavité cylindrique a été considérée pour modéliser une expérience menée au CEA [Cariteau & Tkatschenko 12]. Les résultats numériques sont comparés aux données des expériences et d'un benchmark numérique. L'effet de l'hypothèse d'axisymétrie a été mis en évidence.

Mots-clés mélange binaire, simulation, jet, panache, mélange hélium-air, mélange eau-glycerol

Résumé en anglais

This study focuses on the understanding of the dispersing and mixing mechanisms of helium in air in a semi-confined cavity. This phenomenon is an example of a low-density fluid injected in a high-density ambient fluid which results in a buoyant plume. This is an important safety issue for all hydrogen-based systems. A numerical model has been developed combining the appropriate boundary conditions with the conservation equations for the mixture mass, species mass, momentum and the state law of the mixture as well as the variation laws of the physical properties. First a laminar starting plume of a glycerol-water mixture is considered as a validation test-case by comparison with experimental data [Rogers & Morris 09]. The propagation of the axisymmetric buoyant-jet is modeled for large Grashof numbers and small injection Reynolds numbers. A good agreement has been found for the ascent velocity as well as the two types of head shape. A modified scaling law of the ascent velocity versus a modified Reynolds number is proposed to take into account for the kinetic viscosities of both fluids. For the helium-air mixture, a 2D planar air-filled cavity was first considered. The auto-similar scaling laws for steady plane plumes in unconfined environment [Gebhart et al. 88] have been reproduced for the vertical velocity and the density profiles along the vertical centerline, when considering moments before the plume impact on the top wall. Then a cylindrical container is considered to model the CEA experiment [Cariteau & Tkatschenko 12]. Numerical results are compared to experimental data and to a numerical benchmark. The effect of the axisymmetry assumption is evidence.

Keywords: binary mixture, simulation, buoyant jet, starting plume, helium-air, glycerol-water